

**DENDRITIC POST TRANSITION METAL CATALYSTS FOR HIGHLY
ACTIVE AND FORMATE SELECTIVE ELECTROCHEMICAL
REDUCTION OF CARBON DIOXIDE**

Par
Mengyang Fan

Thèse présentée pour l'obtention
du grade de Philosophiae Doctor (Ph.D.)
en sciences de l'énergie et des matériaux

Jury d'évaluation

Président du jury et
examineur interne

Prof. Mohamed Mohamedi
INRS-ÉMT

Examineur interne

Prof. Ana Tavares
INRS-ÉMT

Examineur externe

Prof. Elena Baranova
University of Ottawa

Examineur externe

Prof. Ali Seifitokaldani
McGill University

Directeur de recherche

Prof. Daniel Guay
INRS-ÉMT

ACKNOWLEDGEMENTS

Firstly, I would like to express my sincere gratitude to my supervisor, Prof. Daniel Guay, for his continuous support during my Ph.D study and related research, for his patience, motivation, and immense knowledge. His guidance helped me throughout the research and writing of this thesis. I am extremely grateful for his unconditional support and for providing me with opportunities to attend international conferences, seminars, and internships, and for encouraging me to compete for various awards. His advice on both research as well as on my career has been invaluable.

I would like to thank Prof. Mohamed Mohamedi, Prof. Ana Tavares, Prof. Elena Baranova, and Prof. Ali Seifitokaldani for being the members of my thesis committee and offering their precious comments and valuable time.

I have been fortunate to collaborate with many excellent individuals, including Prof. Ana C. Tavares, Prof. Gianluigi A. Botton, Prof. Michael H. Eikerling, Prof. David Harrington, Dr. Sagar Prabhudev, and Dr. Mohammad J. Eslamibidgoli, who gave me enormous help both in experimental and theoretical aspects. Their contributions made this thesis possible.

I would also like to thank all the group members. I am very honored to be part of such a supportive, hardworking, and inspiring group. I especially thank Dr. Sebastien Garbarino for suggesting good ideas for my experiments, thank Julie Gaudet for helping me to build up experiment setups, thank Dr. Erwan Bertin for training me to start my research, and thank Minghui Hao for revising French to this thesis.

I would like to thank Prof. Andreas Ruediger, Prof. Mohamedi, Mohamed, Prof. Shuhui Sun, and Prof. Dongling Ma, for the inspiring classes and presentations given by them. I would also like to thank the nice and helpful technicians and administrative staffs in INRS-EMT, especially Christophe Chabanier, Catalin Harnagea, Georges Lamoureux, Sylvain Gingras, Louise Hudon, H el ene Sabourin, H el ene Tanguay, Michelle Marcotte, Priscille Ernotte, and Mathieu Lesage.

I feel lucky to know a lot of friends to share life and feelings with them during the past years, particularly Qingzhe Zhang, Xin Liu, Yuting Lei, Ting Yu, Na Xu, Li Shi, Wanting He, Xiaoying Zheng, Xin Tong, Xin Chai, Xianglei Liu, Jiyun Chen, Min Zhang, Faying Li, Cheng Jiang, Chao Wang, Chen Wang, Yong Wang, Xiaolei Liu, Guolong Song, and many others.

Last but not least, special thanks to my family. Words cannot express how grateful I am to my mother and father, my grandma, and all the family members for their unconditional love, understanding, and support during my life. I love you all.

ABSTRACT

The electrochemical reduction of CO₂ (ERC) into fuels and chemicals is one way to remediate the high CO₂ emission levels arising from human activity. Among the different value-added products that can be obtained from ERC, formate/formic acid has generated sharp interest due to its widespread use and strong market. Post-transition metals such as In, Hg, Pb, and Sn, have attracted the interest of researchers due to their low price and good selectivity for formate production. However, for these post-transition elements, achieving high selectivity is still a challenge. In addition, large onset potentials and high overpotentials are requested in situations when high current density (high production rate) is needed. Therefore, the development of highly active post-transition catalysts that work effectively at ambient pressure and temperature in aqueous electrolytes with low overpotential and large reduction current remains a daunting task. Dendrite-structured catalysts are potentially interesting materials for ERC to achieve high activity and selectivity, due to their large surface area, high density of exposed surface with preferential facet orientations, and the presence of sharp tips at the dendrites' ends.

First, honeycomb porous Pb films with a dendrite-like secondary structure growing along the [100]-axis were prepared by dynamic hydrogen bubble templating (DHBT) and used for CO₂ electroreduction. Detailed physicochemical characterization of these porous films revealed that their thickness (up to 70 μm) and electrochemical active surface area (up to 1500 cm²) could be altered by current density (varied between -1 and -4 A cm⁻²) and deposition time (varied between 3 and 60 seconds). The electrochemical activity and stability of the electrodes in CO₂ electroreduction were investigated in 1 M KHCO₃ electrolyte at standard pressure and room temperature. The Faradic efficiency for formate was above 90% for electrodes with electrochemical surface areas greater than 500 cm², which was attributed to an increased fraction of the [100] surfaces. Compared to plate Pb electrode, the ERC onset potential on the porous Pb dendrites electrode was decreased by 160 mV. The porous Pb film deposited at -4.0 A cm⁻² and 40 seconds proved to be a highly active and stable electrode, with a partial current density (j_{formate}) of -7.5 mA cm⁻² and a Faradaic efficiency of formate of 97% at an overpotential of 800 mV after 6 hours of electrolysis.

Second, the porous Pb dendrite was further modified by highly selective and efficient bismuth dendrites (Bi_{den}). A detailed investigation of the atomic structure of Bi dendrites was achieved through high-resolution transmission electron microscopy (HR-TEM). It was shown that Bi dendrites are made of single crystals with a rhombohedral structure, which grow in the [010]

direction. The terminated dendrite surface is not entirely smooth, but carries surface irregularities in the form of surface steps and high-index facets. Selective decoration of the low-index facets of Bi dendrites was achieved, showing that these surface steps and high-index facets are the most active Bi surface sites. In an H-cell, the ERC at dendritic Bi occurs with a high Faradaic efficiency for formate (98%), and high current density (18.8 mA cm^{-2}) and production rate ($344 \text{ } \mu\text{mol cm}^{-2} \text{ h}^{-1}$) at low overpotential (600 mV). The production rate may be further improved to $1.63 \text{ mmol cm}^{-2} \text{ h}^{-1}$ (or 95 mA cm^{-2} at -0.82 V vs. RHE) when tested in conditions where the CO_2 flux is not limiting performance (high-pressure flow-cell measurements), a three-fold increase over the reported benchmark.

Third, an alloyed Sn_1Pb_3 electrode featuring a dendrite-like structure was fabricated. The deposition conditions for the Sn_1Pb_3 electrode were optimized. Continuous flow-cell electrolysis was applied on the optimal Sn_1Pb_3 electrode, and a high production rate of $295 \text{ } \mu\text{mol cm}^{-2} \text{ h}^{-1}$ was achieved with a current of 17.2 mA cm^{-2} at a low overpotential of 500 mV. The Faradaic efficiency for formate formation was close to 100% in a large potential range from -0.72 V to -1.12 V vs. RHE . Compared to the single dendritic Pb, the ERC onset potential on the dendritic Sn_1Pb_3 electrode was 80 mV lower. Density functional theory computations were performed to uncover the origin of the decrease in onset potential upon alloying Pb with Sn. Explicit treatment of water molecules in DFT calculations was revealed to be crucial in achieving agreement with experimentally-measured onset potentials.

Keywords: carbon dioxide, electrochemical reduction, formate, post-transition metals, lead-based catalysts, dendritic structure, alloy materials, DFT calculations

RÉSUMÉ

La réduction électrochimique du CO₂ (ERC) en carburant et produit chimique est l'un des moyens de remédier aux niveaux élevés d'émissions de CO₂ résultant de l'activité humaine. Parmi les différents produits à valeur ajoutée qui peuvent être obtenus lors de l'ERC, le formiate/acide formique a suscité un vif intérêt en raison de sa large utilisation et de son marché favorable. Les métaux de post-transition, tels que In, Hg, Pb et Sn, ont suscité l'intérêt des chercheurs en raison de leur prix faible et de leur bonne sélectivité pour la production de formiate lors de la réduction électrochimique du processus de CO₂. Cependant, sur ces éléments post-transition, une sélectivité élevée s'accompagne d'une forte demande de pression de CO₂, les potentiels d'initiation sont importants et les surtensions élevées lorsqu'une forte densité de courant (taux de production élevé) est requise. Par conséquent, il est toujours un défi à développer des catalyseurs de post-transition qui fonctionnent bien à la pression atmosphérique, à la température ambiante et à l'électrolyte aqueux, et qui atteignent une faible surtension et un courant de réduction important. Les catalyseurs en structure de type dendrite sont potentiels pour l'ERC hautement actif et sélectif en raison de leur grande surface spécifique, d'une grande densité de surface exposée avec des orientations de facettes préférentielles et de la présence de pointes acérées à la fin des dendrites.

Premièrement, des films de Pb poreux en nid d'abeille avec une structure secondaire de type dendrite se développant le long de l'axe [100] ont été préparés par "Dynamic Hydrogen Bubble Templating" (DHBT) et utilisés pour l'électro-réduction du CO₂. Une caractérisation physico-chimique détaillée des films poreux a révélé que l'épaisseur (jusqu'à 70 µm) et la surface active électrochimique (jusqu'à 1500 cm²) des films poreux en Pb pouvaient être ajustées par la densité de courant (variant entre -1 et -4 A cm⁻²) et le temps de déposition (variant entre 3 et 60 s). L'activité électrochimique et la stabilité des électrodes pour l'électro-réduction du CO₂ ont été étudiées sur l'électrolyte KHCO₃ 1 M à la pression standard et à la température ambiante. L'efficacité faradique pour le formiate était supérieure à 90% pour les électrodes avec des surfaces électrochimiques supérieures à 500 cm² et elle a été attribuée à une fraction accrue des [100] surfaces. Comparé à l'électrode de plaque Pb, le potentiel de début d'ERC sur l'électrode poreuse de dendrites de Pb était de 160 mV diminué. Le film de Pb poreux déposé à -4,0 A cm⁻² et 40 secondes s'est avéré une électrode très active et stable, avec une densité de courant partielle (j_{formate}) de -7,5 mA cm⁻² et une efficacité faradique du formiate de 97% à une surtension de 800 mV après 6 heures d'électrolyse.

Deuxièmement, les dendrites poreuses de Pb ont été encore modifiées par des dendrites de bismuth hautement sélectives et efficaces (Bi_{den}). Une étude détaillée de la structure atomique des dendrites Bi a été réalisée par microscopie électronique à transmission à haute résolution (HR-TEM). Il a été démontré que les dendrites Bi sont constituées de monocristaux à structure rhomboédrique et qu'elles poussent dans le sens [010]. La surface de dendrite terminée n'est pas entièrement lisse mais présente des irrégularités de surface sous la forme de gradin et de facette à indice élevé. Une décoration sélective des facettes à faible indice des dendrites Bi a été réalisée pour montrer que ces gradins de surface et ces facettes à indice élevé sont les sites de surface Bi les plus actifs. Dans une cellule en forme H, l'ERC à dendritique Bi se produit avec une efficacité faradique élevée pour le formiate (98%), et une grande densité de courant ($18,8 \text{ mA cm}^{-2}$) et un taux de production ($344 \mu\text{mol cm}^{-2} \text{ h}^{-1}$) à faible surtension (600 mV). Le taux de production peut être encore amélioré à $1,63 \text{ mmol cm}^{-2} \text{ h}^{-1}$ lorsqu'il est testé dans des conditions où le flux de CO_2 ne limite pas ses performances, qui est 3 fois plus grande que la référence.

Troisièmement, une électrode de Sn_1Pb_3 bien alliée présentant une structure de type dendrite a été fabriquée. Les conditions de dépôt de l'électrode Sn_1Pb_3 ont été optimisées. Une électrolyse en cellule à écoulement continu a été appliquée sur l'électrode optimale Sn_1Pb_3 , et un taux de production élevé de $295 \mu\text{mol cm}^{-2} \text{ h}^{-1}$ a été atteint avec un courant de $17,2 \text{ mA cm}^{-2}$ à une faible surtension de 500 mV. L'efficacité faradique pour la formation de formiate est proche de 100% dans une large plage de potentiel de -0,72 V à -1,12 V par rapport à RHE. Comparé au Pb dendritique unique, le potentiel de début de l'ERC sur l'électrode dendritique de Sn_1Pb_3 était inférieur de 80 mV. Des calculs de théorie fonctionnelle de la densité ont été effectués pour découvrir l'origine de la diminution du potentiel de début lors de l'alliage de Pb avec Sn. Le traitement explicite des molécules d'eau dans les calculs DFT s'avère crucial pour parvenir à un accord avec les potentiels de début mesurés expérimentalement.

Mots-clés: dioxyde de carbone, réduction électrochimique, formiate, métaux post-transition, catalyseurs à base de plomb, structure dendritique, matériaux d'alliage, calculs DFT

TABLE OF CONTENTS

ACKNOWLEDGEMENTS	III
ABSTRACT	V
RÉSUMÉ	VII
TABLE OF CONTENTS	IX
LIST OF FIGURES	XIII
LIST OF TABLES	XVII
LIST OF SYMBOLS AND CHEMICAL FORMULA	XIX
LIST OF ABBREVIATIONS AND ACRONYMS	XXI
1 INTRODUCTION	1
1.1 Background and Motivations.....	1
1.1.1 <i>CO₂ emission and climate change</i>	1
1.1.2 <i>CO₂ storage and CO₂ conversion</i>	1
1.1.3 <i>Electrochemical reduction of CO₂</i>	2
1.2 Electrochemical Reduction of CO ₂ Fundamentals.....	2
1.2.1 <i>Thermodynamic of CO₂ electroreduction</i>	3
1.2.2 <i>Kinetic of CO₂ electroreduction</i>	4
1.2.3 <i>CO₂ electroreduction figure of merit</i>	5
1.3 Metal Catalysts and Mechanisms for ERC	7
1.3.1 <i>Possible reaction pathways and products distribution</i>	8
1.3.2 <i>Selective catalysts for formate/formic acid</i>	9
1.3.3 <i>Selective catalysts for carbon monoxide</i>	13
1.3.4 <i>Selective catalysts for high-order products</i>	15
1.3.5 <i>Challenges and opportunities</i>	16
1.4 Strategies to Enhance the ERC Performance on Metal Catalysts.....	17
1.4.1 <i>Surface roughness enhancing</i>	17
1.4.2 <i>Surface structure tuning</i>	19
1.4.3 <i>Surface decoration</i>	21
1.5 ERC on Hierarchical Dendritic Metal Electrodes	22
1.5.1 <i>Dendritic single metals</i>	22
1.5.2 <i>Dendritic bimetallic metals</i>	27
1.6 Thesis Objectives and Organizations	29
1.6.1 <i>Thesis objectives</i>	29
1.6.2 <i>Thesis organizations</i>	29

2	EXPERIMENTAL	33
2.1	Chemicals and Materials.....	33
2.2	Synthesis of Dendritic Pb Porous Electrode	33
2.2.1	<i>Preparation of Pb substrate</i>	<i>33</i>
2.2.2	<i>Deposition of dendritic Pb porous electrode</i>	<i>33</i>
2.3	Synthesis of Dendritic Bi Modified Porous Pb Electrode	34
2.3.1	<i>Optimization of dendritic Bi</i>	<i>34</i>
2.3.2	<i>Synthesis of dendritic Bi modified porous Pb electrode.....</i>	<i>34</i>
2.4	Synthesis of Dendritic SnPb Binary Alloy Electrodes	34
2.4.1	<i>Optimization of the composition of SnPb binary alloys.....</i>	<i>34</i>
2.4.2	<i>Optimization of the deposition condition of the SnPb alloy electrode.....</i>	<i>34</i>
2.5	Characterizations	35
2.5.1	<i>Physical characterizations</i>	<i>35</i>
2.5.2	<i>Electrochemical characterizations</i>	<i>35</i>
2.6	Products Analysis.....	36
2.7	Flow-Cell Test	36
2.8	Theoretical Calculations.....	37
3	DENDRITIC LEAD FOR HIGHLY EFFICIENT ERC	39
3.1	Introduction.....	40
3.2	Experimental Section	41
3.2.1	<i>Preparation of porous Pb film</i>	<i>41</i>
3.2.2	<i>Physical characterization of porous Pb films</i>	<i>42</i>
3.2.3	<i>Electrochemical characterization of porous Pb films</i>	<i>42</i>
3.3	Results and Discussions	43
3.3.1	<i>Physico-chemical characterization of porous Pb films.....</i>	<i>43</i>
3.3.2	<i>Electrocatalytic activity of porous Pb films for CO₂ reduction.....</i>	<i>49</i>
3.4	Conclusions.....	56
	Acknowledgements	57
3.5	Supporting Information.....	58
4	DENDRITIC BISMUTH MODIFIED LEAD ELECTRODES	71
4.1	Introduction.....	73
4.2	Experimental Section	74
4.2.1	<i>Preparation of Bi dendrites</i>	<i>74</i>
4.2.2	<i>Physical characterization of Bi dendrites</i>	<i>75</i>
4.2.3	<i>Electrochemical characterization of Bi dendrites</i>	<i>75</i>
4.2.4	<i>Flow-cell</i>	<i>76</i>

4.3	Results and Discussions	77
4.3.1	<i>Condition optimization and physiochemical characterization of Bi dendrites</i>	77
4.3.2	<i>Catalytic activity of Bi dendrites and the Pb substrate effect</i>	80
4.3.3	<i>Electrode stability</i>	84
4.3.4	<i>Identification of Bi active sites for high selectivity and long durability</i>	86
4.3.5	<i>Continuous flow-cell test of the Bi_{den}/Pb_{porous} electrode</i>	88
4.4	Conclusions	89
	Acknowledgements	90
4.5	Supporting Information	90
5	DENDRITIC TIN AND LEAD BINARY ALLOY ELECTRODE	101
5.1	Introduction	103
5.2	Experimental Section	104
5.2.1	<i>Preparation of SnPb binary dendrites</i>	104
5.2.2	<i>Physio-chemical and electrochemical characterization</i>	104
5.2.3	<i>Products measurement and flow-cell test</i>	105
5.2.4	<i>Computational details</i>	106
5.3	Results and Discussions	106
5.3.1	<i>Structure characterization and analysis</i>	106
5.3.2	<i>Selectivity and activity for CO₂ electrochemical reduction</i>	108
5.3.3	<i>Mechanism investigation of dendritic Sn₁Pb₃ for enhanced activity</i>	110
5.3.4	<i>Thermodynamic and kinetic analysis</i>	115
5.4	Conclusions	118
	Acknowledgements	119
5.5	Supporting Information	119
6	CONCLUSIONS AND PERSPECTIVES	133
6.1	Conclusions	133
6.2	Perspectives	135
	BIBLIOGRAPHY	137
	LIST OF PUBLICATIONS, CONFERENCE PRESENTATIONS, AND AWARDS	153
	SOMMAIRE RÉCAPITULATIF	155

LIST OF FIGURES

Figure 1.1	Schematic illustration of a typical ERC reaction system in aqueous electrolyte. 2
Figure 1.2	Periodic table for CO ₂ reduction products at -2.2 V vs. SCE in low-temperature 0.05 mol dm ⁻³ KHCO ₃ solution. ³⁵ 7
Figure 1.3	Schematic illustration of simplified reaction mechanism for ERC in aqueous solution. 8
Figure 1.4	Reaction schemes of major pathways considered for CO ₂ reduction toward C ₁ and C ₂₊ products. The green path denotes C ₂ production via OC–CHO coupling; the blue and red path represents C ₂ production via protonation of OCCO to form OCCHO and OCCOH, respectively; the yellow path represents C ₂ production via OC–CHOH coupling. The black path denotes C ₁ production via CHOH and the dashed CH ₂ O. ¹²¹ 16
Figure 1.5	Examples of roughening smooth surfaces. (a-c) Pb electrode, and (d-f) Sn electrode. SEM of (a) polished Pb and (b) roughened Pb after four cycles. (c) Faradaic efficiency of formic acid and H ₂ formation on both roughened and smooth Pb electrodes. ⁸⁰ HRTEM images of (d) Sn-NWs (inset: magnified images), and (e) after acid etch conversion into Sn-pNWs with increased grain boundaries (inset: magnified image). (f) Faradaic efficiency vs. potential for all carbon products. ⁸⁸ 17
Figure 1.6	An example of dispersing target catalyst onto high-surface-area support and its effect on enhancing ERC performance. Scheme illustration for the formation of Sn quantum sheets confined in graphene, (b) TEM image, (c) HRTEM image. (d) Chrono-Amperometry results at the potentials of -1.8 V versus SCE. (e) Faradaic efficiencies for formate at each applied potentials for 4h. ⁸⁷ 18
Figure 1.7	An example of defect-rich Bi-based catalyst. (a) STEM-HAADF image, and (b) corresponding FFT pattern of a Bi ₂ O ₃ nanotube (NT). (c) Schematic illustration of the structure of Bi ₂ O ₃ NTs; the black spheres represent the crystalline inner walls, and the red and purple spheres represent the fragmented outer walls. ¹²⁸ 20
Figure 1.8	An example of High-index Au catalyst. (a) Single nanoparticle with model of concave Rhombic Dodecahedral Au. (b) HRTEM images of eight different sections displaying atomic arrangements. Each atom is marked with a colored sphere. (c) FE _{CO} as function of potentials on different Au catalysts. ⁵⁶ 21
Figure 1.9	Examples of surface decorations. (a) ERC production rate as function of electrolysis potential. The Cu surfaces was decorated by Pb adatoms using under-potential deposition. ¹³⁵ (b) A scheme illustration of surface-Molecule-Mediated Ag Nanoparticles. ⁹⁸ 22
Figure 1.10	Examples of dendritic precious metal catalysts. (a-g) A typical example of enhancing ERC performance at an Au dendrite electrode by higher surface energy facets. SEMs showing the angle between primary growth directions and the angles between adjacent edges of the Au crystals in (a,b) plates and (c,d) dendrites. (e) Cartoons of the plate growth (left and center) and the dendrite growth (right). Arrows represent the growth velocity of corners and edges. ¹³⁷ (Copyright © 2018, American Chemical Society). In (h, j, and l), TEM images; and in (i, k, and m) electric field distribution of Au needles, rods and particles deduced using Kelvin probe atomic force microscopy. (n) Current–voltage curves on Au needles, rods and particles obtained from the linear sweep voltammetry scans. Scan rate, 10 mV s ⁻¹ . (o) CO Faradaic efficiencies on Au needles, rods and particles at different applied potentials. ¹³⁸ 24
Figure 1.11	Examples of dendritic non-noble metal catalyst. Characterization of Bi dendrite electrode. Top-down SEM images of (a) pristine Bi foil, and (b) Bi dendrite. (c) Comparison of performance in terms of total current density (line; left axis) and Faradaic efficiency of

formate (dot; right axis) at -0.74 V for 1 h. DFT calculation results on the CO_2 -to-formate reduction reaction pathways for various possible Bi planes of (003), (012), (110), and (104). (d) Schematic diagram of three possible reaction pathways; path 1 via the formation of $^*\text{COOH}$ intermediate, path 2 via the formation of $^*\text{OCOH}$ intermediate, and path 3 via the formation of $^*\text{H}$. Reaction free energy diagrams for the reaction (e) path 1, (f) path 2, and (g) path 3, when zero overpotential is applied (bias potential $U = -0.21$ VSHE). Noting that (012), (110), and (104) planes are preferentially developed for Bi dendrite compared with the close-packed surface of (003) that is dominant in Bi foil.⁴⁷ (Copyright © 2017, American Chemical Society)..... 25

Figure 1.12	(a-e) Example of a Sn-decorated Cu dendrites electrode. (a) SEM image of Cu-Sn dendrites. (b) Scanning TEM image and (c) high-resolution scanning TEM-EDS elemental mapping of a single Cu-Sn dendrite. (d) High-resolution TEM image of a nanostructure at the tip of a Cu-Sn dendrite. (e) Electron scattering pattern from the region in d. ¹⁵⁰ (Copyright © 2019, American Chemical Society). (f-g) An example of AgCu codeposited dendrites. (f) SEM images of AgCu foam. (g) Raman CO adsorption band area as function as potential. A comparison between single Cu foam and bimetallic AgCu foam. ¹⁵² (Copyright © 2019, American Chemical Society) 28
Figure 3.1	HRSEM images of a porous Pb film deposited at -4.0 A cm^{-2} during 40 seconds. Three different magnifications of the same electrode are shown in (a), (b) and (c). The red circles are representative examples of tips that were used to measure the tip diameter. 44
Figure 3.2	STEM images of a cross-section of prepared from the porous Pb film deposited at -4.0 A cm^{-2} and 40 seconds. (a) Low magnification annular dark-field STEM image of a few filaments presents in the cross-section. The red arrow shows the length and orientation of a perfectly oriented crystal with the $\langle 001 \rangle$ long axis. The segments beyond the arrow are slightly misoriented (by few degrees) with respect to the red arrow direction. Other filaments in the field of view would be randomly oriented with respect to the longest wire. Small cavities (dark spots within the filaments) are also observed within the filaments. A very thin oxide layer is also observed (with intermediate contrast) at the edges (hence the surfaces) of the filaments. (b) High-resolution STEM image of the high-quality crystalline Pb lattice. The major sets of planes are identified with the color-coded arrows (c) Lattice image in the proximity of a cavity showing the very faceted nature of the surfaces with the lattice planes identified in the color coded arrows and Miller indices. 45
Figure 3.3	SEM images of (a, g) a Pb plate and porous Pb films deposited at (b, h), -0.1 A cm^{-2} , (c, i) -0.5 A cm^{-2} , (d, j) -1.0 A cm^{-2} , (e, k) -2.0 A cm^{-2} , and ((f, l) -4.0 A cm^{-2} . The deposition time was 20 seconds. 46
Figure 3.4	Variations of the electrochemical active surface area (EASA) of porous Pb films as a function of (a) the current density at a deposition time of 20 s, and (b) the deposition time at a deposition current density of -4.0 A cm^{-2} 49
Figure 3.5	In (a), linear sweep voltammeter of a Pb plate and porous Pb films in Ar- and CO_2 -saturated 1 M KHCO_3 . The scan rate was 5mV s^{-1} . In (b), variation of the CO_2 electroreduction (ERC) current density at different electrolysis potentials. In (c), variation of the formate Faradic efficiency with respect to the electrode potential. In (d), variation of the CO_2 reduction overpotential with respect to the logarithm of the current density. The porous Pb film was deposited at -4.0 A cm^{-2} during 40 seconds. 50
Figure 3.6	In (a), variation of the partial current density at -0.99 V for the formation of formate with respect to the electrochemically active surface area. In (b) and (c), variation of the formate faradic efficiency with respect to the deposition current density and deposition time, respectively. 52
Figure 4.1	SEM micrographs of $\text{Bi}_{\text{den}}/\text{Pb}_{\text{plate}}$ (a, b, c and d) and $\text{Bi}_{\text{den}}/\text{Pb}_{\text{porous}}$ (e, f, g, and h) at different magnifications. Top view (a through g) and cross-sectional (h) views are shown. 78

Figure 4.2	Elucidation of Bi dendritic structure with an aberration-corrected STEM. (a, b) HAADF-STEM images showing dendritic structure at different magnifications. Note image (b) is shown after bandpass filtering. (c, d) Comparison of observed dendritic lattice arrangement with Bi rhombohedral (R-3m) model along N(100). (e) HAADF-STEM image highlighting the detailed surface-structure of the dendrite. 79
Figure 4.3	In (a), linear sweep voltammograms of Bi-modified Pb electrodes in the CO ₂ -saturated 0.5 M KHCO ₃ electrolyte, with Pb electrodes as the comparison. Scan rate of 5 mV s ⁻¹ , (b) formate faradaic efficiency (formate FE), (c) H ₂ faradaic efficiency (H ₂ FE), and (d) partial current density of formate (j_{formate}) with respect to electrolysis potential in the CO ₂ -saturated 0.5 M KHCO ₃ electrolyte. 82
Figure 4.4	Variation of (a) j , (b) $\log(1/R_{\text{ct}})$ and (c) C_{eff} with respect to iR-corrected potential. The data are shown for Bi _{den} /Pb _{porous} electrode in CO ₂ -saturated 0.5 M KHCO ₃ electrolyte. The current was allowed to stabilize during 30 minutes before starting the IES measurements. 84
Figure 4.5	Variation of (a) the current density and (b) the formate faradaic efficiency as a function of the polarization time. These measurements were performed at -0.82 V vs. RHE on Bi _{den} /Pb _{porous} electrode in CO ₂ -saturated 0.5 M KHCO ₃ electrolyte. SEM images of Bi _{den} /Pb _{porous} electrode (c) before and (d) after 15 h of CO ₂ electrolysis are shown. 85
Figure 4.6	Variation of (a) the loss of Bi EASA and (b) loss of ERC activity with the number of Pb deposition pulses. Details of the experimental procedure are given in the text. The variation of ERC activity loss vs Bi EASA loss is depicted in (c). 87
Figure 4.7	Schematic illustration of (a) flow-cell system and (b) core of the cell. (c) Variation of the current density with the electrolysis time of Bi _{den} /Pb _{porous} electrode. See the main text for all the experimental details. 89
Figure 5.1	SEM images of (a, b) pure Pb, and (c, d) Sn ₁ Pb ₃ alloy. 107
Figure 5.2	In (a), XRD patterns of pure Pb and Sn ₁ Pb ₃ alloy deposits. The expected diffraction peaks of Pb (JCPDS card No. 00-004-0686) and β -Sn (JCPDS card No. 00-004-0673) are also indicated. A restricted 2θ range is shown in (b) to emphasize peaks displacement. Black curve: pure Pb, and red curve: Sn ₁ Pb ₃ alloy. 108
Figure 5.3	In (a), linear sweep voltammetry curves in 0.5 M KHCO ₃ electrolyte recorded at 5 mV s ⁻¹ . In (b), formate Faradaic Efficiency (FE_{formate}) recorded after 30 minutes of electrolysis at each potential. In (c), current density recorded at a Sn ₁ Pb ₃ alloy electrode in a flow-cell system. 110
Figure 5.4	Energy diagrams for CO ₂ reduction. In (a), gas phase conditions at 0 V. In (b), with 12 water molecules at 0 V. 113
Figure 5.5	Optimized structures of HCOO* with 12 water molecules on (a and b) Pb(100) and (c and d) Sn ₁ Pb ₃ (100). Top view and side views are shown in (a and c) and (b and d), respectively. 115

LIST OF TABLES

Table 1.1	Selected standard potentials of CO ₂ reduction under standard conditions in aqueous solution: at pH=7, 1 atm, and 25 °C. ²⁹	3
Table 1.2	Summary of formate/formic acid selective metal catalysts for ERC under standard conditions in aqueous solution: at 1 atm, and 25 °C.....	12
Table 1.3	Summary of CO selective metal catalysts for ERC under standard conditions in aqueous solution: at 1 atm, and 25 °C.....	14
Table 3.1	Comparison of FE _{formate} on different Sn-, Bi- and Pb-based catalysts.	56
Table S4.1	Fitting parameters of Biden/Pbporous electrodes at different applied electrode potentials obtained by using the following equivalent circuit. CPE1 has admittance $T(i\omega)^\phi$	98
Table S4.2	Comparison of CO ₂ electrochemical reduction performance for dendritic Bi and recently reported Bi-cased catalysts in the literature.....	99
Table S5.1	Onset potential vs SHE of different electrodes.	130
Table S5.2	Comparison of the performance of CO ₂ electroreduction towards formate on Pb based materials.....	130
Table S5.3	Thermodynamic quantities of gas-phase molecules (eV). The adsorption energy, zero-point energy (ZPE), and entropy (TS).....	130
Table S5.4	Comparison of the binding energies of HCOO* in parallel and perpendicular configurations at Pb(100) and Sn ₁ Pb ₃ (100) surface. Twelve water molecules were included in the DFT calculations in all cases.	131
Table S5.5	The equilibrium potential of step <i>i</i> , <i>E_{ieq}</i> , on Sn ₁ Pb ₃ (100) and Pb(100), calculated using DFT results from Section 5.3.3.	131

LIST OF SYMBOLS AND CHEMICAL FORMULA

α	Charge transfer coefficient
A_{ox}	Oxidized species
Ag	Silver
Au	Gold
A_{red}	Reduced species
C_{ox}	Chemical activity of oxidizing agent
C_{red}	Chemical activity of reducing agent
CH ₄	Methane
C ₂ H ₄	Ethylene
CH ₃ CHO	Ethanal
CH ₃ OH	Methanol
CO	Carbon monoxide
CO ₂	Carbon dioxide
CO ₂ ^{•-}	CO ₂ ^{•-} anion radical
COOH*	Carboxyl intermediate
E	Electrode potential
E^0	Standard reaction potential
E_{cell}	Cell voltage of full cell
E_{eq}	Equilibrium potential
E_{eq}^{β}	Equilibrium potential of a specific product β
E_{eq}^{OER}	Equilibrium potential of oxygen evolution reaction
E_{red}^0	Standard half-cell reduction potential
e ⁻	Electron
EE	Energy efficiency
F	Faraday constant
FE	Faradic efficiency

ΔG	Gibbs free energy change
HCHO	Formaldehyde
HCOOH	Formic acid
HCOOH _{ads}	Formic acid adsorbate
HCOO*	Formate intermediate
Hg	Mercury
H ₂ SO ₄	Sulfuric acid
In	Indium
j	Electrode net current density
j_0	Exchange current density
j_a	Anode current density
j_c	Cathode current density
j_{co}	Partial current density of CO
$j_{formate}$	Partial current density of formate
j_{total}	Total current density
KHCO ₃	Potassium hydrogen carbonate
K ₂ SO ₄	Potassium sulfate
NaHCO ₃	Sodium bicarbonate
NaOH	Sodium hydroxide
Na ₂ SO ₄	Sodium sulfate
Ni	Nickle
Pb	Lead
Pd	Palladium
Q_{total}	Total electron transfer charge
R	Universal gas constant
Sn	Tin
T	Absolute temperate
z	Number of electron transfer

LIST OF ABBREVIATIONS AND ACRONYMS

Bi _{den}	Bismuth dendrites
CCS	Carbon capture and storage
CNTs	Carbon nanotubes
CNF	Carbon nanofibers
CV	Cyclic voltammetry
DFT	Density functional theory
DHBT	Dynamic hydrogen bubble template
EASA	Electrochemical active surface area
EDX	Energy-dispersive X-ray spectroscopy
EEL	Electron energy loss
EIS	Electrochemical impedance spectroscopy
ERC	Electrochemical reduction of CO ₂
FFT	Fast Fourier transform
FIB	Focused ion beam
FRA	Frequency response analyzers
GC	Gas chromatography
GDL	Gas diffusion layer
GNR	Graphene nanoribbon
HAADF	High-angle annular dark-field
HER	Hydrogen evolution reaction
HR-TEM	High-resolution transmission electron microscopy
IC	Ion chromatography
IPCC	Intergovernmental panel on climate change
KHNTs	Mesoporous hollow kapok-tubes

LSV	Linear sweep voltammetry
MEA	Membrane electrode assembly
N.R.	Not reported
NPs	Nanoparticles
NTs	Nanotubes
OER	Oxygen evolution reaction
Pb _{plate}	Lead plate
Pb _{porous}	Porous Lead
RHE	Reversible hydrogen electrode
SEM	Scanning electron microscope
SCE	Saturated calomel electrode
STEM	Scanning transmission electron microscope
TEM	Transmission electron microscope
UPD	Under-potential deposition
XRD	X-ray diffraction

1 INTRODUCTION

1.1 Background and Motivations

1.1.1 CO₂ emission and climate change

Carbon dioxide (CO₂) is the primary greenhouse gas released because of human activity. CO₂ is released into the atmosphere due to forest fires, fossil fuel combustion, and industrial processes. According to a 2005 special report by the Intergovernmental Panel on Climate Change (IPCC),¹ average global CO₂ emissions increased 1.4% per year between 1995 and 2001, with total global CO₂ emissions reaching 23,684 Mt y⁻¹ in 2001. The unrestricted emission of CO₂ resulting from human activity has exceeded the recycling capability of CO₂ in nature, resulting in a series of environmental problems, including a rise in global temperatures. The IPCC Global Warming reported in 2018 noted that the Earth's surface temperature keeps increasing every decade, and positively correlated to the cumulative CO₂ emissions.² This increases the possibility of extreme weather, the melting of polar ice, and rapidly rising global sea levels, which threaten the entire planet.

1.1.2 CO₂ storage and CO₂ conversion

Carbon sequestration is one of the strategies to prevent the release of CO₂ to the atmosphere.^{2,3} The carbon capture and storage (CCS) started from 1972 in Texas, and now there are 23 large-scale CCS facilities in operation or under construction, capturing almost 40 Mt y⁻¹ of CO₂ from industrial point sources.⁴ There are several main options to store this captured CO₂: ocean storage, geological storage, and mineralization.⁵ The ocean storage consists of the CO₂ injection at great depths forming hydrates or dissolving.⁶ The ocean is considered to be the largest store of CO₂.⁶ However, the increase of CO₂ concentration leads to ocean acidification, affecting the growth of marine life such as the corals. The geological storage is considered a viable way to store CO₂.^{7,8} This method achieves CO₂ injection into depleted oil and gas fields, coal mines, and other geological structure layers. However, the injected CO₂ will acidify the groundwater leading to the dissolution of heavy metals and contamination of the portable water nearby.⁷ The mineralization of CO₂ is using chemical reactions to solidify CO₂ into inorganic carbonates, which provides an opportunity to storage CO₂ permanently during a long period.^{9,10} However, the cost of this CO₂ disposal way is huge, which is rarely economically viable. Thence, the CO₂ emitting cost will be very high and economically unaffordable if the CO₂ cannot be recycled and reutilized.

1.1.3 Electrochemical reduction of CO₂

The conversion of CO₂ into valuable chemicals is one way to facilitate carbon recycling and the reuse of CO₂. This conversion process requires energy and may be achieved through biochemical,^{11,12} photochemical,¹³⁻¹⁹ and electrochemical methods.²⁰⁻²⁵ The electrochemical reduction of CO₂ (ERC) has attracted attention in recent years due to several advantages: (1) The electricity used to drive the process can originate from intermittent energy sources such as solar and wind, allowing for off-the-grid energy storage that can be easily reverted back into the grid as and when needed; (2) The ERC conditions, such as temperature, pressure, and electrolysis potential, are easily controlled; (3) The ERC setup is compact and can be easily scaled up.^{20,26,27} However, several challenges remain before this process can be industrialized: (1) ERC's slow kinetics lead to high electrolysis potentials; (2) The low energy efficiency results in low economic viability for ERC; (3) Insufficient catalyst stability, which leads to high operating costs for ERC.²⁸ Therefore, it is necessary to design and develop highly efficient and stable catalysts for ERC to make this process more feasible and economical.

1.2 Electrochemical Reduction of CO₂ Fundamentals

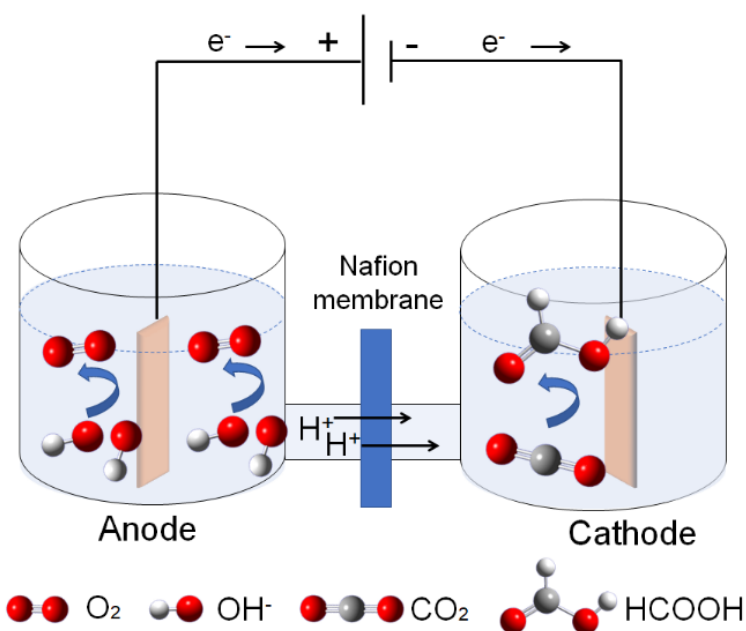


Figure 1.1 Schematic illustration of a typical ERC reaction system in aqueous electrolyte.

Electrochemical reduction of CO₂ is a heterogeneous reaction that the reaction occurs at the electrode-electrolyte interface. The ERC reaction system generally includes a cathode and an anode. The cathode is where the ERC reaction occurs, while the anode is where the oxygen

evolution reaction takes place. The cathode and anode are separated by an ion-exchange membrane, which allows the transfer of protons and prevents the oxidation of the reduction products at the anode. An illustration of a typical ERC system is shown in Figure 1.1.

1.2.1 Thermodynamic of CO₂ electroreduction

The CO₂ electrochemical reduction process needs to overcome thermodynamic barriers. The Gibbs free energy change is associated with the ERC potential difference:

$$\Delta G = -zFE^0 \quad (1.1)$$

where ΔG represents Gibbs free energy change, z is the number of electron transfer, F is the Faraday constant, and E^0 is the standard reaction potential. The ERC can proceed through 2 electrons ($2e^-$), $4e^-$, $6e^-$ and $8e^-$ pathways. The ERC standard electrode potentials are listed in Table 1.1. The reduction of H^+ is the possible competing reaction during the CO₂ electrochemical reduction process.

Table 1.1 Selected standard potentials of CO₂ reduction under standard conditions in aqueous solution: at pH=7, 1 atm, and 25 °C.²⁹

Thermodynamic half-electrochemical reactions	Standard electrode potentials (V vs. SHE)
$CO_2 + e^- \rightarrow CO_2^{\bullet-}$	-1.90
$CO_2 + 2H^+ + 2e^- \rightarrow CO + H_2O$	-0.53
$CO_2 + 2H^+ + 2e^- \rightarrow HCOOH$	-0.61
$CO_2 + 4H^+ + 4e^- \rightarrow HCHO + H_2O$	-0.48
$CO_2 + 6H^+ + 6e^- \rightarrow CH_3OH + H_2O$	-0.38
$CO_2 + 8H^+ + 8e^- \rightarrow CH_4 + 2H_2O$	-0.24
$2H^+ + 2e^- \rightarrow H_2$	-0.41

The one-electron reduction of CO₂, which forms the CO₂^{•-} radical, occurs at a highly negative potential (-1.90 V vs. SHE) and is thermodynamically unfavorable (Table 1.1). A proton-assisted approach to CO₂ reduction, lowers the thermodynamic barrier significantly, such as those $2e^-$, $4e^-$, $6e^-$, $8e^-$ reactions show in Table 1.1. The thermodynamic barrier varies from -0.24 to -0.61, which is much lower than -1.9 V. Catalysts can promote such proton-assisted, multi-electron pathways.

1.2.2 Kinetic of CO₂ electroreduction

In addition to the thermodynamic barriers, the ERC efficiency is also dependent on the reaction kinetics. The ERC process at the interface between electrode and electrolyte is generally composed of three steps: (1) In the first mass transfer step, the reactant species approaches to the electrode surface; (2) In the second electrochemical step, the electrons transfer across the interface; (3) In the third mass transfer step, the product species desorb from the surface and diffuse into the electrolyte.^{30,31}

For a given electrode reaction:



The fundamental relationships in electrochemical kinetics have been shown in the Butler-Vomer equation, which describes how the electrical current depends on the electrode potential. When all sorts of the mass transport limitations are neglected, the current-potential relation is only determined by the kinetics of charge transfer, the cathode and anode current density is described in equation 1.3 and 1.4, respectively:

$$j_c = -j_0 \cdot \exp\left[\frac{-\alpha z F}{RT}(E - E_{eq})\right] \quad (1.3)$$

$$j_a = j_0 \cdot \exp\left[\frac{(1-\alpha)z F}{RT}(E - E_{eq})\right] \quad (1.4)$$

therefore, the electrode net current is:

$$j = j_c + j_a = j_0 \cdot \left\{ \exp\left[\frac{(1-\alpha)z F}{RT}(E - E_{eq})\right] - \exp\left[\frac{-\alpha z F}{RT}(E - E_{eq})\right] \right\} \quad (1.5)$$

to compact it:

$$j = j_0 \cdot \left\{ \exp\left[\frac{(1-\alpha)z F}{RT}\eta\right] - \exp\left[\frac{-\alpha z F}{RT}\eta\right] \right\} \quad (1.6)$$

Where j_c represents the cathode current density, j_a represents the anode current density, j represents the electrode net current density, j_0 represents the exchange current density, E represents electrode potential, E_{eq} represents equilibrium potential, η represents overpotential (defined as $\eta = E - E_{eq}$), α represents the charge transfer coefficient of, z represents number of electrons involved in the electrode reaction, F represents Faraday constant, R represents universal gas constant, and T represents absolute temperature.

Equation 1.6 indicates that the current density at any overpotential is the sum of cathodic and anodic current densities. At the extreme condition of the overpotential being highly negative, the cathodic current density increases while the anodic current density becomes negligible. Then equation 1.6 can be written as:

$$j = -j_c = j_0 \cdot \left\{ \exp \left[\frac{-\alpha z F}{RT} \eta \right] \right\} \quad (1.7)$$

The equation 1.7 can also be written as:

$$\ln (-j_c) = \ln j_0 - \frac{\alpha z F}{RT} \eta \quad (1.8)$$

Equation 1.8 is the cathodic Tafel equation, which provides electrochemical kinetic information. When the cathodic current density and overpotential are obtained from the experiments, the exchange current density can be determined by the Tafel equation. Moreover, the number of electrons for an unknown reaction can be determined by the Tafel slope, which is important for mechanism investigation.

The equilibrium potential is the potential where the net current density is zero. The overpotential is the deviation of the electrode potential E from the equilibrium potential E_{eq} . The overpotential is described as:

$$\eta = E - E_{eq} \quad (1.9)$$

The Nernst equation is used to determine the equilibrium potential E_{eq} for a given composition in the bulk. The link between bulk composition and equilibrium is described as equation 1.10. In a half-cell cathode reaction, the Nernst equation is:

$$E_{eq} = E_{red}^0 - \frac{RT}{zF} \ln \frac{c_{red}}{c_{ox}} \quad (1.10)$$

Where E_{red}^0 is the standard half-cell reduction potential, c_{red} and c_{ox} are the chemical activity of the oxidizing agent and reducing agent, respectively.

1.2.3 CO₂ electroreduction figure of merit

In general, an efficient ERC requires highly active, selective, and stable catalysts. Moreover, the reaction system needs to achieve high mass transport properties and low ohmic resistance.^{32,33} To characterize these features, several figures of merits are generally used to evaluate the performance of the ERC system, which are current density, Faradaic efficiency, energy efficiency, and stability.

The current density is commonly defined as the current flow divided by the geometric area of the electrode at a given potential. The current density is used to characterize the reaction rate of the ERC process. By comparing the current density value, the catalytic activity of catalysts can be evaluated. The current density also depends on catalyst loading or the active surface area of an electrode. In some cases, the current density is normalized by the electrochemical active surface area (EASA) of an electrode. Due to the competitive H₂ evolution reaction (HER) during ERC process, the total current density is generally composed of the currents of both HER and ERC. Therefore, the partial current density of CO₂ electrochemical reduction needs to be further calculated by multiplying the total current density (j_{total}) with the Faradaic efficiency of ERC.

The Faradaic efficiency (FE) describes how efficient the charge facilitating an electrochemical reaction. The Faradaic efficiency is also known as the current efficiency. It can be described by the relation between product mole number and the consumed electricity charge. The function is written as:

$$FE = \frac{znF}{Q_{total}} \quad (1.11)$$

where z is the number of electron transfer, n is the mole number of a specific CO₂ reduction product, F is the Faraday constant, which is 96486 C mol⁻¹, Q_{total} is the total charge consumed during ERC process. When there are several reduction products generated during the ERC process, the Faradaic efficiency can also provide the selectivity information between different products. In general, the total Faradaic efficiency is 100% when all of the reactions are counting in.

The energy efficiency (EE) describes how efficient the input energy stored in the ERC product. The energy efficiency is defined as the ratio between the equilibrium potential for the desired product and the total cell voltage. The cell voltage is the potential difference between cathode and anode. Oxygen evolution (OER) is the anodic reaction. Therefore, for a specific cathodic product β , the energy efficiency of a full cell is written as:

$$EE = \frac{E_{eq}^{\beta} - E_{eq}^{OER}}{E_{cell}} FE_{\beta} \quad (1.12)$$

where E_{eq}^{β} is the equilibrium potential to form the specific product β at the cathode during ERC process, E_{eq}^{OER} is the equilibrium of OER at the anode side, FE_{β} is the Faradaic efficiency of the desired product β , E_{cell} is the cell voltage, which is the potential difference between the cathodic applied potential for ERC and the anodic applied potential for OER.

The stability describes the degradation of an electrode. Normally, the degradation of electrode is accompanied by an overpotential increase and ERC partial current decrease. The increasing overpotential is generally caused by the polarization of electrode, which possibly results from the impurity deposition, reactant concentration change, electrolyte pH change, or the morphology change of catalysts. Good stability is an important factor in minimizing the maintenance and operation costs for a large-scale ERC operation.

1.3 Metal Catalysts and Mechanisms for ERC

A wide range of catalysts for ERC has been studied by researchers over a long period. The ERC performances on various metal catalysts have been reported in the early work of Hori *et al.* in 1985.³⁴ In Hori's work, the metal catalysts were briefly divided into several groups in accordance with the product selectivity. For example, Cd, In, Sn, and Pb are preferred to produce formate; Ag and Au is in favor of CO production with a high Faradaic efficiency of 90%; While CH₄ is more favored on Cu electrodes with a larger Faradaic efficiency of 40% comparing to the low FE_{CH₄} on other metal catalysts.³⁴

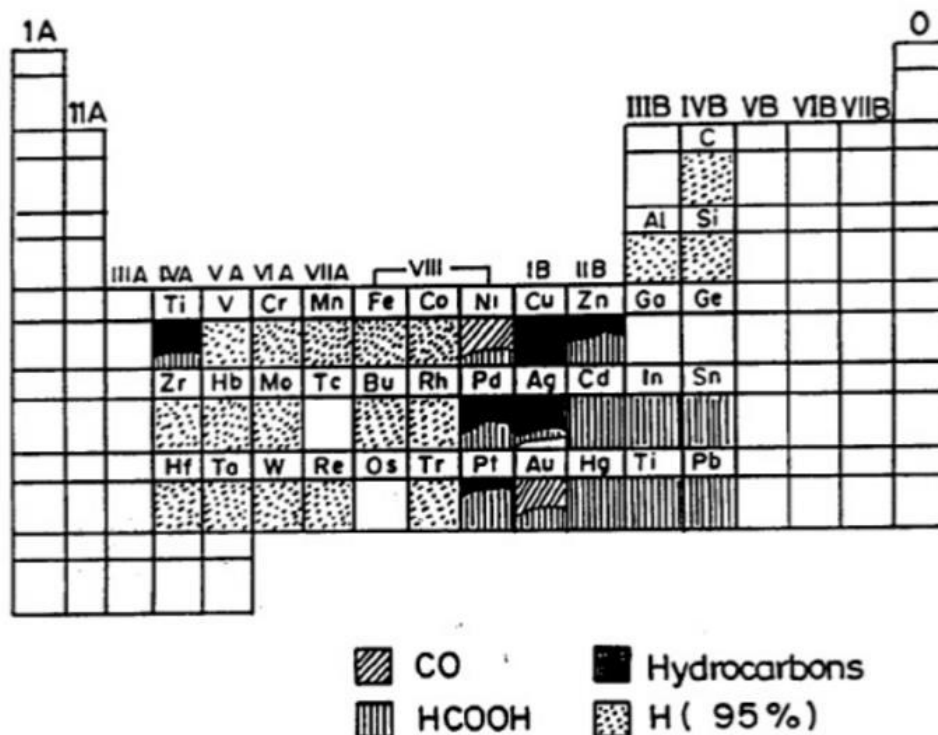


Figure 1.2 Periodic table for CO₂ reduction products at -2.2 V vs. SCE in low-temperature 0.05 mol dm⁻³ KHCO₃ solution.³⁵

In 1990, Azuma *et al.* reported 32 metal electrodes for ERC. A periodic table related to the ERC products distribution was shown in their work (Figure 1.2). It was noted by Azuma *et al.* that heavy

metals in IIB, IIIB, and IVB groups are effective for producing formate/formic. Some of VIII and IB metals, such as Ni and Au, are effective for CO production. Cu has a very high electrocatalytic activity for hydrocarbons formation. It was also suggested by Azuma *et al.* that there is a systematic rule for the CO₂ electrocatalytic reduction on metal surfaces.³⁵

1.3.1 Possible reaction pathways and products distribution

The different ERC product selectivity on various metals can be explained by the different reaction intermediates and various pathways. Experimental and theoretical methods have been carried out to investigate the ERC reaction mechanisms. The ERC reaction pathways for different products are proposed based on Tafel slopes or density functional theory (DFT) calculations.^{36,37} The most popular reaction pathways are shown in Figure 1.3.

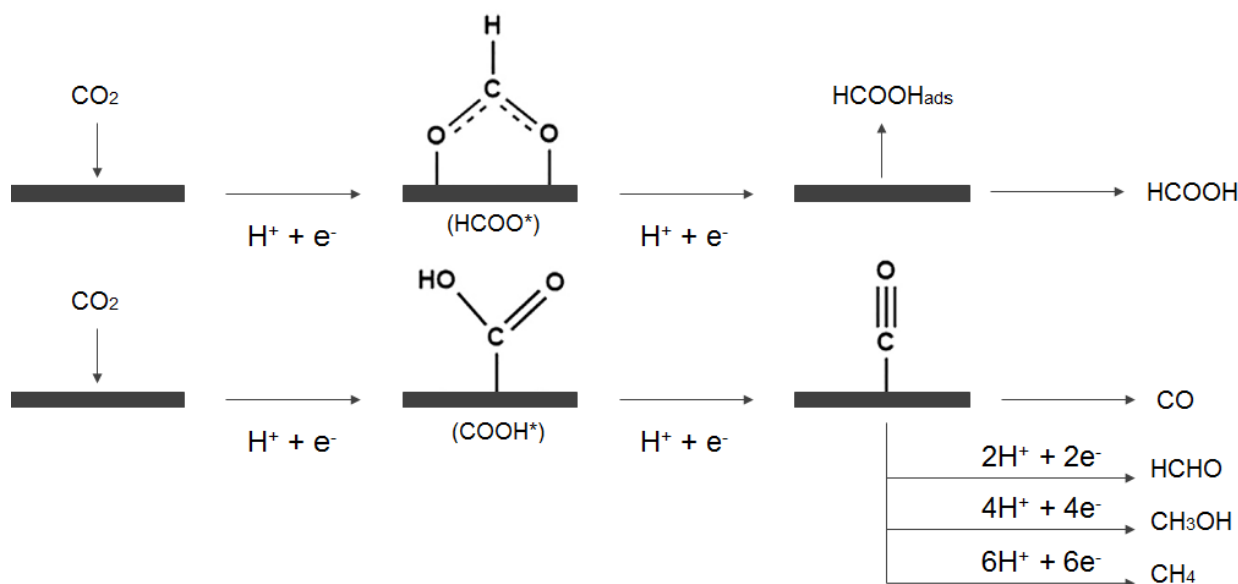


Figure 1.3 Schematic illustration of simplified reaction mechanism for ERC in aqueous solution.

For the formate product, the reaction pathway is associated with the HCOO* intermediate. There are two ways to form the HCOO* intermediate, which related to two different proton-combining methods. In one way, H* is firstly adsorbed at the catalyst's surface, and then, the H* adsorption reacts with the CO₂ to form the HCOO* intermediate.³⁸ This reaction way is called proton-assisted electron transfer pathway. An alternative way is that the CO₂ is coupled with a proton provided by electrolyte firstly, and then, the HCOO* adsorption forms directly at the surface of a catalyst. This pathway is called proton-coupled electron transfer pathway.³⁹ For the heavy metals in IIB, IIIB, and IVB groups (Figure 1.2), such as Hg, Pb, Sn, and In, the formation of HCOO* intermediate is

more energy favorable.⁴⁰ Thus, the formate or formic acid is the predominate product on those metals such like Hg,⁴¹ In,⁴² Sn,⁴²⁻⁴⁴ Pb,^{44,45} and Bi.^{46,47}

For the CO formation, the COOH* intermediate is more favorable. The COOH* adsorption will be further reduced to CO* at the surfaces of metal catalysts, such as Ni, Ag, Au, and Pd. On these metals, CO* desorption occurs before it is further reduced to higher-order products. Therefore, CO is the major product for the metals in group VIII and IB, such as Ni,^{48,49} Ag,⁵⁰⁻⁵² Au,⁵³⁻⁵⁶, Pd,^{54,57-59} and Zn.^{60,61}

For the higher-order product formation, the CO* adsorbate binds stably to the active sites of metal surfaces. Thence, the CO* adsorbate will be further reduced to higher-order reduction products, such as alcohols and hydrocarbons. Cu has been widely studied for higher-order ERC products.^{3,62-66}

1.3.2 Selective catalysts for formate/formic acid

1.3.2.1 Hg electrode

In 1982, Hori *et al.* reported that the current efficiency for formate formation could reach 100% with a constant current density of 0.5 mA cm⁻² at the mercury pool electrode. The electrolysis potential was affected by the pH and the anion species of the electrolyte. It was pointed by Hori *et al.* that the electrolysis potential was lower with the anion sequence of Li⁺ Na⁺ and K⁺.⁶⁷ Todoroki *et al.* found that the Hg electrodes showed a formate Faradaic Efficiency (FE_{formate}) of 12.9% at a constant current of 200 mA cm⁻² in the aqueous electrolyte under atmosphere pressure and room temperature. The FE_{formate} was gradually increased with the increase of CO₂ pressure. The FE_{formate} reached 100% when the CO₂ pressure was increased to 20 atm. Even though Hg is very selective for formate product during the ERC process, it is necessary to apply a very high CO₂ pressure to achieve the high FE_{formate}. Besides, Hg is very toxic, which is not safe for industrial applications.

1.3.2.2 In electrode

It was reported by Todoroki *et al.* that In electrode was also selective for formate product during the ERC process. They noted that the FE_{formate} on In electrode was 30.6% with a partial current density of 15.3 mA cm⁻² at atmosphere pressure and room temperature. When the CO₂ pressure was increased to 60 atm, the FE_{formate} achieved to 100%.⁶⁸ In 1995, Mizuno found that the FE_{formate} on In electrode was obtained to be 100% at -1.8 V vs. Ag/AgCl at a high-pressure condition.⁶⁹ In

recent years, researchers start to investigate the catalytic activity of In electrodes under atmosphere pressure. Bitar *et al.* reported an In coated carbon paper electrode (In/C), at which the FE_{formate} was 45% at -1.2 V vs. RHE, which was 23% enhanced than the FE_{formate} on In foil.⁷⁰ Hegner *et al.* reported an electrodeposited In electrode, and the FE_{formate} on this In electrode reached 94.5% at an electrolysis potential of -1.6 V vs. RHE with a current of 3.8 mA cm⁻².⁷¹ Recently, Luo *et al.* reported a porous In, on which the ERC current achieved to 67.5 mA cm⁻² with a FE_{formate} of 90% at the potential of -1.2 V vs. RHE.⁷² Bohlen *et al.* reported a deposited In electrode using Cu foil as the substrate. This In electrode showed a FE_{formate} of 72.5% at -1.24 V vs. RHE with a reduction current of 27.8 mA cm⁻². Ma *et al.* found that comparing to the commercial In foil, the S-doped In electrode showed a higher FE_{formate} (93%), which was 60% higher than that of commercial In at the potential of -0.98 V vs. RHE. The partial current of formate on S-doped In electrode reached 60 mA cm⁻².⁷³ In recent years, the ERC reduction current on In electrode was significantly improved with a high FE_{formate} of around 90%. However, the ERC electrolysis potential on In electrode is still more negative than -1 V vs. RHE. This large ERC electrolysis potential will lead to low energy efficiency for CO₂ electrochemical reduction.

1.3.2.3 Sn electrode

Sn is also very selective for formate formation in the ERC process. The catalytic activities of Sn foil, Sn granules, Sn particles, and Sn particles-based carbon materials were investigated. In 2003, Koleli *et al.* reported a fixed-bed reactor for ERC using Sn granules as the catalysts. The FE_{formate} on Sn electrode was 74% at the electrolysis potential of -0.8 V vs. RHE with a reduction current of 0.25 mA cm⁻².⁷⁴ In 2012, Wu *et al.* reported a 95% FE_{formate} on Sn foil electrode at the electrolysis potential of -1.3 V vs. RHE with a current of 5 mA cm⁻².⁷⁵ Prakash *et al.* reported an Sn particle coated gas diffusion layer (GDL) electrode, and a 70% FE_{formate} was obtained at -1.1 V vs. RHE with a current of 27.3 mA cm⁻² on this Sn/GDL electrode.⁷⁶ Li *et al.* reported a sulfide-derived Sn, on which the electrolysis potential was reduced to -0.75 V vs. RHE with a FE_{formate} of 84.5% and reduction current of 11.75 mA cm⁻². The ERC overpotential for the Sn electrode is still very large (>1 V), and there is space to improve the reduction current and enhance the FE_{formate} for Sn-based electrodes.⁷⁷ Most recently, Sn-based carbon nanotubes (CNTs)/carbon black hybrid GDL⁷⁸ and Sn-based N-doped carbon nanofibers (N-C)⁷⁹ were investigated, on which the FE_{formate} were both less than 70%. The CO and H₂ productions competed with the formate leading to a relatively low FE_{formate} . Traditional Sn foil, granules, or particles catalysts show a good reduction current (>10

mA cm⁻²) during the ERC process. However, it is still challenging to reduce the large overpotential and enhance the formate Faradaic efficiency.

1.3.2.4 Pb electrode

Pb is very selective for formate production during the ERC process with a suppression of the competitive H₂ evolution reaction (HER). However, the ERC current on Pb electrodes is very low under the atmosphere condition. As reported by Koleli *et al.* in 2003, the ERC current on Pb granules was just 0.79 mA cm⁻² with a FE_{formate} of 90% at -0.8 V vs. RHE.⁷⁴ He *et al.* reported an ERC current of 1.17 mA cm⁻² with a FE_{formate} of 89% at -0.96 V vs. RHE on a roughened Pb electrode.⁸⁰ Lee *et al.* reported a 0.5 mA cm⁻² ERC current on an oxide-derived Pb with a FE_{formate} of 95% at -0.8 V vs. RHE.⁸¹ The ERC reduction current can be significantly improved by using ionic liquid catholyte mixture, which has been reported by Zhu *et al.*. The ERC current was obtained to be 37.6 mA cm⁻² with a FE_{formate} of 91.6% at -2.2 V vs. Ag/AgCl in the ionic liquid/acetonitrile electrolyte.⁸² However, the low ERC current on Pb electrodes in the aqueous electrolyte is still a crucial problem to be solved.

1.3.2.5 Bi electrode

Bi presents attracting properties not only due to its low toxicity and cost but also due to its higher formate selectivity in the aqueous electrolyte. In the most recent investigations, the reported FE_{formate} values on Bi electrodes were over 90%. For example, Zhang *et al.* reported that on nanostructured Bi electrode, the FE_{formate} reached 92% at -0.83 V vs. RHE with a reduction current of 3.7 mA cm⁻².⁴⁶ Lv *et al.* reported that the FE_{formate} was 91.3% at -0.9 V vs. RHE on an electrodeposited Bi electrode and the reduction current was 3 mA cm⁻².⁸³ For the micro-Bi catalyst reported by Zhang *et al.*, the FE_{formate} was obtained to be 98.4% at -0.92 V vs. RHE with a reduction current of 1.5 mA cm⁻².⁸⁴ Avila-Bolivar *et al.* reported that for Bi nanoparticles, the FE_{formate} achieved to 100% at -0.85 V vs. RHE with a reduction current of 4 mA cm⁻².⁸⁵ In most of these findings, the formate selectivity on Bi electrode was very high. However, most ERC currents were less than 5 mA cm⁻², which is still necessary to be enhanced.

The detailed comparisons of formate/formic acid selective metals are shown in Table 1.2.

Table 1.2 Summary of formate/formic acid selective metal catalysts for ERC under standard conditions in aqueous solution: at 1 atm, and 25 °C.

Catalysts	Electrolyte	ERC potential (V vs. RHE)	j_{formate} (mA cm ⁻²)	Formate FE (%)	References
Hg pool electrode	0.1M NaHCO ₃ + 0.55M Na ₂ SO ₄	-1.1	0.5	100	67
Hg electrode	0.5 M KHCO ₃	N.R.*	25.8	12.9	68
In electrode	0.5 M KHCO ₃	N.R.*	15.3	30.6	68
In/C	0.1 M Na ₂ SO ₄	-1.2	2.8	45	70
In	0.05 M NaHCO ₃	-1.6	3.8	94.5	71
Porous In	0.1 M KHCO ₃	-1.2	67.5	90	72
In	0.5 M KHCO ₃	-1.24	27.8	72.5	86
S-doped In	0.5 M KHCO ₃	-0.98	60	93	73
Sn granules	0.5 M KHCO ₃	-0.8	0.25	74	74
Sn foil	0.1 M Na ₂ SO ₄	-1.3	5	95	75
Sn particles	0.5 M NaHCO ₃	-1.1	27.3	70	76
Sn quantum sheets	0.1 M NaHCO ₃	-1.15	21.1	85	87
Sn porous nanowires	0.1 M KHCO ₃	-1.0	10	80	88
Sulfide-derived Sn	0.5 M NaHCO ₃	-0.75	11.75	84.5	77
Sn-based CNTs/carbon black	0.5 M KHCO ₃	-1.0	34.2	69.8	78
Sn particles/ N-C	0.5 M KHCO ₃	-0.8	11	62	79
Pb granules	0.5 M KHCO ₃	-0.8	0.79	90	74
Pb plate	0.5 M NaOH	-0.85	0.6	65	89
Roughened Pb	0.1 M KHCO ₃	-0.96	1.17	89	80
Oxide-derived Pb	0.5 M NaHCO ₃	-0.8	0.5	95	81
Pb-MHKTs	0.5 M KHCO ₃	-1.0	13	85	44
Amine modified Pb	1 M KHCO ₃	-1.09	9.4	94	90
Nanostructured Bi	0.5 M KHCO ₃	-0.82	3.7	92	46
Oxide-derived Bi	0.5 M KHCO ₃	-0.82	1.6	75	91
Electrodeposited Bi	0.1 M KHCO ₃	-0.90	3	91.3	83
Nano-Bi	0.5 M KHCO ₃	-0.92	9.7	98.4	92
Micro-Bi	0.5 M KHCO ₃	-0.78	1.5	90	84
Bi nanoparticles	0.5 M KHCO ₃	-0.85	4	100	85

1.3.3 Selective catalysts for carbon monoxide

1.3.3.1 Ag electrode

Ag is selective for CO formation due to its energy favorable surfaces for the COOH* intermediate.^{50,93} In previous investigations, the Faradaic efficiencies of CO (FE_{CO}) on Ag electrodes were all above 80%. As reported by Kim *et al.*, the FE_{CO} of Ag nanoparticles was 84.4% at -0.75 V vs. RHE with a reduction current of 6 mA cm⁻².⁹⁴ Singh *et al.* reported that the FE_{CO} on Ag electrode reached 82.9% at -1 V with a current of 4 mA cm⁻².⁹⁵ Verma *et al.* reported that the FE_{CO} was obtained to be 99.2% at -0.76 V vs. RHE with a current of 12.7 mA cm⁻² on the Ag/GDL electrode.⁹⁶ Yang *et al.* reported that the FE_{CO} was 85% at -0.8 V vs. RHE with a current of 2.5 mA cm⁻².⁹⁷ Kim *et al.* found that the FE_{CO} can be enhanced to 94.2% at -0.75 V vs. RHE by the amine surface modification.⁹⁸

1.3.3.2 Au electrode

Au has been widely studied for ERC to form CO product. Moreover, Au is also active for H₂ evolution. Therefore, some researchers developed Au catalysts for syngas formation during the ERC process. The ratio between CO and H₂ products can be adjusted by varying the size of Au particles.^{99,100} The other researchers were focusing on the high CO selectivity of the Au electrode. As reported by Gregory *et al.*, at -0.74 V vs. RHE electrolysis potential, the FE_{CO} was 85% on Au electrode with a reduction current of 5 mA cm⁻².¹⁰¹ Chen *et al.* reported that on the oxide derived Au electrode, the FE_{CO} reached 96% at the potential of just -0.35 V vs. RHE.¹⁰² For Au nanoparticles^{103,104} or Au nanowires,¹⁰⁵ the FE_{CO} were all over 90%, as shown in Table 1.3, indicating that Au is super selective for CO production.

1.3.3.3 Pd electrode

In previous investigations, Pd was reported to be highly selective for CO formation during the ERC process. Gao *et al.* reported that the FE_{CO} reached 93.2% on the Pd nanoparticles in an electrolyte with a pH value of 2.2. The ERC potential was -1.19 V vs. RHE with a reduction current of 5.5 mA cm⁻².¹⁰⁶ Gao *et al.* noted that the Faradaic efficiency is related to the particle size of Pd nanoparticles. The highest 93.2% of FE_{CO} was obtained on the 3.7 nm Pd nanoparticles at a relatively lower potential of -0.89 V vs. RHE with a reduction current of 9 mA cm⁻².¹⁰⁷ Guo *et al.* found that the FE_{CO} reached 95% with a reduction current of 9.5 mA cm⁻² at -0.8 V vs. RHE.¹⁰⁸ Huang *et al.* found that the morphology of Pd nanoparticles will affect the FE_{CO}. For the Pd

icosahedra/C, the FE_{CO} was 91.1% at -0.8 V vs. RHE, which is 1.7-fold higher than that of Pd octahedra/C.¹⁰⁹

Table 1.3 Summary of CO selective metal catalysts for ERC under standard conditions in aqueous solution: at 1 atm, and 25 °C.

Catalysts	Electrolyte	ERC potential (V vs. RHE)	J_{CO} (mA cm ⁻²)	CO FE (%)	References
Ag nanoparticles	0.5 M KHCO ₃	-0.75	6	84.4	94
Amine-Ag	0.5 M KHCO ₃	-0.75	1	94.2	98
Ag electrode	0.1 M KHCO ₃	-1	4	82.9	95
Ag/GDL	0.5 M KHCO ₃	-0.76	12.7	99.2	96
Ag nanoparticles	0.1 M KHCO ₃	-0.8	2.5	85.0	97
Au electrode	0.1 M KHCO ₃	-0.74	5	85	101
Oxide derived Au	0.5 M NaHCO ₃	-0.35	2-4	96	102
Au nanoparticles	0.5 M KHCO ₃	-0.67	5	90	103
Au nanowires	0.5 M KHCO ₃	-0.35	4	94	105
Au inverse opal	0.1 M KHCO ₃	-0.5	0.1	99	110
Nanostructured Au	0.25 M NaHCO ₃	-0.4	16	90	104
Nanostructured Au	0.5 M KHCO ₃	-0.79	15	80	111
Pd nanoparticles	0.05 M K ₂ SO ₄ + 0.005 M H ₂ SO ₄	-1.19	5.5	93.2	106
Pd nanoparticles	0.1 M KHCO ₃	-0.89	9	91.2	107
Pd nanoparticles	0.5 M KHCO ₃	-0.8	9.5	95	108
Pd icosahedra/C	0.1 M KHCO ₃	-0.8	2	91.1	109
Zn dendrites	0.5 M NaHCO ₃	-0.9	4	80	61
Hexagonal Zn	0.5 M KHCO ₃	-1.1	8.5	95.4	112
Reducing electrodeposited ZnO	0.5 M KCl	-1.05	4.3	95.9	113
Porous Zn	0.1 M KHCO ₃	-0.79	1.5	81	114
Zn nanosheets	0.5 M NaHCO ₃	-1.13	6	86	115
Zn porous nanosheets	0.1 M KHCO ₃	-1.0	9	90	116

1.3.3.4 Zn electrode

Zn is the non-noble metal that is highly selective for CO during the ERC process. Many investigations were focused on the structure effect on enhancing the CO selectivity. Rosen *et al.*

reported a dendritic Zn, which showed a FE_{CO} of 80% at -0.9 V vs. RHE with a current of 4 mA cm^{-2} . The FE_{CO} on the dendritic Zn electrode was 3-fold enhanced than that on foil Zn electrode.⁶¹ Won *et al.* found that the CO selectivity is related to the surface morphology. Zn(101) facet is favorable to CO formation, whereas Zn(002) facet favors the H_2 evolution during electrolysis. On Hexagonal Zn, the FE_{CO} reached 95.4% at -1.1 V vs. RHE.¹¹² Zhang *et al.* reported the ERC performance of Zn nanosheets. The FE_{CO} was 86% (at -1.13 V vs. RHE), which was 8-fold improved than that of Zn foil.¹¹⁵ Liu *et al.* reported one kind of Zn porous nanoparticles, on which 90% of FE_{CO} was achieved. There was a 20% FE_{CO} enhancement on porous Zn electrode than that of Zn non-porous nanoparticles at the electrolysis potential of -1.0 V vs. RHE.¹¹⁶

The detailed comparisons of CO selective metals are shown in Table 1.3.

1.3.4 Selective catalysts for high-order products

Cu is the non-noble catalyst that has shown a propensity to produce valuable hydrocarbons and alcohols from the electrochemical reduction of CO_2 , such as ethylene and ethanol. There are a variety of factors that impact the ERC activity and selectivity for Cu electrodes, including the catalyst surface structure, catalysts size, electrolyte ions and pH.³ The ERC reaction pathways on the Cu electrode are complicated and many products (C_1 ¹¹⁷ and C_2 ^{62,118} products) will be obtained at the same time. Many efforts have been devoted to enhancing the activity and selectivity of products on Cu electrode, and theoretical calculations were applied to reveal the mechanisms of C_1 and C_2 pathways. Herein, several typical examples are shown to illustrate the catalytic activity and selectivity of high-order ERC products on Cu electrodes.

It was reported by Hori *et al.* in the year 2002 that Cu(100) is favorable for producing C_2H_4 (40.7%) with CH_3OH (12.8%) and CH_3CHO (1.0%) side products at a potential of -1.39 V vs. SHE.¹¹⁹ Luo *et al.* found that the product selectivity of ERC is sensitive to the surface morphology of the Cu electrode. They proposed that at Cu(111) surface, the formation of COH^* is favored, through which CH_4 and C_2H_4 are produced under high overpotential (<-0.8 V vs. RHE). Whereas at Cu(100) surface, the formation of CHO^* is preferred and C_2H_4 formation goes through C-C coupling of two CHO^* species, under relatively lower overpotential (-0.4 to -0.6 V vs. RHE). However, under larger potentials (\sim -1.0 V vs. RHE), C_2 intermediates will be further reduced.¹²⁰ Liu *et al.* proposed a CO_2 reduction pathway for the Cu(211) facet and investigated the effects of potential and pH on the C_1 and C_2 product activity and selectivity. The schematic ERC pathways are shown in Figure 1.4. The researchers found that C_2 products are favored under alkaline conditions during the ERC process.¹²¹

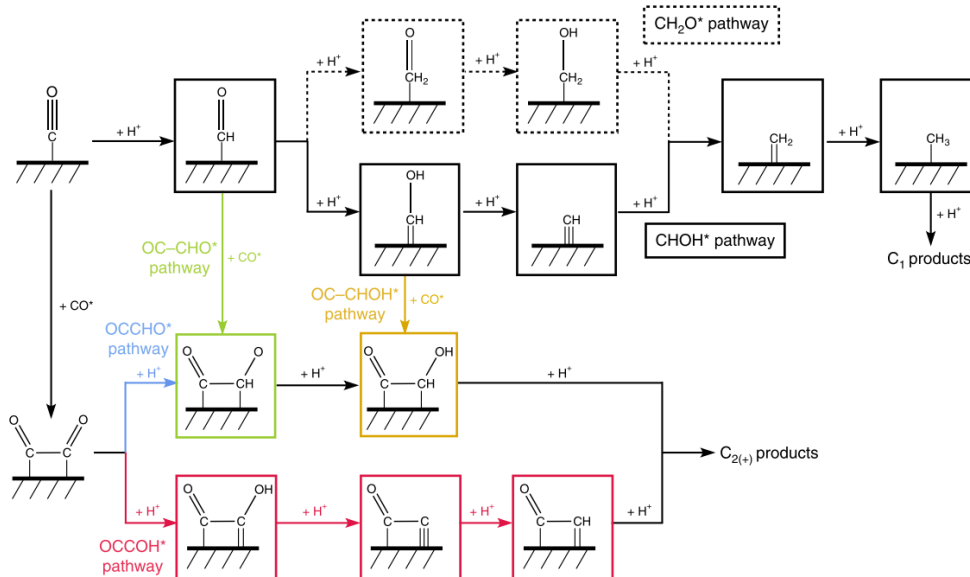


Figure 1.4 Reaction schemes of major pathways considered for CO_2 reduction toward C_1 and C_{2+} products. The green path denotes C_2 production via OC-CHO^* coupling; the blue and red path represents C_2 production via protonation of OCCO to form OCCHO^* and OCCOH^* , respectively; the yellow path represents C_2 production via OC-CHOH^* coupling. The black path denotes C_1 production via CHOH^* and the dashed CH_2O^* .¹²¹

1.3.5 Challenges and opportunities

Among the different value-added products that can be formed during ERC process, formate/formic acid has generated a vivid interest. The ERC to formate/formic acid is a two electrons process. Formate is highly soluble while formic acid is a solid. Both are easy and safe to handle, making them useful in a variety of applications. Formate/formic acid is selling at higher price (~2500 kWh/ton and \$1,200/ton) compared to methane (~40000 kWh/ton and \$200-\$300/ton), which needs more electrons to be produced.¹²² Notably, it is a feedstock in agricultural and industrial production, antibacterial agent of livestock feed, and is used in leather processing, among other areas. It can also be used in direct formic acid fuel cell to generate electricity^{123,124} and as a mediator between electricity and microbial cultivation.¹²⁵

As the discussions above, the most formate-selective catalysts are the post-transition metals including Hg, In, Sn, Pb and Bi. However, there are many challenges in developing highly active post-transition metal catalysts for ERC: (1) The high Faradaic efficiency of formate is desired to be achieved under atmosphere pressure, instead of the high CO_2 pressure; (2) The large overpotential ($> 1 \text{ V}$) is required to be reduced during the CO_2 electrolysis process; (3) Small reduction current ($< 10 \text{ mA cm}^{-2}$) is necessary to be enhanced in aqueous electrolytes; (4) The

mechanisms of the morphology or surface effects on the ERC activity and selectivity of the post-transition metals need to be unrevealed.

1.4 Strategies to Enhance the ERC Performance on Metal Catalysts

Surface engineering has been used as an efficient strategy to enhance the ERC performances. It was reported that the ERC performance depends on the structure of the catalysts, such as the active surface area, the surface defects, surface phase and the exposed facets.³⁰

1.4.1 Surface roughness enhancing

Enhancing surface roughness is realized mainly by: (1) Roughening the smooth electrode surface by applying oxidation-reduction cycles on the flat electrode surface; and (2) Dispersing metal catalyst particles to porous supports with large surface area (such as carbon nanotubes, graphene, copper foam, etc.).

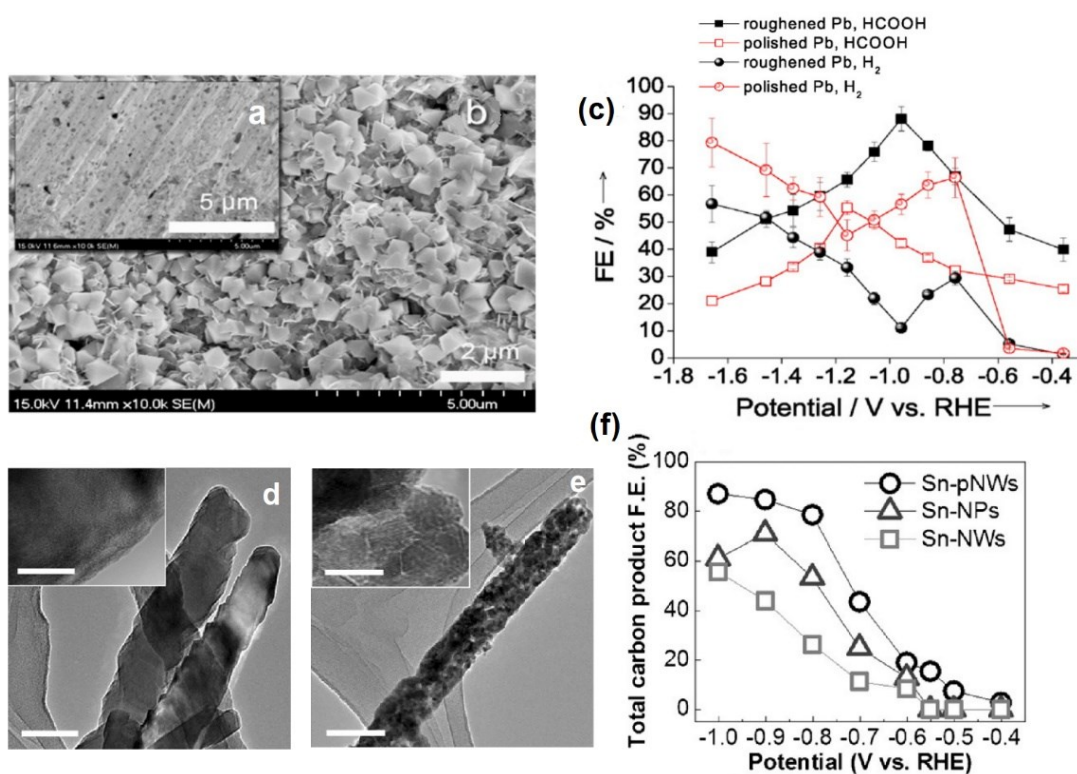


Figure 1.5 Examples of roughening smooth surfaces. (a-c) Pb electrode, and (d-f) Sn electrode. SEM of (a) polished Pb and (b) roughened Pb after four cycles. (c) Faradaic efficiency of formic acid and H₂ formation on both roughened and smooth Pb electrodes.⁸⁰ HRTEM images of (d) Sn-NWs (inset: magnified images), and (e) after acid etch conversion into Sn-pNWs with increased grain boundaries (inset: magnified image). (f) Faradaic efficiency vs. potential for all carbon products.⁸⁸

He *et al.* reported that by applying four oxidation-reduction cycles on a smooth Pb electrode (Figure 1.5a), the Pb surface was roughened as shown in Figure 1.5b. The total formate Faradaic efficiency on the roughened Pb surface was 2-fold higher than that on the smooth Pb at -1.1 V vs. RHE (Figure 1.5c). The enhanced ERC performance on the roughened Pb electrode is attributed to the enlarged active surface area and increased number of reactive species.⁸⁰ Kumar *et al.* reported a reduced SnO₂ porous nanowire (Figure 1.5e), on which the high density of grain boundaries was generated at the surface and the ERC total Faradaic efficiency was 2 to 5-fold increased than that of the SnO₂ smooth nanowire as shown in Figure 1.5f.⁸⁸

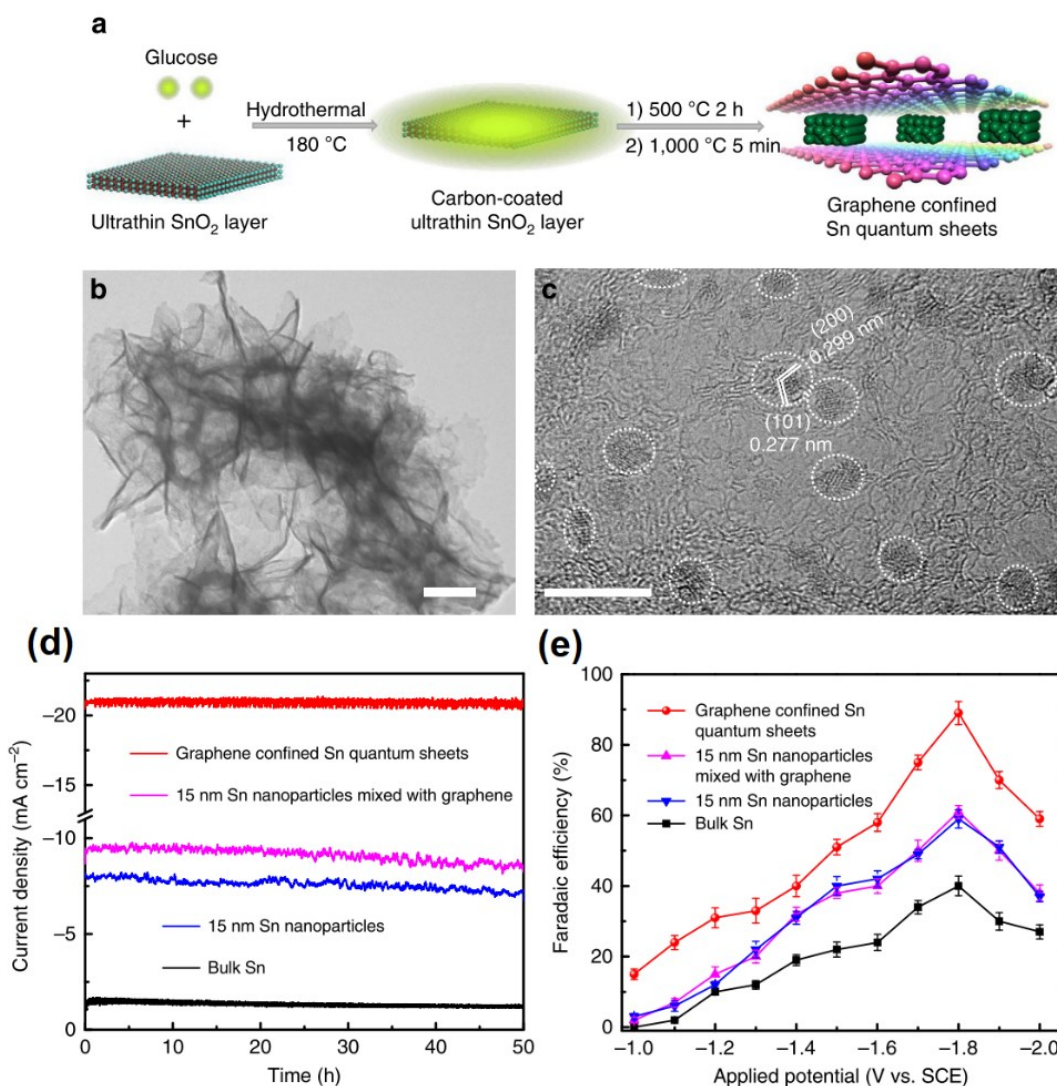


Figure 1.6 An example of dispersing target catalyst onto high-surface-area support and its effect on enhancing ERC performance. Scheme illustration for the formation of Sn quantum sheets confined in graphene, (b) TEM image, (c) HRTEM image. (d) Chrono-Amperometry results at the potentials of -1.8 V versus SCE. (e) Faradaic efficiencies for formate at each applied potentials for 4h.⁸⁷

Lei *et al.* synthesized the Sn quantum sheets confined in graphene (Figure 1.6), by which the electrochemical active surface area was 9-fold increased comparing to the bare Sn quantum sheets. The remarkably increased EASA of the Sn quantum sheets confined in graphene could afford a larger number of active sites for CO₂ efficient adsorption. Thence, the ERC current (3-fold enhanced) and Faradaic efficiency (30% improved) were further enhanced than that of bare Sn quantum (Figure 1.6d-e).⁸⁷ Wang *et al.* reported an electroplated Sn on a Cu foam substrate. The foam Cu has a very large surface area for Sn deposition, which provides more active sites for CO₂ electrochemical reduction. The average current density and the production rate of formate on the Sn/foam-Cu electrode are more than twice, comparing to those on the smooth Sn plate electrode during the ERC process.¹²⁶ Rogers *et al.* demonstrated a composite material for ERC, which the gold nanoparticles (AuNPs) embedded in a bottom-up synthesized graphene nanoribbon (GNR) matrix. The structural and electronic properties of the GNR increase the EASA of AuNPs, which lower the ERC catalytic overpotential and increase the total catalytic ERC output (>100-fold improvement comparing to AuNPs on amorphous carbon).¹²⁷

1.4.2 Surface structure tuning

Surface structural tuning of metal catalysts includes: (1) Tuning surface defects; and (2) Tuning exposed crystal facets (high-index facets or facets with abundant low-coordinate sites).

Gong *et al.* synthesized defect-rich Bi nanocatalysts, as shown in Figure 1.7. This defect-rich Bi shows a very excellent ERC performance with an exclusive formate formation at -0.82 V vs. RHE. By using density functional theory calculations, they found that the excellent activity and selectivity are attributed to the abundant defective bismuth sites, which stabilize the *OCHO intermediate.¹²⁸ Mistry *et al.* reported a defect-rich plasma-activated silver catalyst. On this defect-rich silver foil electrode, the overpotential was decreased and ERC activity was increased due to the enhancing number of low-coordinated catalytic active sites.¹²⁹ Yang *et al.* compared the ERC performances of various sized Ag nanoparticles. They found that the FE_{CO} of the AgNPs-21nm (85%) is 2-time higher than that of AgNPs-87nm, and the CO partial current density of AgNPs-21nm is 2.5-fold larger than that of AgNPs-87nm. This improved ERC performance is attributed to the more abundant defects of the 21 nm AgNPs when comparing to the 87 nm AgNPs.⁹⁷

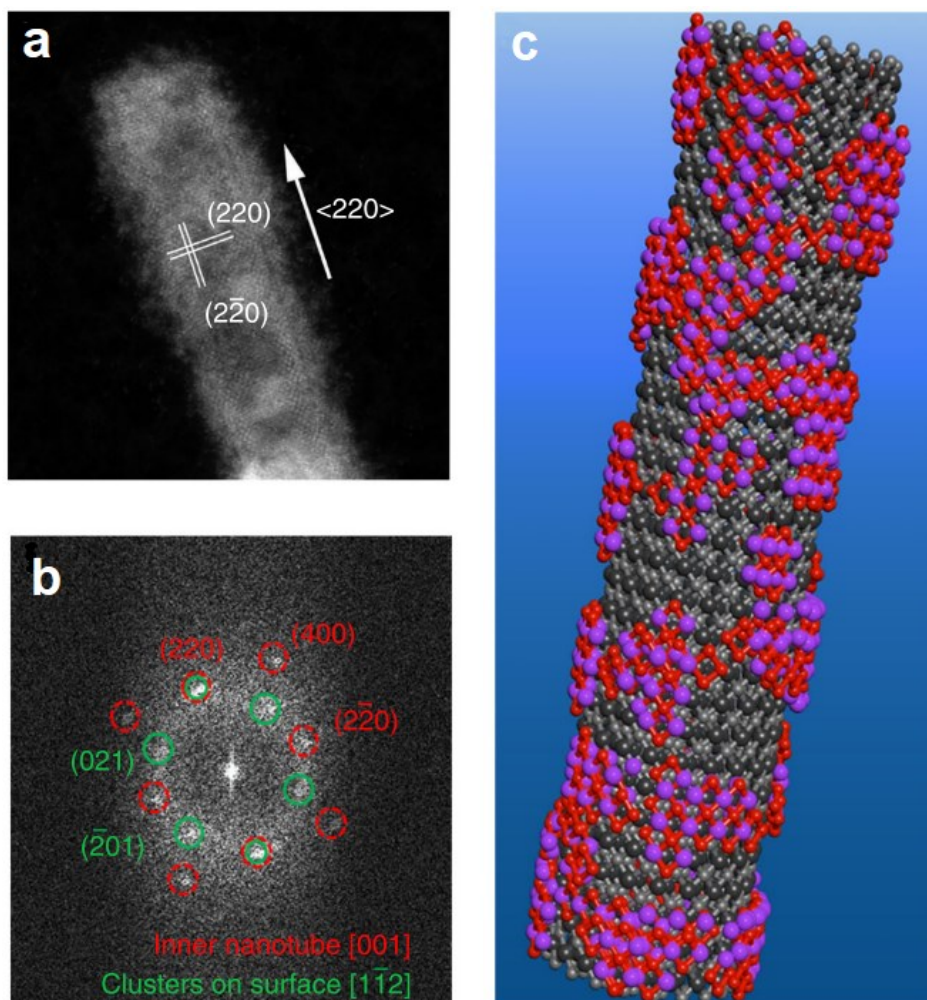


Figure 1.7 An example of defect-rich Bi-based catalyst. (a) STEM-HAADF image, and (b) corresponding FFT pattern of a Bi_2O_3 nanotube (NT). (c) Schematic illustration of the structure of Bi_2O_3 NTs; the black spheres represent the crystalline inner walls, and the red and purple spheres represent the fragmented outer walls.¹²⁸

High-index facets of metal catalysts play an important role in enhancing ERC catalytic activity. Lee *et al.* reported a concave Au catalyst, which is enclosed with high-index facets such as (332) and (775), as shown in Figure 1.8a-b. The FE_{CO} on this concave Au catalyst (95%) is 2-fold increased than the normal cubic Au catalyst (Figure 1.8c). This enhanced ERC performance is mainly due to the higher-index facets, which can introduce a favorable route for CO_2 reduction.⁵⁶ Many researchers have investigated Bi nanosheets for the CO_2 electrochemical reduction.¹³⁰⁻¹³⁴ Yang *et al.* reported one kind of Bi nanosheets which has a well-defined shape with exposed (012), (111), and (101) surface facets. By using DFT calculations, they found that (101) and (111) planes can significantly stabilize HCOO^* . Therefore Yang *et al.* proposed that (101) and (111) planes are the most active planes for the formate formation during the ERC.¹³² The facets effect

was also found on Zn-based catalysts. Won *et al.* found that on the Hexagonal Zn Catalyst, Zn(101) facet is favorable for CO formation whereas Zn (002) facet favors the H₂ evolution during ERC process.¹¹²

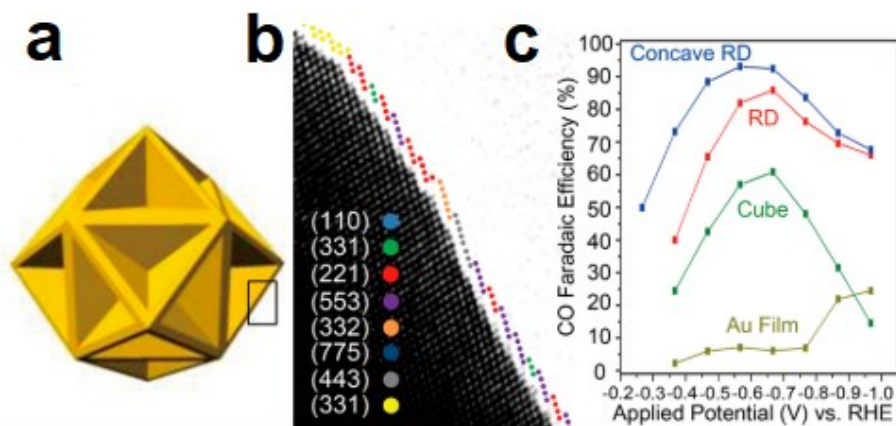


Figure 1.8 An example of High-index Au catalyst. (a) Single nanoparticle with model of concave Rhombic Dodecahedral Au. (b) HRTEM images of eight different sections displaying atomic arrangements. Each atom is marked with a colored sphere. (c) FE_{CO} as function of potentials on different Au catalysts.⁵⁶

1.4.3 Surface decoration

Surface decoration can be realized through (1) Surface decoration by metal atoms; and (2) Surface modification by functional molecules.

As shown in Figure 1.9a, the active Cu surfaces were decorated by Pb adatoms through the Pb under-potential deposition (UPD). Kim *et al.* found that the FE_{formate} was 15 times boosted when the Cu surface was decorated by Pb adatoms. These Pb adatoms effectively suppressed the competitive HER during the CO₂ reduction process by selectively poisoning the hydrogen adsorption sites at Cu surfaces.¹³⁵ Figure 1.9b shows an example of surface modification by functional molecules. Kim *et al.* reported that the amine functional group at the Ag surface was highly effective in improving CO selectivity by suppressing HER, while the thiol group rather increases the HER activity.⁹⁸ Zhao *et al.* reported an amine modified ultrasmall Au catalyst. They found that the FE_{CO} can be improved to 59-75% while Au was modified by amine.¹³⁶ Zouaoui *et al.* reported an amine modified Pb electrode, which shows an enhanced ERC activity and formate selectivity. This improved ERC performance was mainly attributed to the selectively hindering of HER by amine layers modification.⁹⁰

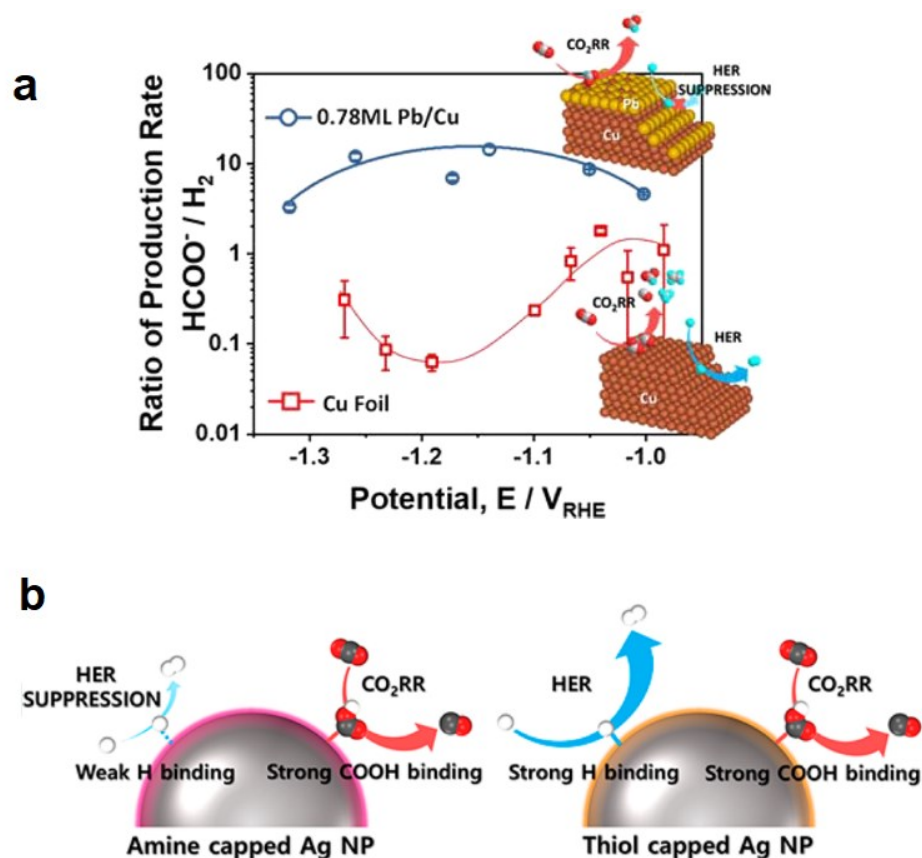


Figure 1.9 Examples of surface decorations. (a) ERC production rate as function of electrolysis potential. The Cu surfaces was decorated by Pb adatoms using under-potential deposition.¹³⁵ (b) A scheme illustration of surface-Molecule-Mediated Ag Nanoparticles.⁹⁸

1.5 ERC on Hierarchical Dendritic Metal Electrodes

Dendrite-structured catalysts have attracted interest of researchers due to their large surface area, high density of exposed surfaces with preferential facet orientations, and the presence of sharp tips at the end of the dendrites.

1.5.1 Dendritic single metals

1.5.1.1 Precious metals

Electrochemical deposition at different potentials is one method used to form various metal catalysts morphologies. Nesbitt *et al.* reported a 20 MHz square-wave electric potential deposition method. Depending on the potentials used, dendritic Au (Figure 1.10c-d) and plate Au (Figure 1.10a-b) could be obtained.¹³⁷ Dendritic Au was formed due to the diffusion limited crystallization.

It was proposed that both dendritic Au and plate Au are polycrystalline, and the low energy {111} facets are predominant. However, dendritic Au has a larger proportion of {110} and {100} facets comparing to plate Au. The ERC performance comparison between dendritic Au and plate Au are shown in Figure 1.10f-g. Dendritic Au shows a larger ERC current density than plate Au at each applied potential step. The Faradaic efficiency of CO shown in Figure 1.10g reveals that dendritic Au have a Faradaic efficiency of approximately 50–60% when the applied potential was lower than -0.35 V vs. RHE. However, plate Au has a CO Faradaic efficiency much lower (10-20%) in the same potential range. It was proposed that the dendritic Au's higher proportion of {110} and {100} facets are better at stabilizing the COOH* intermediate than the low-energy {111} facets, resulting in a superior ERC performance for dendritic Au than platelet Au.

Ham *et al.* reported similar observation for Ag dendrites.⁵¹ The dendritic structure was obtained at a deposition potential of -0.45 V vs. Ag/Cl with 40 mM of ethylenediamine (EN) additive. To investigate the higher energy facets effect on the performance of ERC, Ham *et al.* adopted the intensity ratio of (220) and (111) peaks as a new descriptor for CO₂ reduction. It was found that this higher intensity ratio of (220) and (111) peaks results in better CO Faradaic efficiency during the ERC process.⁵¹

Aside from the high-index facets effect, it was reported by Liu *et al.* that the nano tips at the top of dendrites can enhance the ERC performance by increasing the reagent concentration near the tips.¹³⁸ Figure 1.10i shows the electric field distribution of needle tips of Au dendrites. Comparing to rods and particles, these tips presents larger electric field, which can increase the concentration of surface-adsorbed K⁺ ion. The CO₂ can be stabilized on the sharps of dendrites with the concentrated K⁺, further enhancing the Faradaic efficiency of CO for Au dendrites.¹³⁸ This field induced reagent concentration (FIRC) effect is universal, and also effective on Pd dendrites. Compare to Pd rods and particles, the ERC Faradaic efficiency and reduction current was enhanced due to the FIRC effect of dendritic Pd.¹³⁸

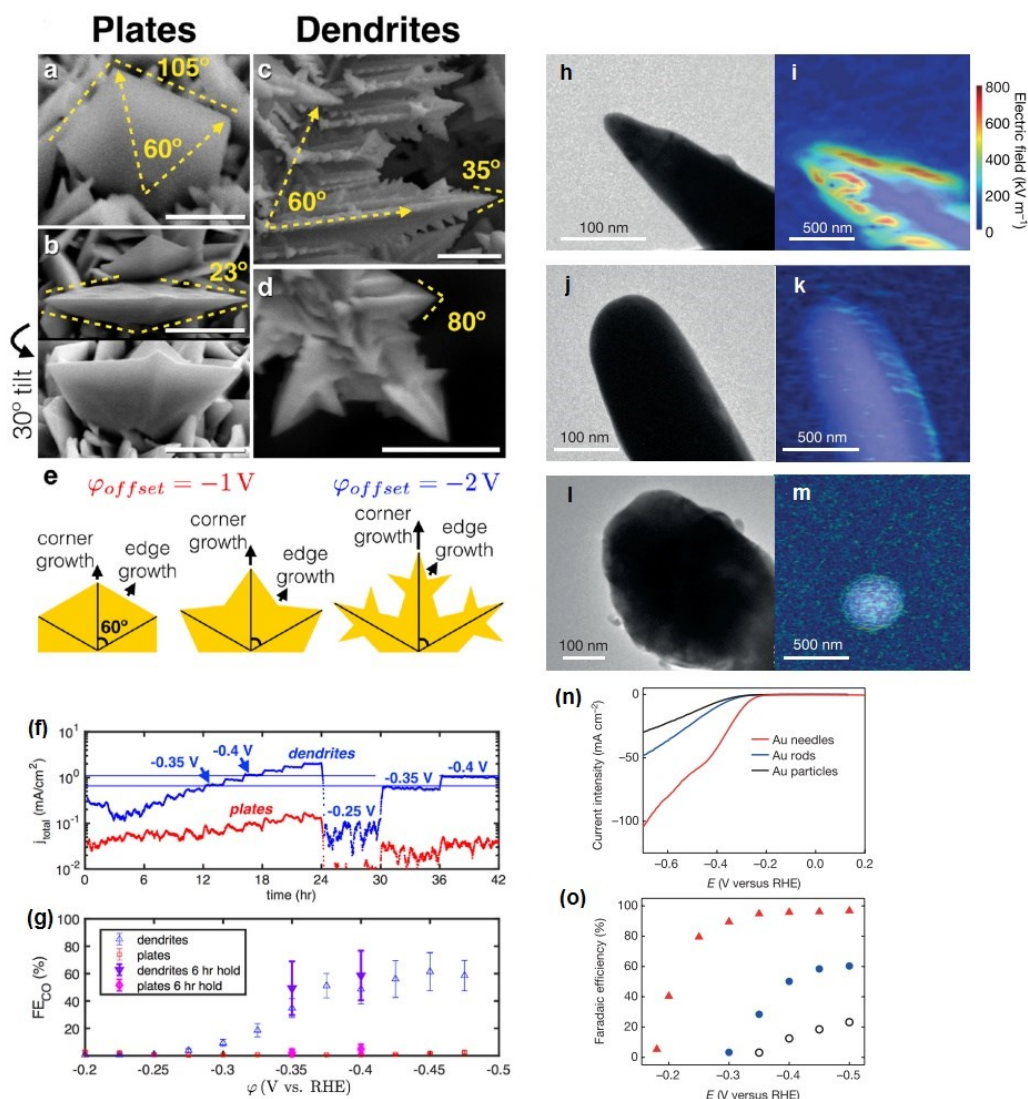


Figure 1.10 Examples of dendritic precious metal catalysts. (a-g) A typical example of enhancing ERC performance at an Au dendrite electrode by higher surface energy facets. SEMs showing the angle between primary growth directions and the angles between adjacent edges of the Au crystals in (a,b) plates and (c,d) dendrites. (e) Cartoons of the plate growth (left and center) and the dendrite growth (right). Arrows represent the growth velocity of corners and edges.¹³⁷ (Copyright © 2018, American Chemical Society). In (h, j, and l), TEM images; and in (i, k, and m) electric field distribution of Au needles, rods and particles deduced using Kelvin probe atomic force microscopy. (n) Current–voltage curves on Au needles, rods and particles obtained from the linear sweep voltammetry scans. Scan rate, 10 mV s⁻¹. (o) CO Faradaic efficiencies on Au needles, rods and particles at different applied potentials.¹³⁸

1.5.1.2 Non-noble metals

Non-noble metals have received attention due to their low cost, stability and high selectivity for the ERC. It was well known that Bi, Pb, Sn and In are highly selective for formate production in the ERC process. Figure 1.11a-b shows the Bi foil and Bi dendrites, respectively. The dendritic Bi shows a five-fold ERC current increase compared to Bi foil, and the formate Faradaic efficiency

of Bi dendrites (90%) is approximately 20% higher than that of Bi foil. The production rate of dendritic Bi exhibited CO₂ reduction activity that was 11 times higher than that of the pristine Bi foil at -0.74 V vs. RHE.⁴⁷ Kol *et al.* proposed that Bi dendrites shows more high-index facets than Bi foil. Density functional theory was used to calculate the surface intermediate energy of three different pathways. The findings presented in Figure 1.11d-g indicates the HCOO* intermediate can be stabilized substantially more on all the high-index facets, (012), (110), and (104) than on the (003) plane. Therefore, high-index facets provide the energetically favorable path for the intermediate HCOO*. This may explain the Bi dendrite's superior performance compared to that of the Bi foil.

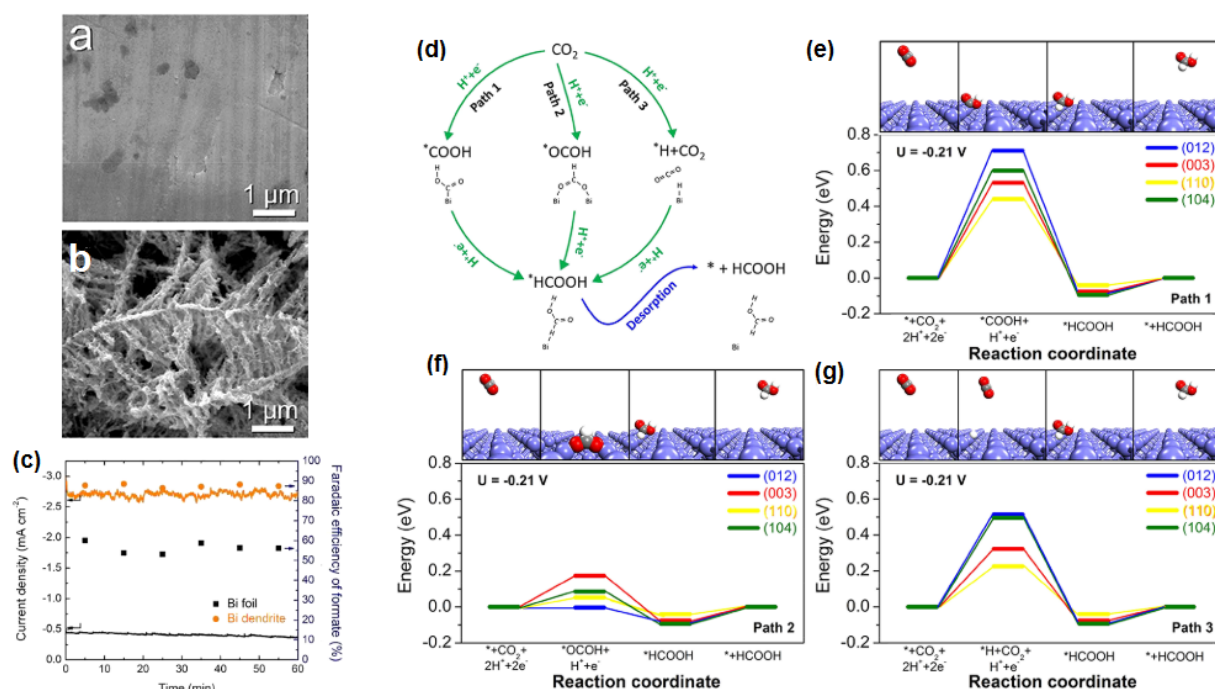


Figure 1.11 Examples of dendritic non-noble metal catalyst. Characterization of Bi dendrite electrode. Top-down SEM images of (a) pristine Bi foil, and (b) Bi dendrite. (c) Comparison of performance in terms of total current density (line; left axis) and Faradaic efficiency of formate (dot; right axis) at -0.74 V for 1 h. DFT calculation results on the CO₂-to-formate reduction reaction pathways for various possible Bi planes of (003), (012), (110), and (104). (d) Schematic diagram of three possible reaction pathways; path 1 via the formation of *COOH intermediate, path 2 via the formation of *OCOH intermediate, and path 3 via the formation of *H. Reaction free energy diagrams for the reaction (e) path 1, (f) path 2, and (g) path 3, when zero overpotential is applied (bias potential U = -0.21 VSHE). Noting that (012), (110), and (104) planes are preferentially developed for Bi dendrite compared with the close-packed surface of (003) that is dominant in Bi foil.⁴⁷(Copyright © 2017, American Chemical Society).

Zhong *et al.* successfully deposited the Bi dendrites on carbon paper substrates. A maximum formate Faradaic efficiency of 96.4% with a current density of 15.2 mA cm⁻² was achieved. Dendritic Bi provided stable ERC current over a 10 h period.¹³⁹ Recently, Piao *et al.* reported an

ion-enhanced ERC on dendritic Bi. Halides and cations were added to influence the selectivity for formate during the ERC process. It was found that the reaction is favored in the presence of Cs⁺ and Cl⁻. The formate Faradaic efficiency reached 100% and the stability of dendritic Bi electrode extended to 360 h.¹⁴⁰

Dynamic hydrogen bubbling template (DHBT) was widely used as a technique to achieve dendrite-like structures. With the help of hydrogen bubbling formation during the metal deposition, a porous electrode can be obtained with a dendrite-like secondary structure. Fan *et al.* reported a dendritic Pb deposited by DHBT technique.¹⁴¹ The dendritic Pb shows a decreased ERC overpotential of -0.99 V vs. RHE, with an enhanced reduction current and formate Faradaic efficiency (97%) compared to that of plate Pb. The DHBT technique was also used for Sn deposition,¹⁴²⁻¹⁴⁴ and In deposition.¹⁴⁵ The Sn and In electrodes fabricated via DHBT technique all show a porous primary structure with a dendritic secondary structure. In addition to the benefits of the dendritic secondary structure, the mass transfer in the porous primary structure also plays an important role in the formate's high selectivity.¹⁴⁵

Zn is selective for CO products during CO₂ electrochemical reduction. Rosen *et al.* reported that at a dendritic Zn electrode, the ERC catalytic activity is over an order of magnitude higher than that of bulk Zn.⁶¹ Rosen *et al.* found that the H₂ evolution was suppressed at dendritic Zn due to a higher density of surface-stepped sites in comparison to bulk Zn. The suppression of competitive H₂ evolution contributes to enhancing the efficiency of the CO₂ reduction reaction.

High energy products such as alcohols or carbon hydrogens were reported to be selective on Cu electrodes.¹⁴⁶ Reller *et al.* reported one dendritic Cu, which is highly selective for ethylene production, with a Faradaic efficiency of 57% at a constant current of 170 mA cm⁻². The large surface area of the dendritic Cu enables high conversion rates comparing to the smooth Cu. Rahaman *et al.* reported that the freshly deposited Cu dendrites are highly selective towards formate and C₂H₄ products at lower and higher overpotentials. However, the oxide derived Cu dendrites are highly selective towards ethanol and n-propanol production.⁶³ Rahaman *et al.* further found that the nanocavities at the surface of the oxide-derived dendritic Cu serve as active sites for alcohol formation, with the main reaction pathway being C₂. However, the freshly-deposited Cu dendrites should be the combined C₁/C₂ pathway, which differs from that of the oxide-derived dendritic Cu.¹⁴⁶ The nanocavities at the oxide-derived dendritic Cu play an important role in enhancing the ethanol production. Zhu *et al.* investigated the Cu(I)/Cu(0) ratio effect on the C₂ product efficiency of ERC at the surface of oxide-derived Cu dendrites. When the Cu(I)/Cu(0) ratio is 1.17, the oxide-derived Cu presents a higher C₂ Faradaic efficiency of 80%

with a current of 11.5 mA cm^{-2} at a low overpotential of 0.53 (for acetic acid) and 0.48 V vs. RHE (for ethanol).¹¹⁸ Scholten *et al.* reported a plasma-modified dendritic Cu. The low pressure O_2 -plasma treatment leads to an increase in the roughness of dendritic Cu surface, which improve the selectivity towards ethylene and ethanol.¹⁴⁷

1.5.2 Dendritic bimetallic metals

Bimetallic dendrite materials are synthesized to improve the catalytic activity of the dendritic single metals. There are two popular ways to synthesize the bimetallic dendrites: (1) Modifying a dendritic single metal by depositing a second metal at the dendrite surface, as the example shown in Figure 1.12(a-e), and; (2) Directly synthesizing dendritic binary alloys by co-deposition in a mixing plating solution, as the example shown in Figure 1.12(f-g).

Yang *et al.* reported an Ag decorated Cu dendritic electrode. Ag was deposited at the Cu dendrites' surface by a second step deposition. A C_2H_4 Faradaic efficiency that was 4.3-fold higher (25%) was achieved at the Ag-decorated Cu dendrites compared to dendritic single Cu. Ag decoration provides strong C and weak O adsorption sites for the carboxylate intermediate, which correlates with the higher C_2H_4 Faradaic efficiency.¹⁴⁸ Low *et al.* reported a Zn decorated Ag foam. The Ag foam acts as a template to disperse the Zn into submicron dendrites. These strained undercoordinated Zn atoms serves as the active sites for methanol formation during CO_2 reduction. The Faradaic efficiency of methanol on Zn-decorated Ag attains 10.5%, which is 10 times higher than that on single Ag and single Zn.¹⁴⁹ Ju *et al.* presented a Sn decorated Cu dendrites. The dendritic structure promotes a high CO_2 concentration at the electrode surface. Compared to the Sn-decorated Cu particle, the Sn-decorated Cu dendrites maintain a high CO Faradaic efficiency (90%) over a broad potential range.¹⁵⁰

Lamaison *et al.* presents a 1.9%-Ag alloyed Zn electrode with an enhanced CO Faradaic efficiency of 90% for 40 h durability at a lower potential of -0.9 V vs. RHE. The introduced Ag sites are lowering ERC overpotentials, compared to single Zn.¹⁵¹ Kottakkat *et al.* reported a dendritic AgCu foam obtained via the DHBT technique. In the presence of Ag, the Raman CO adsorption is observed at a more positive potential (Figure 1.12g), leading to enhanced CO selectivity compared to single Cu. The researchers proposed that this selectivity enhancement was affected by the synergistic effect between the bimetallic components.¹⁵² Kim *et al.* also reported that the metal ratio in Sn-In or Sn-Zn binary system will affect the products distribution. For example, the dendritic $\text{Sn}_{0.29}\text{In}_{0.71}$ catalyst shows a formate Faradaic efficiency of 59.2%, which is 19% increase over the dendritic single Sn. Moreover, the H_2/CO syngas ratio can be varied by modifying the

ratio in Sn-In or Sn-Zn binary alloys.¹⁵³ Park *et al.* studied the AgIn bimetallic dendrites. The catalytic performance of dendritic Ag was enhanced by introducing In, leading to a higher CO selectivity rather than H₂ evolution in highly negative potential regions during ERC process.¹⁵⁴ Hoffman *et al.*¹⁵⁵ and Rasul *et al.*¹⁵⁶ both found that the product distribution and selectivity is correlated to the alloy composition due to the different adsorption strengths of CO and COOH intermediates at Cu and In sites. Therefore, targeting products can be obtained by rationally designing the metal ratio in the dendritic binary system.

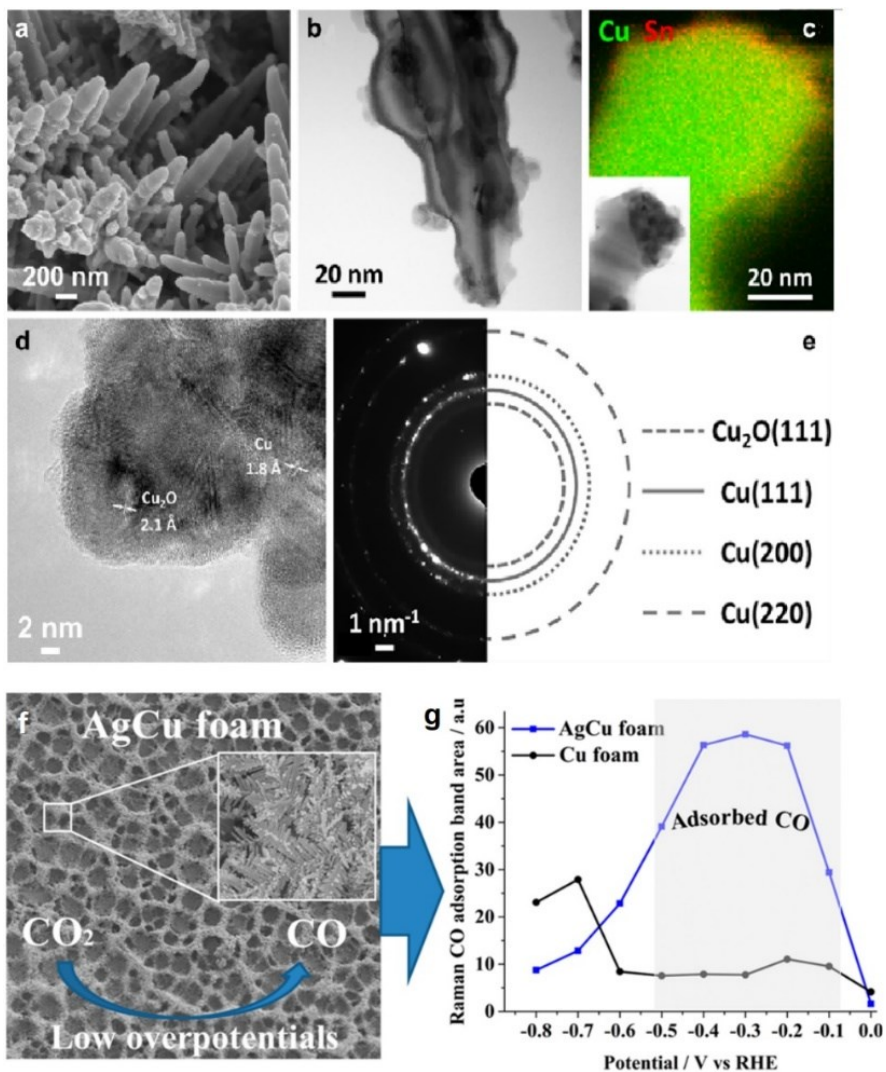


Figure 1.12 (a-e) Example of a Sn-decorated Cu dendrites electrode. (a) SEM image of Cu-Sn dendrites. (b) Scanning TEM image and (c) high-resolution scanning TEM-EDS elemental mapping of a single Cu-Sn dendrite. (d) High-resolution TEM image of a nanostructure at the tip of a Cu-Sn dendrite. (e) Electron scattering pattern from the region in d.¹⁵⁰ (Copyright © 2019, American Chemical Society). (f-g) An example of AgCu codeposited dendrites. (f) SEM images of AgCu foam. (g) Raman CO adsorption band area as function as potential. A comparison between single Cu foam and bimetallic AgCu foam.¹⁵² (Copyright © 2019, American Chemical Society)

1.6 Thesis Objectives and Organizations

1.6.1 Thesis objectives

As discussed above, the electrochemically reducing CO₂ into chemicals is one of the ways to remediate the high levels of CO₂ emissions arising from human activity. Among the different value-added products that can be obtained during ERC, formate/formic acid has generated a vivid interest due to its widespread use and strong market. Post-transition metals, such as In, Hg, Pb, and Sn, have attracted the interest of researchers due to the low price and high formate selectivity properties. However, for these post-transition elements, high selectivity is accompanied by high CO₂ pressure-demand, large onset potentials and high overpotentials requirement when large current density (high production rate) is obtained. Therefore, it is necessary to develop highly active post-transition catalysts working well in ambient pressure, temperature and aqueous electrolyte, achieving large reduction current at low overpotentials. Dendrite-structured catalysts are potential for highly active and selective ERC due to their large surface area, high density of exposed surfaces with preferential facet orientations, and the presence of sharp tips at the end of the dendrites. To date, the reported ERC performance on dendritic post-transition metals remains space to be improved, and the nature of the active sites at the dendrite surface needs to be uncovered through various characterizations or theoretical computations. Therefore, the objectives of this thesis are as follows:

- (1) Synthesizing a dendritic Pb electrode with a porous primary structure to decrease the ERC overpotential and enhance the ERC partial current density.
- (2) Decorating the dendritic Pb by another highly formate selective and non-precious metal (Bi) to further decrease the ERC overpotential and enhance the ERC production rate of formate. Further, investigate the active sites of the decorating metal.
- (3) Introducing another non-precious metal (Sn) to Pb-based dendritic materials and synthesizing binary dendritic alloys to further enhance the ERC performance. Investigate the mechanism of ERC enhancement for alloy materials by DFT calculations.

1.6.2 Thesis organizations

This thesis is composed of 6 chapters and the structures are as follows:

Chapter 1 introduces the background and motivation of my research, and the work fundamental about electrochemical reduction of CO₂. Afterwards, a literature review is presented, focusing on

metal catalysts classified by ERC products' selectivity. Next, examples about the surface engineering effect on the ERC performance are given. Then, the research progress of dendritic metal catalysts is summarized. The publication related to this chapter is:

Fan M, Garbarino S, Tavares AC, Guay D (2020) Progress in the Electrochemical Reduction of CO₂ on Hierarchical Dendritic Metal Electrodes, *Current Opinion in Electrochemistry*, Accepted, DOI: <https://doi.org/10.1016/j.coelec.2020.05.013>.

Chapter 2 provides the experimental and computational details. Synthesis methods of all the samples, physical and electrochemical characterization information, CO₂ reduction products analysis, adopted models and parameters for theoretical calculations are all provided.

Chapter 3 corresponds to the first objective. Dendritic Pb electrodes were synthesized and optimized. The catalytic activity of the dendritic Pb was investigated and the ERC performance on dendritic Pb electrode was tested. The ERC overpotential was reduced and the ERC partial current density for formate formation was increased through the highly active dendritic structure with a super rough surface. The publication related to this chapter is:

Fan M, Garbarino S, Botton GA, Tavares AC, Guay D (2017) Selective Electroreduction of CO₂ to Formate on 3D [100] Pb Dendrites with Nanometer-Sized Needle-Like Tips. *Journal of Materials Chemistry A*, 2(5):20747-20756.

Chapter 4 corresponds to the second objective. The dendritic Pb was decorated by depositing a dendritic Bi outmost layer. The ERC overpotential was further decreased of 200 mV on this Bi decorated dendritic Pb electrode, and the formate production rate was increased. The active sites of the dendritic Bi surface were investigated through physical and electrochemical studies. The publication related to this chapter is:

Fan M, Prabhudev S, Garbarino S, Qiao J, Botton GA, Harrington DA, Tavares AC, Guay D (2020) Uncovering the Nature of Electroactive Sites in Nano Architected Dendritic Bi for Highly Efficient CO₂ Electroreduction to Formate. *Applied Catalysis B: Environmental*, 274:119031.

Chapter 5 corresponds to the third objective. Sn was introduced to the Pb-based dendritic material to form a binary dendritic alloy. The mechanism of alloy effect on the ERC enhancement was investigated by theoretical calculations. The publication related to this chapter is:

Fan M, Eslamibidgoli MJ, Zhu X, Garbarino S, Tavares AC, Eikerling M, Guay D (2020) Understanding the Mechanism of CO₂ Electrochemical Reduction on Dendritic Sn₁Pb₃ alloy: A Computational-Experimental Investigation. *ACS Catalysis*, *Submitted*

Chapter 6 briefly summarizes the main conclusions of my research and provides the challenges and perspectives toward this field.

Following the main body of this thesis is a synopsis of this thesis in French as per the INRS requirements.

2 EXPERIMENTAL

2.1 Chemicals and Materials

Lead(II) perchlorate trihydrate ($\text{Pb}(\text{ClO}_4)_2 \cdot 3\text{H}_2\text{O}$, 99%) was purchased from ACROS Organics. Bismuth(III) nitrate pentahydrate ($\text{Bi}(\text{NO}_3)_3 \cdot 5\text{H}_2\text{O}$, $\geq 99.99\%$) and tin(II) chloride dihydrate ($\text{SnCl}_2 \cdot 2\text{H}_2\text{O}$, 99.99+%), were purchased from Sigma-Aldrich. Hydrogen peroxide (H_2O_2 , 30 wt.% in H_2O), acetic acid (CH_3COOH , $\geq 99.7\%$), nitric acid (HNO_3 , 68-70% solution in water), hydrogen chloride (HCl , 37%), anhydrous ethanol ($\text{CH}_3\text{CH}_2\text{OH}$, 95.27%), perchloric acid (HClO_4 , 70%) and potassium bicarbonate (KHCO_3 , 99.7%) were purchased from Fisher Chemical. Ti plate (99%, 0.2 mm thickness) and Pt gauze (99.9%) were purchased from Alfa Aesar. Pb plate (chemical grade, 1/16-inch thickness) was purchased from Nuclead. Carbon dioxide (CO_2 , 99.99%), and Argon (Ar , 99.99%) were purchased from Air Liquid. Deionized water (resistivity $> 18.2 \text{ M}\Omega \text{ cm}$) was purified by a Millipore Ultrapure water system in our lab.

2.2 Synthesis of Dendritic Pb Porous Electrode

2.2.1 Preparation of Pb substrate

A 0.5 cm^2 Pb plate was firstly electropolished by galvanostatic polarisation at 0.030 mA cm^{-2} for 10 min in a mixed solution of 24 mL anhydrous ethanol, 4 mL 30% H_2O_2 , 2 mL glacial acetic acid and 0.6 mL concentrated HNO_3 . The counter electrode was a piece of 4 cm^2 Ti plate. The electropolished Pb plate was used as the substrate for dendritic Pb deposition after cleaning by deionized water.

2.2.2 Deposition of dendritic Pb porous electrode

The porous Pb films were prepared by galvanostatic deposition from a solution consisting of 0.01 M $\text{Pb}(\text{ClO}_4)_2$ and 1 M HClO_4 . The distance between counter and working electrode was 2 cm. The electrodeposition was carried out by a Solatron 1480A multipotentiostat at varying current densities (from -0.1 to -4.0 A cm^{-2}) and deposition times (from 0 to 60s). The deposited Pb films were labeled as Pb_{j-t} , where j is the deposition current density and t is the deposition time. The deposition current densities were relatively high, leading to simultaneous Pb electrocrystallization and hydrogen evolution. Deposition of films in these conditions is commonly referred to as "Dynamic Hydrogen Bubbling Template (DHBT) technique".¹⁵⁷ After electroplating, the porous Pb

films were rinsed with deionized water (Millipore; specific resistivity > 18.2 MΩ cm) and dried under an Ar stream for 30 min.

2.3 Synthesis of Dendritic Bi Modified Porous Pb Electrode

2.3.1 Optimization of dendritic Bi

The Bi deposition conditions were firstly optimized to achieve a uniform coating of Bi layer onto a Pb plate (Pb_{plate}). The geometric area was 0.5 cm² for the Pb plate and the surface was electropolished to be clean and flat. Bi electrodeposition was carried out from a 1 mM $\text{Bi}(\text{NO}_3)_3$ and 1 M HCl mixed plating solution. Various deposition current densities (from -0.1 to -0.4 A cm⁻²) and deposition times (from 1 to 40 min) were optimized. At these deposition current densities, the deposition potential varies from -1.1 to -1.4 V vs. RHE.

2.3.2 Synthesis of dendritic Bi modified porous Pb electrode

Once the deposition conditions were optimized, the substrate was changed from Pb plate to porous Pb ($\text{Pb}_{\text{porous}}$). The dendritic Bi was deposited at -0.4 A cm⁻² for 40 min on the $\text{Pb}_{\text{porous}}$ substrate. The $\text{Pb}_{\text{porous}}$ substrate electrode was prepared by DHBT electrodeposition at -4 A cm⁻² with the time of 40 s in a plating solution of 10 mM $\text{Pb}(\text{ClO}_4)_2$ + 1 M HClO_4 . All electrodes were rinsed with deionized water (Millipore; resistivity > 18.2 MΩ cm) and dried under a gentle Ar stream for 30 min.

2.4 Synthesis of Dendritic SnPb Binary Alloy Electrodes

2.4.1 Optimization of the composition of SnPb binary alloys

The alloy SnPb electrodes were co-deposited galvanostatically using the DHBT technique on a 0.5 cm² flat Pb substrate at -4 A cm⁻² for 40 s. The plating solution was 10 mM $\text{Pb}(\text{ClO}_4)_2$ mixed with 10 mM SnCl_2 and 1 M HCl was used as the supporting electrolyte. The atom ratio varies (0:100%, 25%:75%, 50%:50%, 75%:25%, and 100%:0) between the two elements in the plating solution to obtain different SnPb alloys. Single dendritic Pb, and Sn were also deposited using the same technique, for comparison purposes.

2.4.2 Optimization of the deposition condition of the SnPb alloy electrode

After the deposition atom ratio was optimized, the deposition time was optimized by varying the deposition time (from 40s to 600s). The -4 A cm⁻² and 600 s are the optimized deposition

conditions for the dendritic SnPb alloy. After deposition, all deposited films were rinsed with deionized water and dried under Ar stream for 30 min.

2.5 Characterizations

2.5.1 Physical characterizations

The materials surface morphologies were characterized by scanning electron microscopy (SEM) equipped with energy-dispersive X-ray spectroscopy (EDX) (TESCAN, VEGA3).

Transmission electron microscopy (TEM) observations were carried out with a FEI Titan 80-300 Cubed Scanning transmission electron microscope (STEM) equipped with a high-brightness field-emission electron source and ultra-fast electron energy loss (EEL) Spectrometer. Specifically, the samples were investigated under high angle annular dark field (HAADF) mode for detailed atomic-level imaging. In cases where a cross-sectional analysis of the dendritic structure needed to be carried out, an ultra-thin area was carefully lift out using Focused ion beam (FIB) technique.

The crystalline structures and phase information for these alloys were investigated by x-ray diffraction (XRD) measurements, using a Bruker D8 Advance operated at 40 kV and 40 mA, with a weighted average Cu $K_{\alpha 1}$ and Cu $K_{\alpha 2}$ radiation of 1.5418 Å.

2.5.2 Electrochemical characterizations

The electrochemical characterization was performed in a three-electrode cell by a Solatron 1480A multipotentiostat. A Pt gauze was chosen as the counter, and a saturated calomel electrode (SCE) was used as electrode reference. The potentials in this study are quoted with respect to the reversible hydrogen electrode (RHE), using the following relation $E_{\text{RHE}} = E_{\text{SCE}} + 0.241 \text{ V} + 0.059 \text{ V} \times \text{pH}$.

The electrochemical active surface area (EASA) was calculated by measuring the double layer capacitance of electrodes at the non-faradaic potential region. Cyclic voltammetry (CV) current at different scan rate was recorded in Ar-saturated 0.5 M KHCO_3 to measure the double layer capacitance.

The ERC catalytic activity of electrode was analyzed by linear sweep voltammograms (LSVs). The LSVs were recorded in Ar-saturated and CO_2 -saturated 0.5 M KHCO_3 within the potential range extending from -0.32 V to -1.32 V vs. RHE at the scan rate of 5 mV s^{-1} .

Electrochemical impedance spectroscopy (EIS) was carried out in a three-electrode cell with the CO₂-saturated 0.5 M KHCO₃ electrolyte. EIS measurements in the CO₂ electroreduction potential range (applied potential ranging from -0.62 to -1.22 V vs. RHE by steps of 0.5 V) were obtained between 0.01 Hz and 200 kHz using an FRA Analyser (Solartron 1255B). In all cases, the current was allowed to stabilize for 30 minutes (see below) before starting the EIS measurements. Fitting to the equivalent circuit was carried out by using Zview.

2.6 Products Analysis

The liquid products were analyzed after 30 min electrolysis of CO₂ at the potential ranging from -0.62 V to -1.22 V vs. RHE. Formate concentration was measured by ion chromatography (IC) (ICS-1500, Dionex, USA) using an IonPac AS9-HC column separation column with a 9 mM Na₂CO₃ mobile phase at a flow rate of 1 mL min⁻¹. All samples were diluted 10 times before measurement.

Gas products were analyzed by gas chromatography (GC) (Agilent Micro 490) at two channels with the thermal conductivity detector. The Faradic Efficiency of H₂ was calculated by:

$$FE_{H_2} (\%) = \frac{\frac{Peak\ area}{\alpha} \times flow\ rate \times t \times \frac{P}{RT} \times z \times F}{Q} \times 100 \quad (2.1)$$

Where α is the conversion factor for H₂ based on the calibration of the gas chromatograph response established with standard samples, *flow rate* is the CO₂ flow rate during the test, *t* is the electrolysis time, *P* is the atmosphere pressure, *T* is the room temperature, *R* is the gas constant, *z* is the electron transfer number, *F* is the Faraday constant, and *Q* is the total charge during the electrolysis. In all cases, the total Faradaic efficiency, which is obtained by the addition of the partial FE for formate and H₂, was 100 ± 5%.

Examples of product analysis were shown in Figure S4.9.

2.7 Flow-Cell Test

A flow-cell was used to test the catalyst's CO₂ reduction capability under higher CO₂ flux. A schematic illustration of the flow-cell is shown in Chapter 5, Figure S5.1. The core of the electrolysis cell was made of a working electrode, a Nafion 117 separating membrane and an anode. This flow-cell is equipped with a saturated calomel electrode (SCE) reference and a Pt gauze counter electrode. Both the working and counter electrodes have a disk shape with a geometric surface of 1 cm². In this setup, the catholyte and anolyte flow rate (Masterflex L/S Easy-

Load® II Model 77200-50 pump head and 06434-17 pump tube) and pressure can be controlled independently. The electrolyte was a CO₂ super-saturated 0.5 M KHCO₃ solution that was prepared by using a soda machine (Sodastream, CO₂ purity 99.999%). The maximum work pressure of the soda machine was 145 psi which was 10-fold larger than the ambient pressure. The maximum dissolved CO₂ in the super-saturated electrolyte was 0.34 mol L⁻¹. The catholyte was circulated at a flow rate of 104 ± 1 mL min⁻¹ and the catholyte pressure was 5 psig over the atmosphere pressure. The anolyte was 0.5 M KHCO₃. It was circulated at a flow rate of 2.3 ± 1 mL min⁻¹ and the anolyte back pressure was 6 psig.

2.8 Theoretical Calculations

DFT calculations were carried out using periodic DFT implemented in the Vienna Ab initio Simulation Package (VASP 5.3.5).¹⁵⁸ The Perdew-Burke-Ernzerhof (PBE) exchange correlation (XC) functional was used.¹⁵⁹ The projector-augmented-wave (PAW) formalism was applied which keeps core electrons frozen and replaces their effect by pseudopotentials whereas valence electrons are expanded in a plane wave basis set up to an energy cutoff of 400 eV.¹⁶⁰ Spin-polarized calculations were carried out. Geometry optimizations were terminated when all forces on ions were less than 0.01 eVÅ⁻¹. The Brillouin zone was sampled using a k-point mesh of (5×5×1) for the 3×3×4 Sn₁Pb₃ unit cell.¹⁶¹

3 DENDRITIC LEAD FOR HIGHLY EFFICIENT ERC

Selective Electroreduction of CO₂ to Formate on 3D [100] Pb Dendrites with Nanometer-Sized Needle-Like Tips

Électroréduction Sélective du CO₂ en Formate sur des Dendrites Pb 3D [100] avec des Pointes de Type Aiguille de Taille Nanométrique

Authors:

Mengyang Fan,¹ Sébastien Garbarino,¹ Gianluigi A. Botton,² Ana C. Tavares,¹ and Daniel Guay^{1*}

1. INRS-Énergie, Matériaux Télécommunications, 1650 Lionel-Boulet Boulevard, P.O. 1020, Varennes, QC, Canada J3X 1S2

2. McMaster University, Brockhouse Institute for Materials Research and Canadian Centre for Electron Microscopy, 1280 Main Street West, Hamilton, ON, Canada L8S 4M1

Publication:

Journal of Chemistry Materials A

Publication Date: September 7, 2017

Volume 5, Issue 39, Pages 20747-20756

DOI: 10.1039/c7ta06528k

Contribution of authors:

Mengyang Fan, Dr. Sébastien Garbarino and Prof. Daniel Guay conceived and designed the research. Mengyang Fan prepared all samples and conducted most of the characterizations, and all the CO₂ electrochemical reduction measurements. Prof. Gianluigi A. Botton and his group carried out all the HR-TEM characterizations. The experiment results were discussed with Dr. Sébastien Garbarino, Prof. Ana C, and Prof. Daniel Guay. Mengyang Fan wrote the manuscript. The manuscript was commented by Prof. Ana C. Tavares and was carefully modified by Prof. Daniel Guay.

3.1 Introduction

Carbon dioxide (CO₂) emission generated by the unrestricted burning of fossil fuels has exceeded the recycle capability of CO₂ in nature, resulting in a series of environmental problems. To deal with the excess CO₂ and resolve the energy crisis, the conversion and utilization of CO₂ into carbon-based chemicals is one of the most promising ways.^{26,36,40,162} Carbon dioxide can be converted to synthetic fuels by photochemical^{36,163,164} and electrochemical methods. This latter approach has attracted widespread attention. Ideally, electricity from renewable sources would be used to drive the electrochemical reduction of CO₂ (ERC), making this process CO₂ neutral. Furthermore, the ERC would allow storing the excess of electricity from renewable sources into carbon-based chemicals that can be used as fuels using the existing technologies. From a technological viewpoint, the ERC has many advantages such as the controllable reaction process at room temperature and pressure, the green and recyclable electrolytes,¹⁶⁵ and the compact reaction system, which can be easily scaled up.^{26,27}

Various products can be achieved by ERC through different pathways, including carbon monoxide,¹⁶⁶⁻¹⁷⁰ formic acid,⁵⁸ hydrocarbon fuels (e.g. methane^{171,172}) and alcohols (e.g. methanol²⁶), among others. Formic acid/formate is one of the most favored products. It is obtained as a result of an easier reduction process using the 2-electron route, with its relatively lower kinetic barriers. Moreover, from a commercial perspective, there is a strong market for formic acid/formate due to its broad applications, including its use as fuel or an energy-storage medium.¹⁷³ However, the reduction of CO₂ to formic acid/formate is still plagued with high overpotentials needed to achieve the high current density that would be compatible with industrial applications, and poor product selectivity and faradaic efficiency. The high overpotentials and poor product selectivity are the result of inappropriate adsorption energies of key reaction intermediates, while the low faradaic efficiencies are due to the competition with the hydrogen evolution reaction (HER).

Post-transition metals such as Sn^{34,74,76,144,174-176} and Bi^{139,91} have been studied for ERC to formic acid/formate because of their high selectivity in aqueous electrolyte under ambient conditions (see Table 3.1). Palladium also exhibits interesting properties in terms of overpotential and Faradic efficiency but this a precious metal that is both scarce and expensive.¹⁷⁷⁻¹⁷⁹

Pb is another promising catalyst with good selectivity for formate. Previous works by Hori *et al.*³⁴, Koleli *et al.*⁷⁴ and Innocent *et al.*⁸⁹ already reported a FE_{formate} of ~65% to 74% using Pb plate or Pb granule electrodes. However, the electrolysis current density with these Pb electrodes was very low, ranging from -1.13 to -5.5 mA cm⁻². Most recently, Lee *et al.*⁸¹ showed that the FE_{formate}

could be enhanced to 98% when oxide-derived Pb (OD-Pb) was used as an electrode. However, the electrolysis current density at this OD-Pb electrode was just -0.6 mA cm^{-2} , which is rather unsatisfactory. There is therefore definitely scope for improvement of Pb-based catalysts.

Herein, we report the development and study of porous Pb electrodes that exhibit outstanding selectivity towards formate in aqueous electrolyte at ambient conditions. These films were prepared by Dynamic Hydrogen Bubble Templating (DHBT) method. They are made of 3D [100] Pb dendrites with nanometer-sized needle-like tips arranged in a porous honeycomb structure, which provides an extended electrode/electrolyte contact surface area. The physical characterizations of the porous Pb were carried out by scanning electron microscopy (SEM), scanning transmission electron microscopy (STEM) and x-ray diffraction (XRD), while electrochemical activities were characterized by cyclic voltammetry (CV), linear sweep voltammetry (LSV), and potentiostatic measurements.

3.2 Experimental Section

3.2.1 Preparation of porous Pb film

Honeycomb porous Pb films were electrodeposited onto electropolished 0.5 cm^2 Pb plate (Nuclead, chemical grade, 1/16-inch thickness). Electropolishing was carried out by galvanostatic polarisation at 0.030 mA cm^{-2} for 10 min in a mixed solution of 24 mL anhydrous ethanol (Fisher Chemical, histological grade), 4 mL 30% H_2O_2 (Fisher Chemical, ACS Reagent), 2 mL glacial acetic acid (Fisher Chemical, ACS Reagent) and 0.6 mL concentrated HNO_3 (Fisher Chemical, ACS Reagent).¹⁸⁰ The negative electrode was a piece of 4 cm^2 Ti plate (Alfa Aesar, 99%, 0.2 mm thickness).

After electropolishing, the Pb plates were used as substrates, and the porous Pb films were prepared by galvanostatic deposition from a solution consisting of 0.01 M $\text{Pb}(\text{ClO}_4)_2$ (ACROS Organics, ACS Reagent) and 1 M HClO_4 (Fisher Chemical, trace metal grade).¹⁸¹ The distance between counter and working electrode was 2 cm. The electrodeposition was carried out by a Solatron 1480A multipotentiostat at varying current densities (from -0.1 to -4.0 A cm^{-2}) and deposition times (from 0 to 60s). The deposited Pb films were labeled as Pb_{j-t} , where j is the deposition current density and t is the deposition time. The deposition current densities were relatively high, leading to simultaneous Pb electrocrystallization and hydrogen evolution. Deposition of films in these conditions is commonly referred to as "Dynamic Hydrogen Bubble Templating (DHBT)".¹⁵⁷ After electroplating, the porous Pb films were rinsed with deionized water

(Millipore; specific resistivity > 18.2 M Ω cm) and dried under an Ar stream for 30 min. A standard calomel electrode (SCE) was used during the deposition experiments; however, all potentials in this study are quoted with respect to the reversible hydrogen electrode (RHE).

3.2.2 Physical characterization of porous Pb films

The surface morphology of the porous Pb films was characterized through scanning electron microscopy (SEM) (JEOL, JSM-6300F) and the thicknesses was measured by SEM cross-section. The crystalline structures of the deposited Pb films were investigated by x-ray diffraction (XRD) measurements using a Bruker D8 Advanced operated at 40 kV and 40 mA, with a weighted average Cu K $_{\alpha 1}$ and Cu K $_{\alpha 2}$ radiation at 1.5418 Å.

High-resolution Scanning Electron Microscopy (HRSEM) was carried out with a Zeiss NVision SEM instrument at 5keV incident energy to enhance the surface sensitivity of the secondary electron signal. Thin sections for Transmission Electron Microscopy (TEM) were prepared using a dual beam Focused Ion Beam (FIB)-SEM instrument (Zeiss NVision 40) with the lift-out technique. Prior to sectioning, the area of interest was covered with a carbon layer deposited with electron beam-enhanced deposition so as to protect the topmost surface of the sample while maintaining a strong contrast between the Pb nanostructures and the protective layer necessary for FIB sectioning. The sectioned areas were thinned with multiple iterations of Ga beam thinning at decreasing incident energy with final polishing typically carried out at 2keV incident ion energy.

TEM observations were carried out with a FEI Titan 80-300 Cubed Scanning Transmission Electron Microscope equipped with a high-brightness electron source and a Gatan Quantum Spectrometer (Model 966).

3.2.3 Electrochemical characterization of porous Pb films

Electrochemical characterization was conducted in a conventional three-electrode system, using Pt gauze as a counter electrode and a SCE as reference electrode. Quantification of the deposited layers' mass was derived by recording stripping voltammograms at a scan rate of 5 mV s $^{-1}$ in Ar-saturated 1 M HClO $_4$ solution at a potential range between -0.25 V and 0.25 V. However, this process led to the dissolution of both the deposited Pb film and the Pb plate. Considering this, Cu plates were used as substrates and the porous Pb films were deposited at the same conditions reported above (these samples are identified as Pb/Cu). After recording the stripping voltammogram, the amount of Pb deposited on the Cu plates was calculated from the stripping charge, according to the following equation:

$$\text{Mass of deposited film} = \frac{Q \times M}{nF} \quad (3.1)$$

in which Q is the charge for the stripping of Pb film per cm^2 ; M is the molar mass of Pb (207.2 g mol^{-1}), n is the electron transfer number ($n = 2$) and F is the Faradaic constant (96485 C mol^{-1}).

The electrochemical active surface area (EASA) was determined by measuring the Pb-Pb²⁺ redox couple in Ar-saturated 0.5 M H₂SO₄ (Fisher Chemical, ACS Reagent) solution in a potential range between -0.93 V and 0.47 V. A charge density of 280 $\mu\text{C cm}^{-2}$ was used as the conversion factor to calculate the EASA.¹⁸²

CO₂ electroreduction performance was tested in an H-type cell, in which a Nafion® 117 membrane was used as a separator. Measurements were carried out in both CO₂-saturated (Air Liquide, 99.99%) and Ar-saturated (Air Liquide, 99.99%) 1 M KHCO₃ (Fisher Chemical, ACS Reagent). A Pt gauze (Alfa Aesar, 99.9%) was used as a counter electrode, and a SCE as the reference electrode. The catalytic activity of porous Pb was evaluated by recording linear sweep voltammograms in CO₂-saturated 1 M KHCO₃ at a scan rate of 5 mV s⁻¹ in a potential range between -0.29 V and -1.29 V. The electrolysis of CO₂ was carried out at potentials ranging from -0.89 V to -1.29 V for 100 min.

Formate concentration was measured by UV-visible spectrophotometry using the absorption region in the range between 190 nm and 240 nm. Calibration curves were recorded by measuring standard samples with HCOOH concentrations ranging from 0.0025 M to 0.025 M. Prior to measurement, all samples were acidified with 2 M H₂SO₄ and heated to 60° C for 10 minutes in order to expel CO₂ from the solution.¹⁸³

3.3 Results and Discussions

3.3.1 Physico-chemical characterization of porous Pb films

Figure 3.1 shows the SEM images of honeycomb Pb films prepared at -4.0 A cm^{-2} for 40 seconds (Pb_{4,40}). The average surface pore size is ~30 μm (Figure 3.1a and b). The walls of the honeycomb structure are composed of dendrite-like structures consisting of stems to which are attached branches (Figure 3.1c). As it will be shown later on, changing the deposition conditions (current density and deposition time) will alter the surface pore size of the primary honeycomb structure but not the dendrite-like secondary structure. Accordingly, we will first concentrate on the dendrite-like structure.

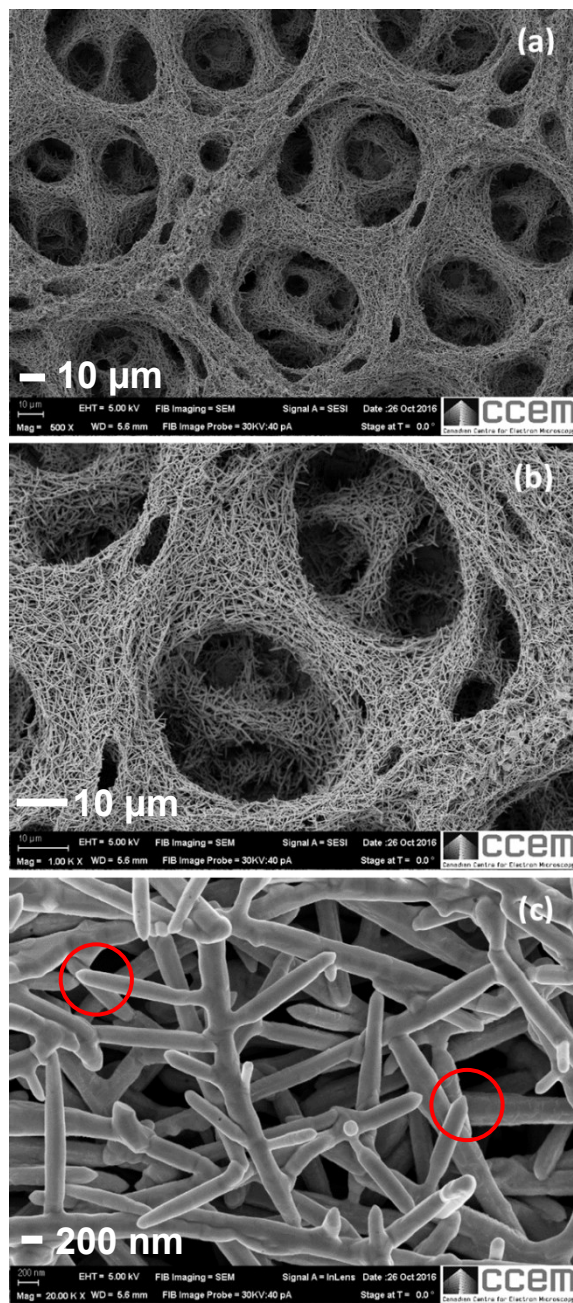


Figure 3.1 HRSEM images of a porous Pb film deposited at -4.0 A cm^{-2} during 40 seconds. Three different magnifications of the same electrode are shown in (a), (b) and (c). The red circles are representative examples of tips that were used to measure the tip diameter.

In Figure 3.2a, STEM characterization shows a dendrite which is essentially made of two single crystals assembled together. Since Pb is soft and therefore liable to bend slightly, there are some twists along the length of the single crystal, which might simply be due to plastic deformation during the preparation of the sample. The dendrite has a diameter of approximately 200 nm and an average length of ca. 6 µm (the whole dendrite is not shown) and a primary growth direction

along the [100] direction. The diameter of the dendrites is constant. High Resolution-STEM shows clearly their crystalline structure (Figure 3.2b) with lattice spacing consistent with the fcc structure of metallic lead ($a = 4.95 \text{ \AA}$). As it could be seen in Figure 3.2a, some voids appear on the surface of the Pb dendrite. These voids (Figure 3.2c) are defined by (111), (002), (1,-1,-1), (1-1-1), and (-1-1-1) facets.

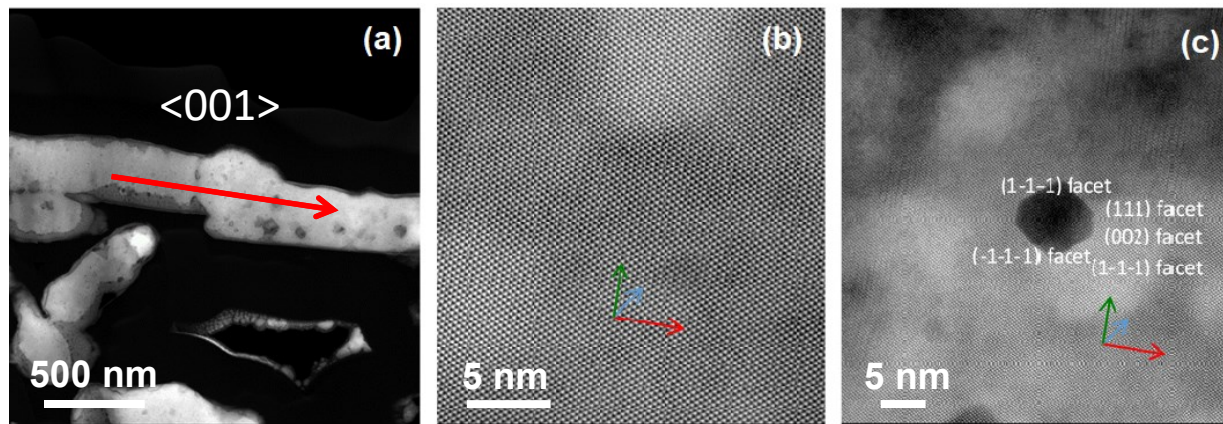


Figure 3.2 STEM images of a cross-section of prepared from the porous Pb film deposited at -4.0 A cm^{-2} and 40 seconds. (a) Low magnification annular dark-field STEM image of a few filaments presents in the cross-section. The red arrow shows the length and orientation of a perfectly oriented crystal with the $\langle 001 \rangle$ long axis. The segments beyond the arrow are slightly misoriented (by few degrees) with respect to the red arrow direction. Other filaments in the field of view would be randomly oriented with respect to the longest wire. Small cavities (dark spots within the filaments) are also observed within the filaments. A very thin oxide layer is also observed (with intermediate contrast) at the edges (hence the surfaces) of the filaments. (b) High-resolution STEM image of the high-quality crystalline Pb lattice. The major sets of planes are identified with the color-coded arrows (c) Lattice image in the proximity of a cavity showing the very faceted nature of the surfaces with the lattice planes identified in the color coded arrows and Miller indices.

Figure 3.3 compares the morphologies of porous Pb films deposited for 20 s at different deposition current densities. The surface of the Pb plate is relatively flat (Figure 3.3a and g). At the lowest deposition current densities (-0.1 and -0.5 A cm^{-2}), the Pb substrate is covered by a limited number of Pb dendrites. The honeycomb primary structure is not observed at the lowest deposition current density (-0.1 A cm^{-2} , Figure 3.3b and h), but starts to develop at -0.5 A cm^{-2} (Figure 3.3c and i). In both cases, the Pb substrate is clearly seen and presumably accessible to the electrolyte. As the deposition current density is increased to -1.0 , and further to -2.0 and -4.0 A cm^{-2} , the Pb substrate is no longer seen. Instead, densely packed [100] Pb dendrites forming a 3D network are observed. They are arranged in a honeycomb porous structure, with a surface pore size that decreases from 68 \mu m (Figure 3.3d) to 30 \mu m (Figure 3.3f) as the deposition current density is increased from -1.0 to -4.0 A cm^{-2} . Figure S3.1 presents SEM cross-section images of the porous Pb film thicknesses. As expected, the porous Pb film's thickness increased with the deposition current density.

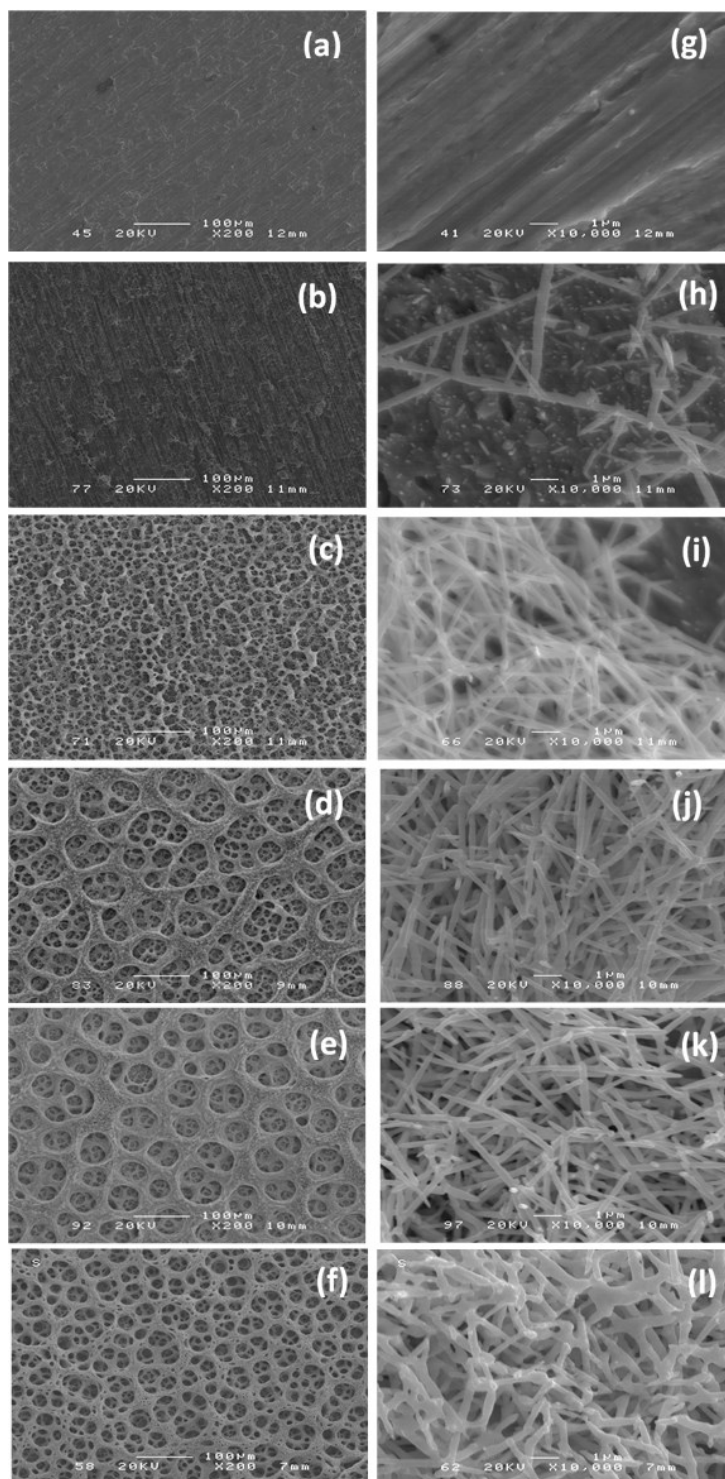


Figure 3.3 SEM images of (a, g) a Pb plate and porous Pb films deposited at (b, h), -0.1 A cm^{-2} , (c, i) -0.5 A cm^{-2} , (d, j) -1.0 A cm^{-2} , (e, k) -2.0 A cm^{-2} , and ((f, l) -4.0 A cm^{-2} . The deposition time was 20 seconds.

Deposition time is another important factor which will affect the characteristic of deposited porous Pb films. Figure S3.2 presents SEM images of porous Pb films deposited at a constant current

density of -4.0 A cm^{-2} , but at varying deposition times of 3, 10, 20, 40 and 60 seconds. Dendrites are formed and a honeycomb structure is observed in all cases.

The surface pore size increases with deposition times (Figure S3.2) and decreases as the deposition current density is increased (Figure 3.3). This reflects the dynamic of hydrogen bubbles formation and release. For thin mesoporous Pb layer, hydrogen bubbles are small but they coalesce into large hydrogen bubbles as the films thicken, thereby leading to larger pore size. In contrast, the smaller surface pore size as the deposition current is increased is due to the smaller un-coalesced bubbles formed at higher current density.¹⁸⁴

As stated above, all films exhibit a dendrite-like secondary structure that does not vary with the deposition conditions. In the literature, it was shown that the growth mode of electrodeposited lead varies with the electrolyte and the deposition current density.¹⁸⁵ In $0.5 \text{ M Pb}(\text{ClO}_4)_2 + 2 \text{ M HClO}_4$, Pb nodules, Pb plates, 2-dimensional [110] Pb dendrites and 3-dimensional [100] Pb dendrites are formed at increasingly high deposition current density ($0 - 0.3$, $0.3 - 0.5$, $0.5 - 0.6$ and $> 0.6 \text{ A cm}^{-2}$, respectively). In the present study, 3-dimensional [100] Pb dendrites were obtained even at the lowest deposition current density (-0.1 A cm^{-2}) and we couldn't evidence any change of the Pb growth mode. This is most probably related to a lower concentration of lead salt in the electrolyte, which is only one fiftieth of that used in reference.¹⁸⁵ A detailed analysis of the dendrite tip radius was conducted based on the SEM micrographs of films prepared at different deposition current densities and deposition times. The average tip radius is $22 \pm 8 \text{ nm}$ (Figure S3.3).

XRD patterns of Pb plate and porous Pb films are shown in Figure S3.4. Combined with the SAED images of the Pb dendrite shown in Figure 3.2b, it could be concluded that metallic lead is the main constituent of porous films. In some rare cases, very small PbO peaks were also identified in the XRD patterns, due to oxide formation on the porous Pb film surface. The presence of these peaks is most probably related to the presence of some residual O_2 molecules that come in contact with the film during the drying process. Indeed, it was shown elsewhere that freshly electrodeposited Pb films are made of metallic Pb which are converted into $\beta\text{-PbO}$ when a freshly electrodeposited and wet Pb films is in contact with gaseous O_2 .¹⁸⁶

To estimate the effect of deposition current density and deposition time on the mass of deposited porous Pb film, the anodic Pb stripping charge was evaluated. For these measurements, porous Pb films were deposited on a Cu substrate and the stripping voltammograms of porous Pb were shown in Figure S3.5. As expected, the mass of deposited Pb porous film linearly increased with

the deposition current density and with deposition times, as shown in Figure S3.6a and S3.6b, respectively. The porosity of the porous Pb films can be calculated as:

$$Porosity = \left(1 - \frac{m}{\rho A t}\right) \times 100\% \quad (3.2)$$

where m is the mass of the deposit, ρ is the density of lead and t is the thickness of the deposit obtained from the SEM cross-section images shown in Figure S3.1. The porosity of DHBT Pb films prepared decrease linearly from 98.5 to 96.5% as the current density is increased from 0.1 to 4.0 A cm⁻² (see Figure S3.7).

The EASA of the electrodes was determined by cyclic voltammetry in Ar-saturated 0.5 M H₂SO₄ at the scan rate of 5 mV s⁻¹. Figure S3.8 provides examples of the Pb oxidation/reduction peaks in the potential range of -0.55 V to -0.05 V. In this potential range, which corresponds to the Pb ↔ Pb⁺² redox reaction, the oxidation and reduction processes are reversible and the ratio between the oxidation and reduction charge is ~ 1. The detailed values of the redox charge are shown in Table S3.1. From these values, the EASA may be calculated as EASA = Q_{red} / 280 μC cm⁻², where 280 μC cm⁻² is the calculated specific charge density of polycrystalline metallic lead, assuming a 2e⁻ process and an equal repartition of (111), (110) and (100) surface orientations.

Figure 3.4a presents the trend of increasing EASA relative to deposition current density. Initially, the EASA of Pb plate was quite low, only about 52 cm². The EASA increased steadily with the deposition current density to reach its maximum value of ca. 1500 cm² on porous Pb deposited at -4.0 A cm⁻². In Figure 3.4b, the curve also shows an ascent trend of EASA relating to increasing deposition times. The maximum EASA increased is reached after ca. 40 s of deposition. Such high EASA values of porous Pb are due to its honeycomb morphology and the dendrite-like secondary structure.

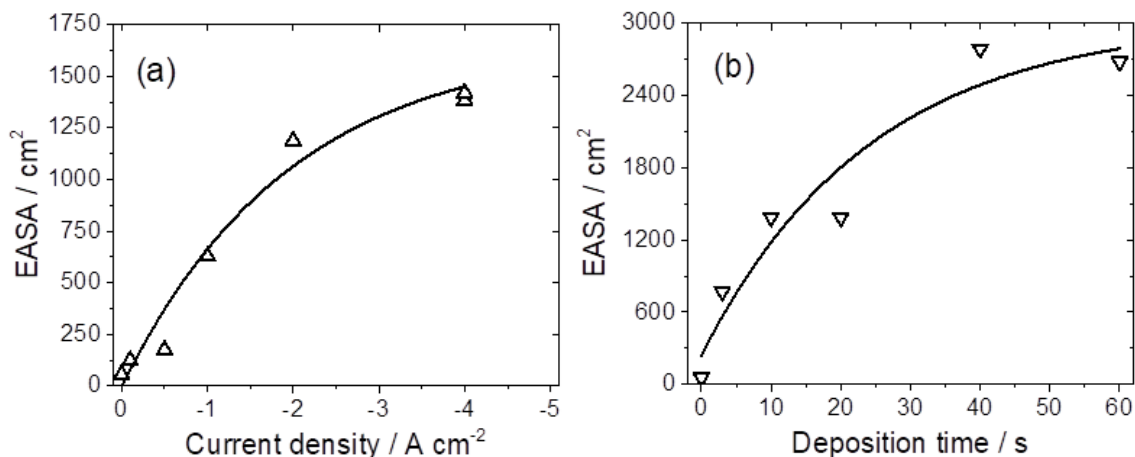


Figure 3.4 Variations of the electrochemical active surface area (EASA) of porous Pb films as a function of (a) the current density at a deposition time of 20 s, and (b) the deposition time at a deposition current density of -4.0 A cm^{-2} .

3.3.2 Electrocatalytic activity of porous Pb films for CO_2 reduction

To characterize the performance of the porous Pb film for CO_2 electroreduction, linear sweep voltammetry was carried out both on Pb plates and on porous Pb films in Ar-saturated and CO_2 -saturated 1 M KHCO_3 solution. As a typical example, Pb_{4-40} with large EASA was selected, and polarization curves are presented in Figure 3.5a. The onset potential (see Figure S3.9) for H_2 evolution on the Pb plate electrode is -1.03 V in Ar-saturated electrolyte, while it is -0.76 V in CO_2 -saturated solution. In comparison, the onset potential of HER was -0.87 for porous Pb_{4-40} film electrode, while the onset potential of ERC was -0.60 V . In CO_2 -saturated solution, the onset potential of porous Pb_{4-40} film is 160 mV more positive than that of the Pb plate, indicating that the CO_2 electroreduction is more facile. Comparing the reduction current density obtained from LSV results at -1.0 V in CO_2 -saturated electrolyte, the porous Pb_{4-40} film shows $\sim 10 \text{ mA cm}^{-2}$, which is higher by a factor of ~ 6 than that of the Pb plate (1.6 mA cm^{-2}). The remarkably enhanced activity of porous Pb_{4-40} film could be partly due to its increased EASA (a 50-fold enhancement) which provides a higher number of catalytic active sites, but also to a change in the nature of the catalytic sites, which also lead to a shift of the onset potential for the hydrogen evolution reaction.

Figure 3.5b shows the CO_2 electroreduction current density on Pb_{4-40} under varying electrolysis potentials in CO_2 -saturated 1 M KHCO_3 solution. The total current density increases with the electrolysis potential. The current density vs time curves are remarkably steady and does not vary with the electrolysis time over the range of potentials investigated. This is in sharp contrast with the bare Pb plate that displays a current density increase from -1 mA cm^{-2} to -6 mA cm^{-2} at -0.99 V during the same period of electrolysis. In that later case, this is thought to be due to the

enhancement of H₂ evolution caused by the pH decline near the electrode surface during continuous electrolysis. This phenomenon is not observed on porous Pb electrodes, mostly because the current efficiency for the production of H₂ at -0.99 V is less than 3% (see Figure 3.5c), which minimizes the pH change in the vicinity of the electrode. The fact that the current density of porous Pb₄₋₄₀ film does not vary over time also suggests the structure of the electrode is extremely stable. SEM images were taken after 100 min of CO₂ electrolysis to investigate the stability of the surface morphology. Remarkably, the porous surface remains unchanged (compare Figure S3.10a and S3.10c), as does the dendrite-like secondary morphology (compare Figure S3.10b and S3.10d).

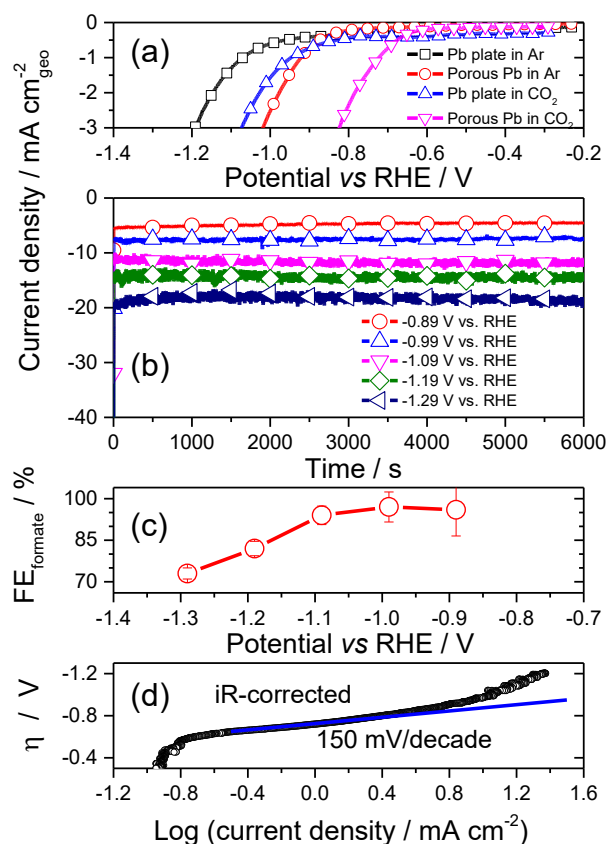


Figure 3.5 In (a), linear sweep voltammeter of a Pb plate and porous Pb films in Ar- and CO₂-saturated 1 M KHCO₃. The scan rate was 5 mV s⁻¹. In (b), variation of the CO₂ electroreduction (ERC) current density at different electrolysis potentials. In (c), variation of the formate Faradaic efficiency with respect to the electrode potential. In (d), variation of the CO₂ reduction overpotential with respect to the logarithm of the current density. The porous Pb film was deposited at -4.0 A cm⁻² during 40 seconds.

The produced formate was quantified by UV-vis, and Figure 3.5c presents the trend of Faradaic efficiency (FE) for formate relative to CO₂ electrolysis potential. FE is ~97% at -0.99 V, corresponding to ca 800 mV overpotential, but it decreases when the electrolysis potential is more

negative than -1.0 V. This is consistent with the fact that porous Pb electrode has an onset potential of -0.87 V for the HER, but it could also be due to mass transport limitation. Indeed, in our experimental conditions, CO₂(gas) is in equilibrium with the electrolyte at all times; therefore, the CO₂(aq) concentration is a constant (0.03416 M) at ambient conditions (101.3 kPa, 25° C).¹⁸⁷ The diffusion limited current density for CO₂ electroreduction was estimated to be 12 mA cm⁻² using the simplified steady-state Nernst diffusion layer model, as follows:¹⁸³

$$I_{lim} = \frac{nFD C_0}{\delta} \quad (3.3)$$

where I_{lim} is the diffusion limited current density, n is the number of electrons in the reaction, F is the Faradaic constant, D is the diffusion coefficient of the reactant (1.9×10^{-7} cm² s⁻¹ in electrolyte),^{187,188} C_0 is the reactant concentration (0.03416 M), and δ is the thickness of the boundary layer (taken as 0.01 cm).¹⁸⁸ From Figure 3.5b, it is seen that at -1.09 V, the current density is approximately equal to the diffusion-limited current density (12 mA cm⁻²). In these conditions, the supply of CO₂ is limited and hydrogen evolution must be responsible for any current density increase.

When comparing our results with those from the literature, we observe a considerable improvement. In our work, an outstanding FE of 97% for formic acid was obtained at an overpotential of 800 mV with a current density as high as -8 mA cm⁻². In most previous studies, similar FE values were obtained at higher overpotential: (i) 72% to 88% formate FE at 1.2 V with a current density of -5.5 mA cm⁻²,³⁴ 40% formate FE at 1.1 V with a current density of -0.5 mA cm⁻²,⁷⁴ 50% formate FE at 1.6 V,¹⁸⁹ and 60% formate FE at 1.0 V.⁸¹ Therefore, considering the activity, selectivity and energy needed, the porous Pb film made of 3D [100] dendrites with nanometer-sized needle-like tips represents a highly encouraging progress in improving the current density and formate FE while decreasing the overpotential in comparison to a Pb plate electrode and to all the pure Pb-based electrodes that have been described in the literature. In the low overpotential regime of CO₂ reduction, the Tafel slope is 150 mV dec⁻¹, which is consistent with the rate determining initial electron transfer to CO₂ to form surface-adsorbed CO₂• as reported elsewhere.⁸¹

As discussed above, the EASA of porous Pb films increases with deposition current density (Figure 3.4a) and deposition time (Figure 3.4b). To ascertain the effect of deposition conditions and EASA on the electroreduction of CO₂, the formate concentration was measured after 100 min of electrolysis at -0.99 V in 1 M CO₂-saturated KHCO₃ solution. As seen in Figure 3.6a, the partial current density for the formation of formate increases with EASA, although the rate of increase of decreases progressively as the EASA is increased. This is not thought to be due to limitation

imposed by mass transfer since the diffusion limiting current density is $12 \text{ mA cm}_{\text{geo}}^{-2}$, well above the current density reported in Figure 3.6a. This behavior is reminiscent of that expected when an irreversible reaction takes place on the walls of a porous electrode. Assuming that the concentration gradient is perpendicular to the porous electrode surface and that no radial distribution perpendicular to the electrode wall inside the pore is considered, and in the absence of forced convection with narrow pore flooded with a highly conductive electrolyte, Keddam *et al.* were able to show that the current density varies as $a \cdot \tanh(b \cdot L)$, where a and b are constants that depend on the concentration and diffusion coefficient of the reacting species, and L is the distance from the top surface where the concentration gradient is zero.¹⁹⁰ So, to be able to resort to this formalism, a plot of the current density vs the thickness of the deposit was drawn, from which the value of L was extracted (Figure S3.11). The effective length of the pores is $39 \mu\text{m}$. The bottom part of pores exceeding this value does not contribute to the total current density of the electrode since the CO_2 concentration gradient is zero for pore length exceeding L . According to Figure S3.12, this corresponds to a deposit having an EASA of ca. 1300 cm^2 .

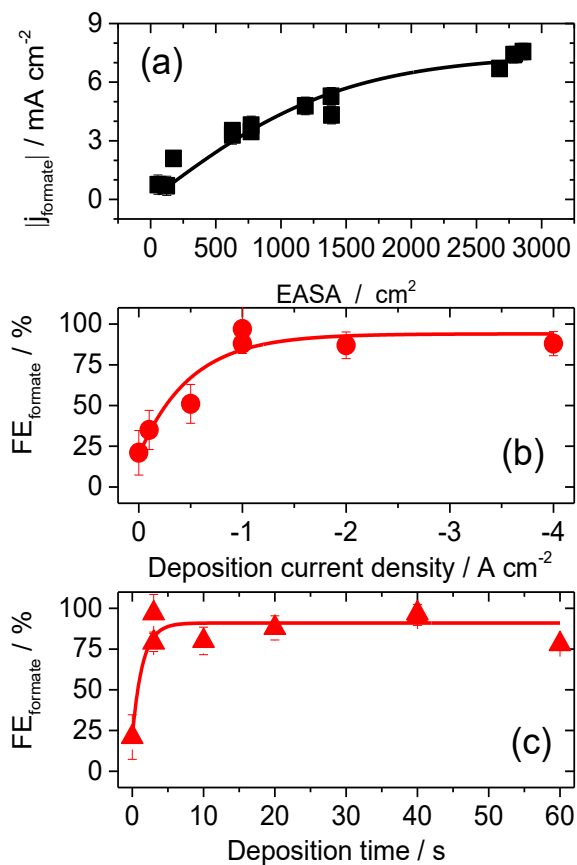


Figure 3.6 In (a), variation of the partial current density at -0.99 V for the formation of formate with respect to the electrochemically active surface area. In (b) and (c), variation of the formate faradaic efficiency with respect to the deposition current density and deposition time, respectively.

Figure 3.6b and c present a comparison of Faradaic efficiency for formate on Pb plates and porous Pb films deposited at different conditions. Figure 3.6b indicates that the FE on the Pb plate is ~21% only, whereas on porous Pb film is constant at ca. 92% and independent of the deposition current density when it is equal to or above -1.0 A cm^{-2} . As shown previously in Figure 3.3b, the Pb plate substrate of porous Pb films prepared at lower deposition current density (-0.10 and -0.50 A cm^{-2}) is clearly discernable in SEM micrographs and most probably accessible to the electrolyte, which explained why the formate FE has an intermediate value. As discussed earlier, there is a significant increase of the surface pore size as the deposition current density is increased but this factor does not affect the formate FE once the Pb plate substrate is no longer accessible by the electrolyte. In the case of deposition time, the FE increases from ~21% for the Pb plate to 92% as soon as a porous Pb film is formed at the surface of the substrate. At 800 mV of overpotential, the formate production rate increases by a factor of 10, from 5.89×10^{-8} to $5.92 \times 10^{-7} \text{ M min}^{-1}$ from the bare Pb electrode to the best mesoporous Pb electrodes studied here. At -1.0 V vs. RHE , the electrode didn't show any sign of degradation over prolonged electrolysis (6 hours) and both the current density and the formate faradaic efficiency stay constant over time (see Figure S3.14). An increase of the formate FE on oxide-derived Pb electrode compared to Pb foil was also observed by Lee and Kanan.⁸¹ In that case, however, this increase was the result of H_2 evolution being suppressed on oxide-derived Pb relative to Pb foil. This was thought to arise as a result of difference in coverage of a metastable Pb^{2+} layer on oxide-derived Pb compared to Pb foil because of a very high density of defects on oxide-derived Pb.⁸¹ It was shown previously that the dendrites are highly crystalline, and while they are not free of defects (see Figure 3.2c), the defect density is certainly limited compared to an oxide-derived Pb film. Also, as shown previously, the H_2 onset potential on porous Pb film is shifted positively (+160 mV) with respect to Pb plate. So, in the present work, the increase in formate FE of porous Pb film compared to Pb foil is not due to the suppression of H_2 evolution.

The increase in formate FE with both deposition time and deposition current density could also be due to an increase in roughness of the deposit. The importance of surface morphology and roughness in controlling selectivity during CO_2 electroreduction was previously demonstrated at roughened Cu electrodes.¹⁹¹ As shown in Figure S3.13, the formate FE depends on the EASA of the porous Pb electrodes and values larger than 90% are reached as soon as EASA is above 500 cm^2 . In the present work, this phenomenon could be exacerbated due to the use of a highly concentrated (1.0 M) KHCO_3 supporting solution. As discussed elsewhere,¹⁹² the thickness of the electric double layer (EDL) decreases as the concentration of the electrolyte increases and

nanoscale pores become more accessible. In the case of nanoporous Cu, the nanopores are accessible at concentrations above 0.5 M KHCO_3 , well below the concentration used in the present study.

It has been proposed that CO_2 electroreduction could proceed through a proton-assisted mechanism, which involves first the formation of adsorbed hydrogen on the Pb surface followed by coupling with dissolved CO_2 to form carboxyl (COOH^*) intermediate species.¹⁸⁹ However, this mechanism seems dubious in our case for several reasons. It is known that the rate determining step for HER at Pb is the formation of adsorbed hydrogen (H_{ads}). The observed onset potential for HER on porous Pb electrode is -0.87 V, which means that H_{ads} coverage is negligible at more positive potential. As noted before, the onset potential for CO_2 electroreduction is -0.60 V, which is more positive than the potential at which significant H adsorption at the surface of Pb is observed. Moreover, the selective CO_2 reduction towards formate (no traces of CO production) cannot be explained using the carboxyl (COOH^*) intermediate mechanism, in which CO and formate ions are competitively formed.²⁹ Thence, at porous Pb electrodes, the quantitative ($\geq 97\%$) production of HCOOK in the applied potential range must correspond to the CO_2 reduction mechanism which involves OCHO^* intermediate, the latter exclusively leading to the formation of formic acid.¹⁹³

The large positive shift (160 mV) of the CO_2 reduction onset potential between Pb plate and porous Pb electrode could be due to the dendrites showing an increase proportion of [100] preferentially oriented surfaces. As mentioned earlier, the Pb dendrites are growing along the [100]-axis and are having a near constant diameter of ca. 200 nm over most of their length (except at the tip of the dendrite). This could happen if the constant diameter sections of the dendrites are terminated by [100] and [110] surfaces since both are parallel to the [100] growing axis. In contrast, the tips could be enclosed by planes like [111], the latter making angle of 54° with the [100] growth axis. Evidence of that could be found in Figure 3.1c (see the circled regions). The presence of (100) surfaces was recently found to shift positively (+ 200 mV) the CO_2 overpotential for HCOOK formation at Cu foams.¹⁹² The same conclusion was reached from theoretical work, emphasizing the spontaneous chemisorption of CO_2 and favorable thermodynamic properties for Fe, Co, and Ni (100) surfaces.¹⁹⁴

Liu *et al.* showed recently that local high electric fields can be achieved at nanostructured electrodes and these can greatly modify the electrocatalytic activity for CO_2 reduction.¹³⁸ In these conditions, a large concentration of electrolyte cations is observed at metallic nanometer-sized tips. Simulations have revealed a ten-fold higher electric fields in the vicinity of nanometer-sized

tips compared to planar electrodes. Experimentation on Au nanoneedles confirm a field-induced reagent concentration that enables the CO₂ reduction reaction to proceed at higher rate and lower overpotential than on Au rods and Au particles.¹³⁸ As shown in the same study, adsorbed K⁺ ions stabilize the various intermediates during CO₂ reduction and lower the thermodynamic energy barrier of the reaction for all facets. This effect is not restricted to Au as it was also observed on Pd needles for the conversion of CO₂ to formic acid/formate. In the present study, the tip diameter is 22 nm, a range where, according to the work of Liu *et al*, a field-induced reagent concentration is expected. Accordingly, another interesting hypothesis to explain the lower overpotential for CO₂ reduction and enhanced reaction rate of porous Pb compared to Pb plate could thus be related to the size of the dendrite tip. However, the same hypothesis could hardly explain the +160 mV shift of the HER onset potential between Pb plate and Pb porous films since the nature of the counterions (Li⁺, Cs⁺, Na⁺ or K⁺) was shown not to have an effect.¹⁹⁵

Finally, it is worth emphasizing the excellent stability of porous Pb electrode, both in terms of current density and formate FE. As shown in Figure S3.14, both the current density and the formate faradic efficiency are remarkably constant at *ca.* 8 mA cm⁻² and 98% over prolonged electrolysis (6h). This is quite remarkable considering that variation of pH and the electrodeposition of metallic (or other) impurities from the electrolyte would contribute to a decline of both the current density and formate faradic efficiency. In that respect, the fact that porous Pb electrodes have a honeycomb primary structure and dendrite-like secondary structure could contribute to the electrode stability in prolonged electrolysis test.

Table 3.1 Comparison of FE_{formate} on different Sn-, Bi- and Pb-based catalysts.

Catalysts	Electrolyte	Electrolysis potential (V vs. RHE)	Current density (mA cm^{-2})	FE_{formate}	Ref.
Sn	0.5 M KHCO_3	-0.97	-5.5	~65%	34
Sn granules	0.5 M KHCO_3	-1.03	-0.54	62%	74
Sn/ SnO_x	0.5 M NaHCO_3	-0.70	-1.7	~40%	174
Sn powder/GDE	0.5 M NaHCO_3	-1.17	-27	~70%	76
Sn	2 M KCl	-1.34	-5	60%	175
Reduced nano SnO_2 /graphene	0.1 M NaHCO_3	-1.16	-10.2	93.6%	176
Sn dendrites	0.1 M KHCO_3	-1.36	-17.1	71.6%	144
Bi dendrites	0.5 M NaHCO_3	-1.13	-15.2	96.5%	139
Pb	0.5 M KHCO_3	-1.17	-5.5	~72%	34
Pb granules	0.5 M KHCO_3	-1.03	-1.13	74%	74
Pb plate	0.5 M NaOH	-0.86	-2.5	65%	89
Oxide-derived Pb	0.5 M NaHCO_3	-0.8	-0.6	98%	81
Porous Pb	1 M KHCO_3	-0.99	-8	97%	This work

3.4 Conclusions

High surface area porous Pb electrodes were prepared through the simple, rapid dynamic hydrogen bubbling template (DHBT) technique. The porous Pb electrodes are formed by a honeycomb primary structure and dendrite secondary structure growing along the [100]-axis. The dendritic structure is made of elongated single crystal having a near constant length of *ca.* 200 nm and a tip diameter of 22 nm. Electroreduction of CO_2 carried out on these electrodes showed Faradic efficiencies for formate larger than 90% for electrochemical surface areas above 500 cm^2 , reaching as much as 97% at -0.99 V vs. RHE with a current density of -7.5 mA cm^{-2} . The porous Pb electrodes showed in addition a remarkable stability both in terms of current density and formate Faradic efficiency, with constant values of *ca.* 8 mA cm^{-2} and 98%, respectively, over

prolonged electrolysis of 6 hours. The enhanced performance of the porous Pb electrodes was attributed to the dendrite secondary structure that could help to concentrate the reactants in the boundary layer.

Acknowledgements

This work was supported by the Natural Sciences and Engineering Research Council of Canada (NSERC). We thank Dr. Glynis de Silveira for the high-resolution scanning electron microscopy work, Travis Casagrande for the FIB sample preparation and Andreas Korinek for the STEM work. High resolution scanning electron microscopy and scanning transmission electron microscopy with electron energy loss spectroscopy were carried out at the Canadian Centre for Electron Microscopy, a facility supported by the Canada Foundation for Innovation under the Major Science Initiative program, NSERC, and McMaster University.

3.5 Supporting Information

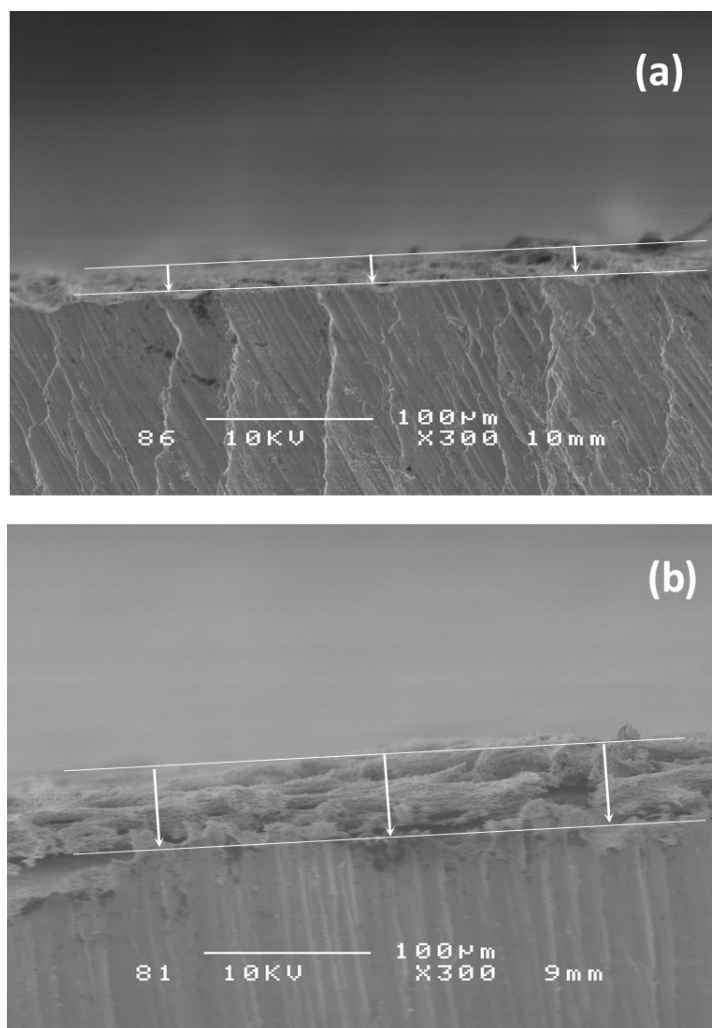


Figure S3.1 SEM cross-sections of porous Pb film on Pb plate, deposited at (a) -1 A cm^{-2} , and (b) -4 A cm^{-2} . The deposition time was 20 seconds.

The thicknesses of porous Pb films were measured by SEM cross-section. When deposition time is fixed, the thickness of porous Pb film increased with deposition current density. Figure S3.1a shows the thickness of porous Pb film deposited at -1 A cm^{-2} is $\sim 20 \mu\text{m}$. When current density increased to -4 A cm^{-2} , the thickness of porous Pb film increased to $48 \mu\text{m}$ (Figure S3.1b).

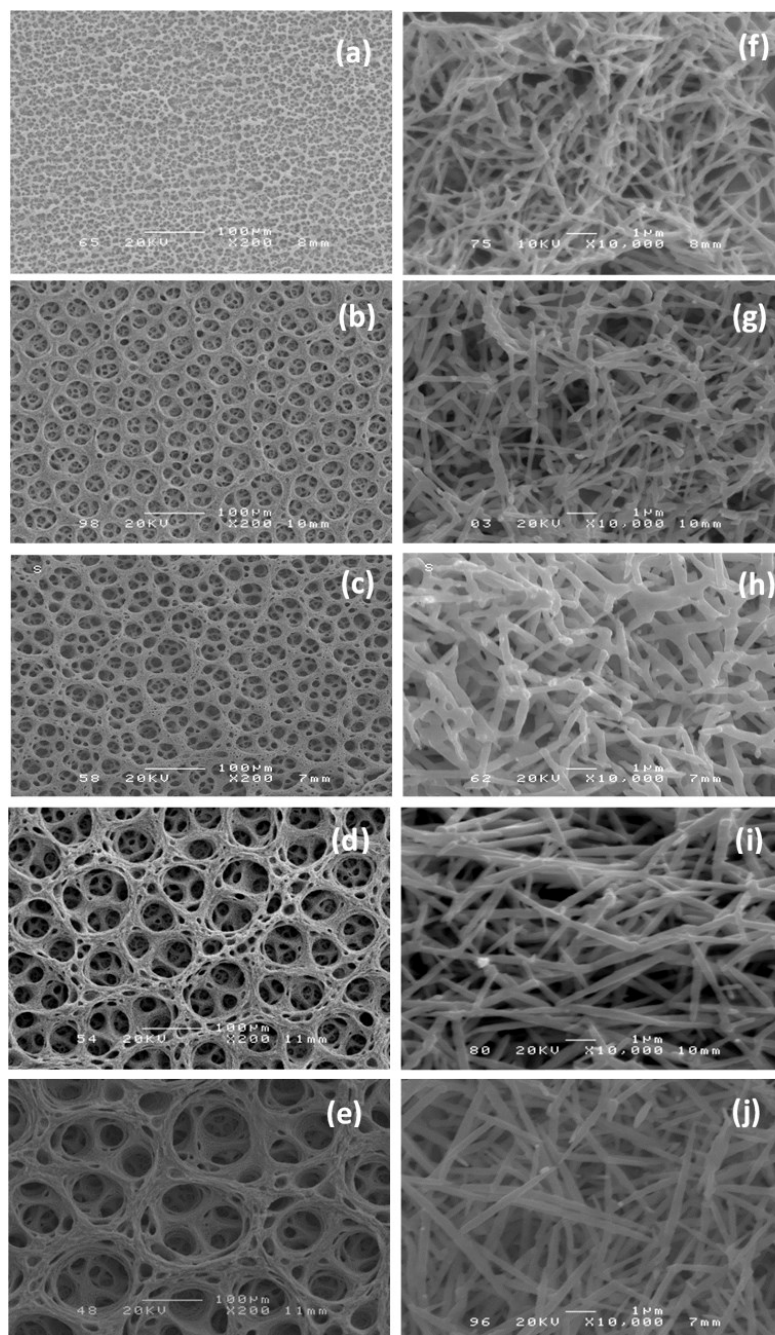


Figure S3.2 SEM images of porous Pb films deposited at (a, f) 3 seconds, (b, g) 10 seconds, (c, h) 20 seconds, (d, i) 40 seconds and (e, j) 60 seconds. The deposition current density was -4 A cm^{-2} .

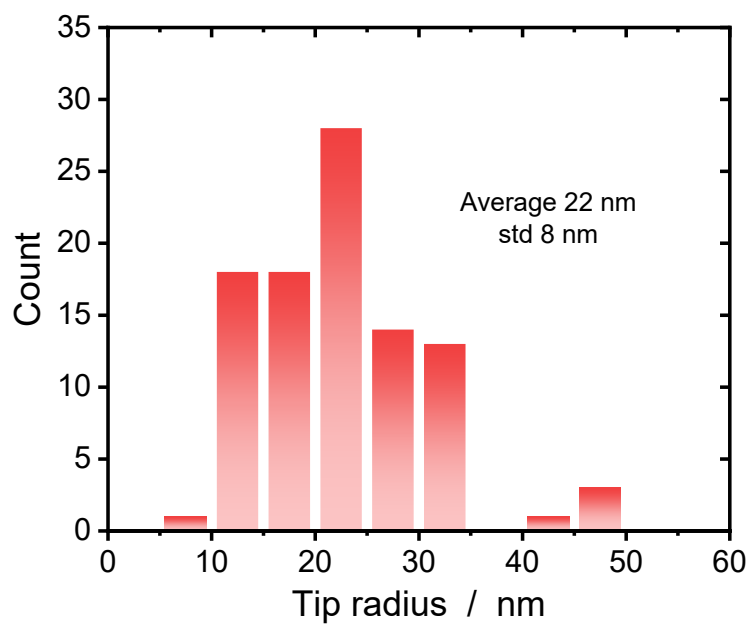


Figure S3.3 Histogram of the tip radius. The tip radius of a total of 96 dendrites were measured from SEM micrographs of samples prepared at different deposition current densities and deposition times.

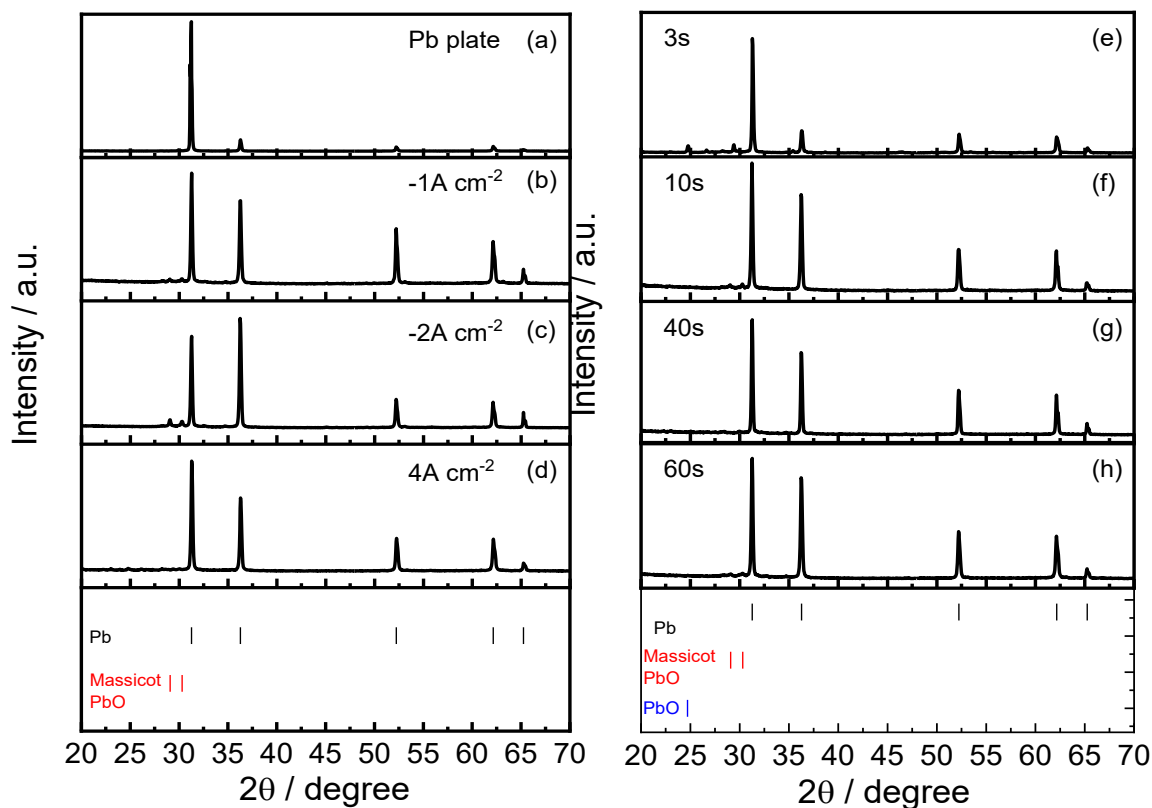


Figure S3.4 XRD patterns of (a) Pb plate; and porous Pb films deposited at (b) -1 A cm^{-2} ; (c) -2 A cm^{-2} ; (d) -4 A cm^{-2} ; for a deposition time of 20 seconds. XRD patterns of porous Pb films deposited at (e) 3 seconds; (f) 10 seconds; (g) 40 seconds; and (h) 60 seconds. The deposition current density was -4 A cm^{-2} .

The XRD patterns indicate that all samples shown in Figure 3.1 and 3.2 are primarily composed of metallic Pb, with the characteristic XRD peaks at 31.2° (111); 36.2° (200); 52.2° (220); 62.1° (311), 65.2° (222). Very small peaks are also observed few surfaces were oxidized at 24.7° (PbO), and 29.1° and 30.3° (massicot PbO). On the Pb plate, the intensity of the (111) plane at 31.2° is very strong indicating the substrate is preferentially oriented along that axis.

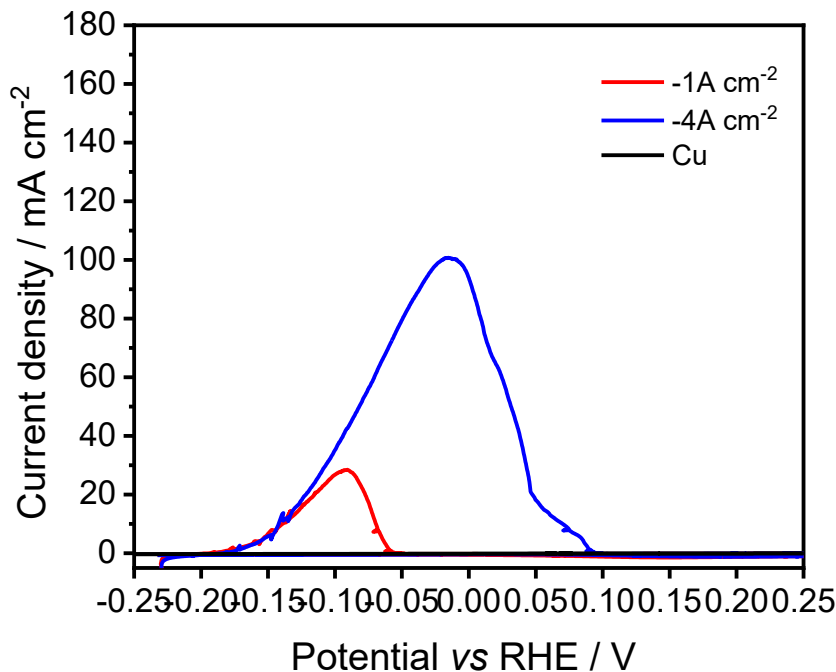


Figure S3.5 Stripping voltammograms of porous Pb/Cu films at 5 mV s⁻¹ in 1 M HClO₄.

To quantify the mass of lead in the porous Pb films, Pb was first deposited on 0.5 cm² Cu plate at the same conditions as Pb depositing on Pb plate. After deposition, stripping voltammetry was carried out in 1 M HClO₄ at 5 mV s⁻¹. Pb films have obvious stripping peaks and the peak integration area increases with deposition current density. However, the Cu substrate did not show a stripping peak in the range of -0.25 V to 0.25 V. The mass of deposited film may be calculated as $Q \cdot M / nF$, in which Q is the charge for reducing Pb film per cm²; M is the molar mass of Pb (207.2 g mol⁻¹); n is the electron transfer number ($n=2$), and F is the Faradaic constant (96485 C mol⁻¹). The Cu substrate does not show any stripping peak in the range of -0.25 V to 0.25 V. In comparison, porous Pb films have obvious stripping peaks and the peak integration area increases with deposition current density.

The Pb deposition charge efficiency may be calculated by determining the ratio of the Pb stripping charge to the total cathodic charge (Pb⁺² reduction and H₂ evolution) during the deposition. The charge efficiency of Pb deposition under varying conditions is similar (~2.5%) and does not vary significantly with the deposition current density and deposition times.

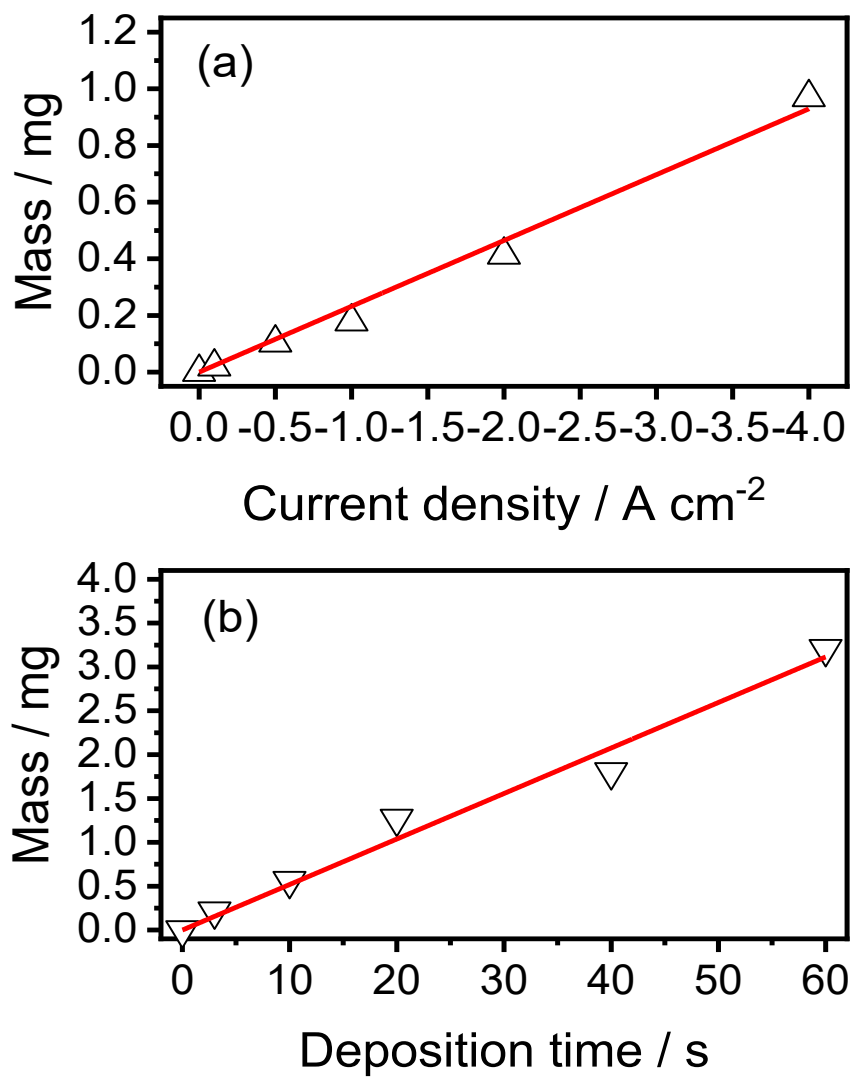


Figure S3.6 Variation of mass for porous Pb films with respect to (a) deposition current density and (b) deposition time.

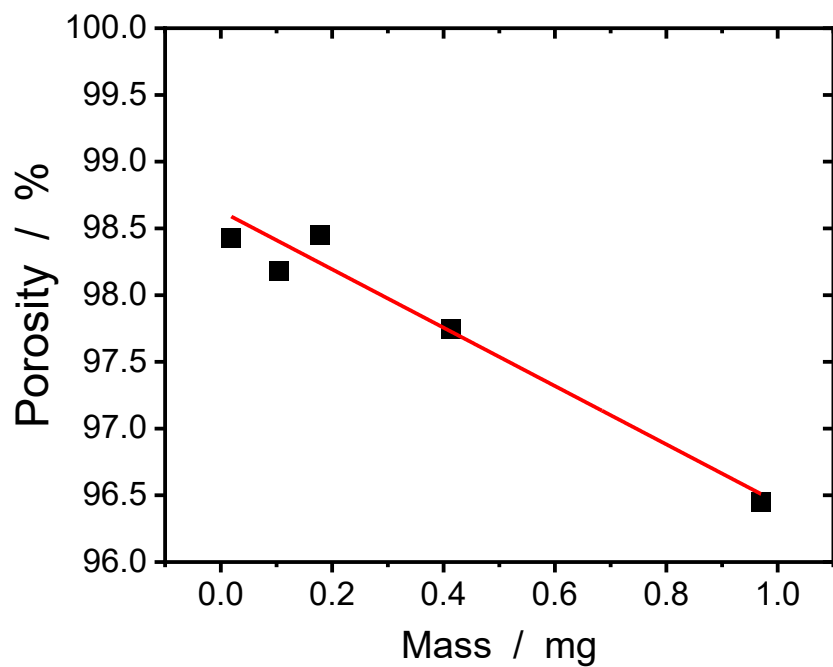


Figure S3.7 Variation of porosity with respect to the mass of lead. The deposition time was fixed at 20s and the deposition current density was increased from 0.1 to 4.0 mA cm⁻².

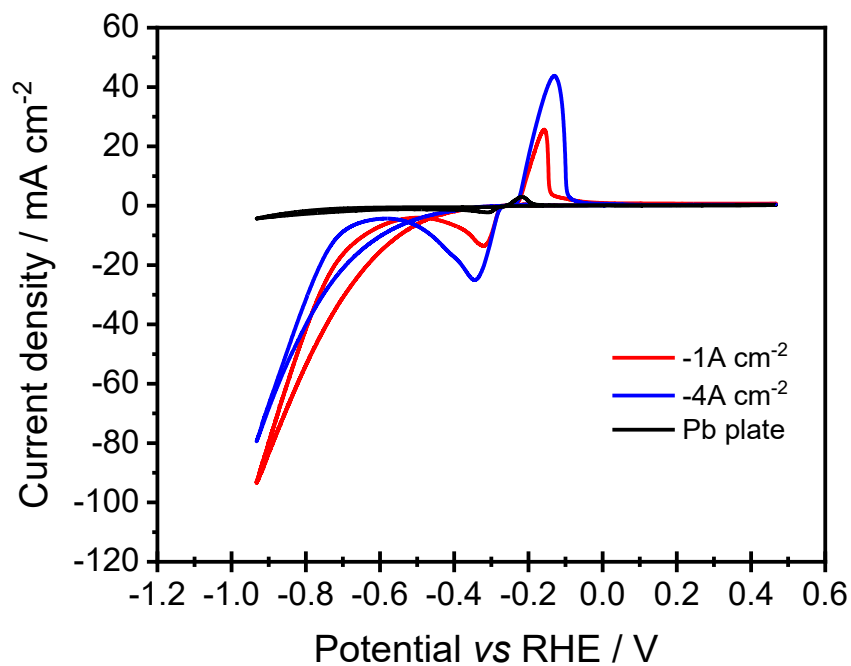


Figure S3.8 CVs in 0.5 M H₂SO₄ solution at 5 mV s⁻¹.

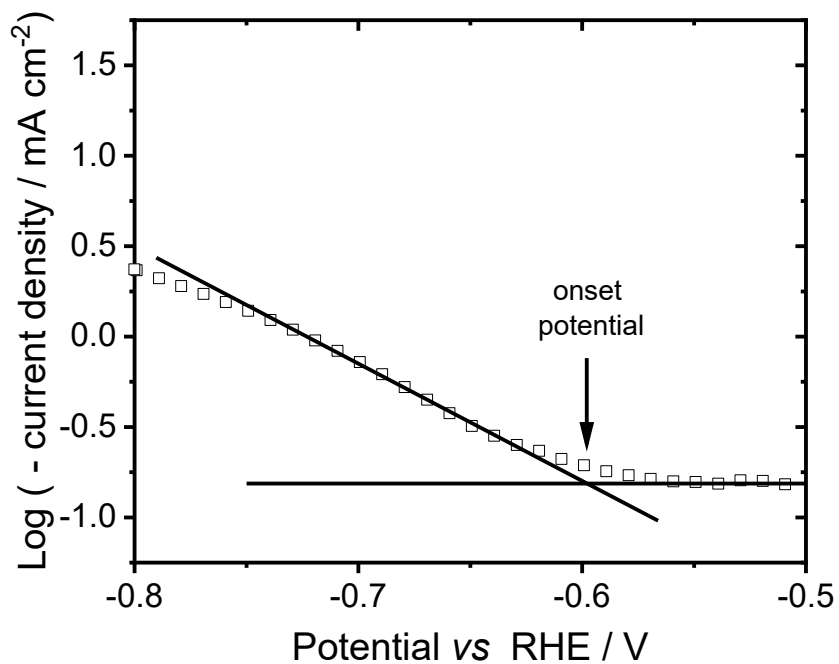


Figure S3.9 Variation of $\log(-j)$ with respect to the electrode potential in linear sweep voltammogram of porous Pb films in CO_2 -saturated 1M KHCO_3 . The scan rate was 5 mV s^{-1} . The porous Pb film was deposited at -4 A cm^{-2} and 40 seconds.

The onset potential for H_2 evolution and CO_2 electroreduction was assessed by drawing $\log(-j)$ vs potential curves like the one shown in Figure S3.9 and taking the onset potential as the potential at which, the solid lines intersect each other.

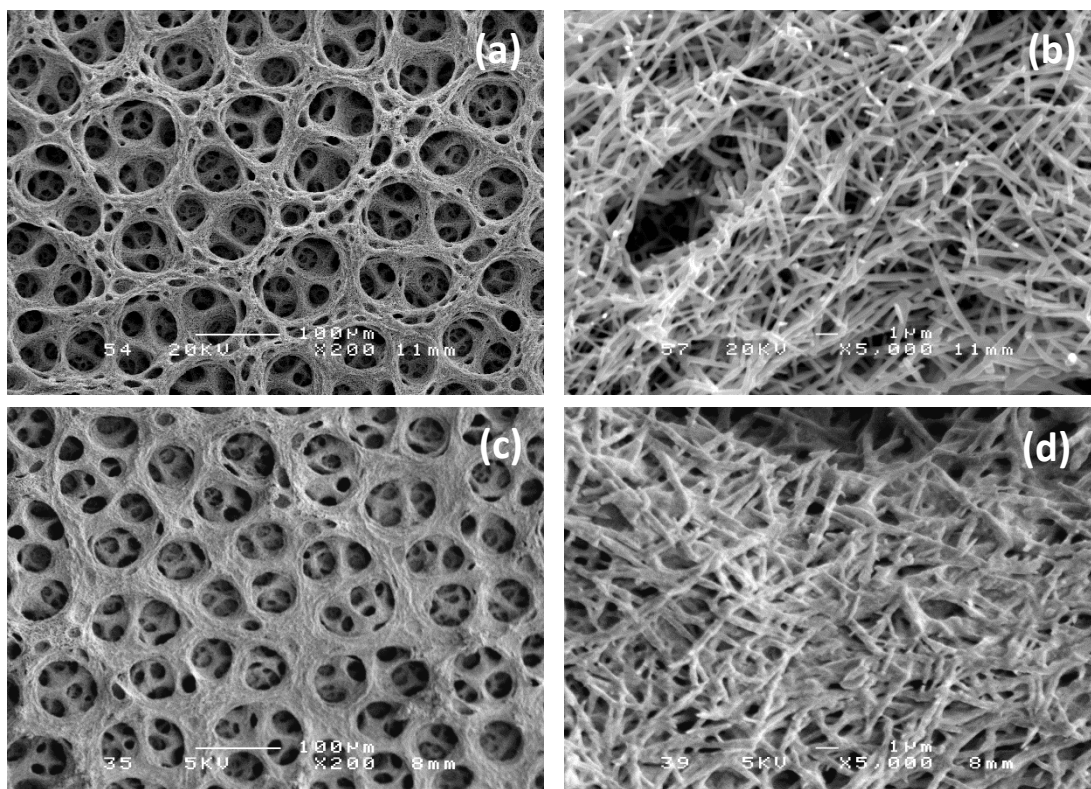


Figure S3.10 SEM images of porous Pb films (a-b) before; and (c-d) after 100 minutes of CO₂ electrolysis.

The morphology of porous Pb electrode is quite stable. Even after 100 minutes of electrolysis, there were no obvious differences in the porous structure and needle-like secondary structure. However, the porous film appears denser as some interspaces between the needle structures were occupied by carbonate salt originating from the electrolyte.

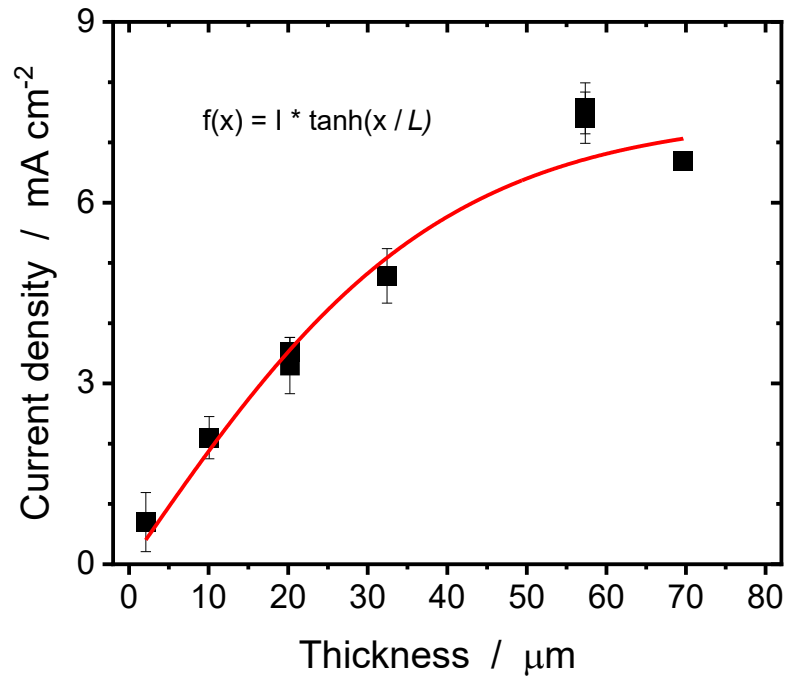


Figure S3.11 Variation of the current density with respect to the thickness of the deposit. The curve shows the best fit obtained using a function $f(x) = I * \tanh(x / L)$.

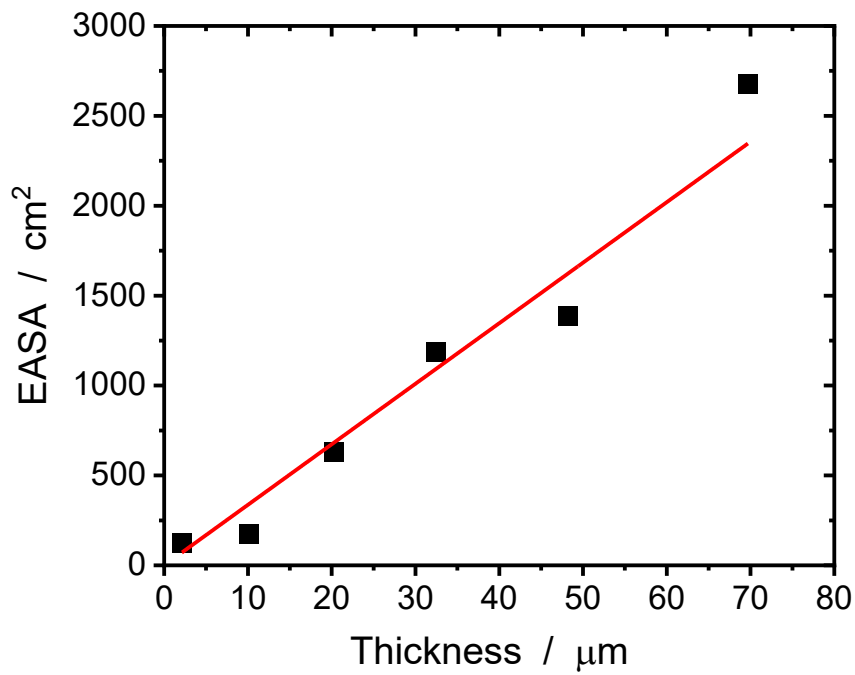


Figure S3.12 Variation of EASA with respect to the thickness of the deposit.

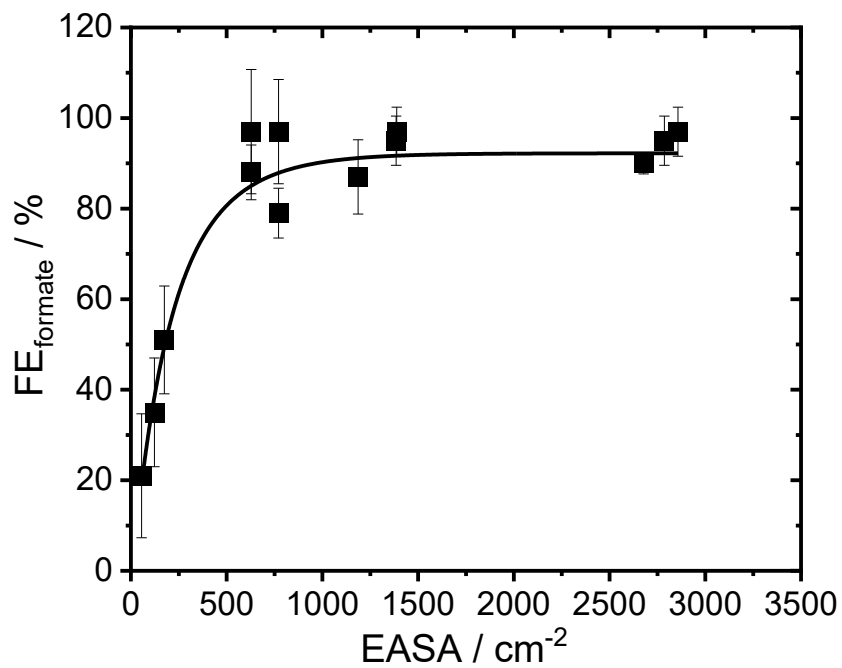


Figure S3.13 Variation of formate Faradic Efficiency with respect to the Electrochemically Active Surface Area. The EASA of all porous Pb films prepared in the present study are shown.

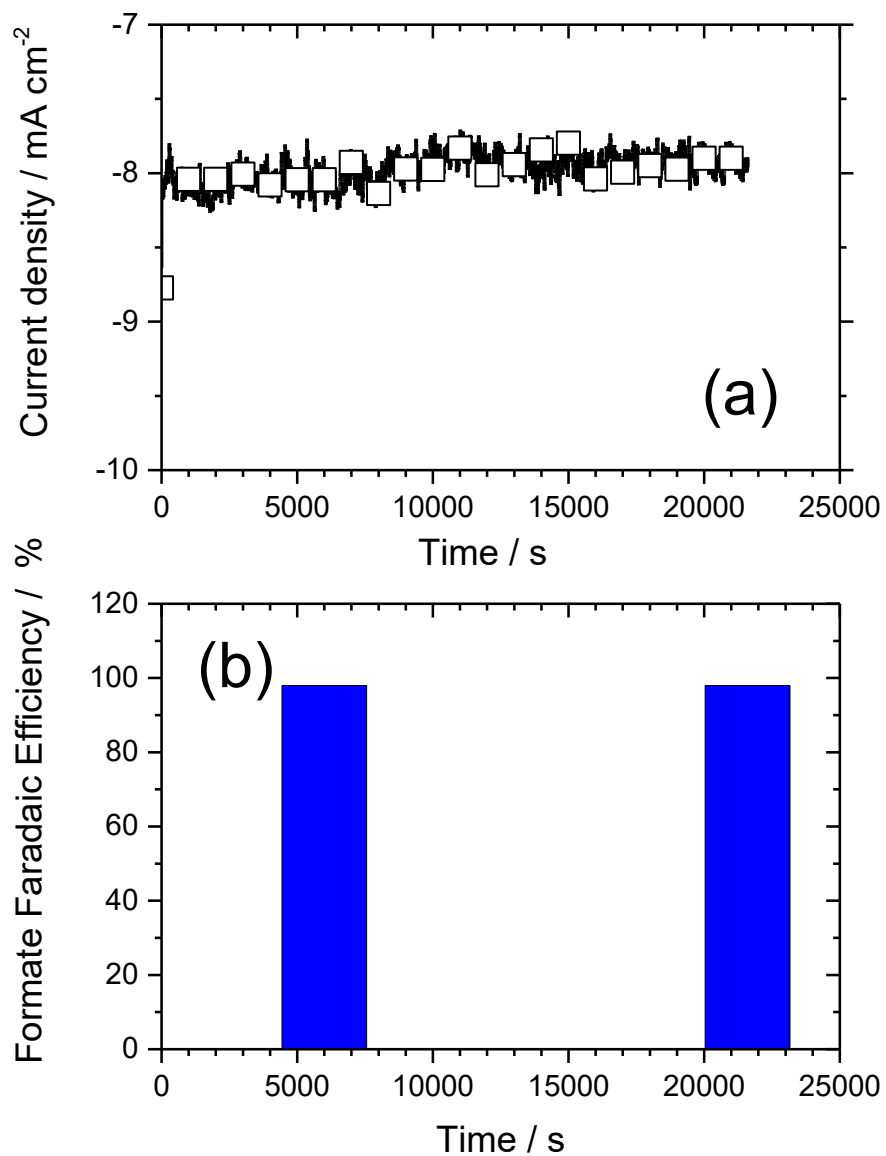


Figure S3.14 Variation of (a) the current density and (b) the formate faradaic efficiency as a function of the polarization time. These measurements were performed on Pb₄₋₄₀ at -0.99 V in CO₂-saturated 1M KHCO₃.

Table S3.1 Integration area of Pb \leftrightarrow Pb²⁺ redox peaks

Samples		Integration charge of oxide peak (C) Pb \rightarrow Pb ²⁺	Integration charge of reduction peak (C) Pb ²⁺ \rightarrow Pb	Charge percentage of oxide peak and reduction peak (%)
-4A cm ⁻²	3 s	0.216	0.210	51:49
	10 s	0.389	0.404	49:51
	20 s	0.388	0.428	48:52
	40 s	0.780	0.792	50:50
	60 s	0.750	0.746	50:50
20 s	-1 A cm ⁻²	0.176	0.174	50:50
	-2 A cm ⁻²	0.332	0.361	48:52
	-4 A cm ⁻²	0.387	0.386	50:50
	-4 A cm ⁻²	0.397	0.396	50:50

4 DENDRITIC BISMUTH MODIFIED LEAD ELECTRODES

Uncovering the Nature of Electroactive Sites in Nano Architected Dendritic Bi for Highly Efficient CO₂ Electroreduction to Formate

Découvrir la Nature des Sites Électroactifs dans le Bi-Dendritique Nano Architecturé pour une Électroréduction de CO₂ très Efficace en Formate

Authors:

Mengyang Fan,¹ Sagar Prabhudev,^{1,2} Sébastien Garbarino,³ Jinli Qiao,⁴ Gianluigi A. Botton,² David A. Harrington,⁵ Ana C. Tavares,¹ and Daniel Guay^{1*}

1. INRS-Énergie, Matériaux Télécommunications, 1650 Lionel-Boulet Boulevard, P.O. 1020, Varennes, QC, Canada J3X 1S2

2. McMaster University, Brockhouse Institute for Materials Research and Canadian Centre for Electron Microscopy, 1280 Main Street West, Hamilton, ON, Canada L8S 4M1

3. PRIMA Québec, 505 Boulevard Maisonneuve Ouest, Montréal, QC, Canada H3A 3C2

4. State Environmental Protection Engineering Center for Pollution Treatment and Control in Textile Industry, College of Environmental Science and Engineering, Donghua University 2999 Ren'min North Road, Shanghai, PR China 201620

5. Department of Chemistry, University of Victoria, 3800 Finnerty Rd, P. O. Box 1700, Victoria, BC, Canada V8W 2Y2

Publication:

Applied Catalysis B: Environmental

Publication Date: April 29, 2020

Volume 274, Pages 119031

DOI: <https://doi.org/10.1016/j.apcatb.2020.119031>

Contribution of authors:

Mengyang Fan, Dr. Sébastien Garbarino and Prof. Daniel Guay conceived and designed the research. Mengyang Fan prepared all samples and conducted most of the characterizations, and

all the CO₂ electrochemical reduction measurements. Dr. Sagar Prabhudev and Prof. Gianluigi A. Botton carried out all the HR-TEM characterizations and analysis. The impedance analysis was performed under the supervision of Prof. David A. Harrington. The experiment results were discussed with Dr. Sagar Prabhudev, Dr. Sébastien Garbarino, Prof. Jinli Qiao and Prof. Daniel Guay. Mengyang Fan wrote the manuscript and it was commented by Prof. Gianluigi A. Botton and Prof. Ana C. Tavares. The manuscript was carefully modified by Prof. Daniel Guay.

Link between articles:

Based on previous research, the dendritic Pb porous electrode is highly selective for CO₂ electrochemical reduction. The Faradaic efficiency selectivity reached 97% with a current of 7.5 mA cm⁻². However, the applied potential to achieve this high FE_{formate} was -0.99 V vs. RHE, which is very large and needs to be improved.

In this work, dendritic Bi was deposited onto the porous Pb. The modification of the outmost dendritic Bi layer significantly reduces the CO₂ electrochemical reduction (ERC) applied potential of 200 mV and increases the ERC reduction partial current to 18.8 mA cm⁻² with remaining the high FE_{formate} of 98%. A detailed investigation of the atomic structure of Bi dendrites was achieved through high-resolution transmission electron microscopy (HR-TEM). It was shown that Bi dendrites are made of single crystal with a rhombohedral structure and that they are growing along the [010] direction. The terminated dendrite surface is not entirely smooth but carry surface-irregularities in the form of surface-steps and high-index facets. Selective decoration of the low-index facets of Bi dendrites was achieved to show that these surface steps and high-index facets are the most active Bi surface sites.

4.1 Introduction

Growing emissions of carbon dioxide from human activities are driving up temperatures. This is increasing the possibility of extreme weather, melting polar ice and hastening global sea level rise. One prominent strategy dealing with rising CO₂ emissions is to convert CO₂ into value-added products by means of biochemical,¹¹ photochemical,¹³ and electrochemical methods.²⁰ Electrochemical reduction of CO₂ (ERC) is one of the promising ways to remediate high levels of CO₂ emissions by converting it to useful chemicals and fuels.^{20,21,26,36,196,197} The process is particularly very attractive when combined with intermittent energy sources such as solar and wind, allowing for off-the-grid energy storage that can be easily reverted back into the grid as and when needed. Among the different value-added products that can be obtained from the ERC, formate/formic acid production has generated a particular interest. The ERC to formate/formic acid is a simple two-electron process. Both chemicals are easy and safe to handle, making them useful in a variety of applications including agricultural and industrial production, livestock feed, and in leather processing. It can also be used in direct formic acid fuel cell to generate electricity^{123,124} and as a mediator between electricity and microbial cultivation.¹²⁵ Formate/formic acid is selling at higher price (~2500 kWh/ton and \$1,200/ton) compared to methane (~40000 kWh/ton and \$200-\$300/ton), which needs more electrons to be produced.¹²²

Several non-noble metal electrocatalysts are known to selective for the ERC to formate/formic acid: (Pb,^{81,141,198} Sn,^{42,176} Zn,¹⁹⁹). Their high selectivity ($\geq 80\%$) is accompanied by large onset potentials and high overpotentials when large current density (i.e., high production rate) is requested. Recently, Bi was considered for the ERC to formate/formic acid. Bismuth is a non-noble and earth-abundant metal with no known adverse effect on the environment. Moreover, it can be commonly obtained as a by-product in copper, lead and tin mining industries. The faradaic efficiency for Bi varies from 81% to almost 100% in the potential range extending from of -0.8 V and -1.12 V vs. RHE, but the current density remains low ($< 10 \text{ mA cm}^{-2}_{\text{geo}}$).^{47,84,91,92,200} Optimizing the structure for higher current-densities would be paramount to enhance the production rates of formate/formic acid from ERC. Zhong *et al* reported a partial current-density values of 15.2 mA cm⁻² measured at -1.12 V vs. RHE on Bi/C catalysts.¹³⁹ Yang *et al* performed similar measurements and found about 18 mA cm⁻² at -1.1 V vs. RHE on Bi nanosheets.¹³² Han *et al* found 24 mA cm⁻² at -1.06 V vs. RHE on Bi nanosheets.¹³⁴ Although high current-densities were achieved in these individual cases, the observed overpotentials were still remained high. Yang *et al* have proposed that (111), (101) and (012) facets at the edges are effective for the enhanced current density.¹³² However, the observed large overpotentials ($> 1 \text{ V}$) poses significant challenge.

It is possible that the 2D nature of these Bi nanosheets samples constrained them from being able to achieve high-index faceting. High-index surfaces are previously shown to enhance surface structure-sensitive reactions.²⁰¹ For example, Pt high-index facets were found to increase formic acid oxidation,⁴⁷ in addition to displaying superior performances for ethanol oxidation.²⁰²⁻²⁰⁵ Also, high-index facets of Pd were shown to maximize the electrocatalytic performances for CO₂ reduction to formate/formic acid through weakening of the CO binding affinity.³⁸ Elsewhere, high-index Au facets were reported to exhibit enhanced ERC activity and high selectivity to form CO.⁵⁶ Formation of high-index faceting seem to be more likely in 3D porous structures compared to 2D structures.^{141,206}

Here we demonstrate, 3D porous electrodes based on Bismuth dendrites (Bi_{den}) fabricated using dynamic hydrogen bubbling templates (DHBT). The dendritic Bi were found to be highly selective for the CO₂ electroreduction to formate with high current density of -18.8 mA cm⁻² achievable a low-overpotential of 600 mV. High Faradaic Efficiency of 98% was achieved with a long durability of 15 h. The defects and high-index facets were found to be most active sites where the reduction of CO₂ to formate occur. Detailed analyses of the dendrite surface-structure using atomic-resolution TEM analyses reveal that the high-index facets are more concentrated at the dendritic-tips in comparison to other regions. The in-operando active surface area measured through electrochemical impedance spectroscopy (EIS) indicates that the Bi layer is totally accessible in the CO₂ reduction process. To better estimate their performance towards more practical applications, high pressure flow-tests were also conducted. The estimated current density as large as 95 mA cm_{geo}⁻² is indicative of their high production rate of 1.63 mmol cm⁻² h⁻¹.

4.2 Experimental Section

4.2.1 Preparation of Bi dendrites

Bi dendrites (Bi_{den}) were first electrodeposited onto a Pb plate (Pb_{plate}) substrate (Nuclead, chemical grade, 1/16-inch thickness) to tune the deposition conditions and investigate their impact on the morphology of the deposit. The geometric area of the Pb plate was 0.5 cm² and the surface was electropolished to be clean and flat. The electropolishing treatment method was reported elsewhere.¹⁴¹ Bi electrodeposition was carried out from a 1 mM Bi(NO₃)₃ (Sigma-Aldrich, ≥99.99% trace metals basis) and 1 M HCl (Fisher Chemical, trace metal grade) plating solution. The Bi dendrites (Bi_{den}) were galvanostatically deposited with the current densities vary from -0.1 to -0.4 A cm⁻², and deposition times vary from 1 to 40 minutes. Once the deposition conditions were optimized, the substrate was changed from Pb plate to porous Pb, Pb_{porous}. The Pb_{porous} substrate

electrode was prepared by dynamic hydrogen bubbling templating (DHBT) electrodeposition at -4 A cm^{-2} with the time of 40 s in a plating solution of $10 \text{ mM Pb}(\text{ClO}_4)_2 + 1 \text{ M HClO}_4$, and the experimental details have been reported in our previous work.¹⁴¹ All electrodes were rinsed with deionized water (Millipore; resistivity $> 18.2 \text{ M}\Omega \text{ cm}$) and dried under a gentle Ar stream for 30 min. A standard calomel electrode (SCE) was used as reference electrode during all these electrodeposition experiments.

4.2.2 Physical characterization of Bi dendrites

The surface morphology was characterized through scanning electron microscopy (SEM) (JEOL, JSM-6300F). In some cases, high-resolution field emission SEM (FE-SEM) (FEI, Magellan) was also performed. TEM observations were carried out with a FEI Titan 80-300 Cubed Scanning Transmission Electron Microscope equipped with a high-brightness field-emission electron source and ultra-fast (electron energy loss) EEL Spectrometer. Specifically, the samples were investigated under high angle annular dark field (HAADF) mode for detailed atomic-level imaging. In cases where a cross-sectional analysis of the dendritic structure needed to be carried out, an ultra-thin area was carefully lifted out using Focused Ion Beam (FIB) technique. Extreme care was taken to avoid exposure of Bi samples to air. The as-synthesized Bi samples were vacuum sealed in a glovebox immediately after preparation and before exporting to FIB-milling station, only to be loaded onto the FIB-holder again in the glovebox. X-ray diffraction (XRD) measurements were performed using a Bruker D8 Advanced with a weighted average $\text{Cu K}\alpha_1$ and $\text{Cu K}\alpha_2$ radiation at 1.5418 \AA .

4.2.3 Electrochemical characterization of Bi dendrites

The electrochemical characterization was performed in a three-electrode cell by a Solatron 1480A multipotentiostat. A Pt gauze was chosen as the counter, and a SCE was used as electrode reference. However, all potentials in this study are quoted with respect to the Reversible Hydrogen Electrode (RHE), using the following relation $E_{\text{RHE}} = E_{\text{SCE}} + 0.241 \text{ V} + 0.059 \text{ V} \times \text{pH}$. The electrochemical active surface area (EASA) was measured in Ar-saturated (Air Liquide, 99.99%) 0.5 M KHCO_3 (Fisher Chemical, ACS Reagent) by recording the cyclic voltammograms (CVs) at different scanning rates ranging from 80 mV s^{-1} to 1000 mV s^{-1} . The EASA of Bi_{den} was determined by calculating the double layer capacitance from $i = f(v)$ curves measured at 0.17 V (see the supplementary section). A factor of $28 \text{ }\mu\text{F cm}^{-2}_{\text{Bi}}$ was used to calculate the EASA.^{91,207} Linear

sweep voltammograms (LSVs) were recorded in Ar-saturated and CO₂-saturated 0.5 M KHCO₃ within the potential range extending from -0.32 V to -1.32 V at the scan rate of 5 mV s⁻¹.

Electrochemical impedance spectroscopy (EIS) was carried out in a three-electrode cell with the CO₂-saturated 0.5 M KHCO₃ electrolyte. EIS measurements in the CO₂ electroreduction potential range (applied potential ranging from -0.62 to -1.22 V by steps of 0.5V) were obtained between 0.01 Hz and 200 kHz using an FRA Analyser (Solartron 1255B). In all cases, the current was allowed to stabilize for 30 minutes (see below) before starting the EIS measurements. Fitting to the equivalent circuit was carried out by using Zview.

The products were analyzed after 30 min electrolysis of CO₂ at the potential ranging from -0.62 V to -1.22 V. Formate concentration was measured by ion chromatography (IC) (ICS-1500, Dionex, USA) using an IonPac AS9-HC column separation column with a 9 mM Na₂CO₃ mobile phase at a flow rate of 1 mL/min. All samples were diluted 10 times before measurement. Gas products were analyzed by gas chromatography (GC) (Agilent Micro 490) at two channels with the thermal conductivity detector. Only formate and H₂ were detected and the total Faradaic efficiency (FE) was 100 ± 5%.

4.2.4 Flow-cell

A flow-cell was designed to test the catalyst's CO₂ reduction capability under higher CO₂ flux. A schematic representation of the flow-cell is shown in Figure 4.7a. The core of the electrolysis cell where the working electrode, the Nafion 117 separating membrane and the anode is shown in the enlarged view of the cell shown in Figure 4.7b. This flow-cell is equipped with a Saturated Calomel Electrode (SCE) reference and a Pt gauze counter electrode. Both the working and counter electrodes have a disk shape with a geometric surface of 1 cm². In this setup, the catholyte and anolyte flow rate (Masterflex L/S Easy-Load[®] II Model 77200-50 pump head and 06434-17 pump tube) and pressure can be controlled independently. A Bi_{den}/Pb_{porous} electrode was used as cathode. The electrolyte was a CO₂ super-saturated 0.5 M KHCO₃ solution that was prepared by using a soda machine (Sodastream, CO₂ purity 99.999%). The catholyte was circulated at a flow rate of 104 ± 1 mL min⁻¹ and the catholyte pressure was 5 psig over the atmosphere pressure. The anolyte was 0.5 M KHCO₃. It was circulated at a flow rate of 2.3 ± 1 mL min⁻¹ and the anolyte back pressure was 6 psig.

4.3 Results and Discussions

4.3.1 Condition optimization and physiochemical characterization of Bi dendrites

The Bi deposition conditions were firstly optimized on a (dense and flat) Pb plate, Pb_{plate} . Different deposition current densities (from -0.1 to -0.4 A cm^{-2}) and deposition times (from 1 to 40 minutes) were investigated. At these deposition current densities, the deposition potentials varied from -1.1 to -1.4 V vs. RHE , and simultaneous Bi deposition and hydrogen evolution occur. Electrodeposition under these conditions is referred to as DHBT.^{157,184,208,209} The Bi electrochemically active surface area, Bi EASA, was determined through cyclic voltammetry experiments in Ar-saturated 0.5 M KHCO_3 . The capacitive current was measured as a function of the sweep rate in a potential region where only double-layer charge/discharge processes occur (see Figure S4.1a). As seen in Figure S4.1b, the Bi EASA increases linearly with deposition current densities. Likewise, the Bi EASA increases steadily, although not linearly, with deposition times (see Figure S4.1c).

SEM micrographs of Bi deposited at -0.4 A cm^{-2} on Pb_{plate} for 40 minutes (and giving the largest Bi EASA) are presented in Figure 4.1. The Bi deposit is very porous. It has a honeycomb-like primary structure with surface pores *ca.* $150 \mu\text{m}$ in diameter (Figure 4.1a). This structure is characteristic of films prepared by electrodeposition under vigorous hydrogen evolution (DHBT deposition conditions). At higher magnification (Figure 4.1c and 4.1d), the Bi deposit's secondary structure is clearly observed; it is composed of dendrites consisting of stems to which branches are attached. The measured length of the stems is *ca.* $1 \mu\text{m}$. As shall be discussed later in Figure 4.2, detailed TEM analyses of these individual branches suggest their dimensions to be about 15 nm in diameter and 70 nm in length. All branches and stems terminate with sharper tips apparent as spherical contours in the SEM images (radius = $5.4 \pm 1.0 \text{ nm}$, see Figure S4.2, in reasonably good agreement with the 7.5 nm radius determined later on by HR-TEM analysis). In the subsequent discussions, we will refer to bismuth deposited in these conditions as dendritic Bi (Bi_{den}).

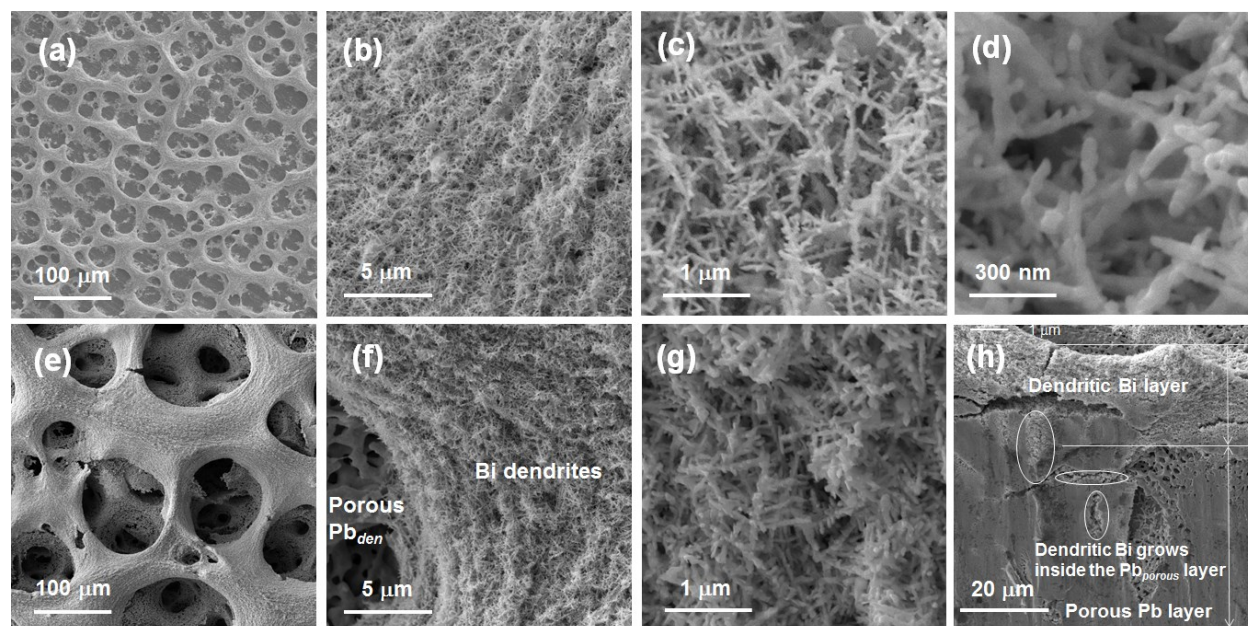


Figure 4.1 SEM micrographs of $\text{Bi}_{\text{den}}/\text{Pb}_{\text{plate}}$ (a, b, c and d) and $\text{Bi}_{\text{den}}/\text{Pb}_{\text{porous}}$ (e, f, g, and h) at different magnifications. Top view (a through g) and cross-sectional (h) views are shown.

After further optimization of these synthetic conditions, the Bi deposition conditions were fixed at -0.4 A cm^{-2} for 40 minutes but the substrate was changed from a flat Pb plate to a highly porous Pb substrate ($\text{Pb}_{\text{porous}}$). The later substrate was prepared based on previously-determined experimental conditions ($10 \text{ mM Pb}(\text{ClO}_4)_2 + 1 \text{ M HClO}_4$, 4 A cm^{-2} deposition current density and a 40-second deposition time).¹⁴¹ Deposition in these conditions (DHBT deposition conditions) yields a very porous Pb substrate (Figure S4.3) whose morphology is similar (although not identical) to that of the dendritic Bi deposit. The dendritic nature of Pb substrate is clearly evidenced in Figure 4.1e and f, which show very distinctive morphology of the underlying porous Pb electrode and dendritic Bi. It is clear that regions of the underlying porous Pb substrate are not covered with Bi dendrites. However, the morphology of those regions which are covered with Bi dendrites are identical to those observed when Bi deposition is performed on a flat (Pb plate) substrate (see Figure 4.1g) indicating that the formation of the Bi dendritic structure is not affected by the increased porosity of the underlying substrate. The cross-sectional micrograph of this electrode (Figure 4.1h) reveals that the Bi dendrites formed are not constrained to the surface regions but rather penetrate deep into porous regions of the underlying Pb substrate. This will prove to be important later on.

Figure 4.2a illustrates atomic-resolution image of a typical Bi dendrite, $\sim 15 \text{ nm}$ in diameter and $\sim 70 \text{ nm}$ in length, as evidenced by the low-magnification TEM image shown in Figure 4.2a-b. The dendritic orientation is determined by comparison to series of reported Bi phases and lattice

distances (ICSD codes #64703, #51674 and #189806, as such). As shown in Figure 4.2c-d, a satisfactory match is achieved for the Bi rhombohedral structure (Space group: R-3m) oriented along [010] growth direction and viewed along plane normal to (100). Similarities in the structure are further obvious from a direct visual comparison of the two images. Figure 4.2e illustrates the dendrite structure with specific focus onto the surface-structure. The atomic-structure revealed and the lattice-distances measured therein show that the rhombohedral structure of Bi in the core is preserved even at the top-most surface layers. No obvious displacements in the surface atoms suggesting binding with oxygen or other contaminants could be determined. These observations ascertain that the Bi needles considered in our work is mostly pristine, expected since extreme care was taken to avoid any sample exposure to oxidation.

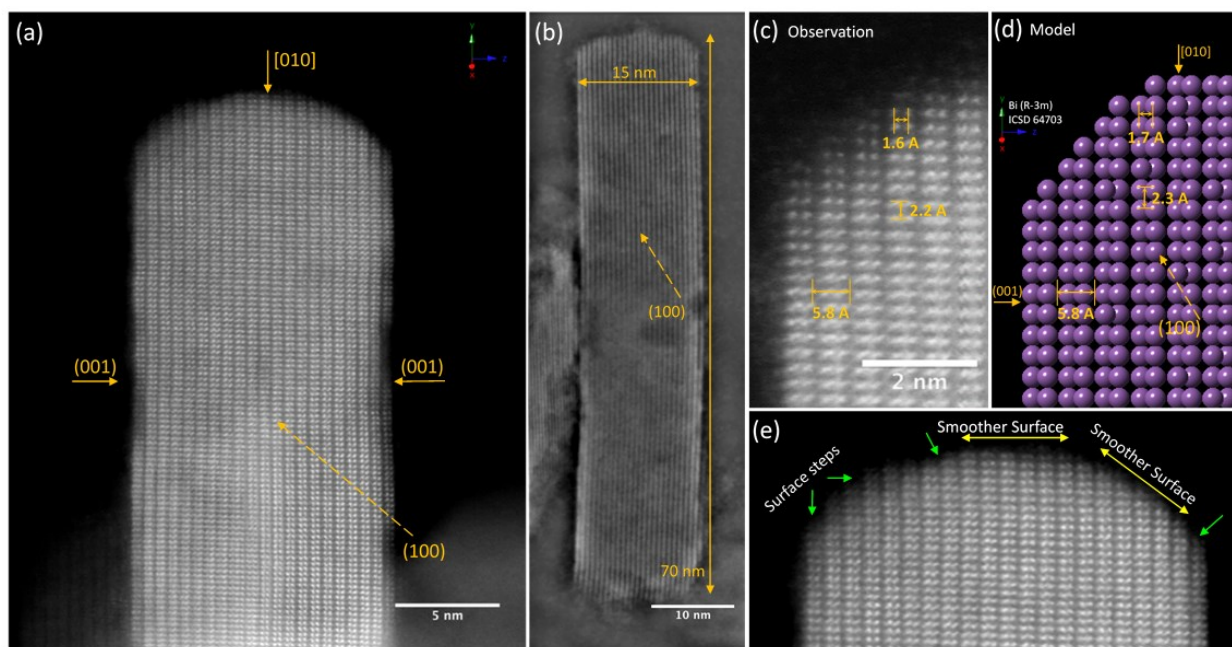


Figure 4.2 Elucidation of Bi dendritic structure with an aberration-corrected STEM. (a, b) HAADF-STEM images showing dendritic structure at different magnifications. Note image (b) is shown after bandpass filtering. (c, d) Comparison of observed dendritic lattice arrangement with Bi rhombohedral (R-3m) model along N(100). (e) HAADF-STEM image highlighting the detailed surface-structure of the dendrite.

As can be seen, the terminated dendrite surface is not entirely smooth (yellow arrows), but has surface irregularities in the form of ‘surface-steps’ (green arrows). Previously, such surface-irregularities have shown to play a key role in enhancing electrochemical reactivities of Pd for formate oxidation,²¹⁰ which is the reverse reaction to the one considered in the present work. In a first approximation, the surface occupied by the tips of the dendrite is given by D / L , where D is the dendrite diameter and L the length of the straight sections. Based on the data of Figure 4.2b, $D / L \sim 20\%$. The concentration of these surface steps and high-index facets is higher at the tips

(~ 20% of the dendrite surface) than on the straight sections (~ 80% of the dendrite surface). It will be shown experimentally later on that these surface irregularities are playing a crucial role in the high activity of Bi dendrites for the ERC.

XRD patterns of dendritic Bi deposits prepared in different deposition conditions are outlined in Figure S4.4a-b. For comparison, the position of the diffraction peaks of Bi, Bi₂O₃ and Pb are also shown. As evident from these XRD traces, there is no trace of bismuth oxide. Indeed, Bi dendrites are made of metallic (rhombohedral) Bi, although the relative intensities of the diffraction peaks differ from polycrystalline Bi. For example, the peak intensity of high-index planes such as (012) is exacerbated, suggesting a preferential texturing of Bi_{den} at the surface of the substrate.

To verify this observation, the texture coefficient ($TC_{(hkl)}$) of the thickest film was calculated by the inverse pole intensity technique using the following equation:²¹¹

$$TC_{(hkl)} = \frac{I_{(hkl)}/I_{R(hkl)}}{\frac{1}{n} \sum_i^n (I_{(hkl)}/I_{R(hkl)})} \quad (4.1)$$

where $I_{(hkl)}$ is the reflected intensity from (hkl) crystallographic planes in the textured specimen, $I_{R(hkl)}$ is the reflected intensity from (hkl) crystallographic planes from the random specimen, and n is the total number of reflections measured. $TC_{(hkl)}$ is proportional to the number of grains oriented with the (hkl) plane parallel to the surface. $TC_{(hkl)} > 1$ (< 1) denotes samples that have more (less) crystallites oriented in the (hkl) direction than randomly oriented polycrystalline Bi. As seen in Figure S4.4a-b, $TC_{(012)} > 1$ and $TC_{(122)} < 1$, indicating the family of planes in (012) direction, are over represented in the Bi dendritic deposit (compared to polycrystalline Bi). As seen in Figure S4.4c, only the (012) and (122) peaks have TC values that deviates by more than 20% from unity. As we are going to see later on, Bi dendrites are growing along the [010] zone axis. The angle between the (012) planes and the [010] growth axis is 90° and accordingly, a significant fraction of Bi dendrites have their growth axis oriented parallel to the surface of the substrate. Consistently, $TC_{(122)}$ is less than 1 since the (122) planes are perpendicular to the (012) planes. A schematic representation of the growth of Bi dendrites is depicted in Figure S4.4d, alongside a SEM micrograph of the early stage of Bi deposition that emphasizes regions where the [010] growth axis of dendritic Bi is parallel to the flat Pb substrate.

4.3.2 Catalytic activity of Bi dendrites and the Pb substrate effect

An evaluation of the electrocatalytic activity of Bi_{den} was first achieved through potentiodynamic measurements (5 mV s⁻¹) in CO₂-saturated 0.5 M KHCO₃ electrolyte at pH = 7.33. In Figure 4.3a

and S4.5, linear sweep voltammograms (LSVs) show that the onset potentials for ERC at both Bi_{den} electrodes are identical (ca. -0.54 V) and independent of the nature of the underlying Pb substrates. On the contrary, the current densities, j , at $\text{Bi}_{\text{den}}/\text{Pb}_{\text{porous}}$ are always larger than at $\text{Bi}_{\text{den}}/\text{Pb}_{\text{plate}}$. It is noteworthy that the onset potentials of Bi_{den} electrodes are smaller, and the total current density are larger, compared to bare lead substrates, emphasizing the critical role dendritic Bi plays in achieving high electrocatalytic activity. For comparison, the ERC onset potential on porous Pb is -0.65 V, which is 110 mV more negative than for Bi_{den} , while the current density of $\text{Pb}_{\text{porous}}$ is at least a factor 10 lower than for electrodes covered with dendritic Bi.

To further explore the catalytic performance of dendritic Bi, the products formed at different potential values during CO_2 reduction were analyzed after 30 minutes of electrolysis. In all cases, only formate (Figure 4.3b) and H_2 (Figure 4.3c) were detected, and the total faradaic efficiency (FE) reached $100 \pm 5\%$. As seen in Figure 4.3b, there was no difference between the $\text{FE}_{\text{formate}}$ vs. potential curves of dendritic Bi deposited on the two different substrates (Pb_{plate} and $\text{Pb}_{\text{porous}}$). In both cases, the maximum $\text{FE}_{\text{formate}}$ value is 98% and is attained at -0.82 V vs. RHE. This is 200 mV more positive than the potential at which the largest value of $\text{FE}_{\text{formate}}$ is attained on the $\text{Pb}_{\text{porous}}$ substrate alone. In the case of the Pb_{plate} substrate, $\text{FE}_{\text{formate}}$ values larger than 80% were never reached even at the more negative potential studied here.

The partial current densities of formate, j_{formate} , which are exclusively associated with formate production, are shown in Figure 4.3d. The j_{formate} values of dendritic Bi deposited on both Pb substrates increase steadily in the low overpotential regime (from -0.6 to -0.9V) to reach a plateau at more negative potential ($\leq -0.9\text{V}$). The j_{formate} plateau value of $\text{Bi}_{\text{den}}/\text{Pb}_{\text{porous}}$ is $\sim 27 \text{ mA cm}^{-2}$, almost 1.6-fold higher than on $\text{Bi}_{\text{den}}/\text{Pb}_{\text{plate}}$ ($\sim 17 \text{ mA cm}^{-2}$). As shown in Figure 4.1h, Bi dendrites are deposited in regions of the porous Pb substrate that are inaccessible on a dense Pb_{plate} substrate. Accordingly, even if the deposition conditions used for the preparation of dendritic Bi are rigorously identical, there are more Bi dendrites accessible to the electrolyte on $\text{Bi}_{\text{den}}/\text{Pb}_{\text{porous}}$ than on $\text{Bi}_{\text{den}}/\text{Pb}_{\text{plate}}$. This is nicely confirmed by the Bi EASA of $\text{Bi}_{\text{den}}/\text{Pb}_{\text{porous}}$ (231 cm^2), which is ca. 1.5-fold larger than $\text{Bi}_{\text{den}}/\text{Pb}_{\text{plate}}$ (156 cm^2) (see Figure S4.7). Indeed, the LSV and the j_{formate} curves of $\text{Bi}_{\text{den}}/\text{Pb}_{\text{plate}}$ and $\text{Bi}_{\text{den}}/\text{Pb}_{\text{porous}}$ are almost superimposed on each other when normalized to the Bi EASA (see Figure S4.8). The Bi EASA is determined through CV measurements in a potential region involving double-layer charge/discharge processes, which are not limited by diffusion. On the contrary, the j_{formate} plateau value is measured in a potential region where CO_2 reduction (faradaic reaction) is occurring. This faradaic reaction is dependent on the diffusion of CO_2 to the reaction site. The fact that j_{formate} scales exactly like the Bi EASA indicates that all

available active Bi active sites are accessible and participating in the faradaic reaction. Therefore, even if the deposition conditions are optimized to promote the formation of a porous dendritic Bi deposit, it is still possible to further increase the areal density of available active sites by using a porous ($\text{Pb}_{\text{porous}}$) instead of a flat substrate (Pb_{plate}).

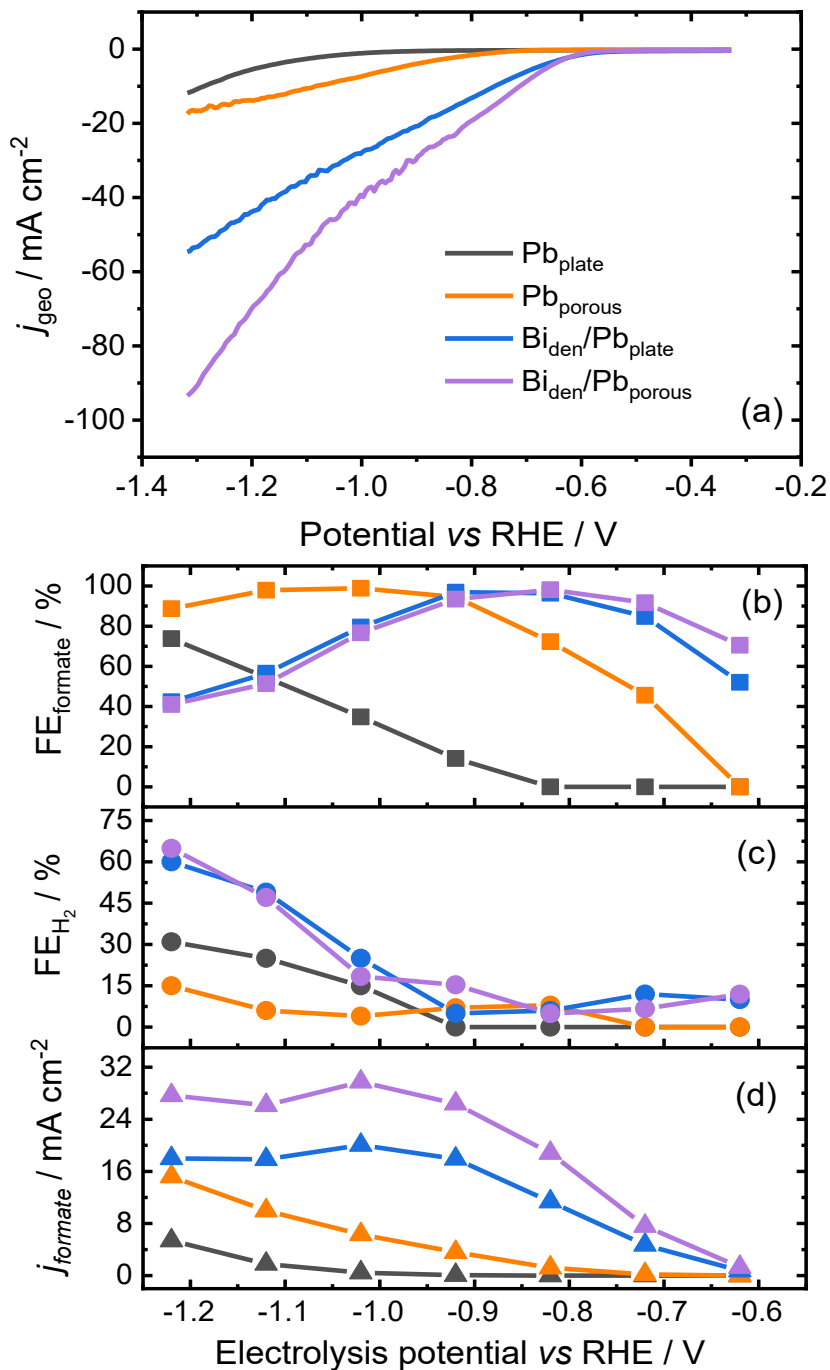


Figure 4.3 In (a), linear sweep voltammograms of Bi-modified Pb electrodes in the CO_2 -saturated 0.5 M KHCO_3 electrolyte, with Pb electrodes as the comparison. Scan rate of 5 mV s^{-1} , (b) formate faradaic efficiency (formate FE), (c) H_2 faradaic efficiency (H_2 FE), and (d) partial current density of formate (j_{formate}) with respect to electrolysis potential in the CO_2 -saturated 0.5 M KHCO_3 electrolyte.

It was shown previously that the current density difference between $\text{Bi}_{\text{den}}/\text{Pb}_{\text{porous}}$ and $\text{Bi}_{\text{den}}/\text{Pb}_{\text{plate}}$ can be rationalized based on the different (3D) structure of both lead substrates. On the contrary, both electrodes exhibit the same ERC onset potentials. This makes sense since the onset potential of a reaction (reduction/oxidation) is the least (negative/positive) potential that should be applied for the reaction to occur (at very low rate and thus very low current density). In that sense, it is not expected that the onset potential will be affected by the EASA. On the contrary, the onset potential is dependent on the nature of the materials but, more importantly for the present study, on its microstructure. So, on Bi flakes, which are formed by electrodeposition at much lower deposition overpotential (50 mV) and thus much lower current density, the onset potential for the ERC is -0.7 V vs. RHE,¹⁴¹ which is 160 mV more negative than on Bi dendrites.

In order to clearly correlate the ERC property to the 3D structure of dendritic Bi, a series of EIS measurements was performed. The impedance spectra of Figure S4.10 shows the classic features of a solution resistance in series with a parallel combination of a constant-phase element representing the double layer and a charge-transfer resistance. The effective double-layer capacitance C_{eff} was obtained from the CPE parameters and the parallel combination of the two resistances using the Brug formula.²¹²

A Tafel analysis of the best performing electrode ($\text{Bi}_{\text{den}}/\text{Pb}_{\text{porous}}$) is given in Figure 4.4. The EIS measurements were carried out at various electrode potentials ranging from -0.62 to -1.07 V vs. RHE. Before each EIS measurement, a potentiostatic current was recorded for 30 min and it reached to a steady state value. These current (j) data points were used to obtain the value of Tafel slope (as shown in Figure 4.4a). The Tafel slope is 156 mV dec^{-1} in the kinetically limited region (potential more positive than -0.75 V). In the region between -0.75 and -0.90, j is almost constant, indicating the reaction reaches its mass transport limitations. At potential more negative than -0.9 V, j increases again, most probably because the hydrogen evolution reaction becomes predominant. This is consistent with the FE_{H_2} starting to increase (Figure 4.3c) and the EIS data becoming noisier (Figure S4.10) at potentials more negative than -0.87 V. As the applied potential is more negative, R_{ct} initially decreases (see Table S4.1), with an exponential (Tafel) potential dependence as expected since $R_{\text{ct}} \approx R_{\text{p}}$. The slope of $\log(1/R_{\text{ct}})$ vs potential curves is 147 mV dec^{-1} (Figure 4.4b), very similar to the Tafel slope determined from j values. C_{eff} does not vary with potential (Figure 4.4c), even when the current is limited by CO_2 mass-transport or increased due to the HER. The mean C_{eff} value is $6.1 \pm 0.4 \text{ mF cm}^2_{\text{geo}}$, a factor ca 215 larger than the specific capacitance of Bi ($28 \mu\text{F cm}^2$). This value is close to the roughness factor of 231 determined from CVs measurements in a potential region where no faradic reaction is occurring, indicating that the

same electrode surface is accessed in both cases. For comparison, C_{eff} of $\text{Bi}_{\text{den}}/\text{Pb}_{\text{plate}}$ are also invariant with the electrode potential (see Figure S4.11), with a mean value of $4.1 \pm 0.2 \text{ mF cm}^2_{\text{geo}}$, which is a factor of ca 1.5 lower than $\text{Bi}_{\text{den}}/\text{Pb}_{\text{porous}}$. The Bi EASA and C_{eff} values are consistently supporting the view that part of the electrode that would not be easily reached by the electrolyte and dissolved CO_2 are readily accessible upon depositing Bi_{den} on a porous substrate.

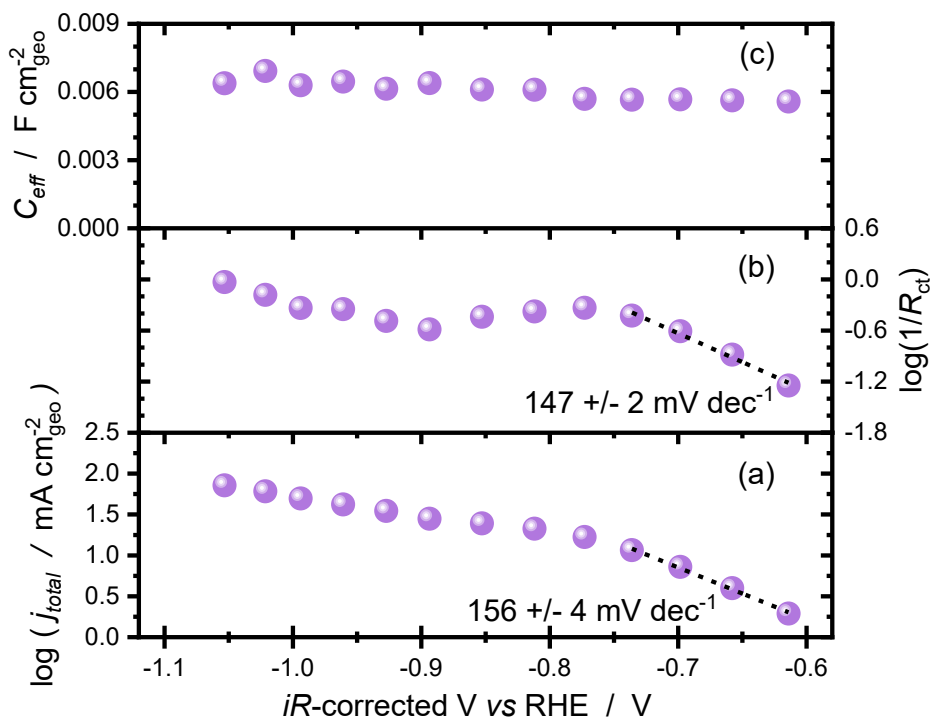


Figure 4.4 Variation of (a) j , (b) $\log(1/R_{\text{ct}})$ and (c) C_{eff} with respect to iR -corrected potential. The data are shown for $\text{Bi}_{\text{den}}/\text{Pb}_{\text{porous}}$ electrode in CO_2 -saturated 0.5 M KHCO_3 electrolyte. The current was allowed to stabilize during 30 minutes before starting the IES measurements.

4.3.3 Electrode stability

Aside from onset potential, overpotential, current density, and current efficiency (which, taken together, have an impact on the energy efficiency of the process), stability is another critical issue for electrodes in the development of an ERC process. Figure 4.5a and 4.5b demonstrate that both the total current density (-18.8 mA cm^{-2}) and faradaic efficiency ($\geq 95\%$) remained constant during a long-term (15 hours) electrolysis test performed at -0.82 V . This indicates that stable operation can be achieved in terms of both current density and selectivity, and that contamination of the electrode surface during electrolysis is not an issue. In the literature, contamination/modification of the electrode surface through electrodeposition of foreign elements contained in the aqueous

electrolyte, or even adsorption of carbonaceous compounds, have often been invoked to explain performance degradation (electrode potential, current density and/or faradaic efficiency) over time.^{213,214} This is not the case in the present study, where the electrode's dendritic structure and large Bi EASA may help mitigate this poisoning effect (if any). This might occur because the number of catalytic sites that are poisoned (and thus not available for the ERC) is small compared to the initial number; alternately, as it will be demonstrated by the intentional deposition of Pb on Bi dendrites, electrodeposition/adsorption of contaminants may be occurring at sites that are less active for the ERC. This is certainly contributing to maintaining a stable electrocatalytic activity for the ERC over a long period. Finally, it is worth noting that the morphology of Bi dendrites remains unchanged even after 15 hours of electrolysis (Figure 4.5c and 4.5d), indicating that the electrode structure is not collapsing during sustained operation, which again demonstrates the stability of the electrode.

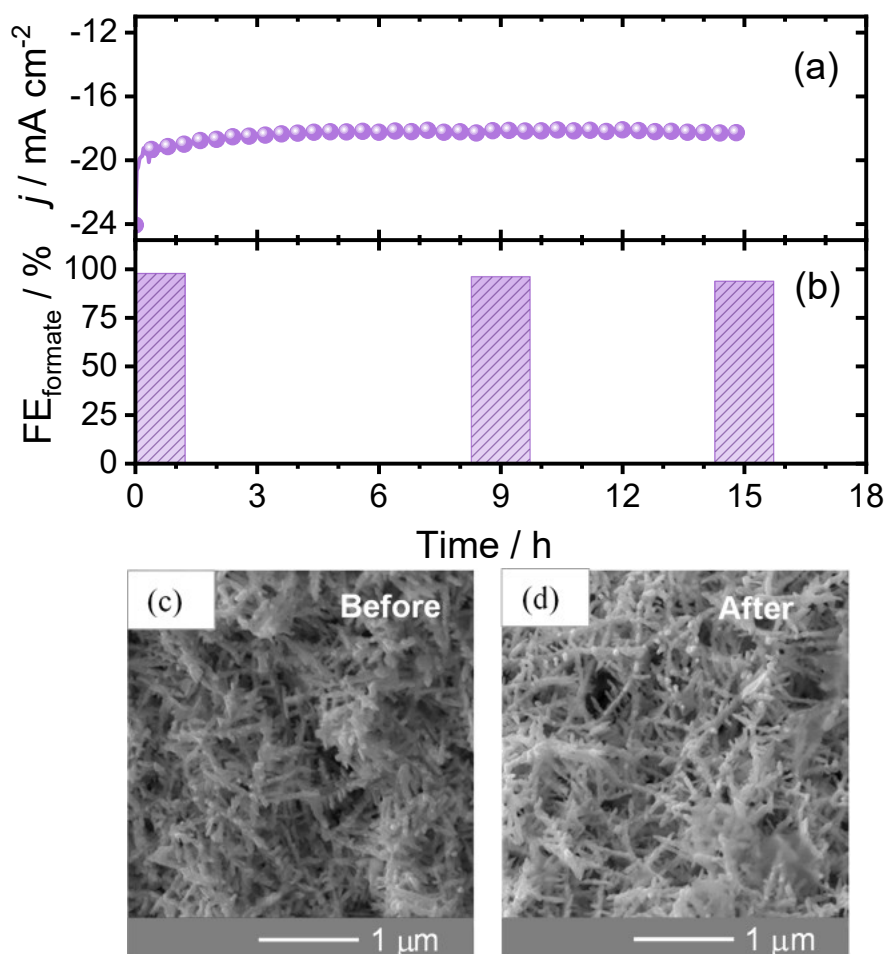


Figure 4.5 Variation of (a) the current density and (b) the formate faradaic efficiency as a function of the polarization time. These measurements were performed at -0.82 V vs. RHE on $\text{Bi}_{\text{den}}/\text{Pb}_{\text{porous}}$ electrode in CO_2 -saturated 0.5 M KHCO_3 electrolyte. SEM images of $\text{Bi}_{\text{den}}/\text{Pb}_{\text{porous}}$ electrode (c) before and (d) after 15 h of CO_2 electrolysis are shown.

4.3.4 Identification of Bi active sites for high selectivity and long durability

To identify the Bi catalytic sites, we undertook to mask selectively certain a fraction of them with a less active material (Pb) for the ERC to formate. To achieve this, Bi_{den} was first electrodeposited. After recording the Bi EASA and the ERC current at -0.82 V vs. RHE in CO₂-saturated 0.5 M KHCO₃ electrolyte, the Bi_{den} sample was rinsed and transferred to a 1 mM Pb(ClO₄)₂ and 0.1 M HClO₄ plating solution. Then, plating of Pb was carried out by applying a series of potentiostatic pulses, with $E_{on} = -0.48$ V vs. SCE with $T_{on} = 1$ s, and $E_{off} = OCP$ with $T_{off} = 10$ s. This potentiostatic pulse sequence was chosen to prevent Pb from being deposited under mass-transport limited conditions (see Figure S4.12). Pb deposition was performed by changing only the number of pulses (from 120 to 760 cycles) to vary the amount of deposited Pb. The EASA of Bi_{den} covered with various amounts of Pb was then measured and the activity for the ERC was assessed again. It is known from the Pb underpotential deposition (UPD) literature that anions in the plating solution can be strongly adsorbed on defects present at an electrode surface, thereby preventing Pb deposition at these high energy sites and favoring it at low index facets and defect-free sites.²¹⁵⁻²¹⁷

As seen in Figure 4.6a, the percent of Bi EASA loss varies linearly with the number Pb deposition cycle. This indicates that every addition of Pb is as effective as the previous ones in masking a constant fraction of the Bi dendritic surface. Almost 75% of the Bi EASA is lost after 800 cycles of Pb deposition. Likewise, the loss of ERC activity (Figure 4.6b) varies linearly with the number of pulses. However, the most interesting piece of information is depicted in Figure 4.6c, which shows the variation of percent loss of ERC with respect to the percent loss of Bi EASA. Three regions were identified. The blue line depicts the behavior expected if Pb was deposited on Bi sites that are equally active for the ERC (a loss of Bi EASA translate into an equivalent loss of ERC). The section of the graph located above and below that blue line indicates regions where the Bi active sites are not all equivalent, and data points in the region below (above) the blue line indicate that Pb is deposited on Bi sites that are not (that are) the most active for the ERC. As seen in Figure 4.6c, there is effectively a linear relationship between the EASA loss and the ERC loss (the slope is 0.36), but all data points are below the blue line. This means that not all Bi surface sites are equivalent for the ERC and that Pb atoms deposit preferentially on the less active Bi surface sites.

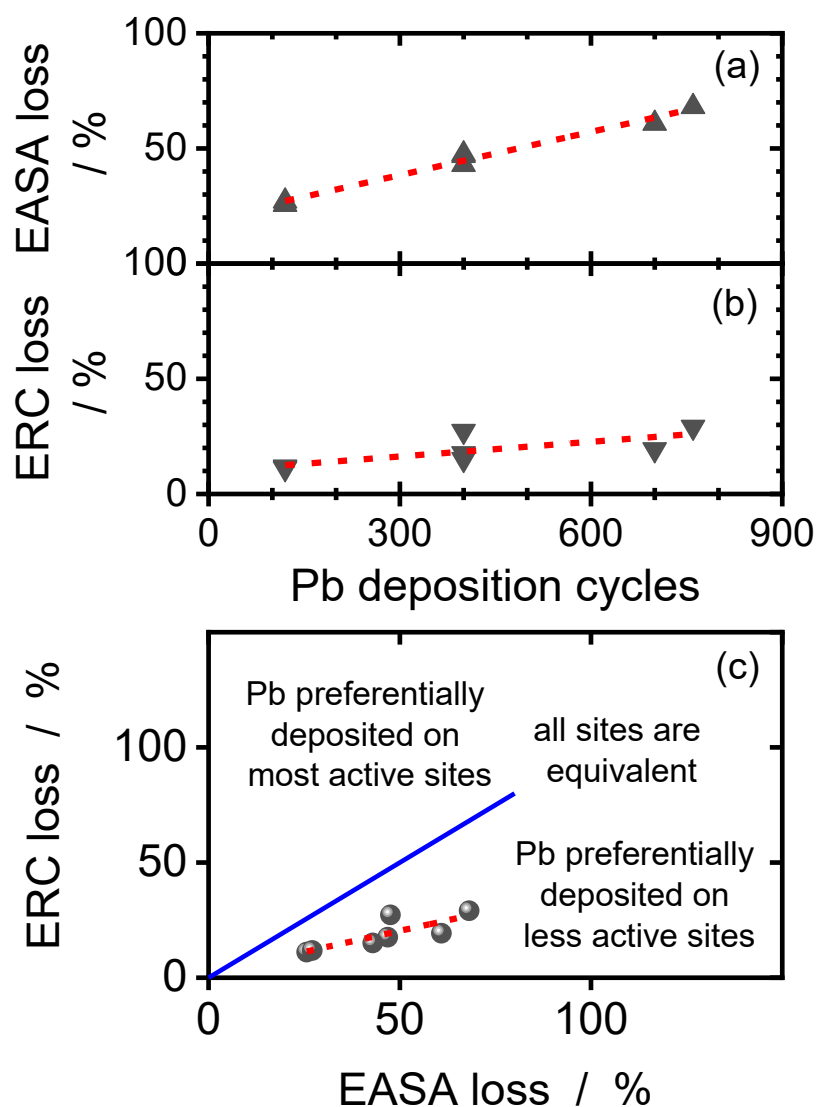


Figure 4.6 Variation of (a) the loss of Bi EASA and (b) loss of ERC activity with the number of Pb deposition pulses. Details of the experimental procedure are given in the text. The variation of ERC activity loss vs Bi EASA loss is depicted in (c).

Geometrical considerations based on the HRTEM micrograph of Figure 4.2 help us to unravel the structure of the most active Bi sites. As seen in Figure 4.2, the surface concentration of defects is larger at the tip of the dendrite than on their walls. Since the deposition of Pb was at a UPD condition, the defect-free Bi sites, which account for more than 80% of the dendrite surface, are supposed to be covered by Pb rather than the active tip sites. Accordingly, the covered defect-free Bi sites would be responsible for a significant decrease of the Bi EASA without causing a proportional change of the ERC activity. The most active Bi sites would be those that accounts

for the smallest fraction of the dendrite surface area that is not covered by Pb in the UPD process. This assertion is consistent with the most recent DFT calculations made by Koh *et al.* showing that high-index (012), (110) and (104) facets stabilize HCOO* more than the compact (003) plane.⁴⁷

4.3.5 Continuous flow-cell test of the Bi_{den}/Pb_{porous} electrode

To increase the production rate of formate, a flow-cell was designed to test the CO₂ reduction capability of Bi_{den}/Pb_{porous} electrodes in conditions where large CO₂ flux can be achieved. A schematic representation of the flow-cell is shown in Figure 4.7. As detailed in the experimental section, the electrolyte was super saturated with CO₂. The average current density was 95 mA cm⁻² at -0.82 V vs. RHE and was constant over the short-term electrolysis test (5 hours) we performed (see Figure 4.7c). Also important, the FE_{formate} was 92%±4%, very close to the value observed in the H-cell. Compared with the 344 μmol cm⁻² hr⁻¹ formate production rate in the H-cell, the production rate in the flow-cell test was 1.63 mmol cm⁻² hr⁻¹, which is around 5-fold larger. This increased current density compared to the H-cell results from overcoming the CO₂ mass transport limitation through increased flow rate and increased amount of CO₂ (oversaturation) in the electrolyte. A detailed comparison of the ERC performances of different Bi-based electrodes is shown in Table S4.2. It emphasizes that Bi_{den}/Pb_{porous} electrodes, thanks to their atomic surface structure with defects and high-index facets, can sustain large current densities and achieve large formate production rate if they are operated in a regime that is not limited by the diffusion of CO₂.

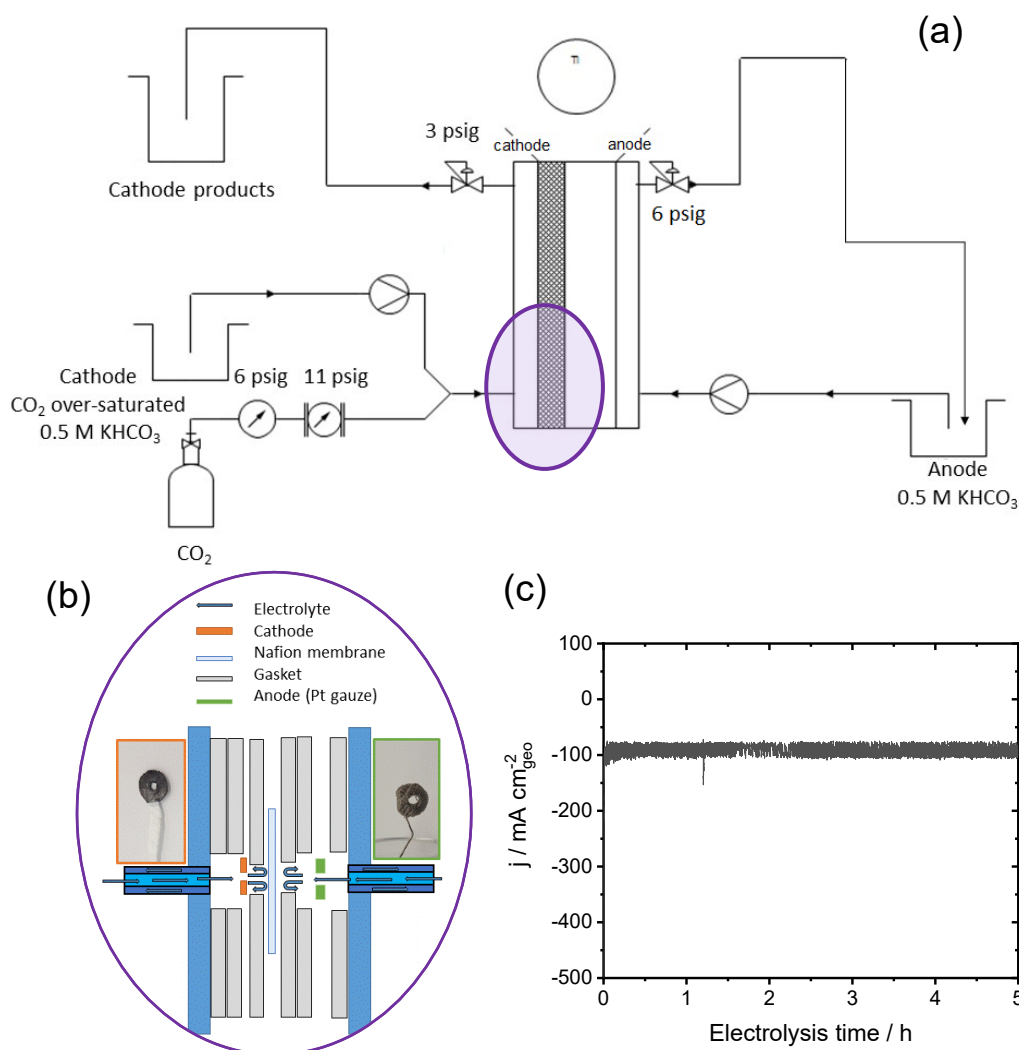


Figure 4.7 Schematic illustration of (a) flow-cell system and (b) core of the cell. (c) Variation of the current density with the electrolysis time of Bi_{den}/Pb_{porous} electrode. See the main text for all the experimental details.

4.4 Conclusions

In summary, dendritic Bi electrode with a large amount of defects and high-index facets was synthesized on a porous Pb substrate. The identification of the most active Bi sites was performed through a detailed atomic scale analysis of the surface of the dendrite and masking of the low-index inactive sites. It was shown that defects and high-index facets of Bi dendrites are the most active sites where the reduction of CO₂ to formate occurred. Dendritic Bi is highly selective for the CO₂ electroreduction to formate with a 98% Faradaic Efficiency and a current density of 18.8 mA cm⁻² (344 μmol cm⁻² hr⁻¹) at -0.82 V vs. RHE, which is only 600 mV more negative than the thermodynamic potential. Both the dendritic structure and CO₂ electrolysis performances are remarkably stable over the longest electrolysis (15 hours) we have conducted. Additionally, much larger production rate (1.63 mmol cm⁻² hr⁻¹ or 95 mA cm⁻² at -0.82 V vs. RHE) without any major

penalty on the formate Faradaic Efficiency ($92\% \pm 4\%$) was achieved with the same electrode operated in conditions where the CO_2 flux is not limiting its performances (high-pressure flow-cell measurements). This work presents a simple method to design and fabricate materials in dendritic form with excellent performances for the ERC. It also provides atomic scale insights into the nature of the active sites at the surface of dendrites. Finally, it illustrates that dendritic electrode materials are able to withstand very large current density and thus achieve very large production rate if the CO_2 supply to the electrode is not limiting.

Acknowledgements

This work was supported by the Natural Sciences and Engineering Research Council of Canada (NSERC) and the Canada Research Chair program. This research was conducted as part of the Engineered Nickel Catalysts for Electrochemical Clean Energy project administered from Queen's University and supported by Grant No. RGPNM 477963-2015 under the Natural Sciences and Engineering Research Council of Canada (NSERC) Discovery Frontiers Program. M. F. acknowledges "Fonds Recherche du Québec - Nature et Technologies" (FRQ-NT) for a Graduate Research Fellowship supporting this work.

4.5 Supporting Information

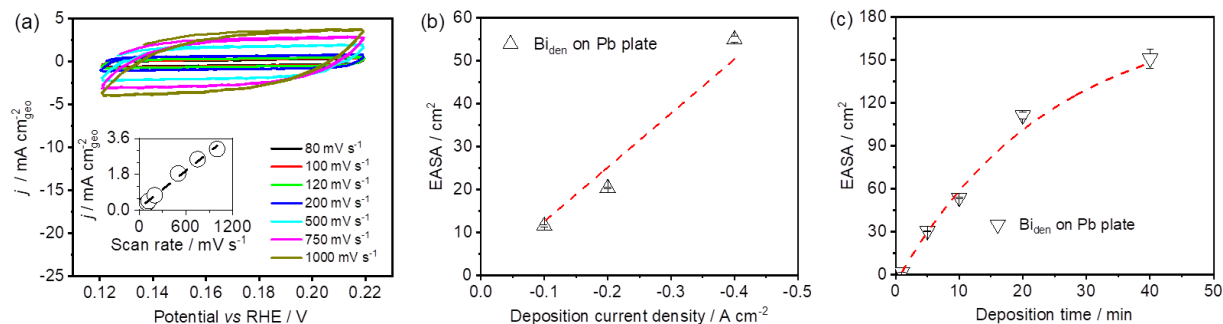


Figure S4.1 EASA of Bi_{den} prepared in different conditions. In (a), CVs of Bi_{den} recorded at different sweep rates in Ar-saturated 0.5 M KHCO₃ solution. The insert shows a plot of the current density recorded at 0.17 V with respect to the sweep rates. The slope of the dotted line was used to calculate the EASA by taking the value of $28 \mu\text{F cm}^{-2}$ as reference (specific charge density of Bi).^{91,207} In (b), variation of the Bi EASA with the deposition current density (the deposition was fixed at $t_{\text{dep}} = 10$ min). In (c), variation of the Bi EASA with the deposition time (the deposition current density was fixed at -0.4 A cm^{-2}). In all cases, a Pb plate was used as substrate.

The EASA of Bi dendrites was measured by recording the cyclic voltammograms (CVs) at different sweep rates in Ar-saturated 0.5 M KHCO₃. The potential range was between 0.12 V and 0.22 V. A typical example is given in Figure S4.1a. Figure S4.1b and S4.1c show the EASA of Bi_{den} with

respect to the deposition current density (at $t_{\text{dep}} = 10$ min) and deposition time (at $j_{\text{dep}} = -0.4 \text{ A cm}^{-2}$, respectively). The Bi EASA increases linearly with the applied deposition current. The Bi EASA increases also with the deposition time.

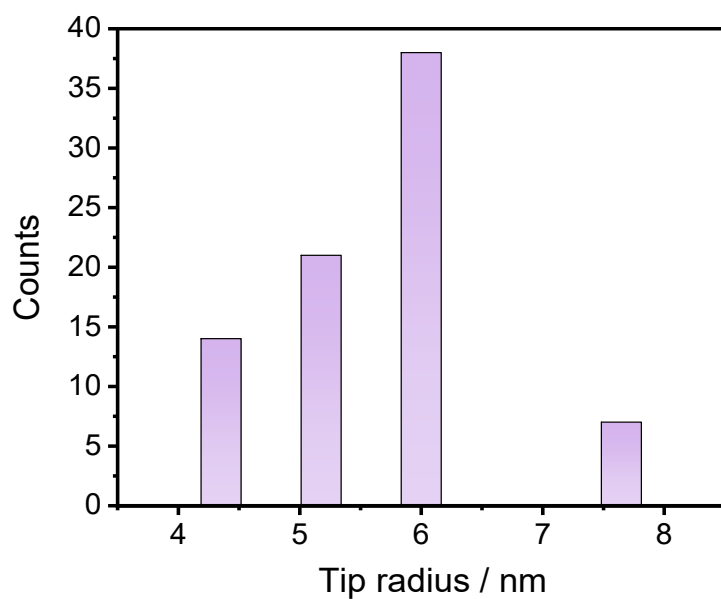


Figure S4.2 Histogram of tip radius obtained from measurements of 80 individual Bi nanoneedles.

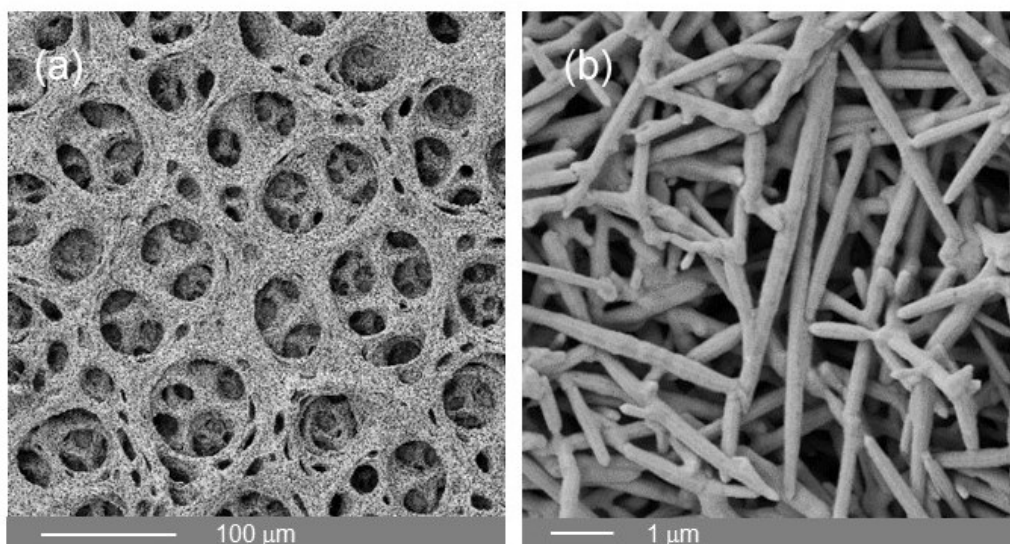


Figure S4.3 SEM images with various magnifications of porous Pb substrate

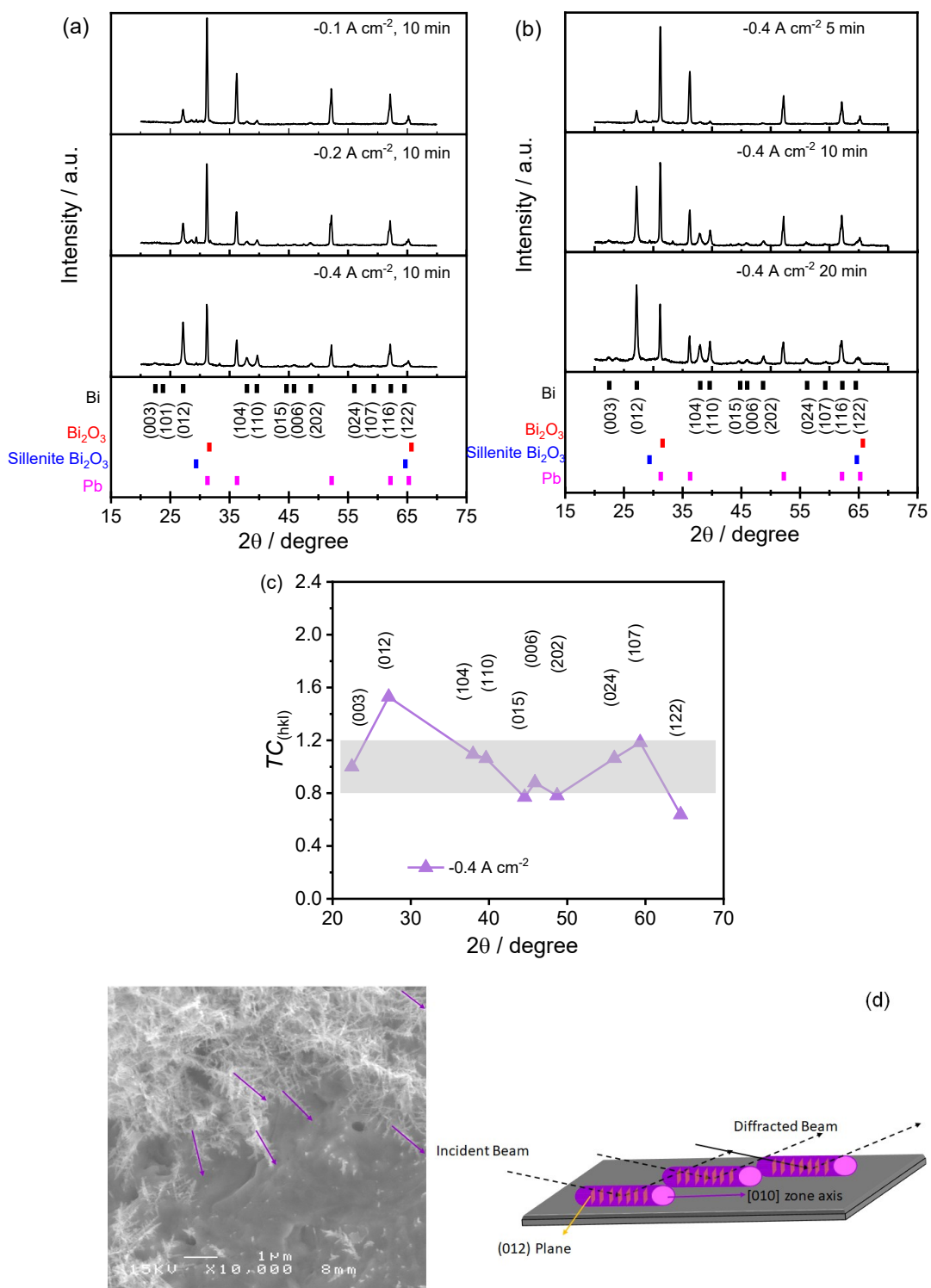


Figure S4.4 XRD patterns of Bi_{den} deposited at (a) different deposition current densities (with $t_{dep} = 10 \text{ min}$) and (b) different deposition times (with $j_{dep} = -0.4 \text{ A cm}^{-2}$). The substrate was a Pb plate in all cases. In (c), texture coefficient, $TC_{(hkl)}$, analysis of the thicker Bi deposit. In (d), schematic representation of the growth of Bi dendrite at the surface of the substrate. The arrows indicate region where Bi grows with their [010] zone axis parallel to the flat substrate.

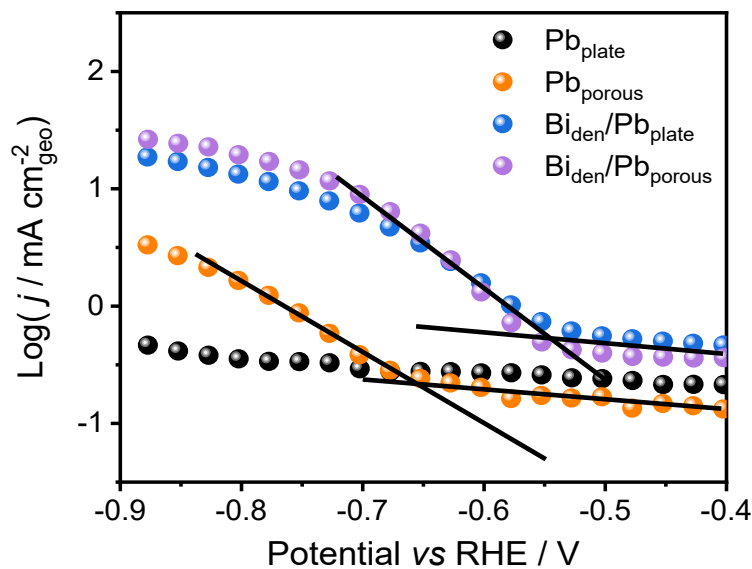


Figure S4.5 Linear sweep voltammograms (5 mV s^{-1}) of electrodes in CO_2 -saturated 0.5 M KHCO_3 .

The onset potential for CO_2 electroreduction was assessed by drawing $\log(-j)$ vs potential curves and taking the onset potential as the potential at which, the solid lines intersect each other.

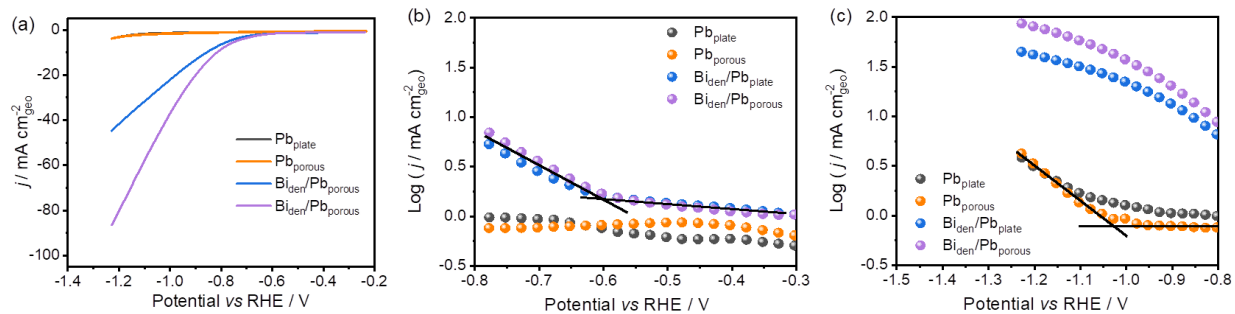


Figure S4.6 Linear sweep voltammograms (5 mV s^{-1}) of electrodes in Ar-saturated 0.5 M KHCO_3 .

The onset potential for CO_2 electroreduction was assessed by drawing $\log(-j)$ vs potential curves and taking the onset potential as the potential at which, the solid lines intersect each other.

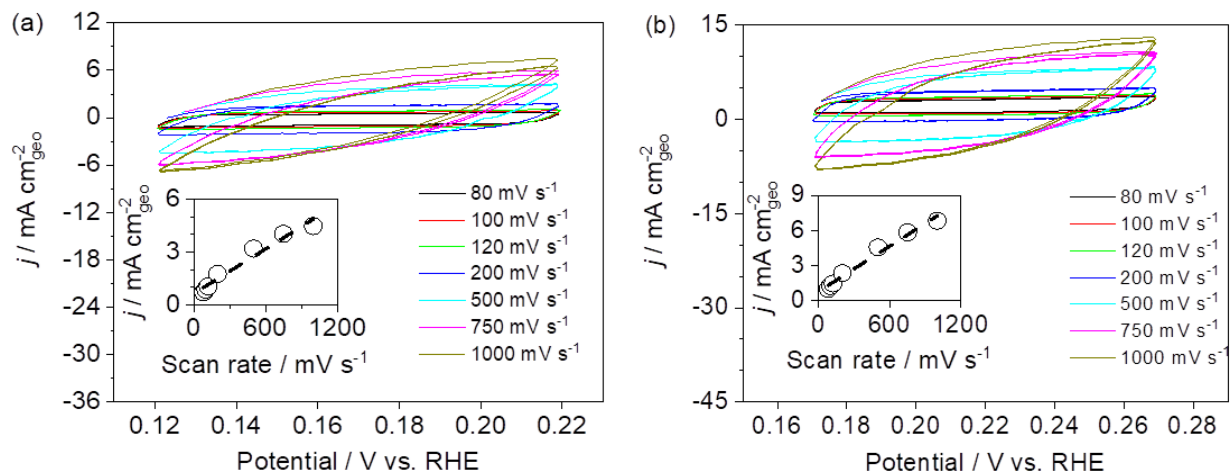


Figure S4.7 Determination of the Bi EASA of dendritic Bi deposited on (a) a Pb plate and (b) on a porous Pb substrate. The EASA of Bi_{den} on Pb_{plate} is 156 cm^2 , while that of Bi_{den} on porous Pb is 231 cm^2 .

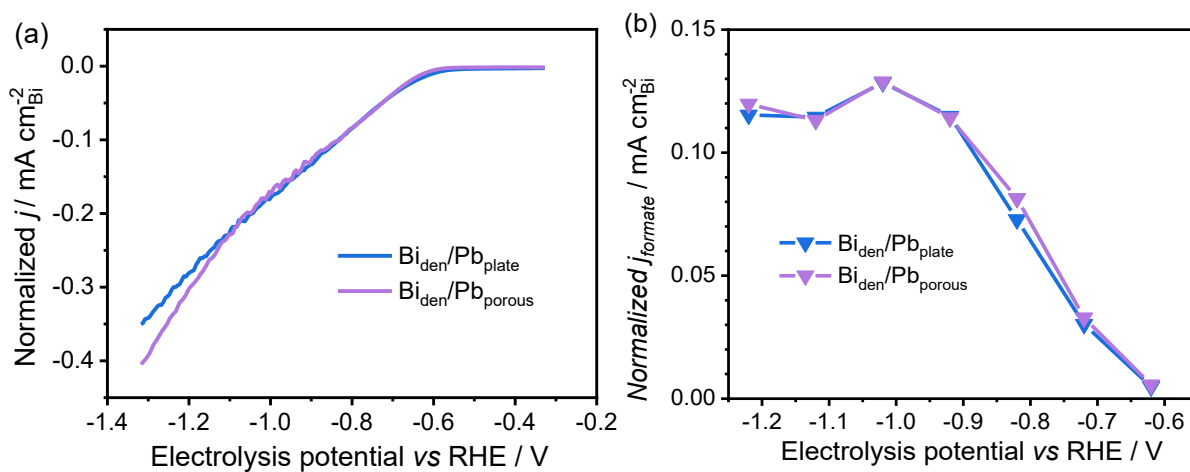


Figure S4.8 Bi EASA normalized (a) j and (b) j_{formate} vs. potential curves.

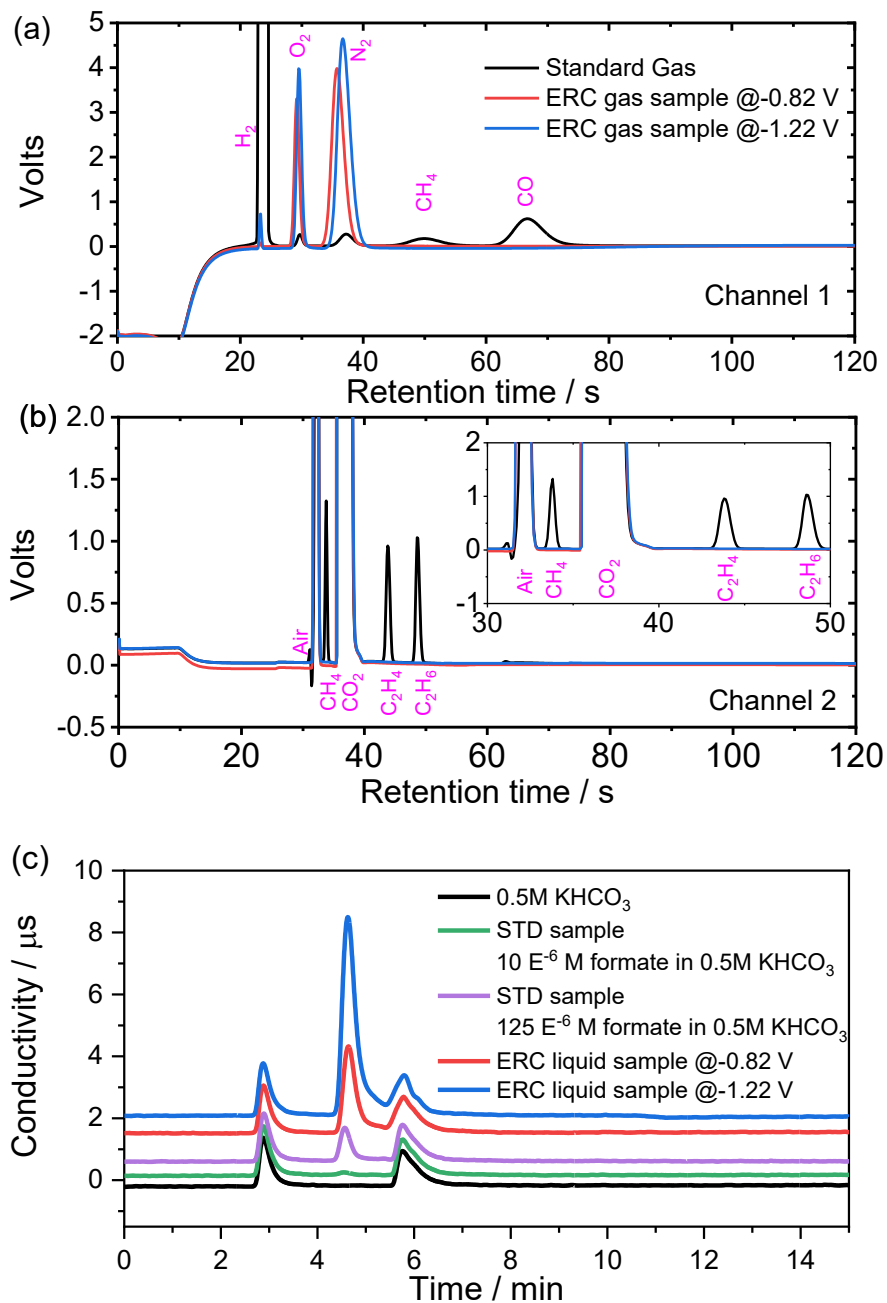


Figure S4.9 Typical examples of (a) GC channel 1, (b) GC channel 2, and (c) IC results. In the GC test, the standard gas sample is composed of H₂, CO, CH₄, C₂H₄, C₂H₆ and CO₂. In (a), H₂, CH₄, and CO are detected in channel 1. In (b), CH₄, CO₂, C₂H₄, and C₂H₆ are detected in channel 2. In (c), the standard (STD) liquid sample is the formate sample dissolved in 0.5 M KHCO₃ solution.

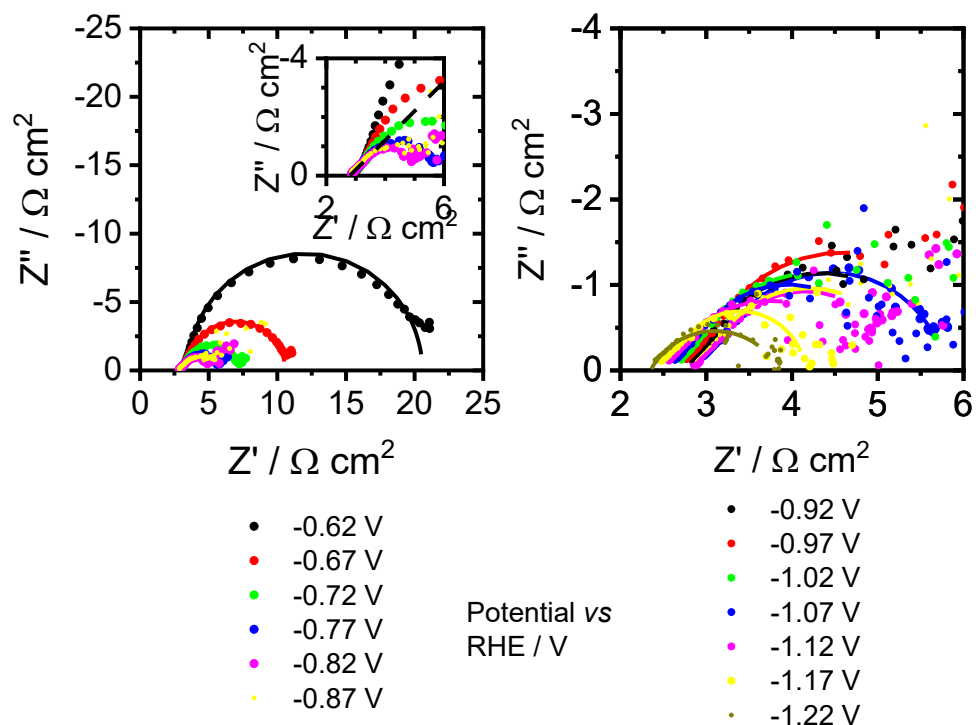
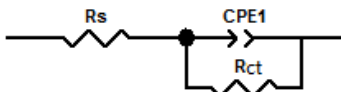


Figure S4.10 Nyquist plot of electrochemical impedance spectra of $\text{Bi}_{\text{den}}/\text{Pb}_{\text{porous}}$ electrodes. The applied electrode potentials were varied by steps of 0.05V from -0.62 V to -1.22 V vs. RHE. The electrolyte was CO_2 -saturated 0.5 M KHCO_3 . The experimental data (dots) and fitted curves (full lines) are shown. The data were analyzed using the following equivalent circuit:



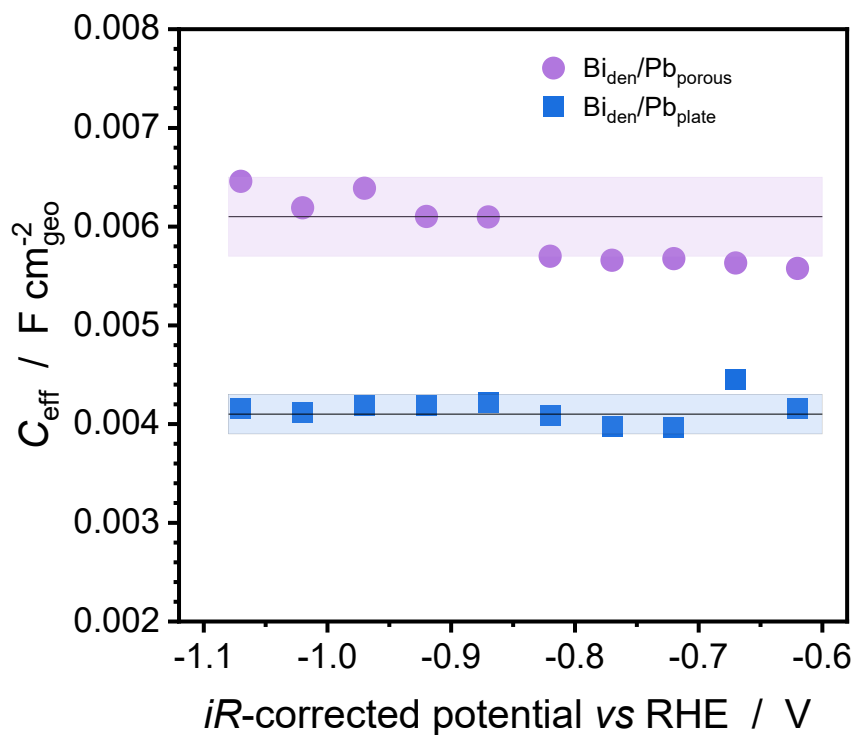


Figure S4.11 Variation of the effective capacitance with the iR -corrected electrode potential. The shading areas corresponds to one standard deviation.

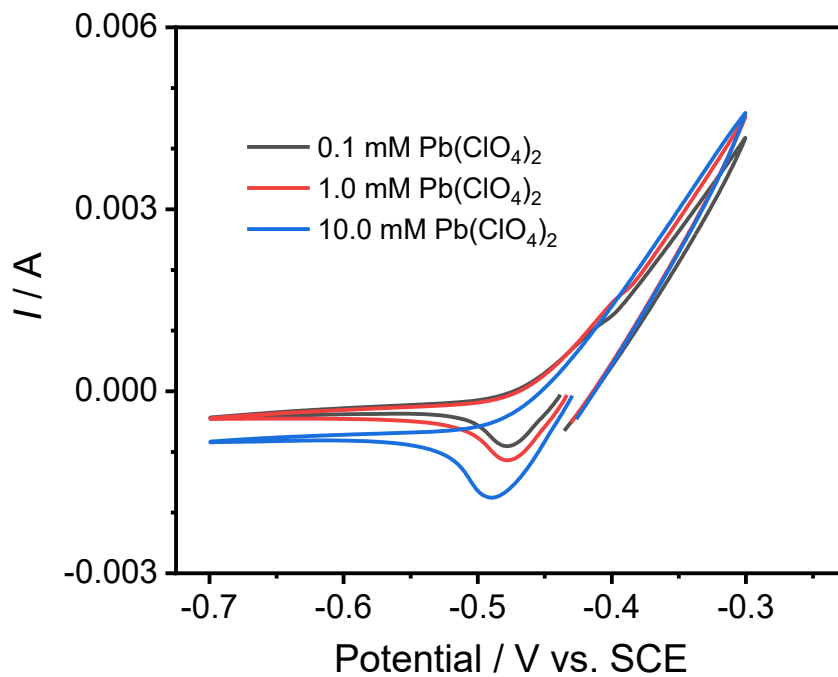


Figure S4.12 CV of $\text{Bi}_{\text{den}}/\text{Pb}_{\text{plate}}$ in $\text{Pb}(\text{ClO}_4)_2 + 0.1 \text{ M HClO}_4$ plating solution. The concentration of $\text{Pb}(\text{ClO}_4)_2$ was varied from 0.1 mM to 1.0 mM. The scan rate was 50 mV s^{-1} .

Table S4.1 Fitting parameters of Biden/Pbporous electrodes at different applied electrode potentials obtained by using the following equivalent circuit. CPE1 has admittance $T(i\omega)^\phi$.



E V vs. RHE	R_s ohm cm ²	R_s error	R_{ct} ohm cm ²	R_{ct} error	T mF cm ⁻² s ^{ϕ-1}	T error	ϕ	ϕ error	C_{eff} mF cm ⁻²	C_{eff} error
-0,62	3,31	0,03	17,64	0,15	7,32	0,12	0,934	0,005	5,576	0,114
-0,67	3,24	0,03	7,66	0,07	7,77	0,20	0,926	0,008	5,630	0,192
-0,72	3,21	0,03	4,06	0,05	7,89	0,25	0,928	0,009	5,675	0,233
-0,77	3,13	0,04	2,66	0,07	9,00	0,59	0,904	0,020	5,660	0,515
-0,82	3,07	0,03	2,16	0,09	9,15	0,95	0,904	0,026	5,699	0,753
-0,87	3,01	0,08	2,38	0,21	11,63	2,33	0,866	0,054	6,097	1,665
-0,92	2,96	0,05	2,75	0,17	10,82	1,47	0,879	0,036	6,103	1,089
-0,97	2,88	0,06	3,86	0,33	14,57	2,22	0,819	0,046	6,389	1,442
-1,02	2,76	0,05	3,07	0,27	14,30	2,70	0,822	0,049	6,144	1,510
-1,07	2,84	0,07	2,23	0,21	8,89	1,87	0,934	0,055	6,458	1,654
-1,12	2,67	0,16	2,16	0,30	13,43	4,27	0,845	0,097	6,298	2,293
-1,17	2,63	0,17	1,52	0,24	9,39	3,47	0,939	0,113	6,925	2,526
-1,22	2,53	0,05	1,08	0,08	6,48	1,23	0,997	0,051	6,381	1,478

The parameters R_s is the solution resistance, r_{ct} is the charge-transfer resistance and c_{eff} is the double-layer capacitance

Table S4.2 Comparison of CO₂ electrochemical reduction performance for dendritic Bi and recently reported Bi-cased catalysts in the literature.

Electrode	Electrolyte	Potential / V vs. RHE	Formate FE / %	j_{formate} / mA cm ⁻²	Production rate* / $\mu\text{mol cm}^{-2} \text{h}^{-1}$	Half-cell power efficiency** / %	Ref.
Bi aggregates	0.5 M KHCO ₃	-0.82	82	-0.3	5	57.1	91
Bi dendrites on carbon paper	0.5 M NaHCO ₃	-1.12	96	-15.0	269	58.3	139
Bi nanoflakes	0.1 M KHCO ₃	-0.80	100	-3.7	69	70.3	200
Bi dendrites	0.5 M KHCO ₃	-0.74	89	-2.7	45	64.5	47
Nano-Bi	0.5 M KHCO ₃	-0.92	98	-9.7	177	65.0	92
BiOCl nanosheets	0.5 M KHCO ₃	-0.83	92	3.7	64	63.7	46
Nano Bi/Cu foil	0.1 M KHCO ₃	-0.89	91	3.1	53	61.2	83
Micro-Bi/GDE	0.5 M KHCO ₃	-0.78	90	1.5	25	63.8	84
Nanoflower Bi	0.1 M KHCO ₃	-0.89	84	9.0	141	56.5	218
BiOx/C	0.5 M NaHCO ₃	-1.14	93	16.0	278	55.9	219
Bi nanosheets	0.5 M NaHCO ₃	-0.82	95	15 ~16	275	66.1	134
p-orbital delocalization-	0.5 M KHCO ₃	-0.86	95	18.0	319	64.8	220
Pb _{den}	1 M KHCO ₃	-0.99	97	-7.5	136	62.3	141
Bi_{den}/ Pb_{porous}	0.5 M KHCO₃	-0.82	98	-18.8	344	68.2	This work
Bi_{den}/Pb_{porous} in flow-cell	0.5 M KHCO₃	-0.82	92	95	1631	64.0	This work

*The production rate = $FE_{\text{formate}} * j / 2F$, where FE_{formate} is the Faradaic Efficiency of formate, j is the steady total current density during potentiostatic CO₂ electrolysis, F is the Faraday constant.

**Half-cell power efficiency = $(1.23 - E_{\text{formate}}) * FE_{\text{formate}} / (1.23 - E_{\text{applied}})$, where E_{formate} is 0.196 V vs. RHE, which is the thermodynamic potential of CO₂ reduction to formate, E_{applied} is the potentiostatic potential applied during CO₂ reduction. FE_{formate} is the Faradaic Efficiency of electroreduction of CO₂ towards formate. The half-cell power conversion efficiency was calculated assuming that the oxygen evolution overpotential was 0.²²⁰

5 DENDRITIC TIN AND LEAD BINARY ALLOY ELECTRODE

Understanding the Mechanism of CO₂ Electrochemical Reduction on Dendritic Sn₁Pb₃ alloy: A Computational-Experimental Investigation

Comprendre le mécanisme de réduction électrochimique du CO₂ sur l'alliage dendritique Sn₁Pb₃: une étude computationnelle-expérimentale

Authors:

Mengyang Fan,¹ Mohammad J. Eslamibidgoli,^{2,3} Xinwei Zhu,³ Sébastien Garbarino,^{1,4} Ana C. Tavares,¹ Michael Eikerling,^{2,3} and Daniel Guay^{1*}

1. INRS-Énergie, Matériaux Télécommunications, 1650 Lionel-Boulet Boulevard, P.O. Box 1020, Varennes, QC, Canada J3X 1S2

2. Department of Chemistry, Simon Fraser University, 8888 University Drive, Burnaby, BC, Canada V5A 1S6

3. Institute of Energy and Climate Research (IEK-13), Theory and Computation of Energy Materials, Forschungszentrum Jülich GmbH, Jülich, Germany 52425

4. PRIMA Québec, 505 de Maisonneuve Boulevard West, Montreal, QC, Canada H3A 3C2

Publication:

ACS Catalysis, Submitted, 2020

Contribution of authors:

Mengyang Fan, and Prof. Daniel Guay conceived and designed the research. Mengyang Fan prepared all samples and conducted most of the characterizations as well as all CO₂ electrochemical reduction measurements. Mengyang Fan also carried out DFT calculations under the supervision of Dr. Mohammad J. Eslamibidgoli. The computational results were analyzed and discussed with Dr. Mohammad J. Eslamibidgoli and Prof. Michael Eikerling. Xinwei Zhu and Prof. Michael Eikerling wrote the section on mechanistic modeling and discussions. Mengyang Fan wrote the original manuscript draft; it was commented by Dr. Sébastien Garbarino and Prof. Ana C. Tavares. The manuscript was carefully edited by Prof. Michael Eikerling and Prof. Daniel Guay.

Link between articles:

The modification of a Pb electrode by a dendritic Bi outmost layer efficiently enhances CO₂ electrochemical reduction (ERC) activity. The ERC overpotential has been reduced, resulting in higher energy efficiency. The ERC reduction current has been increased, leading to a higher production rate. However, the Bi is also active for hydrogen evolution (HER), a competitive reaction to the CO₂ reduction. To reduce the HER competition and enlarge the ERC working potential window, Sn, which is sluggish for HER, was introduced to synthesize a bimetallic dendritic electrode.

In this work, a well-alloyed Sn₁Pb₃ electrode featuring a dendrite-like structure was fabricated. The FE_{formate} reached 99% at -0.72 V vs. RHE, which is 100 mV lower compared to the Bi-modified Pb electrode. The FE_{formate} retains 90% at a large potential window from -0.72 to -1.12 V vs. RHE (-1.16 and -1.56 V vs. SHE).

Compared to the pure dendritic Pb, the ERC onset potential of the Sn₁Pb₃ electrode was 80 mV lower. Density functional theory (DFT) computations were performed to uncover the origin of the drop in onset potential upon alloying Pb with Sn. Explicit treatment of water molecules in DFT calculations turns out to be crucial to achieving agreement with experimentally-measured onset potentials.

5.1 Introduction

The electrochemical conversion of CO₂ into useful chemicals and fuels provides a means to recycle CO₂ and achieve carbon balance.^{26,40,221,222} It is also an effective way to convert the energy of intermittent and renewable sources, and to store it as chemical energy through the formation of value-added products. Several value-added products can be obtained from the electroreduction of CO₂, among them formic acid/formate.^{24,221} The hydrogenation of CO₂ to form HCOOH involves the transfer of only two electrons and two protons.^{24,223} Along with CO formation, this process is the simplest and most effective way to transform CO₂ into value-added products, as it involves only a small number of electro(chemical) steps.

The demand for formic acid/formate is significant due to its versatile uses.^{223,224} Formic acid/formate is used in several industrial sectors including pharmaceutical synthesis, pulp and paper production, textile finishing, as an additive in animal feeds, and as a deicing agent.^{125,225} In addition, formic acid/formate has been identified as a potentially interesting hydrogen carrier, and as a fuel for direct formate fuel cells (DFFC).^{123,226,227} Formic acid/formate is kinetically stable at room temperature and has a hydrogen content of 4.4 wt%.²²⁸ Moreover, it is non-hazardous, non-flammable, and highly soluble in water. It can be handled in solid (formate salts) and liquid (aqueous solution) states, which makes it safe to handle and inexpensive to store and distribute.²²⁹

Years of research have shown that various metals, including Pb, Hg, Bi, and Sn, produce HCOOH as a major product during the electroreduction of CO₂.^{25,26,36} However, this research has also shown that a high Faradic efficiency for the formation of formic acid/formate (high selectivity) is accompanied by a large onset potential and a high overpotential when a large current density (high production rate) is requested. High overpotentials can be handled by increasing the electrochemically active surface area of the electrode; several strategies have been deployed to achieve this^{127,141,230}. Reducing the onset potential for CO₂ electroreduction calls for more subtle manipulation of the electrode composition, since the onset potential is determined by the adsorption energies of reaction intermediates. This can be achieved through alloying with appropriate elements.

For example, Pd-Au,²³¹ Ag-Sn²³², Pd-Sn²³³ and Pt-Ni⁴⁸ have been alloyed together to improve the electrode performance compared to pure elements. High catalytic activity and low overpotential for the ERC are brought upon these systems by the use of precious metals.^{102,107,178} Recently, attempts have been made to achieve the same performances using electrocatalytic materials without precious metal content; to this end, alloys such as Cu-Sn²³⁴⁻²³⁶ and Cu-Zn²³⁷ have been

investigated. However, the ERC performances of these materials remain poor in terms of onset potential and Faradic efficiency, and further improvement is needed.

Herein, the electroreduction of CO₂ on a dendritic Sn-Pb alloy and Pb is investigated. First, the preparation of electrode materials will be presented, followed by their physico-chemical characterization to ascertain their composition, morphology and structure. Then, these materials' performance for ERC will be assessed. Finally, DFT calculation results will be presented, and a structure-activity relationship will be established to explain the improved performances observed on dendritic Sn₁Pb₃ alloy.

5.2 Experimental Section

5.2.1 Preparation of SnPb binary dendrites

The PbSn alloy was galvanostatically co-deposited onto a flat Pb substrate (Nuclead, chemical grade, 1/16-inch thickness, 0.5 cm² geometric surface area) at -4 A cm⁻² for 40 s in a plating solution composed of 10 mM Pb(ClO₄)₂ (ACROS Organics, ACS Reagent) and 10 mM SnCl₂ (Aldrich, Reagent Plus, 99.99+%) in 1 M HClO₄ (Fisher Chemical, trace metal grade) supporting electrolyte. After deposition, the PbSn film was rinsed with deionized water and dried under Ar stream for 30 min.

5.2.2 Physio-chemical and electrochemical characterization

The surface morphology of SnPb alloy was characterized by scanning electron microscopy (SEM) equipped with energy-dispersive X-ray spectroscopy (EDX) (TESCAN, VEGA3). The crystalline structures were investigated by x-ray diffraction (XRD) measurements using a Bruker D8 Advanced operated at 40 kV and 40 mA, with a weighted average Cu K_{α1} and Cu K_{α2} radiation at 1.5418 Å.

The electrochemical measurements were carried out in an H-type cell at room temperature with a Pt gauze as counter electrode and a saturated calomel electrode (SCE) as reference. All the potentials in this study are quoted with respect to the standard hydrogen electrode (SHE). Linear sweep voltammetry (LSV) curves were recorded in Ar- or CO₂-saturated 0.5 M KHCO₃ electrolyte in a potential range from -0.76 to -1.76 V vs. SHE at a scan rate of 5 mV s⁻¹ using a potentiostat (Biologic VSP). The Electrochemically Active Surface Area (EASA) was determined through measurements of double-layer capacitance in the Ar-saturated 0.5 M KHCO₃ electrolyte.

5.2.3 Products measurement and flow-cell test

The products were analyzed after 30 min electrolysis in CO₂-saturated 0.5 M KHCO₃ electrolyte. Ion chromatography (IC, ICS-1500, Dionex, USA) was used to measure the formate concentration. The separation column was an IonPac AS9-HC. The mobile phase was a 9 mM Na₂CO₃ at a flow rate of 1 mL/min. All samples were diluted 10 times before measurement. The gas products were analyzed by gas chromatography (GC, Agilent Micro 490) at two channels with a thermal conductivity detector. H₂ was the only detected gas product. The Faradic efficiency of H₂ was calculated as follows:

$$FE_{H_2}(\%) = \frac{\frac{Peak\ area}{\alpha} \times flow\ rate \times t \times \frac{P}{RT} \times z \times F}{Q} \times 100 \quad (5.1)$$

where α is the conversion factor for H₂ based on the calibration of the gas chromatograph response established with standard samples, *flow rate* is the CO₂ flow rate during the test, *t* is the electrolysis time, *P* is the atmosphere pressure, *T* is the room temperature, *R* is the gas constant, *z* is the electron transfer number, *F* is the Faraday constant, and *Q* is the total charge during electrolysis. In all cases, the total Faradaic efficiency, obtained by the addition of the partial FE for formate and H₂, was 100 ± 5%.

A flow cell was used to test the catalyst's CO₂ reduction capability under higher CO₂ flux. A schematic illustration of the flow cell is shown in Figure S5.1. The core of the electrolysis cell was composed of a working electrode, a Nafion 117 separating membrane, and an anode. This flow cell was equipped with a Saturated Calomel Electrode (SCE) reference and a Pt gauze counter electrode. Both the working and counter electrodes have a disk shape with a geometric surface of 1 cm². In this setup, the catholyte and anolyte flow rate (Masterflex L/S Easy-Load® II Model 77200-50 pump head and 06434-17 pump tube) and pressure can be controlled independently. A dendritic Sn₁Pb₃ alloy electrode was used as cathode. The electrolyte was a CO₂ super-saturated 0.5 M KHCO₃ solution prepared using a soda machine (Sodastream, CO₂ purity 99.999%). The maximum work pressure of the soda machine was 145 psi, which was 10-fold higher than the ambient pressure. The maximum dissolved CO₂ in the super-saturated electrolyte was 0.34 mol L⁻¹. The catholyte was circulated at a flow rate of 104 ± 1 mL min⁻¹ and the catholyte pressure was 5 psig above atmospheric pressure. The anolyte was 0.5 M KHCO₃. It was circulated at a flow rate of 2.3 ± 1 mL min⁻¹ and the anolyte back pressure was 6 psig.

5.2.4 Computational details

DFT calculations were carried out using periodic DFT implemented in the Vienna *ab initio* Simulation Package (VASP 5.3.5).¹⁵⁸ The Perdew-Burke-Ernzerhof (PBE) exchange correlation (XC) functional was used.¹⁵⁹ The projector-augmented-wave (PAW) formalism was applied; this keeps core electrons frozen and replaces their effect with pseudopotentials, whereas valence electrons are expanded in a plane wave set up to an energy cutoff of 400 eV.¹⁶⁰

Spin-polarized calculations were carried out. Geometry optimizations were terminated when all forces on ions were less than $0.01 \text{ eV}\text{\AA}^{-1}$. The Brillouin zone was sampled using a k-point mesh of $(5 \times 5 \times 1)$ for the $3 \times 3 \times 4 \text{ Sn}_1\text{Pb}_3$ unit cell.¹⁶¹

5.3 Results and Discussions

5.3.1 Structure characterization and analysis

The morphologies of Pb and SnPb deposits were characterized by scanning electron microscopy (SEM). The SEM micrographs show that Pb deposits have a honeycomb structure with an average pore size of *ca.* $50 \mu\text{m}$ (Figure 5.1a). The walls of the honeycomb structure are made of dendrites consisting of stems to which branches are attached (Figure 5.1b). The average diameter of the branches is *ca.* 200 nm . When mixing Sn(II) and Pb(II) in the plating solution (1:1 ratio), the resulting SnPb deposit has also a primary honeycomb structure with a secondary dendritic structure (Figure 5.1c and 5.1d). However, in that latter case, the average pore size of the primary structure (*ca.* $20 \mu\text{m}$) and the diameter of the dendritic branches (*ca.* 180 nm) are reduced slightly. Both deposits were prepared at large deposition current densities, leading to simultaneous metal electrodeposition and hydrogen evolution. Deposition under these conditions is known as “Dynamic Hydrogen Bubble Templating (DBHT)”.¹⁵⁷ The pore diameter of the primary structure varies with the dynamics of hydrogen bubble formation and release from the deposit, which in turn depends on the nature of the deposited metallic element and explains the difference observed between both deposits.

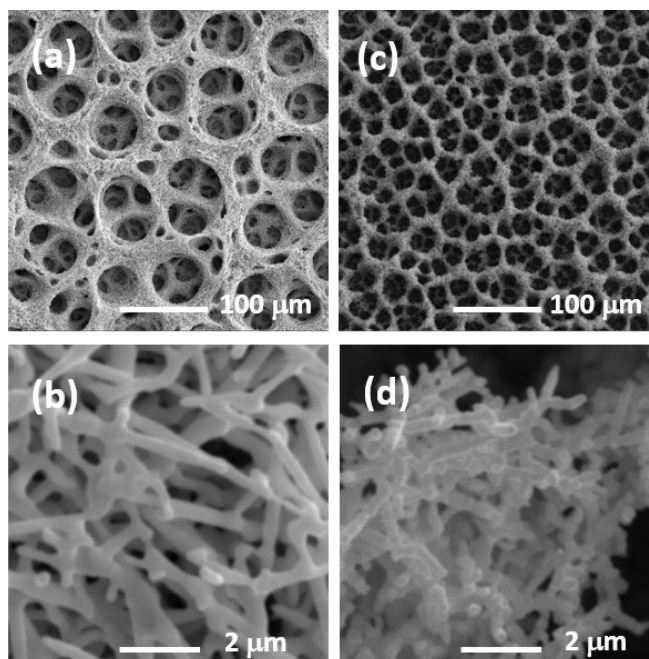


Figure 5.1 SEM images of (a, b) pure Pb, and (c, d) Sn_1Pb_3 alloy.

The X-ray diffraction (XRD) pattern of Pb deposit in Figure 5.2 exhibits only one series of diffraction peaks that are assigned to face centered cubic (*fcc*) polycrystalline Pb, with lattice parameter $a = 4.950 \text{ \AA}$ that closely matches the lattice parameter of bulk Pb, which is 4.9506 \AA (JCPDS card No. 00-004-0686). The main diffraction peaks of the SnPb deposits can also be indexed to an *fcc* phase, although all peaks are shifted to larger 2θ angle compared to Pb deposit. This suggests that Sn is dissolved in *fcc* Pb. The lattice parameter of SnPb deposit is 4.938 \AA , slightly smaller compared to Pb deposits. In previous studies, Fecht *et al.* reported that the lattice parameter of Pb decreases with the increase of the Sn/Pb ratio, and the lattice parameter of *fcc* Pb(Sn) was 4.9397 \AA at $[\text{Sn}] = 29 \text{ at.}\%$.²³⁸ This value corresponds to the actual Sn content of our SnPb deposit. According to the Sn-Pb phase diagram,²³⁹ $[\text{Sn}] = 28 \text{ at.}\%$ also corresponds to the solubility limit of Sn in *fcc* Pb. All data suggest that Sn and Pb are alloyed to form dendritic SnPb deposits. This was further confirmed by the fact that the XRD peaks of β -Sn (body centered tetragonal) are barely observed in Figure 5.2. Also, EDX mapping reveals that both Sn and Pb elements are evenly distributed in the deposits (Figure S5.2), which is expected if Sn is dissolved in *fcc* Pb. In the following, we will therefore refer to these deposits as dendritic Sn_1Pb_3 alloy films. Various deposition conditions (atomic ratio of Sn and Pb cations dissolved in the electrolyte and deposition times) were tried, resulting in deposits with XRD patterns exhibiting different proportions of *fcc* phase and β -Sn. However, the focus of the present study is to understand the

effect of alloying *fcc* Pb with Sn. In this context, it was important to prepare single phase SnPb deposits with as little as possible β -Sn. This was achieved in the experimental conditions described above and using an electrolyte that contains an equimolar concentration of Sn and Pb and a deposition current density of -4 A cm^{-2} .

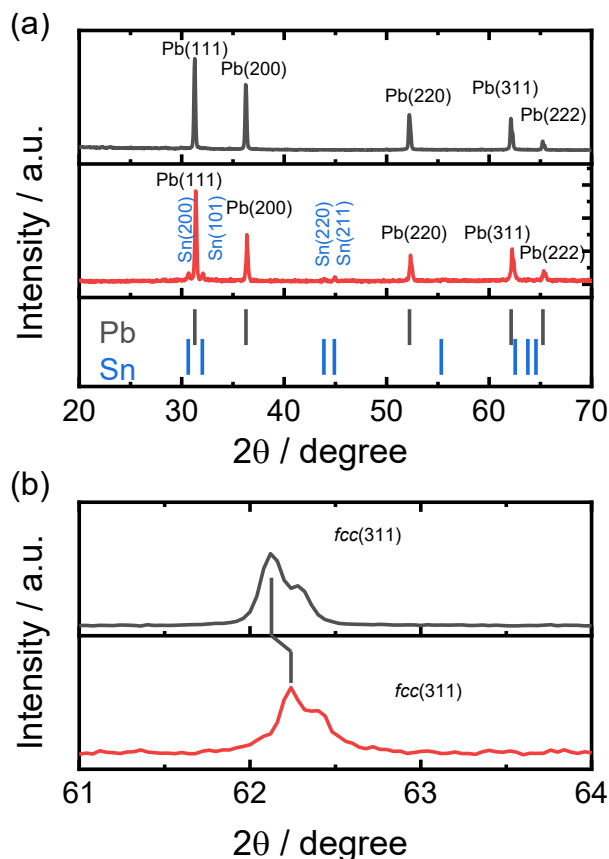


Figure 5.2 In (a), XRD patterns of pure Pb and Sn_1Pb_3 alloy deposits. The expected diffraction peaks of Pb (JCPDS card No. 00-004-0686) and β -Sn (JCPDS card No. 00-004-0673) are also indicated. A restricted 2θ range is shown in (b) to emphasize peaks displacement. Black curve: pure Pb, and red curve: Sn_1Pb_3 alloy.

5.3.2 Selectivity and activity for CO_2 electrochemical reduction

The electrocatalytic activity for the CO_2 electroreduction of dendritic Sn_1Pb_3 alloy was tested by linear sweep voltammetry (LSV) and compared to dendritic Pb. The concentration of formate in the electrolyte was measured by ion chromatography after 30 min of CO_2 electrolysis, in the potential range from -1.16 to -1.66 V vs. SHE . Figure 5.3a shows LSVs at 5 mV s^{-1} in both Ar and CO_2 -saturated 0.5 M KHCO_3 solution. In CO_2 -saturated electrolyte, the onset potentials of both electrodes are shifted to more positive value compared to Ar-saturated 0.5 M KHCO_3 electrolyte (see Table S5.1). This is a clear indication that CO_2 reduction occurs on both electrode materials

and that this reaction is more energetically favorable than hydrogen evolution. The onset potential for the reduction of CO₂ on dendritic Sn₁Pb₃ alloy is -1.01 V vs. SHE, which is 80 mV more positive than the onset potential for dendritic Pb. We infer that the introduction of Sn exerts a pronounced effect on the adsorption energy of CO₂ reduction intermediates. Also, the *EASA*-normalized current density, j_{EASA} , of dendritic Sn₁Pb₃ alloy is larger than that of dendritic Pb (the method used to determine the *EASA* is described in the SI section, Figure S5.3). For example, j_{EASA} at -1.6 V vs. SHE is -1.4 and -0.5 mA cm⁻²_{*EASA*} for dendritic Sn₁Pb₃ alloy and dendritic Pb, respectively, which differs by a factor of almost three. In conclusion, dendritic Sn₁Pb₃ alloy not only has a lower onset potential for the electroreduction of CO₂, but it is also more active when compared at equivalent *EASA*.

The formate faradaic efficiency, $FE_{formate}$, of dendritic Sn₁Pb₃ alloy is shown in Figure 5.3b. It is very close to 100% in the potential range between -1.16 and -1.56 V, and starts to decline only at more negative potential. This is surprising in that the $FE_{formate}$ stays close to 100% at electrode potentials more negative than the onset potential for hydrogen evolution (-1.33 vs SHE). This suggests that the intermediates of both reactions are competing for the same site. For comparison, $FE_{formate}$ of electrodeposited PbSn onto carbon paper does not exceed 80%²⁴⁰. The $FE_{formate}$ of dendritic Pb is considerably less than 100% at potentials more positive than -1.3 V vs. SHE, where the hydrogen evolution reaction does not take place. This reflects the fact that a non-negligible fraction of the charge is consumed to reduce the oxidized Pb surface (see Figure S5.4). This effect is not observed on dendritic Sn₁Pb₃ alloy, and the $FE_{formate}$ reaches 100% in the potential region where a significant fraction of the charge is spent to reduce lead oxide on dendritic Pb. This is most probably related to the presence of Sn in the alloy, which was shown to limit surface oxidation.^{232,240}

The dendritic Sn₁Pb₃ alloy electrode was tested further in a high-pressure flow-cell system that allows larger CO₂ flux to be achieved. At -1.16 V vs. SHE, which corresponds to an overpotential of 500 mV, the average ERC current was -17.4 mA cm_{geo}⁻² with $FE_{formate} = 92%$ (Figure 5.3c). A comparison of the ERC performances with other Pb-based electrode materials is shown in Table S5.2.

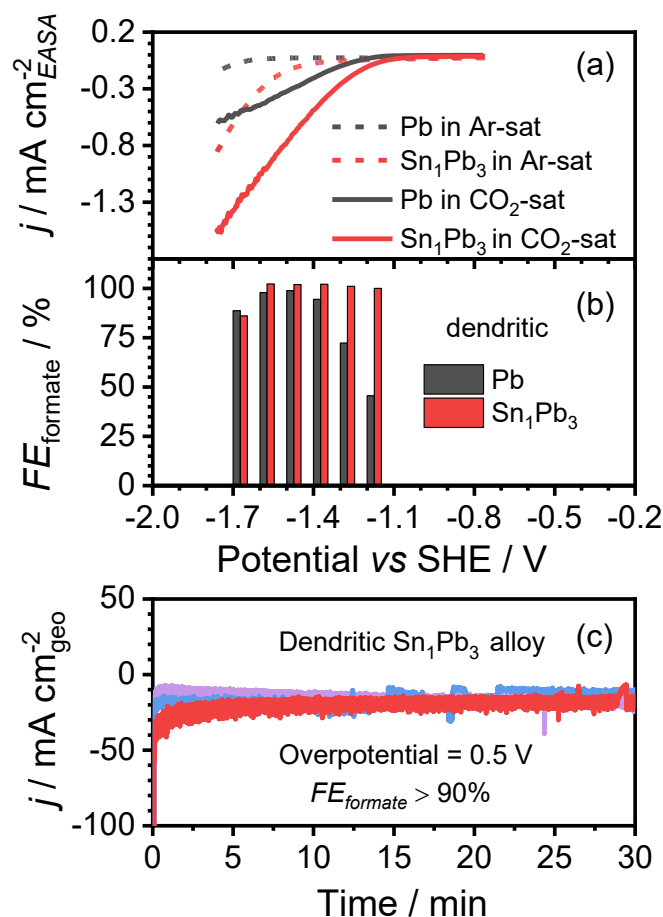


Figure 5.3 In (a), linear sweep voltammetry curves in 0.5 M KHCO₃ electrolyte recorded at 5 mV s⁻¹. In (b), formate Faradaic Efficiency (FE_{formate}) recorded after 30 minutes of electrolysis at each potential. In (c), current density recorded at a Sn₁Pb₃ alloy electrode in a flow-cell system.

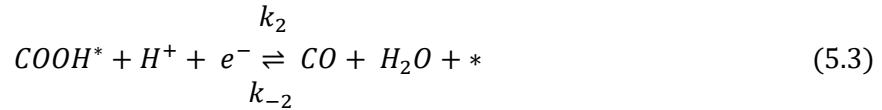
5.3.3 Mechanism investigation of dendritic Sn₁Pb₃ for enhanced activity

DFT calculations were performed to understand the effect of alloying Pb with Sn on the onset potential for the conversion of CO₂ to formate. The calculations were carried out on the (100) surface slab models of Pb and Sn₁Pb₃. Detailed TEM analysis of Pb dendrites showed that they are growing along the <001> axis and that they are enclosed by [100] and [010] surfaces¹⁴¹. As shown in Figure S5.5, these structural characteristics translate into (200) texture coefficient, TC_{200} , larger than 1 for dendritic Pb. Similarly, $TC_{(200)}$ of dendritic Sn₁Pb₃ is also larger than 1, suggesting that the growth mechanism of dendritic Pb and dendritic Sn₁Pb₃ is the same. Accordingly, (100) surface slab models were used to represent both electrocatalytic surfaces. The optimized unit cell parameters of pure Pb and Sn₁Pb₃ alloy obtained from DFT calculations are 5.02 Å and 4.98 Å, respectively. Alloying Pb with Sn decreases the lattice parameter of *fcc* Pb,

which is consistent with the XRD measurements that gave a unit cell parameter of 4.951 Å for Pb and 4.938 Å for Sn₁Pb₃.

The electrochemical reduction of CO₂ on Pb(100) and Sn₁Pb₃(100) slabs was investigated by considering two competing pathways involving either carboxyl (COOH*) or formate (HCOO*) as intermediate. These intermediates are formed through the first coupled proton-electron transfer step.^{38,45,241} In the second step, CO can be formed from COOH* (in pathway A), and HCOOH is obtained from HCOO* (in pathway B), as summarized below,

Pathway A,



Pathway B,



where * stands for an active site on the surface, k_i and k_{-i} stand for the reaction rate in the forward and reverse directions. There are two other mechanisms that have been considered in the literature: (i) the proton-assisted mechanism that involves the adsorption of H* at an active site, which can further react with a CO₂ molecule to form carboxyl (COOH*) or formate (HCOO*), or combine with another H* to form H₂; however, it was shown that the latter reaction has an activation energy (0.20 eV) comparable to that of H* reacting with CO₂ to form HCOO* (0.25 eV). Accordingly, it would be difficult to explain why lead is very selective for formate and the FE_{H_2} is low;³⁹ (ii) adsorption of CO₂ on the electrode, followed by its reduction to form CO₂^{-•}; however, the redox potential of this reaction is very low and, indeed, more negative than the onset potential of CO₂ reduction on various metal electrodes.³⁹ Therefore, these two reaction mechanisms have not been considered in our study.

To investigate the selected reaction mechanisms, the binding energies, ΔE , of COOH* and HCOO* intermediates were calculated on Pb(100) and Sn₁Pb₃(100) surface facets: $\Delta E = E^{slab/ads} - E^{slab} - E^{ads}$, where $E^{slab/ads}$, E^{slab} and E^{ads} are the total energy of the slab and

adsorbed intermediate, clean surface and isolated intermediate in the gas phase, respectively. The energy diagrams of the competing pathways were then generated using the calculated free energy, ΔG , which is given by $\Delta G = \Delta E + eU + ZPE - T\Delta S$, where ZPE is the zero-point energy correction, U is the electrode potential, ΔS is the variation of entropy, and e and T have their usual meanings (see Table S5.3).²⁴² The computational hydrogen electrode (CHE) was used to establish a potential reference for these calculations.²⁴³⁻²⁴⁶

As shown in Figure 5.4a, under gas phase conditions, the HCOO* binding energies are -0.53 and -0.67 eV on Pb(100) and Sn₁Pb₃(100), respectively. On the same surfaces, the COOH* binding energies are +0.67 and +0.44 eV, respectively. A detailed thermodynamic and kinetic analysis will be presented later on, showing that the formation of HCOOH is the preferred pathway for the ERC on the materials considered in the present study. Consistently, our experimental results showed that CO is not detected (within a few percent) on dendritic Pb and dendritic Sn₁Pb₃ alloy. Using the CHE scheme, the potential at which all steps become exothermic for the formation of HCOOH can be calculated from the energy diagram of Figure 5.4a. As depicted in Figure S5.6a-b, this potential is -0.55 V vs SHE on Pb(100) surface while it is -0.69 V vs SHE Sn₁Pb₃(100) surface. However, both values are about 500 mV more positive than the experimentally measured values. More importantly, based on calculations performed under gas phase conditions, the onset potential for the CO₂ reduction on Pb would be less negative than Sn₁Pb₃ alloy. This is not what is observed experimentally (see Table S5.1). Thus, the calculations hitherto reported, *viz.* conducted under gas phase conditions, need to be refined as they lead to wrongful conclusions about the energetics of the reaction.

Considering that the electrocatalytic reduction of CO₂ is carried out in an aqueous electrolyte, the effect of solvent molecules on the binding energies of the various intermediates must be accounted for.⁴⁵ This was realized by including 12 water molecules located in a plane parallel to the Pb(100) and Sn₁Pb₃(100) surfaces in our DFT study. As can be seen in Figure 5.4b, inclusion of the water layer lowers the binding energies of both COOH* and HCOO* intermediates relative to those in the gas phase, indicating that water molecules stabilize these intermediates. Stabilization of the intermediates is a concerted effect that includes contributions from the water-water, water-adsorbate, water-surface, and surface-adsorbate interactions.

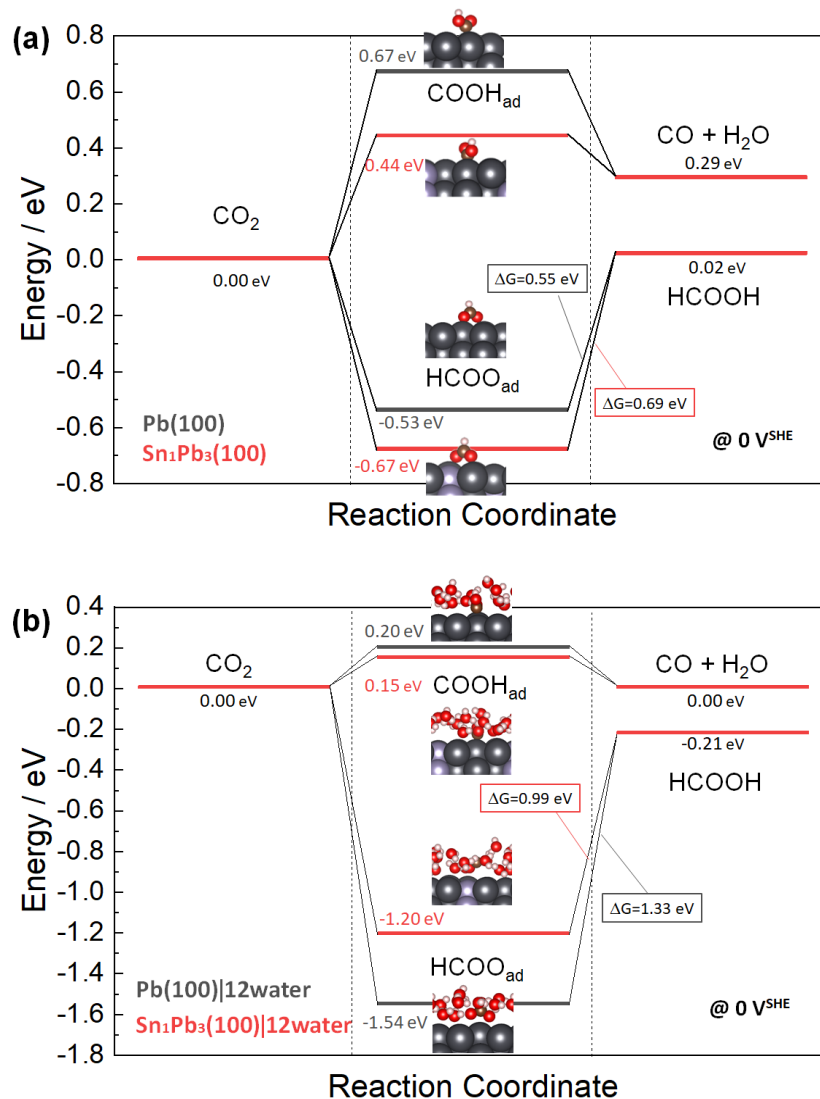


Figure 5.4 Energy diagrams for CO₂ reduction. In (a), gas phase conditions at 0 V. In (b), with 12 water molecules at 0 V.

Compared to gas phase conditions, surface water molecules further stabilize HCOO* on both Pb(100) and Sn₁Pb₃(100) surfaces and the stabilization energy of HCOO* is almost twice as large on Pb(100) (1.01 eV) compared to Sn₁Pb₃(100) (0.53 eV). As a result, HCOO* is less strongly adsorbed on Sn₁Pb₃(100) than on Pb(100) (-1.20 vs -1.54 eV), which reverses the trend observed under gas phase conditions. As a consequence, the potential at which all steps are exothermic is -0.99 V vs. SHE on the Sn₁Pb₃(100) surface as compared to -1.33 V vs. SHE on the Pb(100) surface (see Figure 5.4b and S5.6e-f). Based on these calculations, the onset potential for the reduction of CO₂ on dendritic Sn₁Pb₃ alloy is expected to be more positive than dendritic Pb, which agrees with experimental findings. Therefore, the inclusion of water molecules in DFT calculations

is essential to capture the trends in the onset potentials of dendritic Pb and dendritic Sn₁Pb₃, as observed in experiment.

Similar DFT calculations were performed using 6 water. The introduction of 6 water molecules instead of 12 does not have any marked effect on the energy diagram for CO₂ reduction, but allows a sizeable reduction of the computing time. As shown in Figure S5.7, the energy diagram for CO₂ reduction is barely affected, the maximal energy difference between any two corresponding levels being less than 0.1 eV. DFT calculations performed with 6 water molecules succeeded in capturing the fact that HCOO* is less strongly adsorbed on Sn₁Pb₃(100) than on Pb(100), and thus in correctly predicting that the onset potential for the electroreduction of CO₂ is more positive on Sn₁Pb₃ (-0.89 V) compared to Pb (-1.25 V) (see Figure S5.6c-d). Moreover, on Sn₁Pb₃(100) we compared the adsorption energy of HCOO* on Pb-Pb and Pb-Sn sites (see Figure S5.8). With 12 water molecules included in the DFT calculations, the energy difference between these two adsorption sites is negligible (0.03 eV).

Figure 5.5 shows the optimized structure of HCOO* in the presence of water molecules. The most striking difference is the change of orientation of the HCOO* from perpendicular on Pb(100) to parallel at the surface of Sn₁Pb₃(100), which is best seen in the top view images. Table S5.4 compares the binding energy values of HCOO* in perpendicular and parallel configurations at both surfaces. As can be seen on Sn₁Pb₃(100) the parallel orientation is more stable than the perpendicular orientation by 0.45 eV. On the other hand, on Pb(100) the perpendicular HCOO* orientation is more stable by 0.3 eV than the parallel one. We further investigated this effect by starting the optimization from several different initial configurations of water molecules on Sn₁Pb₃(100). In most cases, HCOO* rotates to obtain a more stable parallel orientation with respect to the surface. 3D charge density difference is shown in Figure S5.9. Various optimized structures are depicted in Figure S5.10 and S5.11

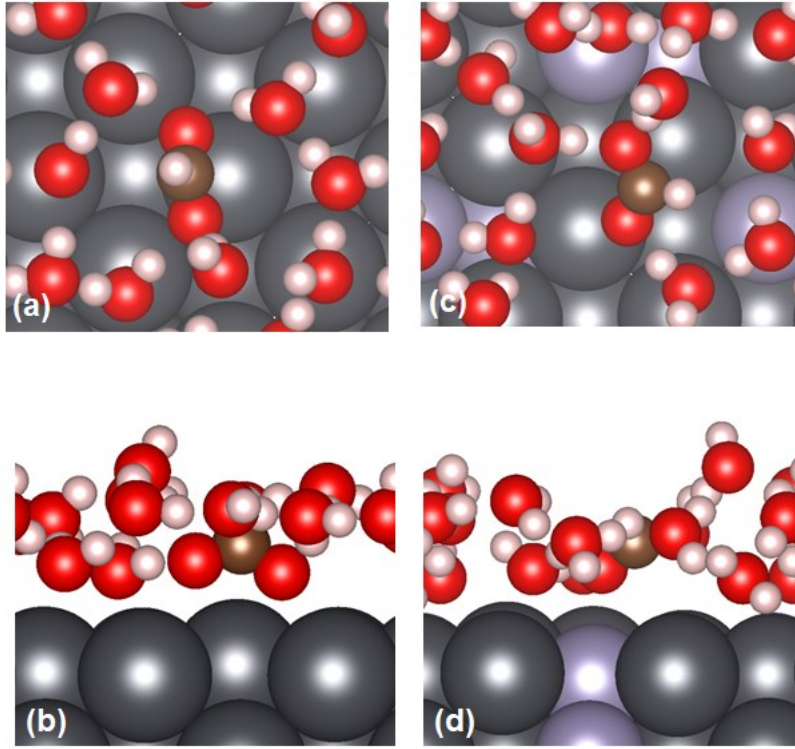


Figure 5.5 Optimized structures of HCOO* with 12 water molecules on (a and b) Pb(100) and (c and d) Sn₁Pb₃(100). Top view and side views are shown in (a and c) and (b and d), respectively.

5.3.4 Thermodynamic and kinetic analysis

In order to further rationalize experimental results, we employ a simple kinetic model to assess the selectivity with regards to reaction pathways (A) and (B) presented in the previous section. The rate equations for elementary steps involved in both pathways are given by,

$$v_1 = k_1[CO_2][H^+](1 - \theta_{COOH} - \theta_{HCOO}) - k_{-1}\theta_{COOH}, \quad (5.6)$$

$$v_2 = k_2\theta_{COOH}[H^+] - k_{-2}[CO](1 - \theta_{COOH} - \theta_{HCOO}), \quad (5.7)$$

$$v_3 = k_3[CO_2][H^+](1 - \theta_{COOH} - \theta_{HCOO}) - k_{-3}\theta_{HCOO}, \quad (5.8)$$

$$v_4 = k_4\theta_{HCOO}[H^+] - k_{-4}[HCOOH](1 - \theta_{COOH} - \theta_{HCOO}), \quad (5.9)$$

where θ_{COOH} and θ_{HCOO} are coverages of COOH* and HCOO* and $[CO_2]$, $[H^+]$, and $[HCOOH]$ are dimensionless concentrations. Rate constants of the forward and reverse reactions, k_i and k_{-i} , are calculated as a function of activation energy using transition state energy,

$$k_{\pm i} = k_i^0 \exp\left(-\frac{G_{a,\pm i}}{k_B T}\right), \quad (5.10)$$

with $k_i^0 = k_B T/h$, where k_B is the Boltzmann constant and h the Planck constant. The activation energy $G_{a,\pm i}$ can be calculated based on the Bronsted-Evans-Polanyi (BEP relation),

$$G_{a,i} = G_{a,i}^{eq} + \beta_i F(E - E_i^{eq}), \quad (5.11)$$

$$G_{a,-i} = G_{a,-i}^{eq} - (1 - \beta_i) F(E - E_i^{eq}), \quad (5.12)$$

where $G_{a,i}^{eq}$ and $G_{a,-i}^{eq}$ are activation energies of step i for forward and reverse reactions at equilibrium and β_i is the transfer coefficient. The equilibrium potential of step i , E_i^{eq} , can be calculated using the Nernst equation, and the results are listed in Table S5.5.

$$E_1^{eq} = -\frac{\Delta G_{COOH}^0 - \Delta G_{CO_2}^0}{e} = -0.15V, \quad (5.13)$$

$$E_2^{eq} = -\frac{\Delta G_{CO+H_2O}^0 - \Delta G_{COOH}^0}{e} = 0.15V, \quad (5.14)$$

$$E_3^{eq} = -\frac{\Delta G_{HCOO}^0 - \Delta G_{CO_2}^0}{e} = 1.2V, \quad (5.15)$$

$$E_4^{eq} = -\frac{\Delta G_{HCOOH}^0 - \Delta G_{COOH}^0}{e} = -0.99V, \quad (5.16)$$

Here, we can neglect the reverse reactions of step 1, 2 and 3 since E_1^{eq} , E_2^{eq} and E_3^{eq} are much higher than the potential range of interest ($< -1.1V$). Assuming that the adsorption of $COOH^*$ and $HCOO^*$ can be described by the Langmuir isotherm, the coverages of $COOH^*$ and $HCOO^*$ satisfy the following differential equations,

$$\frac{d\theta_{COOH}}{dt} = \nu_1 - \nu_2, \quad (5.17)$$

$$\frac{d\theta_{HCOO}}{dt} = \nu_3 - \nu_4. \quad (5.18)$$

By applying the steady-state approximation,

$$\frac{d\theta_{COOH}}{dt} = \frac{d\theta_{HCOO}}{dt} = 0 \quad (5.19)$$

the coverages of COOH* and HCOO* can be derived,

$$\theta_{COOH} = \frac{k_1 k_4 [CO_2][H^+]}{k_2 k_4 [H^+] + k_2 k_{-4} [HCOOH] + k_1 k_4 [CO_2][H^+] + k_2 k_3 [CO_2][H^+]}, \quad (5.20)$$

$$\theta_{HCOO} = \frac{k_2 k_{-4} [HCOOH] + k_2 k_3 [CO_2][H^+]}{k_2 k_4 [H^+] + k_2 k_{-4} [HCOOH] + k_1 k_4 [CO_2][H^+] + k_2 k_3 [CO_2][H^+]}. \quad (5.21)$$

The selectivity FE_{HCOO} can be calculated as,

$$FE_{HCOO} = \frac{\nu_4}{\nu_2 + \nu_4} = \frac{1}{1 + k_1/k_3}, \quad (5.22)$$

where

$$k_1/k_3 = \exp\left(-\frac{G_{a,1}^{eq} - G_{a,3}^{eq}}{k_B T}\right) \exp\left(-\frac{\beta_1(E - E_1^{eq}) - \beta_3(E - E_3^{eq})}{k_B T}\right). \quad (5.23)$$

Without loss of generality, we assume $\beta_1 = \beta_3 = 0.5$, resulting in,

$$\frac{k_1}{k_3} = \exp\left(\frac{G_{a,3}^{eq} - G_{a,1}^{eq}}{k_B T}\right) \exp\left(\frac{0.5(E_1^{eq} - E_3^{eq})}{k_B T}\right). \quad (5.24)$$

Results of DFT calculations reported in the previous section give $E_1^{eq} - E_3^{eq} = -1.35$ V on Sn₁Pb₃(100) and -1.74V on Pb(100). Assuming that differences in the first exponential factor on the right-hand side will be significantly smaller than the energy difference in the second exponential factor, we can conclude that k_1/k_3 will be equal to 0. This assumption should be scrutinized with further DFT studies (which are beyond the scope of the work reported here); we deem it reasonable since step 3 is exothermic and step 1 is endothermic and, therefore, $G_{a,3}^{eq} < G_{a,1}^{eq}$ follows from the BEP relation. The selectivity FE_{HCOO} , given in eq 5.22, will thus be very close to 100%, in agreement with experimental results discussed in Figure 5.3.

As discussed in Section 5.3.3, HCOO* is much more strongly adsorbed on Sn₁Pb₃(100) and Pb(100) than COOH*. Therefore, θ_{HCOO} is almost equal to 1 on both surfaces and the reaction rate of step 4, which represents the activity, can be simplified as,

$$v_4 = \frac{k_B T}{h} \exp\left(-\frac{G_{a,4}^{eq}}{k_B T}\right) \exp\left(-\frac{\beta_4 e(E - E_4^{eq})}{k_B T}\right) [H^+]. \quad (5.25)$$

The key parameter to differentiate the activity of CO₂ electroreduction on catalyst surfaces of different composition is the equilibrium potential, E_4^{eq} . With $E_4^{eq} = -0.99$ V on Sn₁Pb₃(100) and $E_4^{eq} = -1.33$ V on Pb(100), the overpotential driving the reaction is lower on Sn₁Pb₃(100). Therefore, the activity will be larger on Sn₁Pb₃(100) than on Pb(100), confirming experimental observations discussed in Section 5.3.2.

5.4 Conclusions

In summary, we have investigated the catalytic activity of dendritic Sn₁Pb₃ alloy for the electroreduction of CO₂ to formate and compare it to dendritic Pb. The concentration of Sn in the deposit was chosen to match the solubility limit of Sn in *fcc* Pb. The onset potential for the reduction of CO₂ to formate is -1.01 vs. SHE, 80 mV more positive than that on dendritic Pb. $FE_{formate}$ is very close to 100% over the potential range from -1.16 V to -1.56 vs SHE. The dendritic Sn₁Pb₃ alloy electrode exhibits an ERC current density of 17.2 mA cm_{geo}⁻² (295 μmol h⁻¹ cm⁻²) with $FE_{formate} = 92\%$ at 500 mV overpotential in a flow-cell system. DFT calculations suggest that the electroreduction of CO₂ on both Pb(100) and Sn₁Pb₃(100) surfaces proceeds through the HCOO* intermediate, leading to the exclusive formation of formic acid/formate.

The DFT studies also shows that the observed decrease of onset potential can only be understood if water layer is added in the slab model (as opposed to modelling under vacuum conditions). In these conditions (and only in these conditions), DFT calculations are able to predict the beneficial effect of adding Sn to the metal on the onset potential of lead. Indeed, the onset potentials for the formation of formate predicted by DFT calculations are -0.99 and -1.33 V vs. SHE for Sn₁Pb₃(100) and Pb(100) surfaces, which reproduce the trend seen in experimental values (-1.01 and -1.08 vs. SHE, respectively). On Sn₁Pb₃(100) surface, the HCOO* intermediate is less strongly adsorbed than on Pb(100), which reduces the onset potential. This reflects the Sabatier principle, which states that reaction intermediates should not adsorb too strongly at the surface of the electrode.

Our work emphasizes the fact that it is an absolute necessity to account for the effect of solvent molecules when calculating adsorption energies of reaction intermediates. This is even more critical in the present case since the effect of Sn on the adsorption energy of HCOO* intermediate is mediated through its interaction with the water layer.

Acknowledgements

This research was conducted as part of the Engineered Nickel Catalysts for Electrochemical Clean Energy project administered from Queen's University and supported by Grant No. RGPNM 477963-2015 under the Natural Sciences and Engineering Research Council of Canada (NSERC) Discovery Frontiers Program. The financial support of the NSERC Discovery program (RGPIN-2015-05821) is acknowledged also. One of us (M. F.) would also like to acknowledge the "Fonds Recherche du Québec - Nature et Technologies" (FRQNT) for a Graduate Research Fellowship.

5.5 Supporting Information

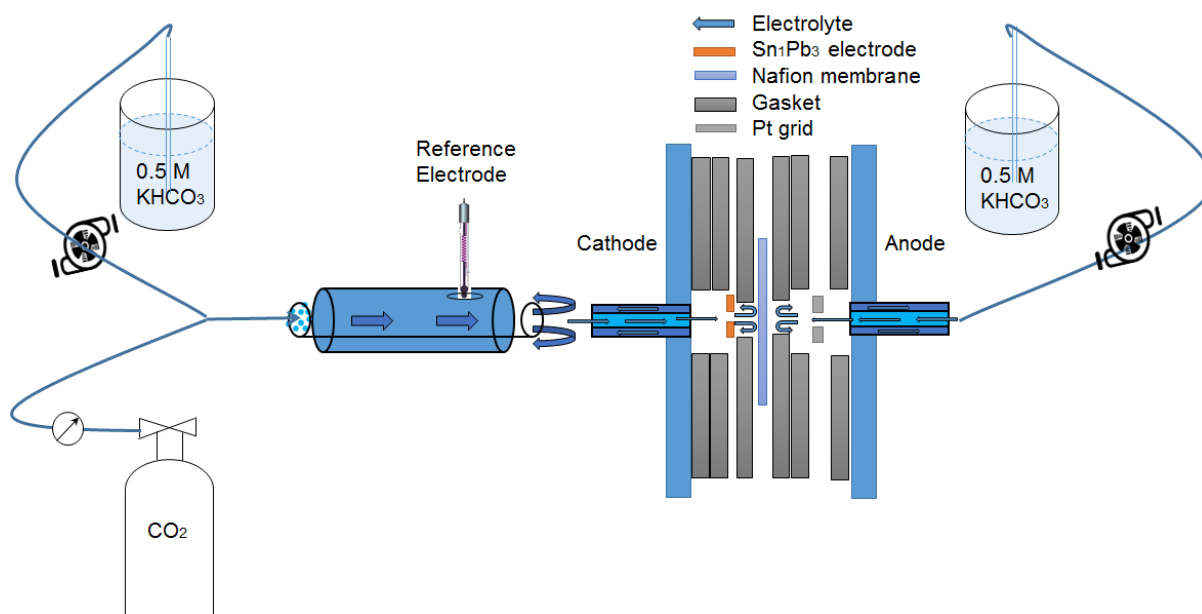


Figure S5.1 Schematic illustration of the flow cell system.

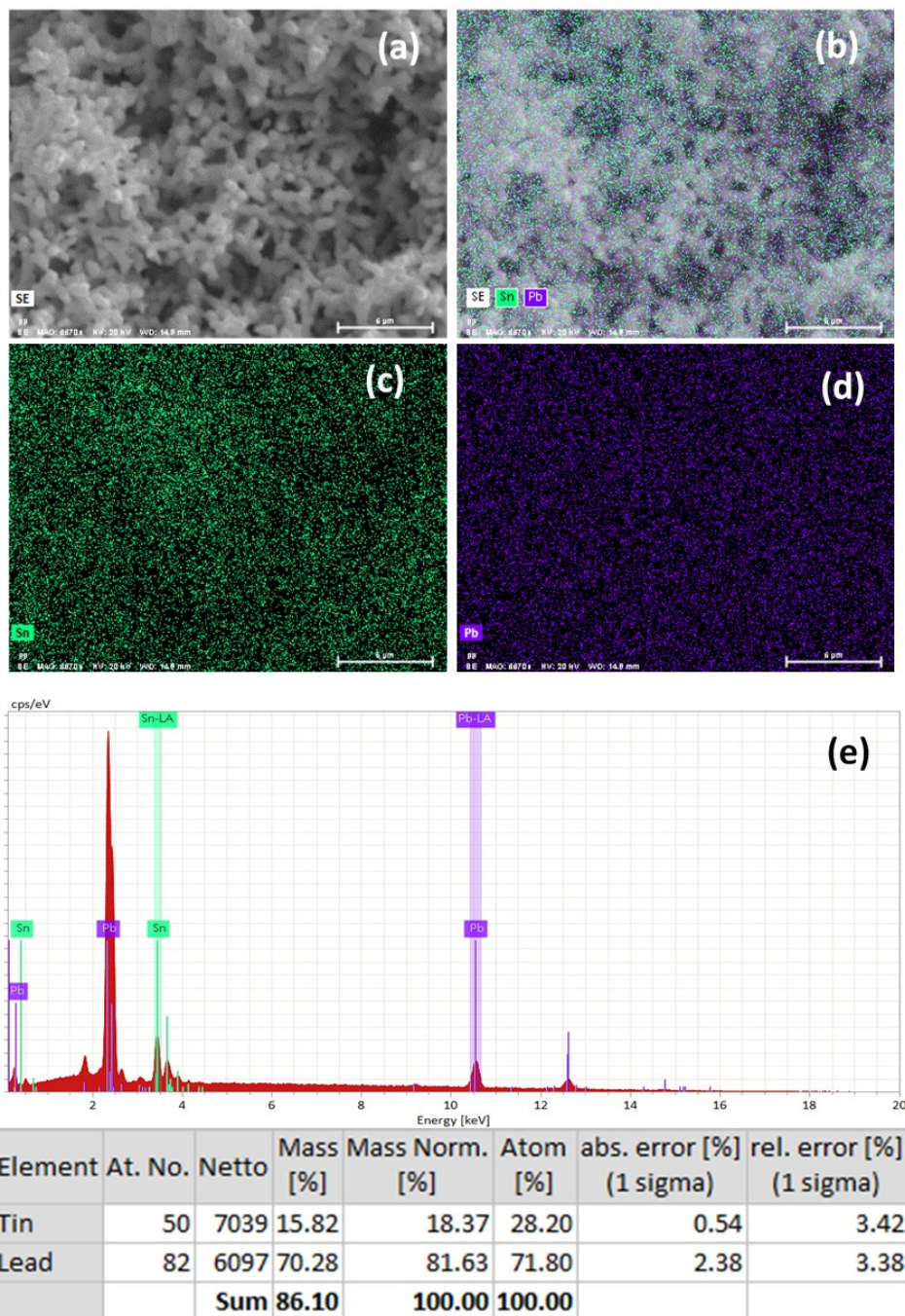


Figure S5.2 In (a-e), SEM and EDX mappings of dendritic Sn_1Pb_3 alloy. Pb: purple dots and lines. Sn: green dots and lines.

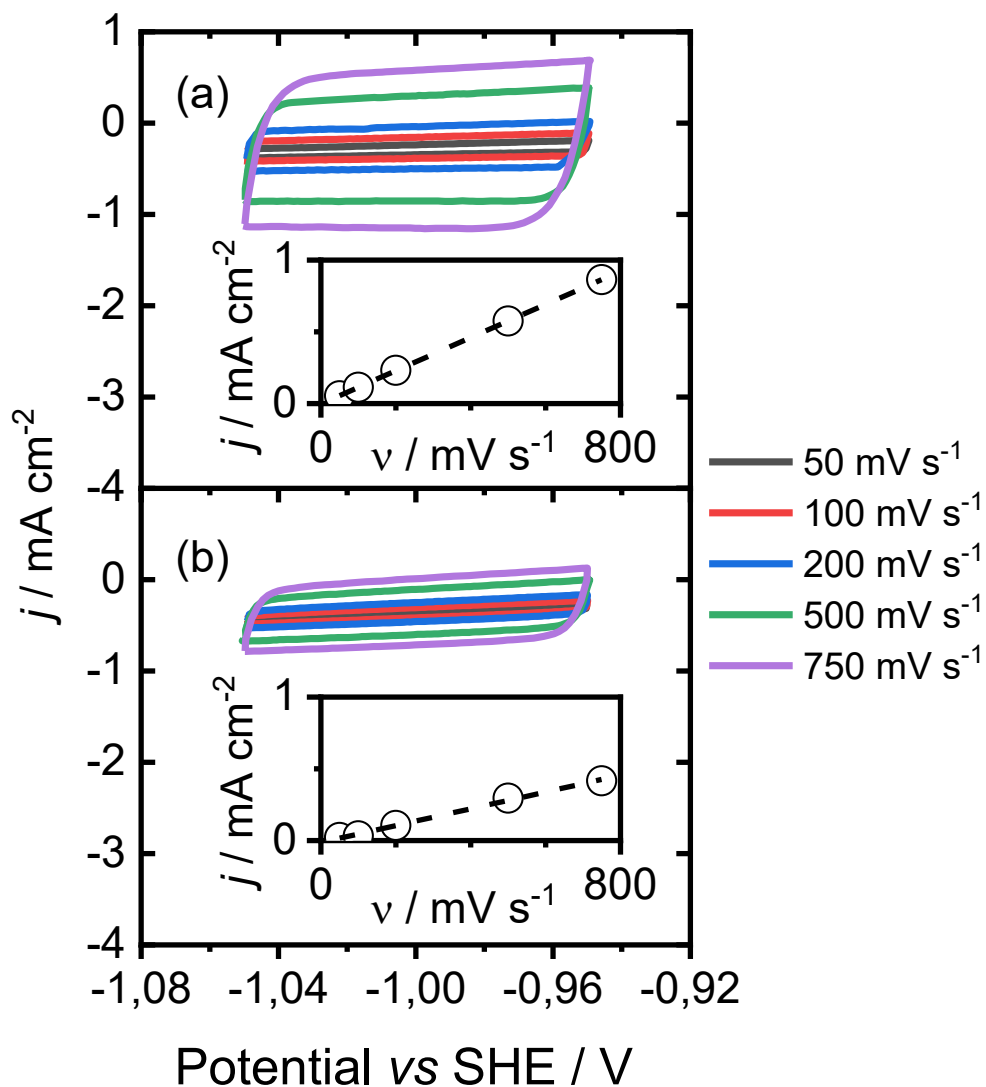


Figure S5.3 Double layer capacitance measurements of (a) dendritic Pb and (b) dendritic Sn_1Pb_3 alloy.

The LSV curves shown in Figure 5.3a were normalized by the electrochemical active surface area (EASA), which was determined from CVs measurements performed at different scan rates in Ar-saturated 0.5 M KHCO_3 . The double layer capacitance of dendritic Pb was $1150 \mu\text{F cm}^{-2}_{\text{geo}}$, and $585 \mu\text{F cm}^{-2}_{\text{geo}}$ for dendritic Sn_1Pb_3 alloy. The bare substrate was used reference (specific capacitance of $40 \mu\text{F cm}^{-2}_{\text{geo}}$). Therefore, the roughness factor of dendritic Pb and dendritic Sn_1Pb_3 alloy was 28.8 and 14.6 respectively.

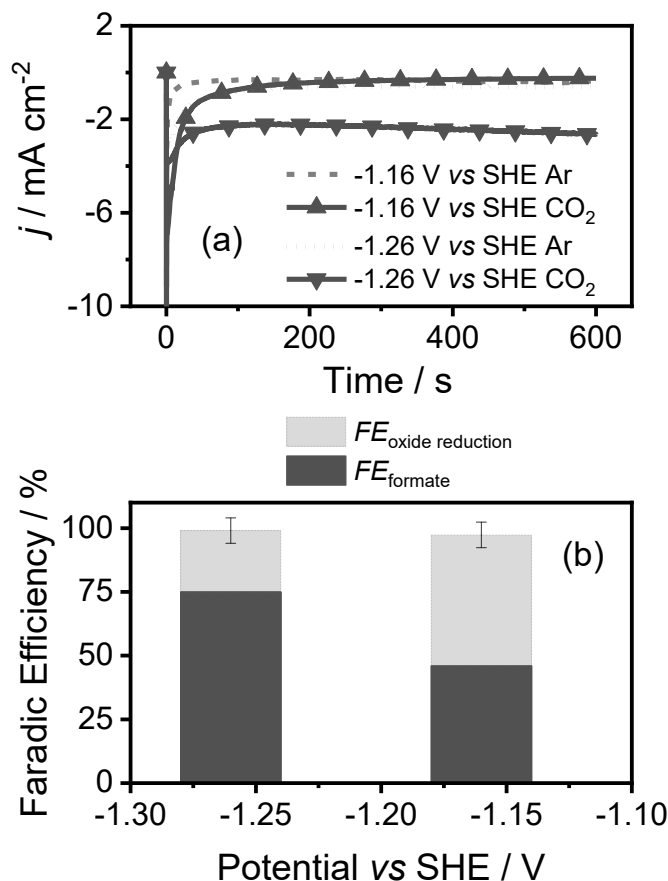


Figure S5.4 In (a), chronopotentiostatic curves of dendritic Pb electrode recorded in Ar-saturated 0.5 M KHCO_3 . In (b), Faradaic Efficiency as function of electrode potential.

The electrolysis of both dendritic Sn_1Pb_3 alloy and dendritic Pb were conducted in CO_2 -saturated 0.5 M KHCO_3 electrolyte and the electrolysis currents are shown in Figure S5.4a. As shown in Figure S5.4b, the FE_{formate} of dendritic Pb is 46% at -1.16 V and 74% at -1.26 V vs. SHE. At these potentials, H_2 and CO were not detected (the FE for these products is zero).

To figure out why the total FE of dendritic Pb is different from 100% even if only formate is detected, we carried out potentiostatic electrolyses in Ar-saturated 0.5 M KHCO_3 electrolyte (Figure S5.4a). In the Ar-saturated electrolyte, no products (formate, H_2 and CO) were detected even if a significant charge is passed through the system. At -1.16 and -1.26 V vs. SHE, the total charge in the Ar-saturated electrolyte, Q_{Ar} , accounts for 51% and 24% of the total charge recorded for dendritic Pb in the CO_2 -saturated electrolyte, respectively. This charge is associated with the reduction of lead oxide present at the surface of dendritic Pb. As shown in Figure S5.4b, the sum of the faradaic efficiency for the reduction of lead oxide and FE_{formate} adds up to a value very close to 100%.

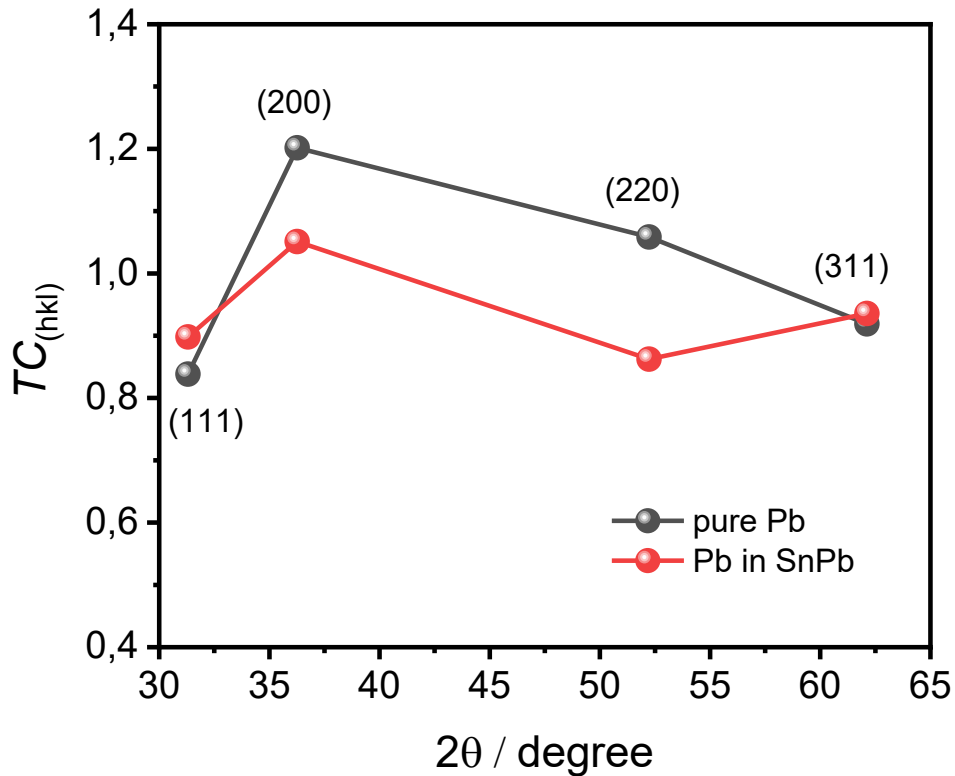


Figure S5.5 Texture coefficient, $TC_{(hkl)}$, analysis of the dendritic deposits. This analysis was performed using the XRD patterns shown in Figure 5.2.

The value of the texture coefficient ($TC_{(hkl)}$) was calculated by the inverse pole intensity technique using the following equation:

$$TC_{(hkl)} = \frac{I_{(hkl)}/I_{R(hkl)}}{\frac{1}{n} \sum_i^n (I_{(hkl)}/I_{R(hkl)})}$$

where $I_{(hkl)}$ is the reflected intensity from (hkl) diffracted planes of Pb and Sn_1Pb_3 , $I_{R(hkl)}$ is the intensity from (hkl) planes of polycrystalline Pb and Sn_1Pb_3 , and n is the total number of measured planes. $TC_{(hkl)}$ is proportional to the number of grains orientated with this facet. $TC_{(hkl)} > 1$ denotes that the sample has more crystallites with (hkl) facets than polycrystalline Pb and Sn_1Pb_3 , whereas $TC_{(hkl)} < 1$ suggests the synthesized sample has less crystallites in that (hkl) direction than polycrystalline Pb and Sn_1Pb_3 . It was hypothesized that the relative intensity of the XRD peaks of polycrystalline *fcc* Sn_1Pb_3 are identical to that of polycrystalline *fcc* Pb.

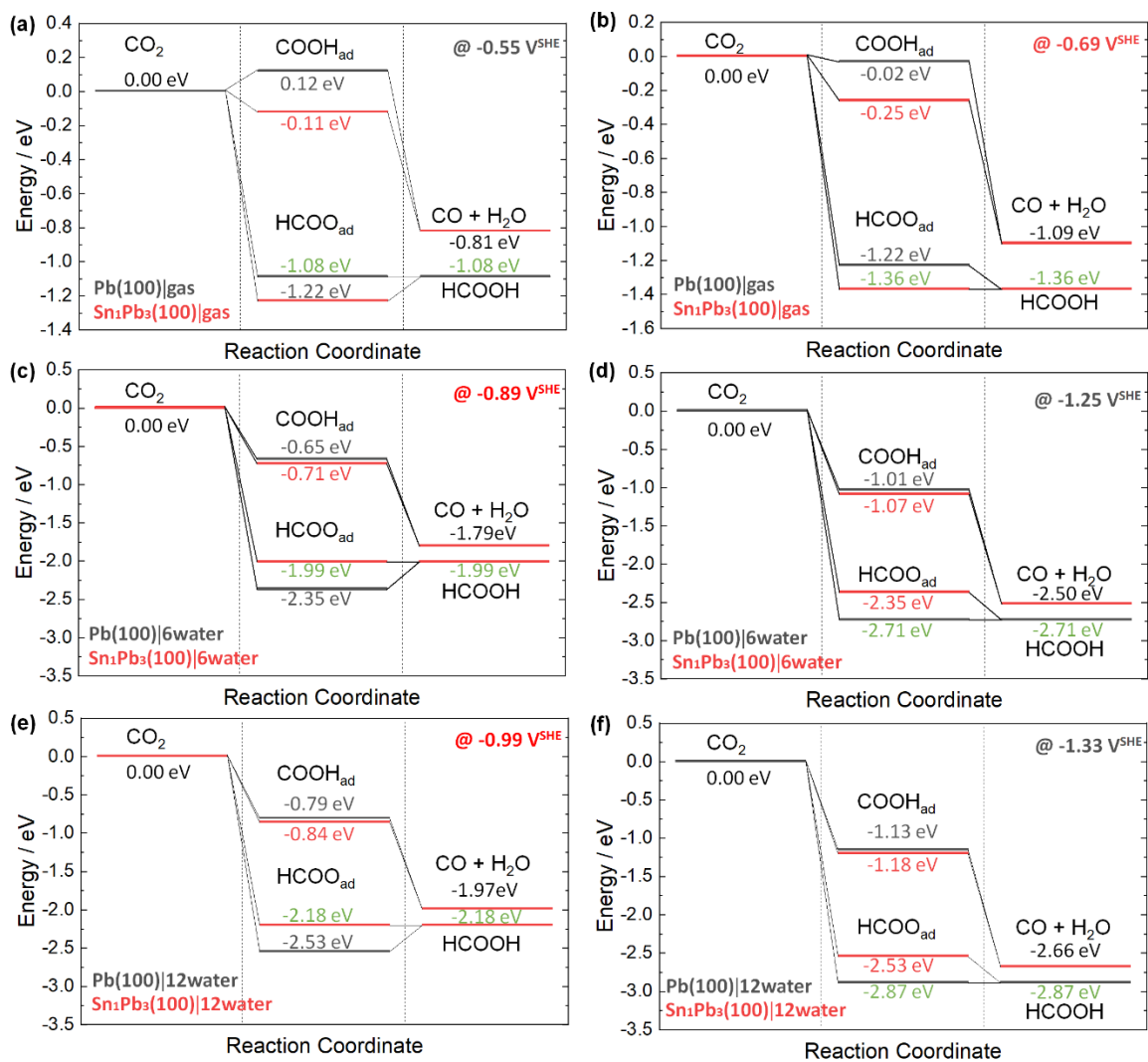


Figure S5.6 Energy diagrams for CO₂ reduction. In (a), gas phase conditions at -0.55 V. In (b), gas phase conditions at -0.69 V. In (c), with 6 water molecules at -0.89 V. In (d), with 6 water molecules at -1.25 V. In (e), with 12 water molecules at -0.99 V. In (f), with 12 water molecules at -1.33 V. The black curves stand for Pb(100) surface, while the red curve stands for Sn₁Pb₃(100).

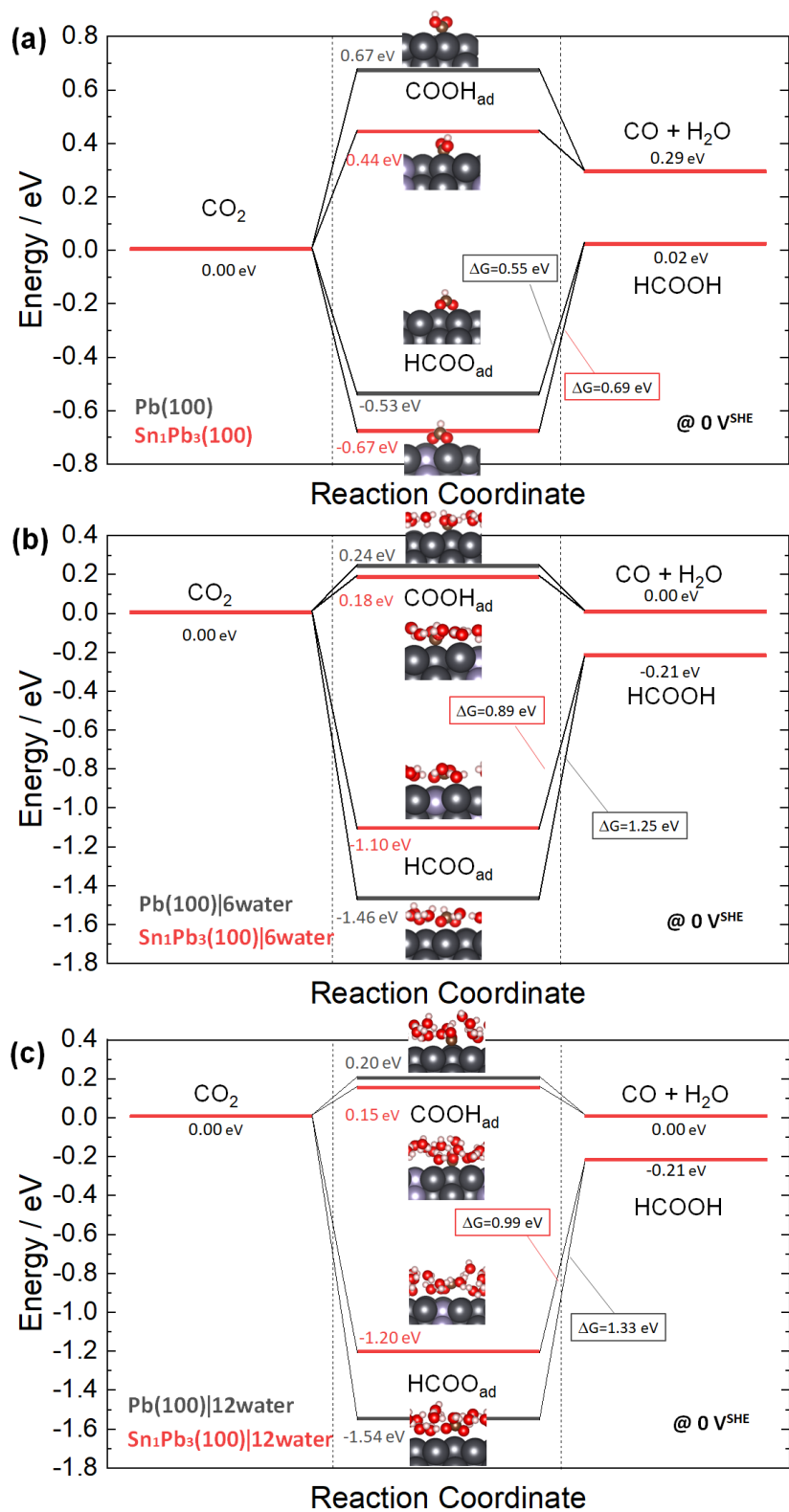


Figure S5.7 Energy diagrams for CO₂ reduction. In (a), gas phase conditions at 0 V. In (b), with 6 water molecules at 0 V. In (c), with 12 water molecules at 0 V.

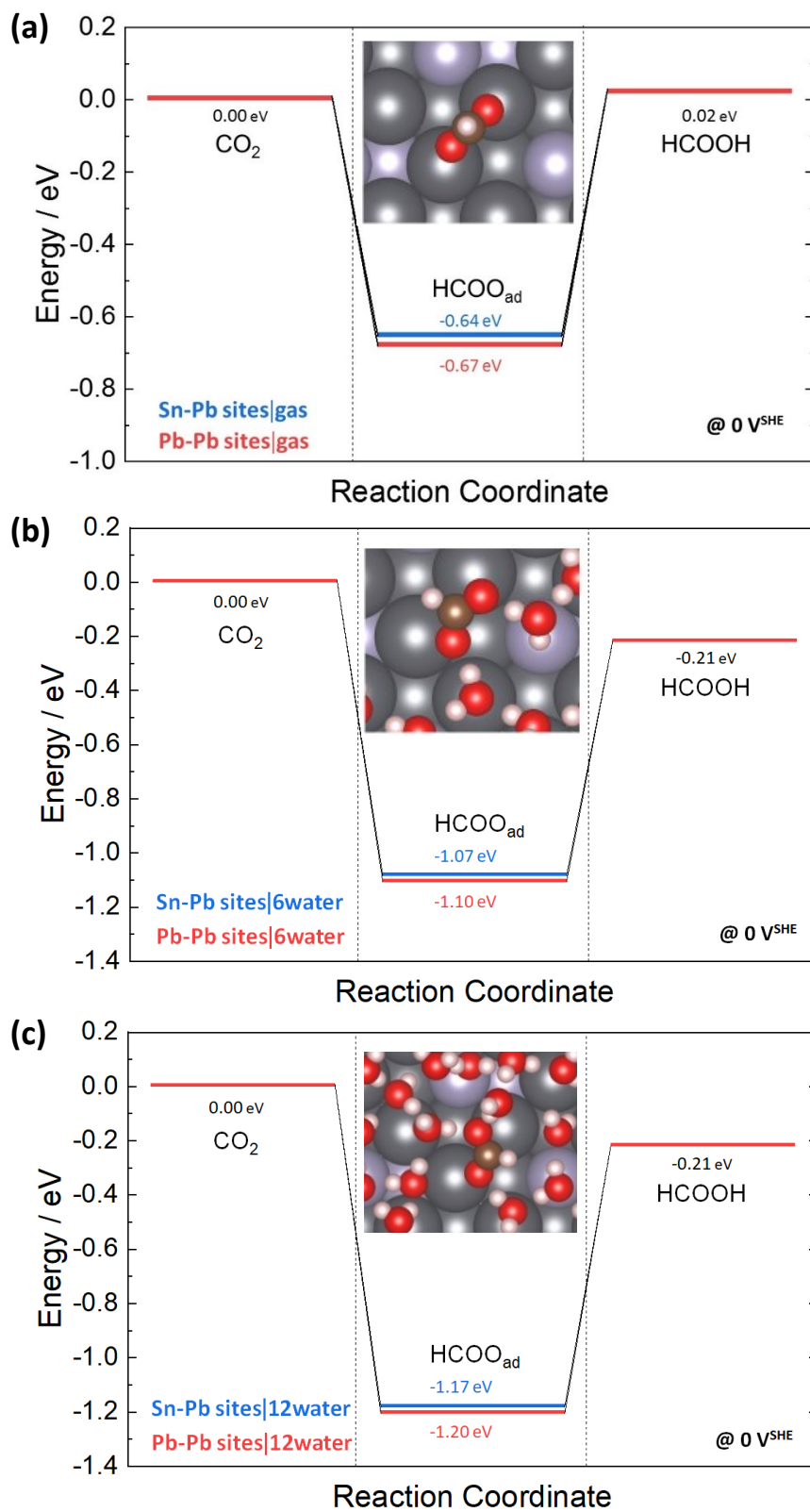


Figure S5.8 Binding Energy of HCOO* adsorbed at different adsorption sites on Sn₁Pb₃(100) surface. In (a), gas phase conditions. In (b), with 6 water molecules. In (c), with 12 water molecules. The blue curves stand for adsorbed HCOO* at Sn-Pb sites, while the red curve stands for HCOO* adsorbed on Pb-Pb sites.

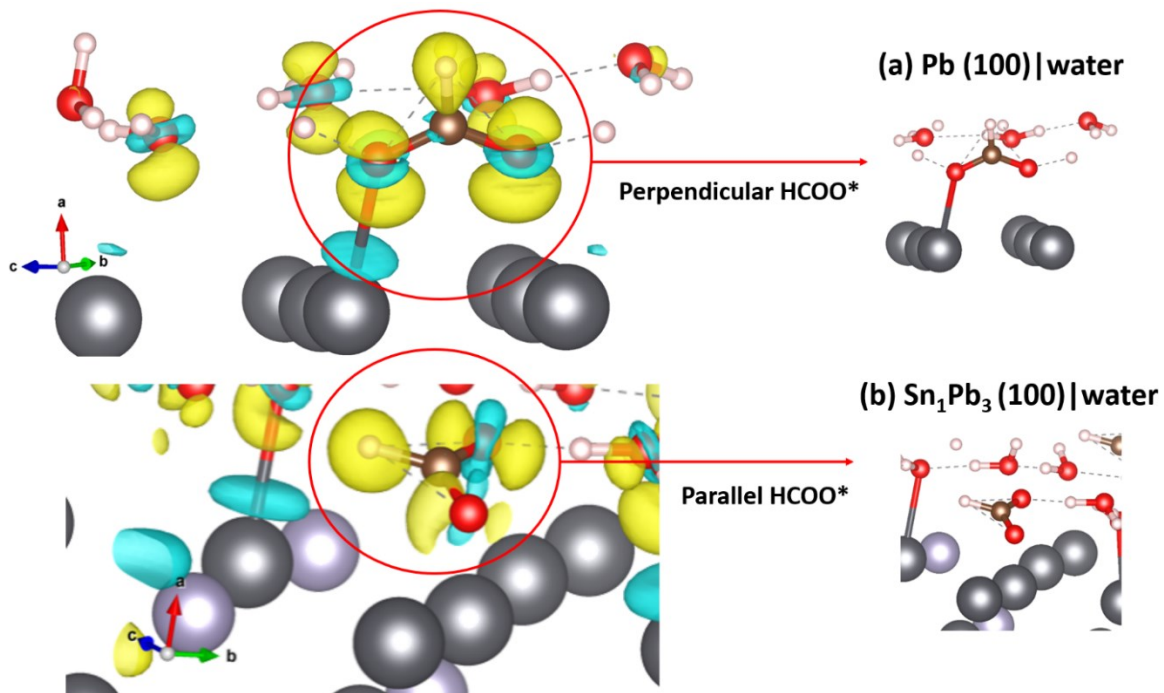


Figure S5.9 3D charge density difference along with the most stable configurations of HCOO* in the presence of 12 water molecules on (a) Pb(100) and (b) Sn₁Pb₃(100). For clarity, only a restricted number of water molecules are shown around HCOO*.

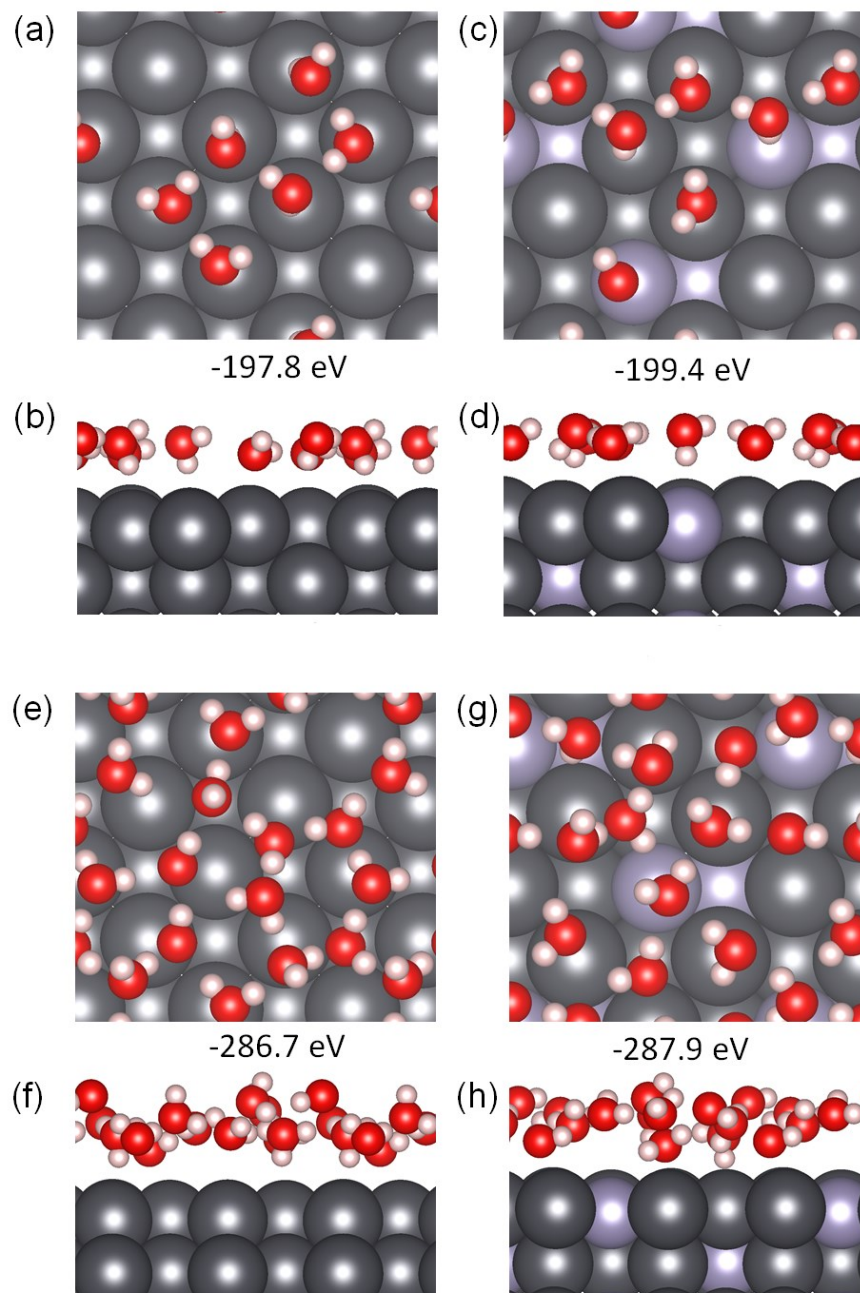


Figure S5.10 Optimized structures adopted by 6 water molecules when in contact with (a, b) Pb(100), and (c, d) Sn₁Pb₃(100) surfaces. Optimized structures adopted by 12 water molecules when in contact with (e, f) Pb(100), and (g, h) Sn₁Pb₃(100) surfaces.

Optimized structures of 6 and 12 water molecules in the absence of any other adsorbates. The binding energy of the 12 water molecules on Pb(100) and Sn₁Pb₃(100) surfaces is $\Delta E = -286.7$ eV and -287.9 eV, respectively.

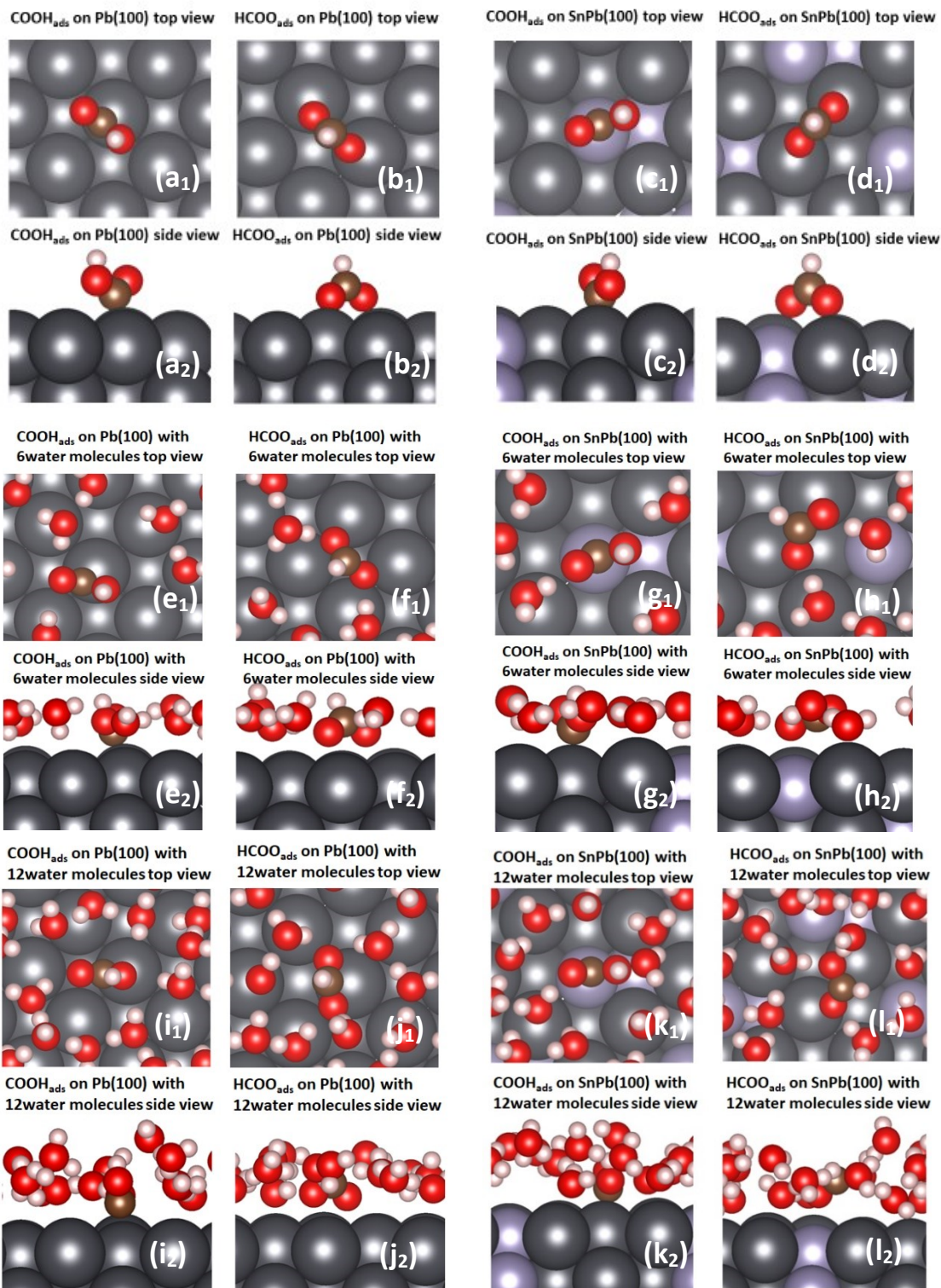


Figure S5.11 Optimized structures in gas phase condition: (a₁₋₂) COOH* on Pb(100), (b₁₋₂) HCOO* on Pb(100), (c₁₋₂) COOH* on Sn₁Pb₃(100) and (d₁₋₂) HCOO* on Sn₁Pb₃(100). Optimized structures with 6 water molecules: (e₁₋₂) COOH* on Pb(100), (f₁₋₂) HCOO* on Pb(100), (g₁₋₂) COOH* on Sn₁Pb₃(100), and (h₁₋₂) HCOO* on Sn₁Pb₃(100). Optimized structures with 12 water molecules: (i₁₋₂) COOH* on Pb(100), (j₁₋₂) HCOO* on Pb(100), (k₁₋₂) COOH* on Sn₁Pb₃(100), and (l₁₋₂) HCOO* on Sn₁Pb₃(100).

Table S5.1 Onset potential vs SHE of different electrodes.

Electrodes	CO ₂ -saturated 0.5 M KHCO ₃	Ar-saturated 0.5 M KHCO ₃
Dendritic Pb	-1.09	-1.5
Dendritic Sn ₁ Pb ₃ alloy	-1.01	-1.33

Table S5.2 Comparison of the performance of CO₂ electroreduction towards formate on Pb based materials.

Catalysts	Electrolyte	FE _{formate}	Overpotential / V	<i>J</i> / mA cm ⁻²	Reference
Pb-granule	0.2 M K ₂ CO ₃	94%	0.9	0.41	247
Oxide derived Pb	0.5 M NaHCO ₃	97%	0.8	1	81
Pb	1 M KHCO ₃	97%	0.8	7.5	141
Amine modified Pb	1 M KHCO ₃	97%	0.9	6	90
Dendritic Sn₁Pb₃ alloy	0.5 M KHCO₃	92%	0.5	17.4	This work

Table S5.3 Thermodynamic quantities of gas-phase molecules (eV). The adsorption energy, zero-point energy (ZPE), and entropy (TS).

	E _{ad} (eV)	ZPE (eV)	TS (eV)
CO ₂	-23.15	0.31	0.1
H ₂ O	-14.25	0.56	0.1
CO	-15.22	0.13	0.09
H ₂	-6.72	0.27	0.09
HCOOH	-30.02	0.89	0.11

The energy of CO₂, CO, and HCOOH was corrected by calculated values of -0.10 eV, -0.29 eV, and -0.23 eV respectively, owing to solvent stabilization. ZPE and TS were taken from an earlier report by Klinkona *et al.*³⁸

Table S5.4 Comparison of the binding energies of HCOO* in parallel and perpendicular configurations at Pb(100) and Sn₁Pb₃(100) surface. Twelve water molecules were included in the DFT calculations in all cases.

Surface	HCOO* configuration	Binding Energy
Pb(100)	Perpendicular	-1.54 eV
Pb(100)	Parallel	-1.24 eV
Sn ₁ Pb ₃ (100)	Perpendicular	-0.75 eV
Sn ₁ Pb ₃ (100)	Parallel	-1.20 eV

Table S5.5 The equilibrium potential of step i , E_i^{eq} , on Sn₁Pb₃(100) and Pb(100), calculated using DFT results from Section 5.3.3.

Step i	Sn ₁ Pb ₃ (100)	Pb(100)
1	-0.15 V	-0.2 V
2	0.15 V	0.2 V
3	1.2 V	1.54 V
4	-0.99V	-1.33 V

6 CONCLUSIONS AND PERSPECTIVES

6.1 Conclusions

Post-transition metals have attracted researchers' interest due to their low price and high formate selectivity for CO_2 electrochemical reduction. However, for these post-transition elements, high selectivity is accompanied by high CO_2 pressure-demand and high overpotential when high current density (high production rate) is obtained. Therefore, development of highly active post-transition catalysts, which can work well in ambient pressure, temperature and aqueous electrolyte, and achieve low overpotential and large reduction current at the same time, is urgently needed. In this thesis, three kinds of dendritic post-transition metal catalysts, which were highly active and formate selective for CO_2 electrochemical reduction, were designed and synthesized. The specific conclusions are as follows.

In Chapter 3, high surface area porous Pb electrodes were prepared through the simple, rapid dynamic hydrogen bubbling template (DHBT) technique. The resulting porous Pb electrodes were characterized by a honeycomb primary structure and dendrite secondary structure growing along the [100]-axis. The dendritic structure was made of elongated single crystals with a near-constant length of ca. 200 nm and a tip diameter of 22 nm. CO_2 electroreduction carried out on these electrodes showed Faradic efficiencies for formate above 90% for electrochemical surface areas greater than 500 cm^2 , achieving as much as 97% at -0.99 V vs. RHE with a current density of -7.5 mA cm^{-2} . Additionally, the porous Pb electrodes demonstrated remarkable stability in terms of both current density and formate Faradic efficiency, with constant values of ca. 8 mA cm^{-2} and 98%, respectively, over prolonged electrolysis for 6 hours. The porous Pb electrodes' enhanced performance was attributed to the secondary dendrite structure, which might help concentrate the reactants in the boundary layer.

In Chapter 4, a dendritic Bi electrode with a high number of defects and high-index facets was synthesized on a porous Pb substrate. The most active Bi sites were identified through a detailed atomic scale analysis of the dendrite surface, and masking of the low-index inactive sites. It was shown that Bi dendrite defects and high-index facets are the most active sites where the reduction of CO_2 to formate occurred. Dendritic Bi is highly selective for CO_2 electroreduction to formate, with a 98% Faradaic efficiency and a current density of 18.8 mA cm^{-2} ($344 \mu\text{mol cm}^{-2} \text{ hr}^{-1}$) at -0.82 V vs. RHE , only 600 mV more negative than the thermodynamic potential. Both the dendritic structure and CO_2 electrolysis performances were remarkably stable over the longest electrolysis period (15 hours) conducted. Additionally, we achieved a much higher production rate (1.63 mmol

cm⁻² hr⁻¹ or 95 mA cm⁻² at -0.82 V vs. RHE) without significant penalty on the formate Faradaic efficiency (92% ± 4%) with the same electrode operated in conditions where the CO₂ flux was not limiting performance (high-pressure flow-cell measurements).

This work presents a simple method to design and fabricate materials in dendritic form with excellent performance for ERC. It also provides atomic scale insights into the nature of the active sites at the dendrites' surface. Finally, it illustrates that dendritic electrode materials are able to withstand very high current density, and thus achieve a very high production rate if the CO₂ supply to the electrode is not limiting.

In Chapter 5, Pb was alloyed with Sn to synthesize dendritic SnPb alloy electrode. We investigated the catalytic activity of dendritic Sn₁Pb₃ alloy for CO₂ electroreduction to formate and compared it to dendritic Pb. The Sn concentration in the deposit was chosen to match the solubility limit of Sn in *fcc* Pb. The onset potential for CO₂ reduction to formate was -1.01 V vs SHE (-0.57 V vs. RHE), 80 mV more positive than that of dendritic Pb. FE_{formate} was very close to 100% over the potential range from -1.16 to -1.56 V vs SHE (-0.72 to -1.12 V vs. RHE). The dendritic Sn₁Pb₃ alloy electrode exhibited an ERC current density of 17.2 mA cm_{geo}⁻² (295 μmol h⁻¹ cm⁻²) with $FE_{\text{formate}} = 92\%$ at 500 mV overpotential in a flow-cell system. DFT calculations suggest CO₂ electroreduction on both Pb(100) and Sn₁Pb₃(100) surfaces proceeds through the HCOO* intermediate, leading to the exclusive formation of formic acid/formate. DFT studies also showed that the observed decrease in onset potential can only be understood if a water layer simulating the electrolyte is introduced in the modelling domain for DFT (as opposed to modelling under vacuum conditions). In these conditions (and only in these conditions), DFT calculations can predict the beneficial effect of dissolved Sn on the onset potential of lead. Indeed, the onset potentials for formate formation predicted by the DFT calculations are -0.99 and -1.33 V vs. SHE for Sn₁Pb₃(100) and Pb(100) surfaces, respectively, in reasonable agreement (considering the simplified computational model) with the experimentally-measured values of -1.01 and -1.08 V vs. SHE, respectively. On Sn₁Pb₃(100) surfaces, the HCOO* intermediate is more weakly adsorbed than on Pb(100), which reduces the onset potential. This is a vivid illustration of the Sabatier principle, which states that reaction intermediates should not adsorb too strongly at the electrode surface.

6.2 Perspectives

We have tried different strategies to enhance the activity and production rate of electrochemical reduction of CO₂. The advantages of dendritic materials have been used to enhance the ERC performance. However, challenges and opportunities for the dendritic catalyst field and the CO₂ electrochemical reduction research area remain. Significant efforts are still required to further develop these research areas. Challenges and perspectives are shown as follows:

(1) For the dendritic materials research area, the targeting growth of high-index facets should be controlled. In most current research, the high-index facets of the dendritic catalysts show higher density than the non-dendritic material; however, the high-index facets are still not predominant. Thus, enhancing the density of high-index facets or targeting synthesis of high-index dendrites must be investigated.

(2) Further, a mechanism for improving catalytic activity of CO₂ electrochemical reduction at dendritic catalysts has been proposed by many researchers, through computational simulations. Moving forward, it would be interesting to combine *in situ* spectra techniques with computational simulations to confirm these active sites, and better understand the mechanism of CO₂ electrochemical reduction on dendritic material.

(3) For the CO₂ electrochemical reduction field, continued efforts are required to improve the reaction energy efficiency and decrease the operating overpotential to reduce the costs associated with energy requirements. Along these lines, efforts need to be devoted to improving the activity of catalysts to push it working at a lower overpotential with good selectivity and high reduction current. Precious metals, which can work at a lower ERC overpotential, can be adopted to decorate or modify the non-noble materials to reduce the ERC applied potential and enhance the energy efficiency.

(4) Further, limited by the CO₂ mass transfer in the electrochemical cells, the ERC reduction current is hard to meet the requirement for the realistic industrial applications. The electrolyzers, such as flow cell reactors, need to be developed and improved. The membrane electrode assembly (MEA) for the highly efficient and stable CO₂ electrochemical reduction used in the electrolyzers needs to be fabricated and optimized.

BIBLIOGRAPHY

1. Anthony Adegbulugbe, Øyvind Christophersen, Hisashi Ishitani, William Moomaw, Moreira J (2005) *IPCC Special Report on Carbon Dioxide Capture and Storage*. Cambridge University, United Kingdom.
2. Masson-Delmotte V, P. Zhai H-OP, D. Roberts, J. Skea, P.R. Shukla, A. Pirani, W. Moufouma-Okia, C. Péan RP, S. Connors, J.B.R. Matthews, Y. Chen, X. Zhou, M.I. Gomis, E. Lonnoy, T. Maycock, M. Tignor, Waterfield T (2018) *Global Warming of 1.5°C*. IPCC, Switzerland.
3. Nitopi S, Bertheussen E, Scott SB, Liu X, Engstfeld AK, Horch S, Seger B, Stephens IEL, Chan K, Hahn C, Norskov JK, Jaramillo TF, Chorkendorff I (2019) Progress and Perspectives of Electrochemical CO₂ Reduction on Copper in Aqueous Electrolyte. *Chem. Rev.* 119(12):7610–7672.
4. CCS (2018) *The Global Status Report*. Global CCS Institute, Australia.
5. Pires JCM, Martins FG, Alvim-Ferraz MCM, Simões M (2011) Recent Developments on Carbon Capture and Storage: An Overview. *Chem. Eng. Res. Des.* 89(9):1446-1460.
6. Hsien H. Khoo, Tan RBH (2006) Life Cycle Investigation of CO₂ Recovery and Sequestration. *Environ. Sci. Technol.* 40(12):4016-4024.
7. Celia MA, Nordbotten JM (2009) Practical Modeling Approaches for Geological Storage of Carbon Dioxide. *Ground Water* 47(5):627-638.
8. Stevens JG, Gómez P, Bourne RA, Drage TC, George MW, Poliakoff M (2011) Could the Energy Cost of Using Supercritical Fluids be Mitigated by Using CO₂ From Carbon Capture and Storage (CCS)? *Green Chem.* 13(10):2727-2733.
9. Daniel J. Allen, Brent GF (2010) Sequestering CO₂ by Mineral Carbonation: Stability Against Acid Rain Exposure. *Environ. Sci. Technol.* 44(7):2735–2739.
10. Baldyga J, Henczka M, Sokolnicka K (2011) Mineral Carbonation Accelerated by Dicarboxylic Acids as a Disposal Process of Carbon Dioxide. *Chem. Eng. Res. Des.* 89(9):1841-1854.
11. Appel AM, Bercaw JE, Bocarsly AB, Dobbek H, DuBois DL, Dupuis M, Ferry JG, Fujita E, Hille R, Kenis PJ, Kerfeld CA, Morris RH, Peden CH, Portis AR, Ragsdale SW, Rauchfuss TB, Reek JN, Seefeldt LC, Thauer RK, Waldrop GL (2013) Frontiers, Opportunities, and Challenges in Biochemical and Chemical Catalysis of CO₂ Fixation. *Chem. Rev.* 113(8):6621-6658.
12. Sousa FL, Preiner M, Martin WF (2018) Native Metals, Electron Bifurcation, and CO₂ Reduction in Early Biochemical Evolution. *Curr. Opin. Microbiol.* 43:77-83.
13. White JL, Baruch MF, Pander Iii JE, Hu Y, Fortmeyer IC, Park JE, Zhang T, Liao K, Gu J, Yan Y, Shaw TW, Abelev E, Bocarsly AB (2015) Light-Driven Heterogeneous Reduction of Carbon Dioxide: Photocatalysts and Photoelectrodes. *Chem. Rev.* 115(23):12888-12935.
14. Windle CD, Perutz RN (2012) Advances in Molecular Photocatalytic and Electrocatalytic CO₂ Reduction. *Coordin. Chem. Rev.* 256(21-22):2562-2570.
15. Low J, Cheng B, Yu J (2017) Surface Modification and Enhanced Photocatalytic CO₂ Reduction Performance of TiO₂: A Review. *Appl. Surf. Sci.* 392:658-686.

16. Ola O, Maroto-Valer MM (2015) Review of Material Design and Reactor Engineering on TiO₂ Photocatalysis for CO₂ Reduction. *J. Photoch. Photobio. C* 24:16-42.
17. Liu L, Li Y (2014) Understanding the Reaction Mechanism of Photocatalytic Reduction of CO₂ with H₂O on TiO₂-Based Photocatalysts: A Review. *Aerosol Air Qual. Res.* 14(2):453-469.
18. Li K, An X, Park KH, Khraisheh M, Tang J (2014) A Critical Review of CO₂ Photoconversion: Catalysts and Reactors. *Catal. Today* 224:3-12.
19. Khalil M, Gunlazuardi J, Ivandini TA, Umar A (2019) Photocatalytic Conversion of CO₂ using Earth-Abundant Catalysts: A Review on Mechanism and Catalytic Performance. *Renew. Sust. Energ. Rev.* 113:109246.
20. Costentin C, Robert M, Saveant JM (2013) Catalysis of the Electrochemical Reduction of Carbon Dioxide. *Chem. Soc. Rev.* 42(6):2423-2436.
21. Benson EE, Kubiak CP, Sathrum AJ, Smieja JM (2009) Electrocatalytic and Homogeneous Approaches to Conversion of CO₂ to Liquid Fuels. *Chem. Soc. Rev.* 38(1):89-99.
22. Lim RJ, Xie M, Sk MA, Lee J-M, Fisher A, Wang X, Lim KH (2014) A Review on the Electrochemical Reduction of CO₂ in Fuel Cells, Metal Electrodes and Molecular Catalysts. *Catal. Today* 233:169-180.
23. Long C, Li X, Guo J, Shi Y, Liu S, Tang Z (2018) Electrochemical Reduction of CO₂ over Heterogeneous Catalysts in Aqueous Solution: Recent Progress and Perspectives. *Small Methods* 3(3):1800369.
24. Kondratenko EV, Mul G, Baltrusaitis J, Larrazábal GO, Pérez-Ramírez J (2013) Status and Perspectives of CO₂ Conversion into Fuels and Chemicals by Catalytic, Photocatalytic and Electrocatalytic Processes. *Energy Environ. Sci.* 6(11):3112-3135.
25. Zhang W, Hu Y, Ma L, Zhu G, Wang Y, Xue X, Chen R, Yang S, Jin Z (2018) Progress and Perspective of Electrocatalytic CO₂ Reduction for Renewable Carbonaceous Fuels and Chemicals. *Adv. Sci.* 5(1):1700275.
26. Qiao J, Liu Y, Hong F, Zhang J (2014) A Review of Catalysts for the Electroreduction of Carbon Dioxide to Produce Low-carbon Fuels. *Chem. Soc. Rev.* 43(2):631-675.
27. Oloman C, Li H (2008) Electrochemical Processing of Carbon Dioxide. *ChemSusChem* 1(5):385-391.
28. Qiao J, Liu Y, Zhang J (2016) *Electrochemical Reduction of Carbon Dioxide: Fundamentals and Technologies*. CRC Press, United States.
29. Schneider J, Jia H, Muckerman JT, Fujita E (2012) Thermodynamics and Kinetics of CO₂, CO, and H⁺ Binding to the Metal Centre of CO₂ Reduction Catalysts. *Chem. Soc. Rev.* 41(6):2036-2051.
30. Sun Z, Ma T, Tao H, Fan Q, Han B (2017) Fundamentals and Challenges of Electrochemical CO₂ Reduction Using Two-Dimensional Materials. *Chem* 3(4):560-587.
31. Sun D, Chen Y (2016) *Electrochemical Reduction of Carbon Dioxide: Fundamentals and Technologies*, CRC Press, United States.
32. Martín AJ, Larrazábal GO, Pérez-Ramírez J (2015) Towards Sustainable Fuels and Chemicals Through the Electrochemical Reduction of CO₂: Lessons from Water Electrolysis. *Green Chem.* 17(12):5114-5130.

33. Jouny M, Luc W, Jiao F (2018) General Techno-Economic Analysis of CO₂ Electrolysis Systems. *Ind. Eng. Chem. Res.* 57(6):2165-2177.
34. Yoshio Hori, Katsuhei Kikuchi, Suzuki S (1985) Production of CO and CH₄ in electrochemical reduction of CO₂ at metal electrodes in aqueous hydrogencarbonate solution. *Chem. Lett.* 11(11):1695-1698.
35. Masashi Azuma, Kazuhito Hashimoto, Hiramoto M (1990) Electrochemical Reduction of Carbon Dioxide on Various Metal Electrodes in Low-Temperature Aqueous KHCO₃ Media. *J. Electrochem. Soc.* 137(6):1772-1778.
36. Gong J, Zhang L, Zhao ZJ (2017) Nanostructured Materials for Heterogeneous Electrocatalytic CO₂ Reduction and Related Reaction Mechanisms. *Angew. Chem. Int. Ed. Engl.* 129(38):11482–11511.
37. Lin W, Stocker KM, Schatz GC (2017) Mechanisms of Hydrogen-Assisted CO₂ Reduction on Nickel. *J. Am. Chem. Soc.* 139(13):4663-4666.
38. Klinkova A, De Luna P, Dinh C-T, Voznyy O, Larin EM, Kumacheva E, Sargent EH (2016) Rational Design of Efficient Palladium Catalysts for Electroreduction of Carbon Dioxide to Formate. *ACS Catal.* 6(12):8115-8120.
39. Back S, Kim JH, Kim YT, Jung Y (2016) On the Mechanism of High Product Selectivity for HCOOH Using Pb in CO₂ Electroreduction. *Phys. Chem. Chem. Phys.* 18(14):9652-9657.
40. Jones J-P, Prakash GKS, Olah GA (2014) Electrochemical CO₂ Reduction: Recent Advances and Current Trends. *Isr. J. Chem.* 54(10):1451-1466.
41. R.P.S. CHAPLIN, WRAGG AA (2003) Effects of Process Conditions and Electrode Material on Reaction Pathways for Carbon Dioxide Electroreduction with Particular Reference to Formate Formation. *J. Appl. Electrochem.* 33(12):1107-1123.
42. Pander JE, Baruch MF, Bocarsly AB (2016) Probing the Mechanism of Aqueous CO₂ Reduction on Post-Transition-Metal Electrodes using ATR-IR Spectroelectrochemistry. *ACS Catal.* 6(11):7824-7833.
43. Baruch MF, Pander JE, White JL, Bocarsly AB (2015) Mechanistic Insights into the Reduction of CO₂ on Tin Electrodes using in Situ ATR-IR Spectroscopy. *ACS Catal.* 5(5):3148-3156.
44. Huang J, Guo X, Huang X, Wang L (2019) Metal (Sn, Bi, Pb, Cd) In-Situ Anchored on Mesoporous Hollow Kapok-Tubes for Outstanding Electrocatalytic CO₂ Reduction to Formate. *Electrochim. Acta* 325:134923.
45. Zhao CX, Bu YF, Gao W, Jiang Q (2017) CO₂ Reduction Mechanism on the Pb(111) Surface: Effect of Solvent and Cations. *J. Phys. Chem. C* 121(36):19767-19773.
46. Zhang H, Ma Y, Quan F, Huang J, Jia F, Zhang L (2014) Selective Electro-Reduction of CO₂ to Formate on Nanostructured Bi from Reduction of BiOCl Nanosheets. *Electrochem. Commun.* 46:63-66.
47. Koh JH, Won DH, Eom T, Kim N-K, Jung KD, Kim H, Hwang YJ, Min BK (2017) Facile CO₂ Electro-Reduction to Formate via Oxygen Bidentate Intermediate Stabilized by High-Index Planes of Bi Dendrite Catalyst. *ACS Catal.* 7(8):5071-5077.
48. Liu D, Li Y, Kottwitz M, Yan B, Yao S, Gamalski A, Grolimund D, Safonova OV, Nachtegaal M, Chen JG, Stach EA, Nuzzo RG, Frenkel AI (2018) Identifying Dynamic Structural Changes of Active Sites in Pt–Ni Bimetallic Catalysts Using Multimodal Approaches. *ACS Catal.* 8(5):4120-4131.

49. Cui X, Pan Z, Zhang L, Peng H, Zheng G (2017) Selective Etching of Nitrogen-Doped Carbon by Steam for Enhanced Electrochemical CO₂ Reduction. *Adv. Energy Mater.* 7(22):1701456.
50. Rosen J, Hutchings GS, Lu Q, Rivera S, Zhou Y, Vlachos DG, Jiao F (2015) Mechanistic Insights into the Electrochemical Reduction of CO₂ to CO on Nanostructured Ag Surfaces. *ACS Catal.* 5(7):4293-4299.
51. Ham YS, Choe S, Kim MJ, Lim T, Kim S-K, Kim JJ (2017) Electrodeposited Ag Catalysts for the Electrochemical Reduction of CO₂ to CO. *Appl. Catal. B-Environ.* 208:35-43.
52. Ham YS, Kim MJ, Lim T, Kim D-K, Kim S-K, Kim JJ (2018) Direct Formation of Dendritic Ag Catalyst on a Gas Diffusion Layer for Electrochemical CO₂ Reduction to CO and H₂. *Int. J. Hydrogen Energy* 43(24):11315-11325.
53. Back S, Kim JH, Kim YT, Jung Y (2016) Bifunctional Interface of Au and Cu for Improved CO₂ Electroreduction. *ACS Appl. Mater. Inter.* 8(35):23022-23027.
54. Valenti M, Prasad NP, Kas R, Bohra D, Ma M, Balasubramanian V, Chu L, Gimenez S, Bisquert J, Dam B, Smith WA (2019) Suppressing H₂ Evolution and Promoting Selective CO₂ Electroreduction to CO at Low Overpotentials by Alloying Au with Pd. *ACS Catal.* 9(4):3527-3536.
55. Zhang Q, Wang H (2014) Facet-Dependent Catalytic Activities of Au Nanoparticles Enclosed by High-Index Facets. *ACS Catal.* 4(11):4027-4033.
56. Lee H-E, Yang KD, Yoon SM, Ahn H-Y, Lee YY, Chang H, Jeong DH, Lee Y-S, Kim Y-S, Nam KT (2015) Concave Rhombic Dodecahedral Au Nanocatalyst with Multiple High-Index Facets for CO₂ Reduction. *ACS Nano* 9(8):8384-8393.
57. Gao D, Zhou H, Cai F, Wang J, Wang G, Bao X (2018) Pd-Containing Nanostructures for Electrochemical CO₂ Reduction Reaction. *ACS Catal.* 8(2):1510-1519.
58. Kortlever R, Peters I, Koper S, Koper MTM (2015) Electrochemical CO₂ Reduction to Formic Acid at Low Overpotential and with High Faradaic Efficiency on Carbon-Supported Bimetallic Pd-Pt Nanoparticles. *ACS Catal.* 5(7):3916-3923.
59. Zhu W, Kattel S, Jiao F, Chen JG (2019) Shape-Controlled CO₂ Electrochemical Reduction on Nanosized Pd Hydride Cubes and Octahedra. *Adv. Energy Mater.* 9(9):1802840.
60. Dobrovetsky R, Stephan DW (2013) Catalytic Reduction of CO₂ to CO by Using Zinc(II) and In Situ Generated Carbodiphosphoranes. *Angew. Chem. Int. Ed. Engl.* 52(9):2516-2519.
61. Rosen J, Hutchings GS, Lu Q, Forest RV, Moore A, Jiao F (2015) Electrodeposited Zn Dendrites with Enhanced CO Selectivity for Electrocatalytic CO₂ Reduction. *ACS Catal.* 5(8):4586-4591.
62. Garza AJ, Bell AT, Head-Gordon M (2018) Mechanism of CO₂ Reduction at Copper Surfaces: Pathways to C₂ Products. *ACS Catal.* 8(2):1490-1499.
63. Reller C, Krause R, Volkova E, Schmid B, Neubauer S, Rucki A, Schuster M, Schmid G (2017) Selective Electroreduction of CO₂ toward Ethylene on Nano Dendritic Copper Catalysts at High Current Density. *Adv. Energy Mater.* 7(12):1602114.
64. Roberts FS, Kuhl KP, Nilsson A (2015) High Selectivity for Ethylene from Carbon Dioxide Reduction over Copper Nanocube Electrocatalysts. *Angew. Chem. Int. Ed. Engl.* 54(17):5179-5182.

65. Chen CS, Handoko AD, Wan JH, Ma L, Ren D, Yeo BS (2015) Stable and Selective Electrochemical Reduction of Carbon Dioxide to Ethylene on Copper Mesocrystals. *Catal. Sci. Technol.* 5(1):161-168.
66. Kas R, Kortlever R, Yılmaz H, Koper MTM, Mul G (2015) Manipulating the Hydrocarbon Selectivity of Copper Nanoparticles in CO₂ Electroreduction by Process Conditions. *ChemElectroChem* 2(3):354-358.
67. Yoshio Hori, Suzuki S (1982) Electrolytic Reduction of Carbon Dioxide at Mercury Electrode in Aqueous Solution. *Bull. Chem. Soc. Jpn.* 55(3):660-665.
68. Makoto Todoroki, Kohjiro Hara, Akihiko Kudo, Sakata T (1995) Electrochemical Reduction of High Pressure CO₂ at Pb, Hg and In Electrodes in an Aqueous KHCO₃ Solution. *J. Electroanal. Chem.* 394(1-2):199-203.
69. Mizuno T, Ohta K, Sasaki A, Akai T, Hirano M, Kawabe A (1995) Effect of Temperature on Electrochemical Reduction of High-Pressure CO₂ with In, Sn, and Pb Electrodes. *Energy Sources* 17(5):503-508.
70. Bitar Z, Fecant A, Trela-Baudot E, Chardon-Noblat S, Pasquier D (2016) Electrocatalytic Reduction of Carbon Dioxide on Indium Coated Gas Diffusion Electrodes—Comparison with Indium Foil. *Appl. Catal. B-Environ.* 189:172-180.
71. Hegner R, Rosa LFM, Harnisch F (2018) Electrochemical CO₂ Reduction to Formate at Indium Electrodes with High Efficiency and Selectivity in pH Neutral Electrolytes. *Appl. Catal. B-Environ.* 238:546-556.
72. Luo W, Xie W, Li M, Zhang J, Züttel A (2019) 3D Hierarchical Porous Indium Catalyst for Highly Efficient Electroreduction of CO₂. *J. Mater. Chem. A* 7(9):4505-4515.
73. Ma W, Xie S, Zhang XG, Sun F, Kang J, Jiang Z, Zhang Q, Wu DY, Wang Y (2019) Promoting Electrocatalytic CO₂ Reduction to Formate via Sulfur-Boosting Water Activation on Indium Surfaces. *Nat. Commun.* 10:892.
74. F. Koleli, T. Atılan, N. Palamut, A. M. Gizir, R. Aydin, Hamann CH (2003) Electrochemical reduction of CO₂ at Pb- and Sn-electrodes in a fixed-bed reactor in aqueous K₂CO₃ and KHCO₃ media. *J. Appl. Electrochem.* 33(5):447–450.
75. Wu J, Risalvato FG, Ke F-S, Pellechia PJ, Zhou X-D (2012) Electrochemical Reduction of Carbon Dioxide I. Effects of the Electrolyte on the Selectivity and Activity with Sn Electrode. *J. Electrochem. Soc.* 159(7):F353-F359.
76. Prakash GKS, Viva FA, Olah GA (2013) Electrochemical Reduction of CO₂ over Sn-Nafion[®] Coated Electrode for a Fuel-Cell-Like Device. *J. Power Sources* 223:68-73.
77. Li F, Chen L, Xue M, Williams T, Zhang Y, MacFarlane DR, Zhang J (2017) Towards a Better Sn: Efficient Electrocatalytic Reduction of CO₂ to Formate by Sn/SnS₂ Derived from SnS₂ Nanosheets. *Nano Energy* 31:270-277.
78. Wang Q, Wang X, Wu C, Cheng Y, Sun Q, Yu H (2018) Enhanced Electroreduction of CO₂ and Simultaneous Degradation of Organic Pollutants Using a Sn-Based Carbon Nanotubes/Carbon Black Hybrid Gas Diffusion CSathode. *J. CO2 UTIL.* 26:425-433.
79. Zhao Y, Liang J, Wang C, Ma J, Wallace GG (2018) Tunable and Efficient Tin Modified Nitrogen-Doped Carbon Nanofibers for Electrochemical Reduction of Aqueous Carbon Dioxide. *Adv. Energy Mater.* 8(10).

80. He Z, Shen J, Ni Z, Tang J, Song S, Chen J, Zhao L (2015) Electrochemically Created Roughened Lead Plate for Electrochemical Reduction of Aqueous CO₂. *Catal. Commun.* 72:38-42.
81. Lee CH, Kanan MW (2015) Controlling H⁺ vs CO₂ Reduction Selectivity on Pb Electrodes. *ACS Catal.* 5(1):465-469.
82. Zhu Q, Ma J, Kang X, Sun X, Liu H, Hu J, Liu Z, Han B (2016) Efficient Reduction of CO₂ into Formic Acid on a Lead or Tin Electrode using an Ionic Liquid Catholyte Mixture. *Angew. Chem. Int. Ed. Engl.* 55(31):9012-9016.
83. Lv W, Zhou J, Bei J, Zhang R, Wang L, Xu Q, Wang W (2017) Electrodeposition of Nano-sized Bismuth on Copper Foil as Electrocatalyst for Reduction of CO₂ to Formate. *Appl. Surf. Sci.* 393:191-196.
84. Zhang X, Lei T, Liu Y, Qiao J (2017) Enhancing CO₂ Electrolysis to Formate on Facilely Synthesized Bi Catalysts at Low Overpotential. *Appl. Catal. B-Environ.* 218:46-50.
85. Avila-Bolivar B, Garcia-Cruz L, Montiel V, Solla-Gullon J (2019) Electrochemical Reduction of CO₂ to Formate on Easily Prepared Carbon-Supported Bi Nanoparticles. *Molecules* 24(11):2032.
86. Bohlen B, Wastl D, Radomski J, Sieber V, Vieira L (2020) Electrochemical CO₂ Reduction to Formate on Indium Catalysts Prepared by Electrodeposition in Deep Eutectic Solvents. *Electrochem. Commun.* 110:106597.
87. Lei F, Liu W, Sun Y, Xu J, Liu K, Liang L, Yao T, Pan B, Wei S, Xie Y (2016) Metallic Tin Quantum Sheets Confined in Graphene toward High-Efficiency Carbon Dioxide Electroreduction. *Nat. Commun.* 7:12697.
88. Kumar B, Atla V, Brian JP, Kumari S, Nguyen TQ, Sunkara M, Spurgeon JM (2017) Reduced SnO₂ Porous Nanowires with a High Density of Grain Boundaries as Catalysts for Efficient Electrochemical CO₂-into-HCOOH Conversion. *Angew. Chem. Int. Ed. Engl.* 56(13):3645-3649.
89. Innocent B, Liaigre D, Pasquier D, Ropital F, Léger JM, Kokoh KB (2009) Electro-Reduction of Carbon Dioxide to Formate on Lead Electrode in Aqueous Medium. *J. Appl. Electrochem.* 39(2):227-232.
90. Zouaoui N, Ossoonon BD, Fan M, Mayilukila D, Garbarino S, de Silveira G, Botton GA, Guay D, Tavares AC (2019) Electroreduction of CO₂ to formate on amine modified Pb electrodes. *J. Mater. Chem. A* 7(18):11272-11281.
91. Bertin E, Garbarino S, Roy C, Kazemi S, Guay D (2017) Selective Electroreduction of CO₂ to Formate on Bi and Oxide-Derived Bi Films. *J. CO₂ UTIL.* 19:276-283.
92. Qiu Y, Du J, Dong W, Dai C, Tao C (2017) Selective Conversion of CO₂ to Formate on a Size Tunable Nano-Bi Electrocatalyst. *J. CO₂ UTIL.* 20:328-335.
93. Firet NJ, Smith WA (2016) Probing the Reaction Mechanism of CO₂ Electroreduction over Ag Films via Operando Infrared Spectroscopy. *ACS Catal.* 7(1):606-612.
94. Kim C, Jeon HS, Eom T, Jee MS, Kim H, Friend CM, Min BK, Hwang YJ (2015) Achieving Selective and Efficient Electrocatalytic Activity for CO₂ Reduction Using Immobilized Silver Nanoparticles. *J Am. Chem. Soc.* 137(43):13844-13850.
95. Singh MR, Kwon Y, Lum Y, Ager JW, 3rd, Bell AT (2016) Hydrolysis of Electrolyte Cations Enhances the Electrochemical Reduction of CO₂ over Ag and Cu. *J. Am. Chem. Soc.* 138(39):13006-13012.

96. Verma S, Lu X, Ma S, Masel RI, Kenis PJ (2016) The Effect of Electrolyte Composition on the Electroreduction of CO₂ to CO on Ag Based Gas Diffusion Electrodes. *Phys. Chem. Chem. Phys.* 18(10):7075-7084.
97. Yang W, Ma W, Zhang Z, Zhao C (2018) Ligament Size-Dependent Electrocatalytic Activity of Nanoporous Ag Network for CO₂ Reduction. *Faraday Discuss* 210:289-299.
98. Kim C, Eom T, Jee MS, Jung H, Kim H, Min BK, Hwang YJ (2016) Insight into Electrochemical CO₂ Reduction on Surface-Molecule-Mediated Ag Nanoparticles. *ACS Catal.* 7(1):779-785.
99. Trindell JA, Clausmeyer J, Crooks RM (2017) Size Stability and H₂/CO Selectivity for Au Nanoparticles during Electrocatalytic CO₂ Reduction. *J. Am. Chem. Soc.* 139(45):16161-16167.
100. Marques Mota F, Nguyen DLT, Lee J-E, Piao H, Choy J-H, Hwang YJ, Kim DH (2018) Toward an Effective Control of the H₂ to CO Ratio of Syngas through CO₂ Electroreduction over Immobilized Gold Nanoparticles on Layered Titanate Nanosheets. *ACS Catal.* 8(5):4364-4374.
101. Gregory B. Stevens, Torsten Reda, Raguse B (2002) Energy Storage by the Electrochemical Reduction of CO₂ a Porous Au Film. *J. Electroanal. Chem.* 526(1-2):125–133.
102. Chen Y, Li CW, Kanan MW (2012) Aqueous CO₂ Reduction at Very Low Overpotential on Oxide-Derived Au Nanoparticles. *J. Am. Chem. Soc.* 134(49):19969-19972.
103. Zhu W, Michalsky R, Metin O, Lv H, Guo S, Wright CJ, Sun X, Peterson AA, Sun S (2013) Monodisperse Au Nanoparticles for Selective Electrocatalytic Reduction of CO₂ to CO. *J Am Chem Soc* 135(45):16833-16836.
104. Kim H, Jeon HS, Jee MS, Nursanto EB, Singh JP, Chae K, Hwang YJ, Min BK (2016) Contributors to Enhanced CO₂ Electroreduction Activity and Stability in a Nanostructured Au Electrocatalyst. *ChemSusChem* 9(16):2097-2102.
105. Zhu W, Zhang YJ, Zhang H, Lv H, Li Q, Michalsky R, Peterson AA, Sun S (2014) Active and Selective Conversion of CO₂ to CO on Ultrathin Au Nanowires. *J Am. Chem. Soc.* 136(46):16132-16135.
106. Gao D, Wang J, Wu H, Jiang X, Miao S, Wang G, Bao X (2015) pH Effect on Electrocatalytic Reduction of CO₂ over Pd and Pt Nanoparticles. *Electrochem. Commun.* 55:1-5.
107. Gao D, Zhou H, Wang J, Miao S, Yang F, Wang G, Wang J, Bao X (2015) Size-Dependent Electrocatalytic Reduction of CO₂ over Pd Nanoparticles. *J. Am. Chem. Soc.* 137(13):4288-4291.
108. Guo R-H, Liu C-F, Wei T-C, Hu C-C (2017) Electrochemical Behavior of CO₂ Reduction on Palladium Nanoparticles: Dependence of Adsorbed CO on Electrode Potential. *Electrochem. Commun.* 80:24-28.
109. Huang H, Jia H, Liu Z, Gao P, Zhao J, Luo Z, Yang J, Zeng J (2017) Understanding of Strain Effects in the Electrochemical Reduction of CO₂: Using Pd Nanostructures as an Ideal Platform. *Angew. Chem. Int. Ed. Engl.* 56(13):3594-3598.
110. Hall AS, Yoon Y, Wuttig A, Surendranath Y (2015) Mesostructure-Induced Selectivity in CO₂ Reduction Catalysis. *J. Am. Chem. Soc.* 137(47):14834-14837.
111. Kim H, Park HS, Hwang YJ, Min BK (2017) Surface-Morphology-Dependent Electrolyte Effects on Gold-Catalyzed Electrochemical CO₂ Reduction. *J. Phys. Chem. C* 121(41):22637-22643.

112. Won da H, Shin H, Koh J, Chung J, Lee HS, Kim H, Woo SI (2016) Highly Efficient, Selective, and Stable CO₂ Electroreduction on a Hexagonal Zn Catalyst. *Angew. Chem. Int. Ed. Engl.* 55(32):9297-9300.
113. Nguyen DLT, Jee MS, Won DH, Jung H, Oh H-S, Min BK, Hwang YJ (2017) Selective CO₂ Reduction on Zinc Electrocatalyst: The Effect of Zinc Oxidation State Induced by Pretreatment Environment. *ACS Sustain. Chem. Eng.* 5(12):11377-11386.
114. Morimoto M, Takatsuji Y, Hirata K, Fukuma T, Ohno T, Sakakura T, Haruyama T (2018) Visualization of Catalytic Edge Reactivity in Electrochemical CO₂ Reduction on Porous Zn Electrode. *Electrochimica Acta* 290:255-261.
115. Zhang T, Li X, Qiu Y, Su P, Xu W, Zhong H, Zhang H (2018) Multilayered Zn Nanosheets as an Electrocatalyst for Efficient Electrochemical Reduction of CO₂. *J. Catal.* 357:154-162.
116. Liu K, Wang J, Shi M, Yan J, Jiang Q (2019) Simultaneous Achieving of High Faradaic Efficiency and CO Partial Current Density for CO₂ Reduction via Robust, Noble-Metal-Free Zn Nanosheets with Favorable Adsorption Energy. *Adv. Energy Mater.* 9(21):1900276.
117. Nie X, Luo W, Janik MJ, Asthagiri A (2014) Reaction Mechanisms of CO₂ Electrochemical Reduction on Cu(111) Determined with Density Functional Theory. *J. Catal.* 312:108-122.
118. Zhu Q, Sun X, Yang D, Ma J, Kang X, Zheng L, Zhang J, Wu Z, Han B (2019) Carbon Dioxide Electroreduction to C₂ Products over Copper-Cuprous Oxide Derived from Electrosynthesized Copper Complex. *Nat. Commun.* 10:3851.
119. Hori Y, Takahashi I, Koga O, Hoshi N (2002) Selective Formation of C₂ Compounds from Electrochemical Reduction of CO₂ at a Series of Copper Single Crystal Electrodes. *J. Phys. Chem. B* 106(1):15-17.
120. Luo W, Nie X, Janik MJ, Asthagiri A (2016) Facet Dependence of CO₂ Reduction Paths on Cu Electrodes. *ACS Catal.* 6(1):219-229.
121. Liu X, Schlexer P, Xiao J, Ji Y, Wang L, Sandberg RB, Tang M, Brown KS, Peng H, Ringe S, Hahn C, Jaramillo TF, Norskov JK, Chan K (2019) pH Effects on the Electrochemical Reduction of CO₍₂₎ towards C₂ Products on Stepped Copper. *Nat. Commun.* 10:32.
122. Durst J, Rudnev A, Dutta A, Fu Y, Herranz J, Kaliginedi V, Kuzume A, Permyakova AA, Paratcha Y, Broekmann P, Schmidt TJ (2015) Electrochemical CO₂ Reduction - A Critical View on Fundamentals, Materials and Applications. *Chimia* 69(12):769-776.
123. Aresta M, Dibenedetto A, Angelini A (2014) Catalysis for the Valorization of Exhaust Carbon: from CO₂ to Chemicals, Materials, and Fuels. Technological Use of CO₂. *Chem. Rev.* 114(3):1709-1942.
124. Yu X, Pickup PG (2008) Recent Advances in Direct Formic Acid Fuel Cells (DFAFC). *J. Power Sources* 182(1):124-132.
125. Yishai O, Lindner SN, Gonzalez de la Cruz J, Tenenboim H, Bar-Even A (2016) The Formate Bio-Economy. *Curr. Opin. Chem. Biol.* 35:1-9.
126. Wang Y, Zhou J, Lv W, Fang H, Wang W (2016) Electrochemical Reduction of CO₂ to Formate Catalyzed by Electroplated Tin Coating on Copper Foam. *Appl. Surf. Sci.* 362:394-398.
127. Rogers C, Perkins WS, Veber G, Williams TE, Cloke RR, Fischer FR (2017) Synergistic Enhancement of Electrocatalytic CO₂ Reduction with Gold Nanoparticles Embedded in Functional Graphene Nanoribbon Composite Electrodes. *J. Am. Chem. Soc.* 139(11):4052-4061.

128. Gong Q, Ding P, Xu M, Zhu X, Wang M, Deng J, Ma Q, Han N, Zhu Y, Lu J, Feng Z, Li Y, Zhou W, Li Y (2019) Structural Defects on Converted Bismuth Oxide Nanotubes Enable Highly Active Electrocatalysis of Carbon Dioxide Reduction. *Nat. Commun.* 10(1):2807.
129. Mistry H, Choi YW, Bagger A, Scholten F, Bonifacio CS, Sinev I, Divins NJ, Zegkinoglou I, Jeon HS, Kisslinger K, Stach EA, Yang JC, Rossmeisl J, Roldan Cuenya B (2017) Enhanced Carbon Dioxide Electroreduction to Carbon Monoxide over Defect-Rich Plasma-Activated Silver Catalysts. *Angew. Chem. Int. Ed. Engl.* 56(38):11394-11398.
130. Wu D, Liu J, Liang Y, Xiang K, Fu XZ, Luo JL (2019) Electrochemical Transformation of Facet-Controlled BiOI into Mesoporous Bismuth Nanosheets for Selective Electrocatalytic Reduction of CO₂ to Formic Acid. *ChemSusChem* 12(20):4700-4707.
131. Zhang W, Hu Y, Ma L, Zhu G, Zhao P, Xue X, Chen R, Yang S, Ma J, Liu J, Jin Z (2018) Liquid-Phase Exfoliated Ultrathin Bi Nanosheets: Uncovering the Origins of Enhanced Electrocatalytic CO₂ Reduction on Two-Dimensional Metal Nanostructure. *Nano Energy* 53:808-816.
132. Yang H, Han N, Deng J, Wu J, Wang Y, Hu Y, Ding P, Li Y, Li Y, Lu J (2018) Selective CO₂ Reduction on 2D Mesoporous Bi Nanosheets. *Adv. Energy Mater.* 8(35):1801536.
133. Su P, Xu W, Qiu Y, Zhang T, Li X, Zhang H (2018) Ultrathin Bismuth Nanosheets as a Highly Efficient CO₂ Reduction Electrocatalyst. *ChemSusChem* 11(5):848-853.
134. Han N, Wang Y, Yang H, Deng J, Wu J, Li Y, Li Y (2018) Ultrathin Bismuth Nanosheets from In Situ Topotactic Transformation for Selective Electrocatalytic CO₂ Reduction to Formate. *Nat. Commun.* 9(1):1320.
135. Kim C, Möller T, Schmidt J, Thomas A, Strasser P (2018) Suppression of Competing Reaction Channels by Pb Adatom Decoration of Catalytically Active Cu Surfaces During CO₂ Electroreduction. *ACS Catal.* 9(2):1482-1488.
136. Zhao Y, Wang C, Liu Y, MacFarlane DR, Wallace GG (2018) Engineering Surface Amine Modifiers of Ultrasmall Gold Nanoparticles Supported on Reduced Graphene Oxide for Improved Electrochemical CO₂ Reduction. *Adv. Energy Mater.* 8(25):1801400.
137. Nesbitt NT, Ma M, Trzeźniewski BJ, Jaszewski S, Tafti F, Burns MJ, Smith WA, Naughton MJ (2018) Au Dendrite Electrocatalysts for CO₂ Electrolysis. *J. Phys. Chem. C* 122(18):10006-10016.
138. Liu M, Pang Y, Zhang B, De Luna P, Voznyy O, Xu J, Zheng X, Dinh CT, Fan F, Cao C, de Arquer FP, Safaei TS, Mepham A, Klinkova A, Kumacheva E, Filleter T, Sinton D, Kelley SO, Sargent EH (2016) Enhanced Electrocatalytic CO₂ Reduction via Field-Induced Reagent Concentration. *Nature* 537(7620):382-386.
139. Zhong H, Qiu Y, Zhang T, Li X, Zhang H, Chen X (2016) Bismuth Nanodendrites as a High Performance Electrocatalyst for Selective Conversion of CO₂ to Formate. *J. Mater. Chem. A* 4(36):13746-13753.
140. Piao G, Yoon SH, Han DS, Park H (2019) Ion-Enhanced Conversion of CO₂ into Formate on Porous Dendritic Bismuth Electrodes with High Efficiency and Durability. *ChemSusChem* 13(4):698-706.
141. Fan M, Garbarino S, Botton GA, Tavares AC, Guay D (2017) Selective Electroreduction of CO₂ to Formate on 3D [100] Pb Dendrites with Nanometer-Sized Needle-Like Tips. *J. Mater. Chem. A* 5(39):20747-20756.

142. Zhang Y, Zhang X, Bond AM, Zhang J (2018) Identification of a New Substrate Effect that Enhances the Electrocatalytic Activity of Dendritic Tin in CO₂ Reduction. *Phys. Chem. Chem. Phys.* 20(8):5936-5941.
143. Du D, Lan R, Humphreys J, Sengodan S, Xie K, Wang H, Tao S (2016) Achieving Both High Selectivity and Current Density for CO₂ Reduction to Formate on Nanoporous Tin Foam Electrocatalysts. *ChemistrySelect* 1(8):1711–1715.
144. Won da H, Choi CH, Chung J, Chung MW, Kim EH, Woo SI (2015) Rational Design of a Hierarchical Tin Dendrite Electrode for Efficient Electrochemical Reduction of CO₂. *ChemSusChem* 8(18):3092-3098.
145. Xia Z, Freeman M, Zhang D, Yang B, Lei L, Li Z, Hou Y (2018) Highly Selective Electrochemical Conversion of CO₂ to HCOOH on Dendritic Indium Foams. *ChemElectroChem* 5(2):253-259.
146. Rahaman M, Dutta A, Zanetti A, Broekmann P (2017) Electrochemical Reduction of CO₂ into Multicarbon Alcohols on Activated Cu Mesh Catalysts: An Identical Location (IL) Study. *ACS Catal.* 7(11):7946-7956.
147. Scholten F, Sinev I, Bernal M, Roldan Cuenya B (2019) Plasma-Modified Dendritic Cu Catalyst for CO₂ Electroreduction. *ACS Catal.* 9(6):5496-5502.
148. Yang Y, Ajmal S, Feng Y, Li K, Zheng X, Zhang L (2019) Insight into the Formation and Transfer Process of First Intermediate of CO₂ Reduction over Ag-Decorated Dendritic Cu. *Chem. Eur. J* 10.1002/chem.201904063.
149. Low QH, Loo NWX, Calle-Vallejo F, Yeo BS (2019) Enhanced Electroreduction of Carbon Dioxide to Methanol Using Zinc Dendrites Pulse-Deposited on Silver Foam. *Angew. Chem. Int. Ed. Engl.* 58(8):2256-2260.
150. Ju W, Zeng J, Bejtka K, Ma H, Rentsch D, Castellino M, Sacco A, Pirri CF, Battaglia C (2018) Sn-Decorated Cu for Selective Electrochemical CO₂ to CO Conversion: Precision Architecture beyond Composition Design. *ACS Appl. Energy Mater.* 2(1):867-872.
151. Lamaison S, Wakerley D, Blanchard J, Montero D, Rousse G, Mercier D, Marcus P, Taverna D, Giaume D, Mougel V, Fontecave M (2020) High-Current-Density CO₂-to-CO Electroreduction on Ag-Alloyed Zn Dendrites at Elevated Pressure. *Joule* 4(2):395-406.
152. Kottakkat T, Klingan K, Jiang S, Jovanov ZP, Davies VH, El-Nagar GAM, Dau H, Roth C (2019) Electrodeposited AgCu Foam Catalysts for Enhanced Reduction of CO₂ to CO. *ACS Appl. Mater. Inter.* 11(16):14734-14744.
153. Kim H, Lee H, Lim T, Ahn SH (2018) Facile Fabrication of Porous Sn-Based Catalysts for Electrochemical CO₂ Reduction to HCOOH and Syngas. *J. Ind. Eng. Chem.* 66:248-253.
154. Park H, Choi J, Kim H, Hwang E, Ha D-H, Ahn SH, Kim S-K (2017) AgIn Dendrite Catalysts for Electrochemical Reduction of CO₂ to CO. *Appl. Catal. B-Environ.* 219:123-131.
155. Hoffman ZB, Gray TS, Moraveck KB, Gunnoe TB, Zangari G (2017) Electrochemical Reduction of Carbon Dioxide to Syngas and Formate at Dendritic Copper–Indium Electrocatalysts. *ACS Catal.* 7(8):5381-5390.
156. Rasul S, Anjum DH, Jedidi A, Minenkov Y, Cavallo L, Takanabe K (2015) A Highly Selective Copper-Indium Bimetallic Electrocatalyst for the Electrochemical Reduction of Aqueous CO₂ to CO. *Angew. Chem. Int. Ed. Engl.* 54(7):2146-2150.
157. Shin H-C, Dong J, Liu M (2003) Nanoporous Structure Prepared by an Electrochemical Deposition Process. *Adv. Mater.* 15(19):1610-1614.

158. Kresse G, Furthmüller J (1996) Efficient Iterative Schemes for Ab Initio Total-Energy Calculations Using a Plane-Wave Basis Set. *Phys. Rev. B* 54(16):11169-11186.
159. Perdew JP, Burke K, Ernzerhof M (1996) Generalized Gradient Approximation Made Simple. *Phys. Rev. Lett.* 77(18):3865-3868.
160. Blochl PE (1994) Projector Augmented-Wave Method. *Phys. Rev. B* 50(24):17953-17979.
161. Pack JD, Monkhorst HJ (1977) "Special Points for Brillouin-Zone Integrations"—A Reply. *Phys. Rev. B* 16(4):1748-1749.
162. Gimkiewicz C, Hegner R, Gutensohn MF, Koch C, Harnisch F (2017) Study of Electrochemical CO₂ Reduction for Future Use in Secondary Microbial Electrochemical Technologies. *ChemSusChem* 10(5):1-11.
163. Tamaki Y, Morimoto T, Koike K, Ishitani O (2012) Photocatalytic CO₂ Reduction with High Turnover Frequency and Selectivity of Formic Acid Formation Using Ru(II) Multinuclear Complexes. *Proc. Natl. Acad. Sci. U. S. A.* 109(39):15673-15678.
164. Tamaki Y, Watanabe K, Koike K, Inoue H, Morimoto T, Ishitani O (2012) Development of Highly Efficient Supramolecular CO₂ Reduction Photocatalysts with High Turnover Frequency and Durability. *Faraday Discuss.* 155:115-127.
165. Bevilacqua M, Filippi J, Miller HA, Vizza F (2015) Recent Technological Progress in CO₂ Electroreduction to Fuels and Energy Carriers in Aqueous Environments. *Energy Technol.* 3(3):197-210.
166. DiMeglio JL, Rosenthal J (2013) Selective Conversion of CO₂ to CO with High Efficiency Using an Inexpensive Bismuth-Based Electrocatalyst. *J. Am. Chem. Soc.* 135(24):8798-8801.
167. Hansen HA, Varley JB, Peterson AA, Norskov JK (2013) Understanding Trends in the Electrocatalytic Activity of Metals and Enzymes for CO₂ Reduction to CO. *J. Phys. Chem. Lett.* 4(3):388-392.
168. Medina-Ramos J, DiMeglio JL, Rosenthal J (2014) Efficient Reduction of CO₂ to CO With High Current Density Using In Situ or Ex Situ Prepared Bi-Based Materials. *J. Am. Chem. Soc.* 136(23):8361-8367.
169. Medina-Ramos J, Pupillo RC, Keane TP, DiMeglio JL, Rosenthal J (2015) Efficient Conversion of CO₂ to CO Using Tin and Other Inexpensive and Easily Prepared Post-Transition Metal Catalysts. *J. Am. Chem. Soc.* 137(15):5021-5027.
170. Shen J, Kortlever R, Kas R, Birdja YY, Diaz-Morales O, Kwon Y, Ledezma-Yanez I, Schouten KJ, Mul G, Koper MT (2015) Electrocatalytic Reduction of Carbon Dioxide to Carbon Monoxide and Methane at an Immobilized Cobalt Porphyrin. *Nat. Commun.* 6:8177.
171. Kaneco S, Hiei N-h, Xing Y, Katsumata H, Ohnishi H, Suzuki T, Ohta K (2003) High-efficiency electrochemical CO₂-to-methane reduction method using aqueous KHCO₃ media at less than 273 K. *J. Solid State Electrochem.* 7(3):152-156.
172. Khadka N, Dean DR, Smith D, Hoffman BM, Raugei S, Seefeldt LC (2016) CO₂ Reduction Catalyzed by Nitrogenase: Pathways to Formate, Carbon Monoxide, and Methane. *Inorg. Chem.* 55(17):8321-8330.
173. Lu X, Leung DYC, Wang H, Leung MKH, Xuan J (2014) Electrochemical Reduction of Carbon Dioxide to Formic Acid. *ChemElectroChem* 1(5):836-849.

174. Chen Y, Kanan MW (2012) Tin Oxide Dependence of the CO₂ Reduction Efficiency on Tin Electrodes and Enhanced Activity for Tin/Tin Oxide Thin-Film Catalysts. *J. Am. Chem. Soc.* 134(4):1986-1989.
175. Anawati A, Frankel GS, Agarwal A, Sridhar N (2014) Degradation and Deactivation of Sn Catalyst Used for CO₂ Reduction as Function of Overpotential. *Electrochim. Acta* 133:188-196.
176. Zhang S, Kang P, Meyer TJ (2014) Nanostructured Tin Catalysts for Selective Electrochemical Reduction of Carbon Dioxide to Formate. *J. Am. Chem. Soc.* 136(5):1734-1737.
177. Zhao C, Yin Z, Wang J (2015) Efficient Electrochemical Conversion of CO₂ to HCOOH Using Pd-polyaniline/CNT Nanohybrids Prepared In Situ. *ChemElectroChem* 2(12):1974-1982.
178. Min X, Kanan MW (2015) Pd-Catalyzed Electrohydrogenation of Carbon Dioxide to Formate: High Mass Activity at Low Overpotential and Identification of the Deactivation Pathway. *J. Am. Chem. Soc.* 137(14):4701-4708.
179. Gao D, Zhou H, Cai F, Wang D, Hu Y, Jiang B, Cai W-B, Chen X, Si R, Yang F, Miao S, Wang J, Wang G, Bao X (2017) Switchable CO₂ Electroreduction via Engineering Active Phases of Pd Nanoparticles. *Nano Res.* 10(6):2181-2191.
180. J. Hernaez, A. Pardo, Aja MI (1986) Improved Metallographic Preparation of Lead by Electropolishing. *Metallography* 19(1):5-17.
181. Cherevko S, Xing X, Chung C-H (2011) Hydrogen Template Assisted Electrodeposition of Sub-Micrometer Wires Composing Honeycomb-Like Porous Pb Films. *Appl. Surf. Sci.* 257(18):8054-8061.
182. Y. Liu, S. Bliznakov, Dimitrov N (2009) Comprehensive Study of the Application of a Pb Underpotential Deposition-Assisted Method for Surface Area Measurement of Metallic Nanoporous Materials. *J. Phys. Chem. C* 113(28):12362-12372.
183. Narayanan SR, Haines B, Soler J, Valdez TI (2011) Electrochemical Conversion of Carbon Dioxide to Formate in Alkaline Polymer Electrolyte Membrane Cells. *J. Electrochem. Soc.* 158(2):A167-A173.
184. Plowman BJ, Jones LA, Bhargava SK (2015) Building with Bubbles: the Formation of High Surface Area Honeycomb-like Films via Hydrogen Bubble Templated Electrodeposition. *Chem. Commun.* 51(21):4331-4346.
185. Wranglén G (1960) Dendrites and Growth Layers in the Electrocrystallization of Metals. *Electrochim. Acta* 2:130-143.
186. S. Sawatani, S. Ogawa, T. Yoshida, Minoura H (2005) Formation of Highly Crystallized β -PbO Thin Films by Cathodic Electrodeposition of Pb and Its Rapid Oxidation in Air. *Adv. Funct. Mater.* 15(2):297-301.
187. Gupta N, Gattrell M, MacDougall B (2006) Calculation for the Cathode Surface Concentrations in the Electrochemical Reduction of CO₂ in KHCO₃ Solutions. *J. Appl. Electrochem.* 36(2):161-172.
188. Hori Y, Murata A, Takahashi R (1989) Formation of Hydrocarbons in the Electrochemical Reduction of Carbon Dioxide at a Copper Electrode in Aqueous Solution. *J. Chem. Soc.-Faraday Trans. 1* 85(8):2309-2326.
189. Kwon Y, Lee J (2010) Formic Acid from Carbon Dioxide on Nanolayered Electrocatalyst. *Electrocatalysis* 1(2-3):108-115.

190. Keddam M, Rakotomavo C, Takenouti H (1984) Impedance of a Porous Electrode with an Axial Gradient of Concentration. *J. Appl. Electrochem.* 14(4):437-448.
191. Tang W, Peterson AA, Varela AS, Jovanov ZP, Bech L, Durand WJ, Dahl S, Norskov JK, Chorkendorff I (2012) The Importance of Surface Morphology in Controlling the Selectivity of Polycrystalline Copper for CO₂ Electroreduction. *Phys. Chem. Chem. Phys.* 14(1):76-81.
192. Sen S, Liu D, Palmore GTR (2014) Electrochemical Reduction of CO₂ at Copper Nanofoams. *ACS Catal.* 4(9):3091-3095.
193. Andrew A. Peterson, Frank Abild-Pedersen, Felix Studt, Rossmeisl J, Nørskov JK (2010) How Copper Catalyzes the Electroreduction of Carbon Dioxide into Hydrocarbon Fuels. *Energy Environ. Sci.* 3(9):1311-1315.
194. Liu C, Cundari TR, Wilson AK (2012) CO₂ Reduction on Transition Metal (Fe, Co, Ni, and Cu) Surfaces: In Comparison with Homogeneous Catalysis. *J. Phys. Chem. C* 116(9):5681-5688.
195. B. E. Conway, H. Angerstein-Kozłowska, Sattar MA (1983) Study of a Decomposing Hydride Phase at Nickel Cathodes by Measurement of Open-Circuit Potential Decay. *J. Electrochem. Soc.* 130(9):1825-1836.
196. D. T. Whipple, P. J. A. Kenis (2010) Prospects of CO₂ Utilization via Direct Heterogeneous Electrochemical Reduction. *J. Phys. Chem. Lett.* 1(24):3451-3458.
197. Zheng Y, Zhang W, Li Y, Chen J, Yu B, Wang J, Zhang L, Zhang J (2017) Energy Related CO₂ Conversion and Utilization: Advanced Materials/Nanomaterials, Reaction Mechanisms and Technologies. *Nano Energy* 40:512-539.
198. Eneau-Innocent B, Pasquier D, Ropital F, Léger JM, Kokoh KB (2010) Electroreduction of Carbon Dioxide at a Lead Electrode in Propylene Carbonate: A Spectroscopic Study. *Appl. Catal. B-Environ.* 98(1-2):65-71.
199. Zhang T, Zhong H, Qiu Y, Li X, Zhang H (2016) Zn Electrode with a Layer of Nanoparticles for Selective Electroreduction of CO₂ to Formate in Aqueous Solutions. *J. Mater. Chem. A* 4(42):16670-16676.
200. Kim S, Dong WJ, Gim S, Sohn W, Park JY, Yoo CJ, Jang HW, Lee J-L (2017) Shape-Controlled Bismuth Nanoflakes as Highly Selective Catalysts for Electrochemical Carbon Dioxide Reduction to Formate. *Nano Energy* 39:44-52.
201. Solla-Gullón J, Vidal-Iglesias FJ, Feliu JM (2011) Shape Dependent Electrocatalysis. *Annu. Rep. Prog. Chem., Sect. C* 107:263-297.
202. Tian N, Zhou Z-Y, Sun S-G, Ding Y, Wang ZL (2007) Synthesis of Tetrahedral Platinum Nanocrystals with High-Index Facets and High Electro-Oxidation Activity. *Science* 316(5825):732-735.
203. Huang X, Zhao Z, Fan J, Tan Y, Zheng N (2011) Amine-Assisted Synthesis of Concave Polyhedral Platinum Nanocrystals Having {411} High-Index Facets. *J. Am. Chem. Soc.* 133(13):4718-4721.
204. Zhou ZY, Huang ZZ, Chen DJ, Wang Q, Tian N, Sun SG (2010) High-Index Faceted Platinum Nanocrystals Supported on Carbon Black as Highly Efficient Catalysts for Ethanol Electrooxidation. *Angew. Chem. Int. Ed. Engl.* 49(2):411-414.
205. Zhang J, Zhang L, Xie S, Kuang Q, Han X, Xie Z, Zheng L (2011) Synthesis of Concave Palladium Nanocubes with High-index Surfaces and High Electrocatalytic Activities. *Chem. Eur. J* 17(36):9915-9919.

206. Kumar A, Gonçalves JM, Selva JSG, Araki K, Bertotti M (2019) Correlating Selective Electrocatalysis of Dopamine and Ascorbic Acid Electrooxidation at Nanoporous Gold Surfaces with Structural-Defects. *J. Electrochem. Soc.* 166(14):H704-H711.
207. Ivaništšev V, Nazmutdinov RR, Lust E (2010) Density Functional Theory Study of the Water Adsorption at Bi(111) Electrode Surface. *Surf. Sci.* 604(21-22):1919-1927.
208. Li Y, Jia W-Z, Song Y-Y, Xia X-H (2007) Superhydrophobicity of 3D Porous Copper Films Prepared Using the Hydrogen Bubble Dynamic Template. *Chem. Mater.* 19(23):5758-5764.
209. Rafailović LD, Gammer C, Rentenberger C, Trišović T, Kleber C, Peter Karnthaler H (2013) Enhanced Oxygen Evolution and Reduction Reactions of Porous Ternary NiCoFe Foam Electrodes Prepared by Dynamic Hydrogen Template Deposition. *Nano Energy* 2(4):523-529.
210. Patra S, Viswanath B, Barai K, Ravishankar N, Munichandraiah N (2010) High-surface Step Density on Dendritic Pd Leads to Exceptional Catalytic Activity for Formic Acid Oxidation. *ACS Appl. Mater. Inter.* 2(11):2965-2969.
211. Moran E, Cattaneo C, Mishima H, López de Mishima BA, Silveti SP, Rodriguez JL, Pastor E (2007) Ammonia Oxidation on Electrodeposited Pt-Ir Alloys. *J. Solid State Electr.* 12(5):583-589.
212. Brug GJ, van den Eeden ALG, Sluyters-Rehbach M, Sluyters JH (1984) The Analysis of Electrode Impedances Complicated by the Presence of a Constant Phase Element. *J. Electroanal. Chem.* 176(1-2):275-295.
213. Hori Y, Konishi H, Futamura T, Murata A, Koga O, Sakurai H, Oguma K (2005) "Deactivation of Copper Electrode" in Electrochemical Reduction of CO₂. *Electrochim. Acta* 50(27):5354-5369.
214. P. Friebe, P. Bogdanoff, N. Alonso-Vante, H. Tributsch (1997) A Real-Time Mass Spectroscopy Study of the (Electro)chemical Factors Affecting CO₂ Reduction at Copper. *J. Catal.* 168(2):374-385.
215. V. D. Jović, B. M. Jović, A. R. Despić (1990) The Influence of Solution Composition on Lead, Cadmium and Thallium Underpotential Deposition on (111) Oriented Silver Single Crystal Surfaces. *J. Electroanal. Chem.* 288(1-2):229-243.
216. T. Vitanov, A. Popov, G. Staikov, E. Budevski, W. J. Lorenz, Schmidt E (1986) Slow Transformation Phenomena of Lead Adsorbates on Electrolytically Grown Ag(111) and Ag(100) Electrode Surfaces. *Electrochim. Acta* 31(8):981-989.
217. Herrero E, Buller LJ, Abruña HD (2001) Underpotential Deposition at Single Crystal Surfaces of Au, Pt, Ag and Other Materials. *Chem. Rev.* 101(7):1897-1930.
218. Bei J, Zhang R, Chen Z, Lv W, Wang W (2017) Efficient Reduction of CO₂ to Formate Using in Situ Prepared Nano-Sized Bi Electrocatalyst. *Int. J. Electrochem. Sci.* 10.20964/2017.03.72(3):2365-2375.
219. Lee CW, Hong JS, Yang KD, Jin K, Lee JH, Ahn H-Y, Seo H, Sung N-E, Nam KT (2018) Selective Electrochemical Production of Formate from Carbon Dioxide with Bismuth-Based Catalysts in an Aqueous Electrolyte. *ACS Catal.* 8(2):931-937.
220. He S, Ni F, Ji Y, Wang L, Wen Y, Bai H, Liu G, Zhang Y, Li Y, Zhang B, Peng H (2018) The p-Orbital Delocalization of Main-Group Metals to Boost CO₂ Electroreduction. *Angew. Chem. Int. Ed. Engl.* 57(49):16114-16119.

221. Centi G, Quadrelli EA, Perathoner S (2013) Catalysis for CO₂ Conversion: A Key Technology for Rapid Introduction of Renewable Energy in the Value Chain of Chemical Industries. *Energy Environ. Sci.* 6(6):1711-1731.
222. Olah GA, Prakash GK, Goeppert A (2011) Anthropogenic Chemical Carbon Cycle for a Sustainable Future. *J. Am. Chem. Soc.* 133(33):12881-12898.
223. Klankermayer J, Wesselbaum S, Beydoun K, Leitner W (2016) Selective Catalytic Synthesis Using the Combination of Carbon Dioxide and Hydrogen: Catalytic Chess at the Interface of Energy and Chemistry. *Angew. Chem. Int. Ed. Engl.* 55(26):7296-7343.
224. Agarwal AS, Zhai Y, Hill D, Sridhar N (2011) The Electrochemical Reduction of Carbon Dioxide to Formate/Formic Acid: Engineering and Economic Feasibility. *ChemSusChem* 4(9):1301-1310.
225. Hietala J, Vuori A, Johnsson P, Pollari I, Reutemann W, Kieczka H (2016) *Formic Acid. In Ullmann's Encyclopedia of Industrial Chemistry*, Wiley-VCH, Weinheim.
226. Francke R, Schille B, Roemelt M (2018) Homogeneously Catalyzed Electroreduction of Carbon Dioxide-Methods, Mechanisms, and Catalysts. *Chem. Rev.* 118(9):4631-4701.
227. Yi Q, Li W, Feng J, Xie K (2015) Carbon Cycle in Advanced Coal Chemical Engineering. *Chem. Soc. Rev.* 44(15):5409-5445.
228. Zhu Q-L, Xu Q (2015) Liquid Organic and Inorganic Chemical Hydrides for High-Capacity Hydrogen Storage. *Energy Environ. Sci.* 8(2):478-512.
229. An L, Chen R (2016) Direct Formate Fuel Cells: A Review. *J. Power Sources* 320:127-139.
230. Dutta A, Morstein CE, Rahaman M, Cedeño López A, Broekmann P (2018) Beyond Copper in CO₂ Electrolysis: Effective Hydrocarbon Production on Silver-Nanofoam Catalysts. *ACS Catal.* 8(9):8357-8368.
231. Zhu S, Wang Q, Qin X, Gu M, Tao R, Lee BP, Zhang L, Yao Y, Li T, Shao M (2018) Tuning Structural and Compositional Effects in Pd-Au Nanowires for Highly Selective and Active CO₂ Electrochemical Reduction Reaction. *Adv. Energy Mater.* 8(32):1802238.
232. Luc W, Collins C, Wang S, Xin H, He K, Kang Y, Jiao F (2017) Ag-Sn Bimetallic Catalyst with a Core-Shell Structure for CO₂ Reduction. *J. Am. Chem. Soc.* 139(5):1885-1893.
233. Bai X, Chen W, Zhao C, Li S, Song Y, Ge R, Wei W, Sun Y (2017) Exclusive Formation of Formic Acid from CO₂ Electroreduction by a Tunable Pd-Sn Alloy. *Angew. Chem. Int. Ed. Engl.* 56(40):12219-12223.
234. Morimoto M, Takatsuji Y, Iikubo S, Kawano S, Sakakura T, Haruyama T (2019) Experimental and Theoretical Elucidation of Electrochemical CO₂ Reduction on an Electrodeposited Cu₃Sn Alloy. *J. Phys. Chem. C* 123(5):3004-3010.
235. Fan M, Ma C, Lei T, Jung J, Guay D, Qiao J (2018) Aqueous-Phase Electrochemical Reduction of CO₂ Based on SnO₂-CuO Nanocomposites with Improved Catalytic Activity and Selectivity. *Catal. Today* 318(SI):2-9.
236. Morimoto M, Takatsuji Y, Yamasaki R, Hashimoto H, Nakata I, Sakakura T, Haruyama T (2017) Electrodeposited Cu-Sn Alloy for Electrochemical CO₂ Reduction to CO/HCOO⁻. *Electrocatalysis* 9(3):323-332.
237. Katah A, Uchida H, Shibata M, Watanabe M (1994) Design of Electrocatalyst for CO₂ Reduction V. Effect of the Microcrystalline Structures of Cu-Sn and Cu-Zn Alloys on the Electrocatalysis of CO₂ Reduction. *J. Electrochem. Soc.* 141(8):2054-2058.

238. Fecht HJ, Pereprako JH (1989) Metastable Phase Equilibria in the Lead-Tin Alloy System: Part I. Experimental. *Metall. Trans. A* 20(5):785-794.
239. Okamoto H, Schlesinger ME, Mueller EM (2016) *ASM Handbook Volume 3: Alloy Phase Diagrams*, ASM International, Ohio.
240. Choi SY, Jeong SK, Kim HJ, Baek I-H, Park KT (2016) Electrochemical Reduction of Carbon Dioxide to Formate on Tin–Lead Alloys. *ACS Sustain. Chem. Eng.* 4(3):1311-1318.
241. Wen G, Lee DU, Ren B, Hassan FM, Jiang G, Cano ZP, Gostick J, Croiset E, Bai Z, Yang L, Chen Z (2018) Orbital Interactions in Bi-Sn Bimetallic Electrocatalysts for Highly Selective Electrochemical CO₂ Reduction toward Formate Production. *Adv. Energy Mater.* 8(31):1802427.
242. Calle-Vallejo F, Koper MTM (2012) First-Principles Computational Electrochemistry: Achievements and Challenges. *Electrochim. Acta* 84(SI):3-11.
243. Nørskov JK, Rossmeisl J, Logadottir A, Lindqvist L, Kitchin JR, Bligaard T, Jónsson H (2004) Origin of the Overpotential for Oxygen Reduction at a Fuel-Cell Cathode. *J. Phys. Chem. B* 108(46):17886-17892.
244. Varley JB, Hansen HA, Ammitzbøll NL, Grabow LC, Peterson AA, Rossmeisl J, Nørskov JK (2013) Ni–Fe–S Cubanes in CO₂ Reduction Electrocatalysis: A DFT Study. *ACS Catal.* 3(11):2640-2643.
245. Tripkovic V, Vanin M, Karamad M, Björketun ME, Jacobsen KW, Thygesen KS, Rossmeisl J (2013) Electrochemical CO₂ and CO Reduction on Metal-Functionalized Porphyrin-like Graphene. *J. Phys. Chem. C* 117(18):9187-9195.
246. Karamad M, Hansen HA, Rossmeisl J, Nørskov JK (2015) Mechanistic Pathway in the Electrochemical Reduction of CO₂ on RuO₂. *ACS Catal.* 5(7):4075-4081.
247. Köleli F, Balun D (2004) Reduction of CO₂ under high pressure and high temperature on Pb-granule electrodes in a fixed-bed reactor in aqueous medium. *Appl. Catal. A-Gen.* 274(1-2):237-242.

LIST OF PUBLICATIONS, CONFERENCE PRESENTATIONS, AND AWARDS

Peer-Reviewed Articles

1. **Fan M**, Prabhudev S, Garbarino S, Qiao J, Botton GA, Harrington DA, Tavares AC, Guay D (2020) Uncovering the Nature of Electroactive Sites in Nano Architected Dendritic Bi for Highly Efficient CO₂ Electroreduction to Formate. *Appl. Catal. B-Environ.*, 274:119031.
2. **Fan M**, Lei T, Ma C, Jung J, Guay D, Qiao J (2018) Aqueous-Phase Electrochemical Reduction of CO₂ Based on SnO₂CuO Nanocomposites with Improved Catalytic Activity and Selectivity. *Catal. Today*, 318:2-9.
3. **Fan M**, Garbarino S, Tavares AC, Guay D (2020) Progress in the Electrochemical Reduction of CO₂ on Hierarchical Dendritic Metal Electrodes, *Curr. Opin. Electrochem.*, Accepted.
4. **Fan M**, Garbarino S, Botton GA, Tavares AC, Guay D (2017) Selective Electroreduction of CO₂ to Formate on 3D [100] Pb Dendrites with Nanometer-Sized Needle-Like Tips. *J. Mater. Chem. A*, 2(5):20747-20756. (2017 Journal of Materials Chemistry A HOT Papers)
5. **Fan M**, Bai Z, Zhang Q, Ma C, Zhou XD, Qiao J (2014) Aqueous CO₂ Reduction on Morphology Controlled Cu₂O Nanocatalysts at Low Overpotential. *RSC Adv.*, 4:44583-44591.
6. **Fan M**, Eslamibidgoli MJ, Zhu X, Garbarino S, Tavares AC, Eikerling M, Guay D (2020) Understanding the Mechanism of CO₂ Electrochemical Reduction on Dendritic Sn₁Pb₃ alloy: A Computational-Experimental Investigation. *ACS Catal. Submitted.*
7. **Fan M**, Zouaoui N, Galipaud J, Honrado B, Martin MH, Yang J, Gaudet J, Kazemi S, Garbarino S, Soleymani L, Botton GA, Tavares AC, Guay D (2020) Effect of pH on the deactivation of Pb during electroreduction of CO₂. *ChemSusChem. Submitted.*
8. **Fan M**, Garbarino S, Tavares AC, Guay D (2020) Binary Alloys for Exclusively Formate-Selective CO₂ Electrochemical Reduction at Low Overpotentials. *Submitted.*
9. Liu Y, **Fan M**, Zhang X, Zhang Q, Guay D, Qiao J (2017) Design and Engineering of Urchin-Like Nanostructured SnO₂ Catalysts via Controlled Facial Hydrothermal Synthesis for Efficient Electro-Reduction of CO₂. *Electrochim. Acta*, 248:128-132.
10. Qiao J, **Fan M**, Fu Y, Bai Z, Ma C, Liu Y, Zhou XD (2015) Highly-Active Copper Oxide/Copper Electrocatalysts Induced from Hierarchical Copper Oxide Nanospheres for Carbon Dioxide

Reduction Reaction. *Electrochim. Acta*, 153(20):559-565.

11. Zouaoui N, Ossoonon BD, **Fan M**, Mayilukila D, Garbarino S, Silveira G, Botton GA, Guay D, Tavares AC (2019) *J. Mater. Chem. A*, 7(18):11272-11281.
12. Tam B, Duca M, Wang A, **Fan M**, Garbarino S, Guay D (2019) Promotion of Glycerol Oxidation by Selective Ru Decoration of (100) Domains at Nanostructured Pt Electrodes. *ChemElectroChem*, 6(6):1784-1793

Book Chapter

13. **Fan M**, Qiao J (2016) *Electrochemical Reduction of Carbon Dioxide: Fundamentals and Technologies: Chapter 10 Challenges and Perspectives of CO₂ Electroreduction*, CRC Press, United States.

Conference Presentations

1. CQMF Annual Student Symposium (2019) November 18, Montreal, Canada, **Oral presentation**
2. 9th ECS Montreal Student Symposium (2019) May 10, Montreal, Canada, **Poster presentation, Best Poster Award**
3. ECS Canadian Section Fall Meeting (2018) November 10, Montreal, Canada. **Poster presentation**
4. VIU PhD Academy Sustainable Energy (2018) July 9-13, Venice, Italy, **Poster presentation, Best Poster Award**
5. CQMF Advanced Materials Annual Conference (2018) May 3-4, Montreal, Canada, **Oral Presentation**
6. ECS Canadian Section Fall Symposium (2017) November 4, Kington, Canada. **Poster Presentation**
7. MRS Fall Meeting & Exhibit (2016) Nov. 27- Dec. 2, Boston, USA. **Poster Presentation**

Awards and Honors

1. **Internship Scholarship** (2019) provided by Ni Electro Can project (NSERC)
2. **Doctoral Scholarship** (2018-2019) provided by Fonds de recherche du Québec - Nature et technologies (FRQNT)
3. **VIU International PhD Academy on Sustainable Energy Fellowship** (2018)

SOMMAIRE RÉCAPITULATIF

L'introduction

Le dioxyde de carbone (CO₂) est le gaz à effet de serre qui est largement attribué aux activités humaines. CO₂ émis dans l'atmosphère par la combustion de la forêt, par la combustion de combustibles fossiles et par les processus industriels. L'émission illimitée de CO₂ résultant des êtres humains a dépassé la capacité de recyclage du CO₂ dans la nature, entraînant une série de problèmes environnementaux. Les émissions croissantes de dioxyde de carbone provenant des activités humaines font monter les températures. Le réchauffement climatique du GIEC rapporté en 2018 montre que la température de la surface de la Terre continue d'augmenter chaque décennie, et qu'elle est positivement corrélée aux émissions cumulées de CO₂. Cela augmente les risques de conditions météorologiques extrêmes, de fonte des glaces polaires et d'accélération de l'élévation du niveau de la mer, ce qui menace le monde entier.

La conversion du CO₂ en produits chimiques précieux permet le recyclage et la réutilisation du carbone. Ce processus de conversion nécessite de l'énergie et peut être réalisé au moyen de méthodes biochimiques, photochimiques et électrochimiques. La réduction électrochimique du CO₂ (ERC) a attiré une grande attention ces dernières années en raison de plusieurs avantages: (1) l'électricité utilisée pour conduire le processus peut être combinée avec des sources d'énergie intermittentes telles que l'énergie solaire et éolienne, permettant une énergie hors réseau stockage pouvant être facilement réintégré dans la grille au fur et à mesure des besoins; (2) l'état de l'ERC, comme la température, la pression et le potentiel d'électrolyse, est facilement contrôlé; (3) la configuration d'ERC est compacte et peut être mise à l'échelle. Cependant, les défis de l'ERC demeurent: (1) la cinétique lente de l'ERC conduisant à des potentiels d'électrolyse élevés appliqués; (2) La faible efficacité énergétique entraînant une faible viabilité économique de l'ERC; (3) La stabilité insuffisante conduisant à un coût de fonctionnement élevé pour l'ERC. Par conséquent, il est nécessaire de concevoir et de développer des catalyseurs hautement efficaces et stables pour l'ERC afin de rendre le processus ERC plus faisable et économique.

La réduction électrochimique du CO₂ en carburant et produit chimique est l'un des moyens de remédier aux niveaux élevés d'émissions de CO₂ résultant de l'activité humaine. Parmi les différents produits à valeur ajoutée qui peuvent être obtenus pendant l'ERC, le formiate / acide formique a suscité un vif intérêt en raison de sa large utilisation et de son marché favorable. Les métaux de post-transition, tels que In, Hg, Pb et Sn, ont suscité l'intérêt des chercheurs en raison

de leur faible prix et de leur bonne sélectivité pour la production de formiate lors de la réduction électrochimique du processus de CO₂. Cependant, sur ces éléments de post-transition, une sélectivité élevée s'accompagne d'une forte demande de pression de CO₂, les potentiels de débuts importants et les surtensions élevées lorsqu'une forte densité de courant (taux de production élevé) sont requis. Par conséquent, il est toujours un défi à développer des catalyseurs de post-transition qui fonctionnent bien à la pression atmosphérique, à la température ambiante et dans l'électrolyte aqueux, et qui atteignent une faible surtension et un courant de réduction important. Les catalyseurs en structure de type dendrite sont potentiels pour l'ERC hautement actif et sélectif en raison de leur grande surface spécifique, d'une grande densité de surface exposée avec des orientations de facettes préférentielles et de la présence de pointes acérées à la fin des dendrites. À ce jour, les performances d'ERC reportés et sur les métaux dendritiques de post-transition restent à améliorer, et les sites actifs à la surface de la dendrite doivent être démêlés. La publication liée à ce chapitre est:

Fan M, Garbarino S, Tavares AC, Guay D (2020) Progress in the Electrochemical Reduction of CO₂ on Hierarchical Dendritic Metal Electrodes, *Curr. Opin. Electrochem.*, Accepted, DOI: <https://doi.org/10.1016/j.coelec.2020.05.013>.

Objectif de la thèse

Les objectifs de cette thèse sont les suivants:

- (1) Synthétiser des électrodes poreuses dendritiques en Pb pour diminuer la surtension d'ERC et améliorer la densité de courant partielle d'ERC sur des électrodes à base de Pb.
- (2) Décorer le Pb poreux dendritique par un autre métal hautement sélectif à formiate et non précieux afin de diminuer davantage la surtension d'ERC et d'améliorer le taux de production de formiate dans l'ERC. Examinez les sites actifs du métal de décoration.
- (3) Introduire un autre métal non précieux dans les matériaux dendritiques à base de Pb et synthétiser des alliages dendritiques binaires pour améliorer encore les performances de l'ERC. Étudier les mécanismes d'amélioration de l'ERC sur les matériaux en alliage par des calculs DFT.

Section expérimentale

Le chapitre 2 fournit les détails expérimentaux et informatiques. Les méthodes de synthèse de tous les échantillons, les informations de caractérisation physique et électrochimique, l'analyse

des produits de réduction de CO₂ et les modèles et paramètres adoptés pour les calculs théoriques sont tous fournis.

Résultats et discussions

Le chapitre 3 correspond au premier objectif. Des électrodes poreuses dendritiques en Pb ont été synthétisées et optimisées. L'activité catalytique du Pb dendritique a été étudiée et la performance d'ERC a été testée. La surtension d'ERC a été diminuée et la densité de courant partiel de réduction du formiate a été augmentée grâce à la structure dendritique hautement active avec une surface super rugueuse. La publication liée à ce chapitre est:

Fan M, Garbarino S, Botton GA, Tavares AC, Guay D (2017) Selective Electroreduction of CO₂ to Formate on 3D [100] Pb Dendrites with Nanometer-Sized Needle-Like Tips. *J. Mater. Chem. A*, 2(5):20747-20756.

Des électrodes poreuses en Pb avec surface spécifique élevée ont été préparées par la technique simple et rapide de modèle dynamique de bulles d'hydrogène (DHBT). Les électrodes poreuses en Pb sont formées par une structure primaire en nid d'abeille et une structure secondaire en dendrite se développant le long de l'axe [100]. La structure dendritique est composée de monocristal allongé ayant une longueur quasi constante d'environ 200 nm et un diamètre de pointe de 22 nm.

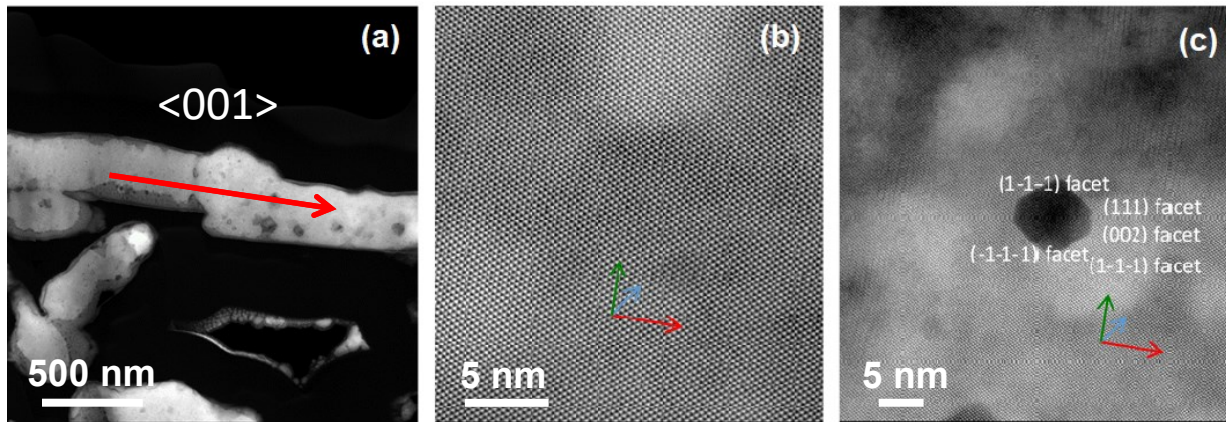


Figure R1 Images STEM d'une coupe transversale préparée à partir du film poreux de Pb déposé à -4,0 A cm⁻² et 40 secondes. (a) Image STEM à fond noir annulaire à faible grossissement de quelques filaments présents dans la section transversale. La flèche rouge indique la longueur et l'orientation d'un cristal parfaitement orienté avec l'axe long <001>. Les segments au-delà de la flèche sont légèrement désorientés (de quelques degrés) par rapport à la direction de la flèche rouge. D'autres filaments dans le champ de vision seraient orientés de manière aléatoire par rapport au fil le plus long. Des petites cavités (taches sombres à l'intérieur des filaments) sont également observées à l'intérieur des filaments. Une couche d'oxyde très mince est également observée (avec un contraste intermédiaire) sur les bords (d'où les surfaces) des filaments. (b) Image STEM à haute résolution du réseau cristallin de Pb de haute qualité. Les principaux ensembles de plans sont identifiés par les flèches codées en couleur (c) Image de réseau à proximité d'une cavité montrant la nature très facettée des surfaces avec les plans de réseau identifiés par les flèches codées par couleur et les indices Miller.

L'électro-réduction du CO₂ effectuée sur ces électrodes a montré des rendements faradiques pour le formiate supérieur à 90% pour les surfaces électrochimiques supérieures à 500 cm², atteignant jusqu'à 97% à -0,99 V vs RHE avec une densité de courant de -7,5 mA cm⁻². Les électrodes poreuses en Pb ont en outre montré une stabilité remarquable à la fois en termes de densité de courant et d'efficacité faradique de formiate, avec des valeurs constantes d'environ 8 mA cm⁻² et 98%, respectivement, sur une électrolyse prolongée de 6 heures. Les performances améliorées des électrodes poreuses en Pb ont été attribuées à la structure secondaire en dendrite qui pourrait aider à concentrer les réactifs dans la couche limite.

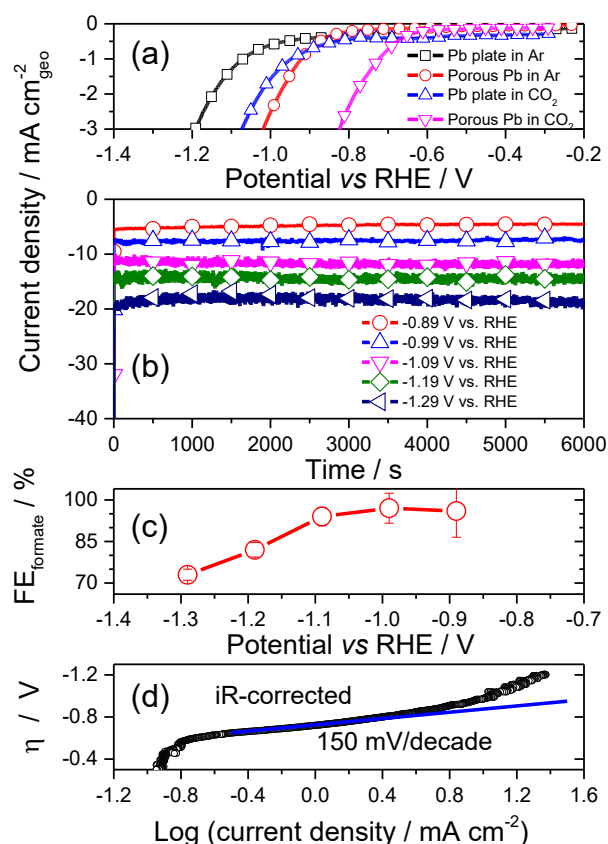


Figure R2 En (a), voltampérométrie à balayage linéaire d'une plaque de Pb et de films de Pb poreux dans KHCO₃ 1 M saturé en Ar et CO₂. Le taux de balayage était de 5 mV s⁻¹. En (b), variation de la densité de courant d'électroréduction de CO₂ (ERC) à différents potentiels d'électrolyse. En (c), variation de l'efficacité faradique du formiate par rapport au potentiel d'électrode. En (d), variation de la surtension de réduction du CO₂ par rapport au logarithme de la densité de courant. Le film poreux de Pb a été déposé à -4,0 A cm⁻² pendant 40 secondes.

Le chapitre 4 correspond au deuxième objectif. Le Pb poreux dendritique a été décoré en déposant une couche extrême de Bi dendritique. La surtension d'ERC a encore diminué de 200 mV sur ce Pb dendritique décoré avec Bi, et le taux de production de formiate a été augmenté.

Les sites actifs de la surface dendritique de Bi ont été étudiés et démêlés grâce à des études physiques et électrochimiques. La publication relative à ce chapitre est:

Fan M, Prabhudev S, Garbarino S, Qiao J, Botton GA, Harrington DA, Tavares AC, Guay D (2020) Uncovering the Nature of Electroactive Sites in Nano Architected Dendritic Bi for Highly Efficient CO₂ Electroreduction to Formate. *Appl. Catal. B-Environ.*, 274:119031.

L'électrode dendritique de Bi avec une grande quantité de défauts et des facettes à haut indice a été synthétisée sur un substrat de Pb poreux. L'identification des sites de Bi les plus actifs a été réalisée grâce à une analyse détaillée à l'échelle atomique de la surface de la dendrite et au masquage des sites inactifs à faible indice. Il a été démontré que les défauts et les facettes à indice élevé des dendrites de Bi sont les sites les plus actifs où la réduction du CO₂ en formiate s'est produite.

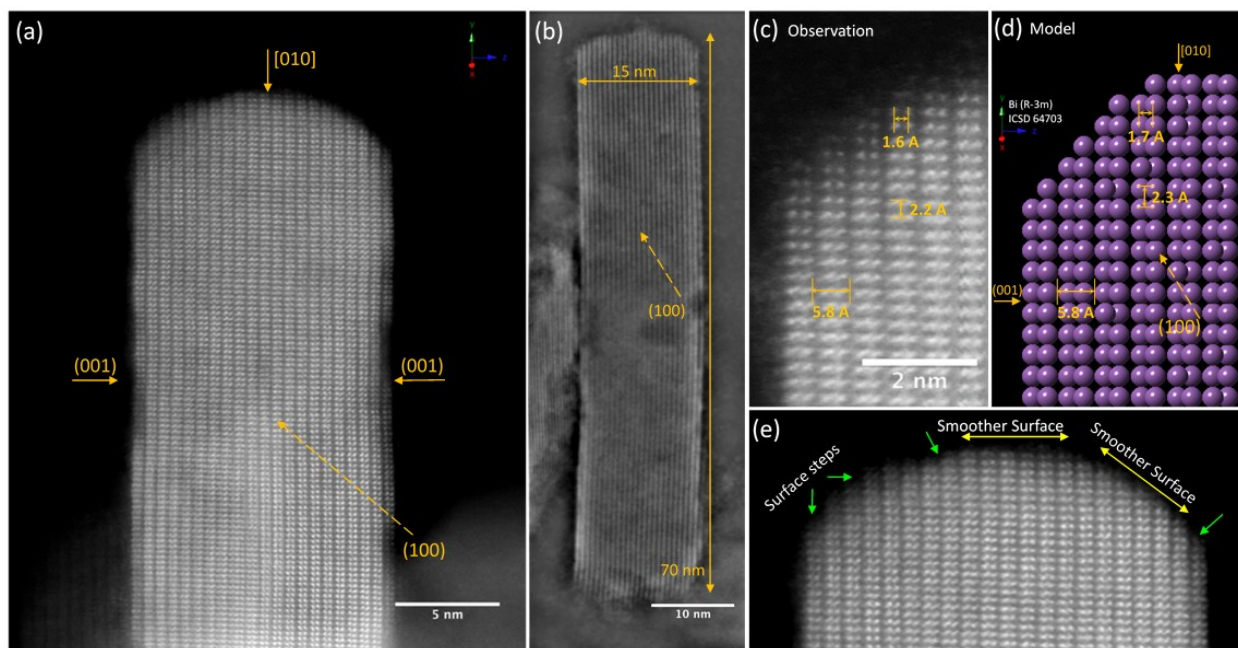


Figure R3 Éluclation de la structure dendritique bi avec une tige corrigée des aberrations. (a, b) Images HAADF-STEM montrant la structure dendritique à différents grossissements. Remarque: l'image (b) s'affiche après le filtrage passe-bande. (c, d) Comparaison de l'arrangement de réseau dendritique observé avec le modèle bi rhomboédrique (R-3m) le long de N (100). (e) Image HAADF-STEM mettant en évidence la structure de surface détaillée de la dendrite.

Le dendrite de Bi est hautement sélectif pour l'électroréduction de CO₂ en formiate avec une efficacité faradique de 98% et une densité de courant de 18,8 mA cm⁻² (344 μmol cm⁻² hr⁻¹) à -0,82 V vs RHE, ce qui n'est que de 600 mV de plus négatif que le potentiel thermodynamique. La structure dendritique et les performances d'électrolyse de CO₂ sont remarquablement stables au cours de l'électrolyse la plus longue (15 heures) que nous ayons réalisée. De plus, un taux de

production beaucoup plus élevée ($1,63 \text{ mmol cm}^{-2} \text{ h}^{-1}$ ou 95 mA cm^{-2} à $-0,82 \text{ V}$ par rapport à RHE) sans aucune pénalité majeure sur l'efficacité faradique de formiate ($92\% \pm 4\%$) a été atteinte avec le même électrode fonctionnant dans des conditions où le flux de CO_2 ne limite pas ses performances (mesures dans cellule d'écoulement à haute pression).

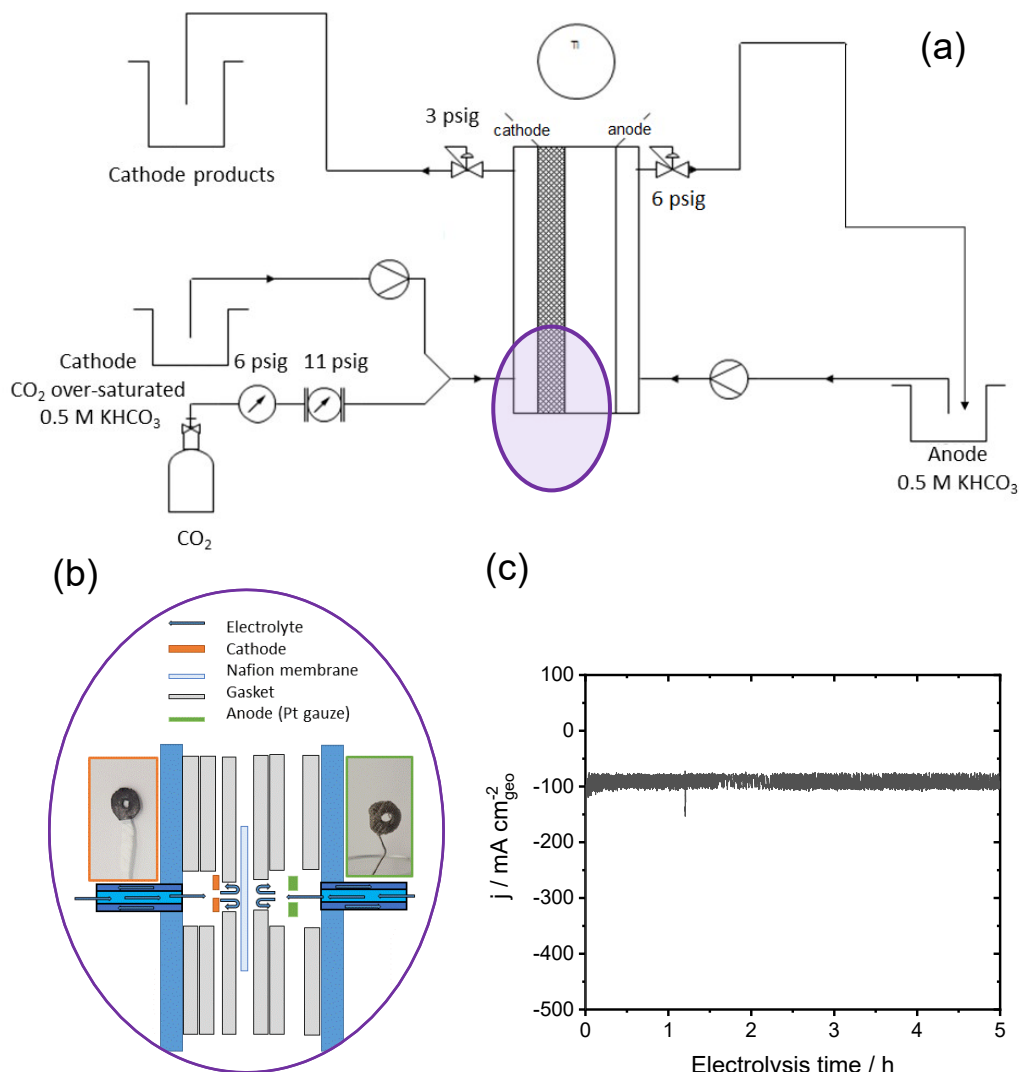


Figure R4 Illustration schématique (a) du système de cellule d'écoulement et (b) du cœur de la cellule. (c) Variation de la densité de courant avec le temps d'électrolyse de l'électrode de $\text{Bi}_{\text{den}} / \text{Pb}_{\text{porous}}$. Voir le texte principal pour tous les détails expérimentaux.

Ce travail présente une méthode simple pour concevoir et fabriquer des matériaux sous forme dendritique avec d'excellentes performances pour l'ERC. Il fournit également des informations à l'échelle atomique sur la nature des sites actifs à la surface des dendrites. Enfin, il illustre que les matériaux d'électrodes dendritiques sont capables de résister à une très forte densité de courant

et donc d'atteindre un taux de production très important si l'alimentation de CO₂ à l'électrode n'est pas limitative.

Le chapitre 5 correspond au troisième objectif. Le Sn a été introduits dans les matériaux dendritiques à base de Pb pour former des alliages dendritiques binaires. Le mécanisme de l'effet d'alliage sur l'amélioration d'ERC a été étudié par les calculs théoriques. La publication relative à ce chapitre est:

Fan M, Eslamibidgoli MJ, Zhu X, Garbarino S, Tavares AC, Eikerling M, Guay D (2020) Understanding the Mechanism of CO₂ Electrochemical Reduction on Dendritic Sn₁Pb₃ alloy: A Computational-Experimental Investigation. *ACS Catal.*, *Submitted*.

Le Sn a été allié avec du Pb pour synthétiser l'électrode d'alliage dendritique de SnPb. Nous avons étudié l'activité catalytique de l'alliage dendritique Sn₁Pb₃ pour l'électroréduction du CO₂ en formiate et le comparé avec du Pb dendritique. La concentration de Sn dans le dépôt a été choisie pour correspondre à la limite de solubilité de Sn dans le fcc de Pb. Le potentiel de début de la réduction du CO₂ en formiate est de -1,01 vs SHE, 80 mV plus positif que celui du Pb dendritique. Le FE_{formate} est très proche de 100% sur la plage de potentiel de -1,16 V à -1,56 vs SHE. L'électrode en alliage dendritique Sn₁Pb₃ présente une densité de courant d'ERC de 17,2 mA cm_{geo}⁻² (295 μmol h⁻¹ cm⁻²) avec FE_{formate} = 92% à une surtension de 500 mV dans un système de cellule d'écoulement.

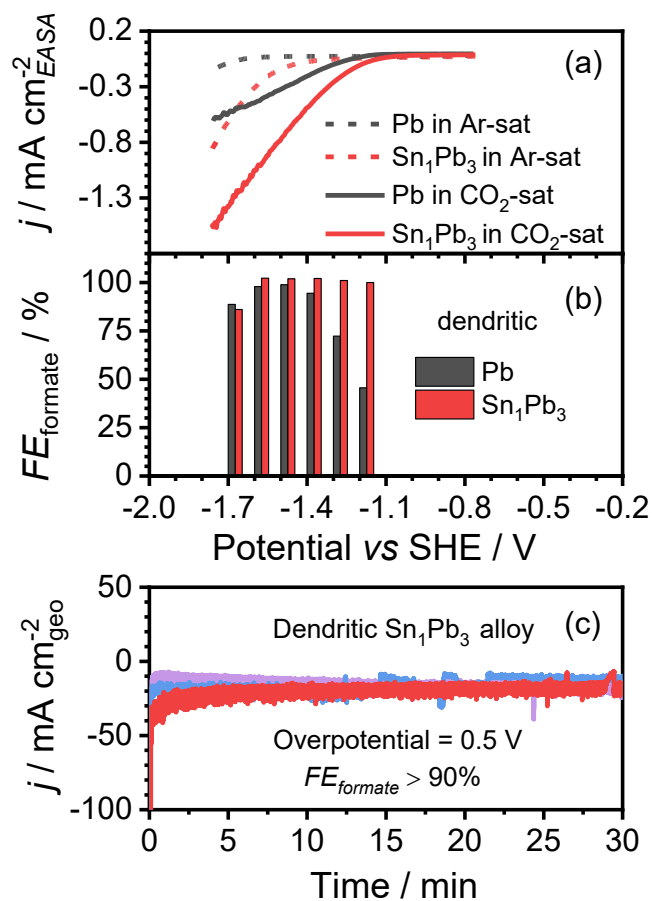


Figure R5 En (a), courbes de voltampérométrie à balayage linéaire dans d'électrolyte de 0,5 M KHCO₃ enregistrées à 5 mV s⁻¹. En (b), efficacité faradique de formiate (FE_{formate}) enregistré après 30 minutes d'électrolyse à chaque potentiel. En (c), densité de courant enregistrée au niveau d'une électrode en alliage Sn₁Pb₃ dans un système de cellule d'écoulement.

Les calculs de DFT suggèrent que l'électroréduction de CO₂ sur les surfaces de Pb (100) et de Sn₁Pb₃ (100) passe par l'intermédiaire de HCOO*, conduisant à la formation exclusive d'acide formique / formiate. Les études DFT montrent également que la diminution observée du potentiel de début ne peut être comprise que si une couche d'eau simulant l'électrolyte est introduite dans le domaine de la modélisation pour la DFT (par opposition à la modélisation sous vide). Dans ces conditions (et uniquement dans ces conditions), les calculs DFT sont en mesure de prédire l'effet bénéfique du Sn dissous sur le potentiel de début du plomb. En effet, les potentiels de début pour la formation de formiate prédits par les calculs DFT sont de -0,99 et -1,33 V vs SHE pour les surfaces Sn₁Pb₃ (100) et Pb (100), respectivement, en accord raisonnable (en considérant le modèle de calcul simplifié) avec des valeurs mesurées expérimentalement, qui sont respectivement de -1,01 et -1,08 par rapport à SHE. Sur la surface de Sn₁Pb₃ (100), l'intermédiaire HCOO* est moins fortement adsorbé que sur Pb (100), ce qui réduit le potentiel

de début. Ceci est une illustration vivante du principe de Sabatier qui stipule que les intermédiaires de réaction ne doivent pas s'adsorber trop fortement à la surface de l'électrode. Cet effet de déstabilisation de Sn dissous dans du fcc Pb se produit grâce à une hydrophilie accrue de l'électrode qui conduit à une réorientation de l'intermédiaire HCOO^* à la surface de l'électrode.

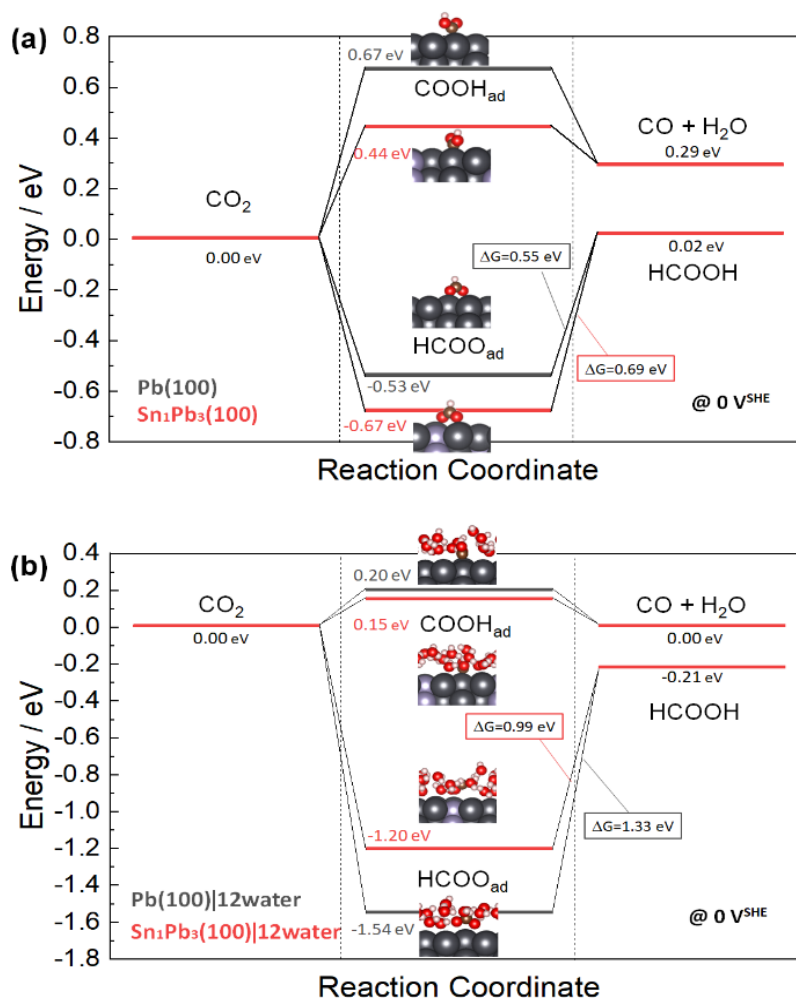


Figure R6 Diagrammes d'énergie pour la réduction de CO_2 . En (a), conditions de la phase gazeuse à 0 V. En (b), avec 12 molécules d'eau à 0 V.

Conclusions

Le chapitre 6 résume brièvement les principales conclusions de mes recherches et fournit les défis et les perspectives dans ce domaine.